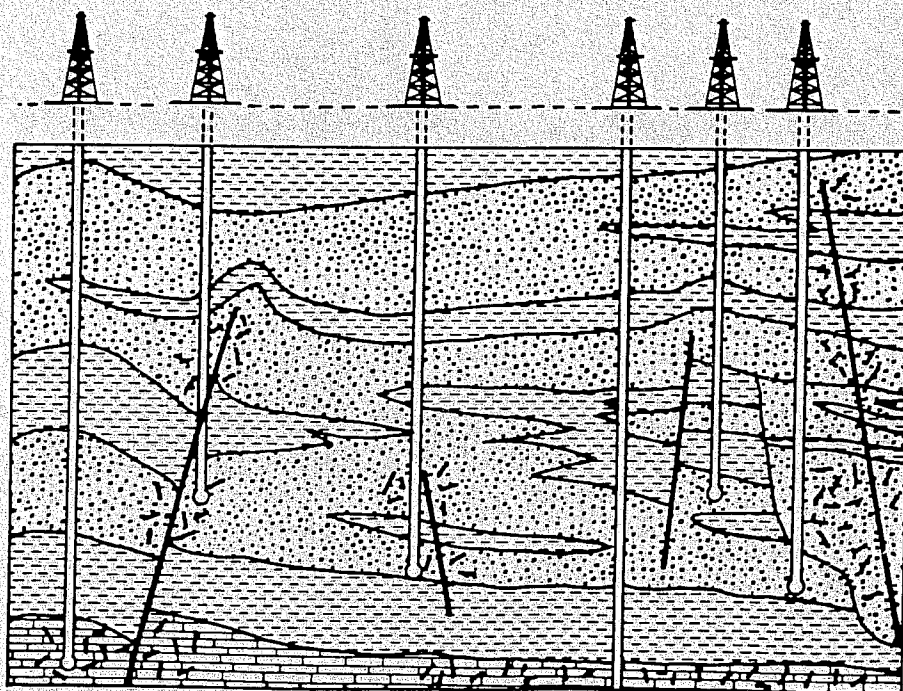
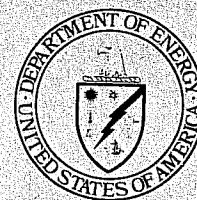
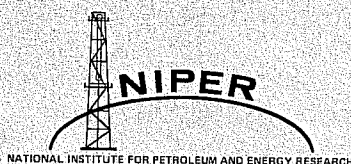


PREPRINTS

VOLUME 2: Poster Presentations

THIRD INTERNATIONAL
RESERVOIR
CHARACTERIZATION
TECHNICAL CONFERENCE

November 3 - 5, 1991
Tulsa, Oklahoma



Co-Sponsors

IIT Research Institute • National Institute for Petroleum and Energy Research
and
U.S. Department of Energy

PREPRINTS

VOLUME 2: Poster Presentations

THIRD INTERNATIONAL
RESERVOIR
CHARACTERIZATION
TECHNICAL CONFERENCE

November 3 - 5, 1991
Tulsa, Oklahoma

Co-Chairmen

Thomas E. Burchfield, NIPER

Thomas C. Wesson, U.S. DOE

Steering Committee

Edith Allison, U.S. DOE
Bill Almon, Texaco Exploration & Production Co.
Rod Boade, Phillips Petroleum Company
Frank Carlson, Amoco Production Company
Howard Dennis, McKenzie Petroleum Company
Neil Humphreys, Mobil Expl & Prod Services
Mohan Kelkar, University of Tulsa
Bob Lemmon, U.S. DOE
Mike Madden, NIPER
Min Tham, NIPER

Lee Allison, Utah Geological Survey
Steve Begg, BP Exploration
Jack Caldwell, Schlumberger
Dwight Dauben, K&A Energy Consultants
Mike Fowler, Exxon USA
Susan Jackson, NIPER
Charles Kerans, Bur of Econ Geol, Univ of Texas
Bill Linville, NIPER
James Russell, Russell Petroleum Co.

Co-Sponsors

IIT Research Institute • National Institute for Petroleum and Energy Research
and
U.S. Department of Energy

TABLE OF CONTENTS

- 3RC-02 *Description of Thin-Layered Sandbody Reservoir During State of Exploration and Development*, Liu Zerong and Hou Jiagen, University of Petroleum Peoples Republic of China
- 3RC-03 *How to Estimate Confidentiality of Reserve: A Quick Practical Solution*, T. Kuhn and Dr. Zs. Komlosi, Hungarian Hydrocarbon Institute
- 3RC-07 *An Optimal Method for Averaging The Absolute Permeability*, T. Gallouet, Universite de Chambéry and, D. Guerillot, Institut Francais du Petrole
- 3RC-13 *Fractal Analysis of Core Photographs With Application to Reservoir Characterization*, H.H. Hardy, Conoco, Inc., Ponca City, Oklahoma
- 3RC-19 *Electromagnetic Oil Field Mapping for Improved Process Monitoring and Reservoir Characterization*, John R. Waggoner and A.J. Mansure, Sandia National Laboratories, Albuquerque, New Mexico
- 3RC-21 *Reservoir Simulation of Fluvial Reservoirs: Two Prognostic Models*, Kelly Tyler and Adolfo Henriquez, Statoil, Stavanger, Norway
- 3RC-25 *Detecting Permeability Anisotropy and Cross-Bedding Patterns by Using Mini-Field-Permeameters*, Y. Aasum, E. Kasap, and M. Kelkar, The University of Tulsa, Tulsa, Oklahoma
- 3RC-26 *Defining Water-Drive Gas Reservoirs: Strategies for Data Acquisition and Evaluation*, W.M. Colleary, J.R. Hulme, and S.M. Al-Haddad, Colorado School of Mines, Golden, Colorado
- 3RC-30 *Renormalization: A Multilevel Methodology for Upscaling*, A.D.W. Jones, P.R. King, C. McGill, and J.K. Williams, BP Research, Middlesex, United Kingdom
- 3RC-31 *Estimating Effective Permeability: A Comparison of Techniques*, C. McGill, P.R. King, and J.K. Williams, BP Research, Middlesex, United Kingdom
- 3RC-35 *Earth Stress Orientation -- A Control on, and Guide to, Flooding Directionality in a Majority of Reservoirs*, K.J. Heffer and J.C. Lean, BP International Limited, Middlesex, United Kingdom
- 3RC-38 *Thermal Simulation of Shallow Oil Zone Light Oil Steamflood Pilot in the Elk Hills Oil Field*, Bob Harris, U.S. Department of Energy; Alan Burziaff, Bergeson; and Vernon Brait, Simtech
- 3RC-45 *Characterization of Reservoir Heterogeneity, Fuller Reservoir and Haybarn Fields, Paleocene Fort Union Formation, Fremont County, Wyoming*, C.Wm. Keighin and R.M. Flores, U.S. Geological Survey, Denver, Colorado
- 3RC-46 *Microscopic to Field-Wide Diagenetic Heterogeneity in Deltaic Reservoirs From Brazil: Description, Quantification and Integration With Other Reservoir Properties*, Marco A. S. Moraes and Ronald C. Surdam, PETROBRAS/University of Wyoming, Laramie, Wyoming

- 3RC-52 *Variability in Carbonate Reservoir Heterogeneity Among Jurassic Smackover Oil Plays of Southwest Alabama*, E.A. Mancini, R.M. Mink, B.H. Tew, D.C. Kopaska-Merkel, and S.D. Mann, Geological Survey of Alabama, Tuscaloosa, Alabama
- 3RC-55 *Minipermeameter Study of Fluvial Deposits of the Frio Formation (Oligocene), South Texas: Implications for Gas Reservoir Compartments*, D.R. Kerr, A.R. Scott, J.D. Grigsby, and R.A. Levey, Bureau of Economic Geology, The University of Texas at Austin
- 3RC-59 *High Resolution Seismic Imaging of Fractured Rock*, Ernest L. Majer, Larry R. Myer, and John E. Peterson, Lawrence Berkeley Laboratory, Berkeley, California
- 3RC-62 *Natural Gas Reserve Replacement Via Infield Reserve Growth: An Example From Stratton Field, Onshore Texas Gulf Coast Basin*, R.A. Levey, M.A. Sippel, R.P. Langford, and R.J. Finley, Bureau of Economic Geology The University of Texas at Austin
- 3RC-64 *An Expert System for the Network Modelling of Pore Structure and Transport Properties of Porous Media*, I. Chatzis, M. Ioannides, and A. Kantzas, University of Waterloo, Waterloo, Ontario, Canada
- 3RC-65 *Formation Evaluation Techniques for Identifying Secondary Gas Resources: Examples From the Middle Frio, Onshore Texas Gulf Coast Basin*, J.M. Vidal and W.E. Howard, ResTech and, R.A. Levey, B.E.G., Houston, Texas
- 3RC-68 *Reservoir Characterization and Geostatistical Modeling - The Integration of Geology Into Reservoir Flow Simulation: East Painter Reservoir Field, Wyoming*, D.S. Singdahlsen, Chevron U.S.A. Inc., Denver, Colorado
- 3RC-76 *Integrated Field, Analog, and Shelf-Scale Geologic Modeling of Oolitic Grainstone Reservoirs in the Upper Pennsylvanian Kansas City Group in Kansas (USA)*, W. Lynn Watney, J.A. French, Jr., J.C. Wong, and W.J. Guy, Jr., Kansas Geological Survey, Lawrence, Kansas
- 3RC-82 *Characterization of Reservoir Heterogeneities From Outcrop and Core Drills (Upper Triassic Fluvatile Sandstone)*, P. Houel, J. Delmas, G. Desaubliaux, Y. Mathieu, F. Verdier, Institut Francais du Petrole
- 3RC-89 *Global Sedimentary Databases as Engineering Resources*, Jim Myers, University of Houston, Houston, Texas

A TECHNIQUE OF THE THIN LAYER SANDBODY INTERPRETATION IN EXPLORATION AND DEVELOPMENT STAGE

Liu Zerong Hou Jiagen and Xin Quanlin

Department of Exploration
University of Petroleum
Dongying, Shandong, P. R. China

I. INTRODUCTION

The NZ oilfield is mainly in primary lithological primary lithological pools in sandstone/mudstone sequences of the Tertiary in east of China. There had been no significant achievement in oil production for a long time, because the subsurface geology is quite complicated and that the reservoir rocks, the deep water turbidite sandstones, are small in size, thin layer, deep burial. Up to now we have discovered quantitatively 55 sandbodies by means of the technique of the thin layer sandbody interpretation. The Z20 fault block in which three sandbodies are interpretation quantitatively is an experimental developing area in this oilfield. Five evaluation wells are designed, The drilling program verified our interpretation quite exact. In about 3000m deep target intervals, the predicted depth error is less than 10m, the predictable minimum thickness is about 10m. These evaluation wells also produce commercial oil from three sandbodies.

II. THE THIN LAYER SANDBODY INTERPRETATION TECHNIQUE

The characteristics of the technique is combined usage of the seismic, geological and well-logging information. It works on following steps:

A. Reservoir Calibrating

The seismic interpretation of reservoir sandbodies is generally starting with available well data. For this reason, it is necessary to know the locations of the seismic records corresponding to the actual sandbodies. This process is known as reservoir calibrating. We have used three methods of calibrating: the depth-time conversion, VSP and the synthetic seismogram.

B. Horizontal Tracing

Considering the geological information of the studied areas and analysing one-dimension or two-dimension seismic models, we have understood the reflection characters of different sandbodies with different shapes, thickness and combinations with mudstones. In conclusion, we have established four sandbody reflection patterns which are the basement on tracing and predicting the sandbodies in this area.

1. Lens single wave, correspond to the sandbody less than $\lambda/4$ in thickness (λ is wavelet length).
2. Lens compound wave, correspond to the $\lambda/4 - \lambda/2$ thick sandbody.
3. Parallel double track wave, correspond to the seismic responses of the $\lambda/2 - \lambda$ thick sandbody.
4. Apparent high frequency multi-wave, correspond to the sandstone groups over λ thick which are the river-mouth sandbars.

C. Model Checking

The model checking will improve our recognizations of the reservoir reflection dynamics. As a lot of experiences obtained, we can summarize or set up reservoir reflection models.

D. Integral Interpretation

After horizontal tracing, we can draw a series of maps for the interpreted sandbodies such as the sandbody distribution map, isotime (TO) map or isopach of the sandbody's top depth, isopach of the sandbody's thickness. All of the maps mentioned above is on the base of interpretation of the waveform and amplitudes of the seismic reflection. In order to be accurate and reliable, one must make use as much information as possible in the integral interpretations i.e. synthetic acoustic logging section, frequency spectrum, test well data, and so on,

E. Effect Testing

The thin sandbody interpretation can only be tested by well drilling.

III. DISCUSSION

We have detailly analysed the key factors that the technique are applied successfully in the NZ oilfield and summarized some points of views as follows:

A. Special Geological Conditions

The NZ oilfield locates in the deep lacuna. The structure is simple or not complicated by many faults.

B. Favourable Stratum column

In this ares, the target intervals are mainly turbidites sandstones frequently alternating with the deep lacuna. The structure is simpe or not complicated by many faults.

C. The Study of Velocity as a Foundation of Sandbody Interpretation

D. High quality seismic data

The main fators of high quality seismic data is that the area has been explored by high resolution seismics for many years and there are the seismic experiments in the field and in the laboratory. The seismic frequency is high and wide. So the high-fidelity waveform and amplitude are obtained.

E. Application of Integral Information

It is necessary to apply many kinds of seismic methods, including waveform, amplitude, frequency spectrum, impendence and theoritical model etc., to compensate and verify each other.

F. A Special Reservoir Forming Condition

In the oil source lacuna, the turbidite sandbodies are surrounded by source rocks and form primary lithological oil pools. Therefore the problem of surveying complex lithological oil pools is simplified to the recognizing reservoir bodies.

HOW TO ESTIMATE THE RELIABILITY OF RESERVES? A QUICK AND PRACTICAL SOLUTION

Tibor Kuhn
Zsolt Komlosi

Hungarian Hydrocarbon Institute
Budapest, Hungary

1. ERROR IN ORIGINAL RESERVE IN PLACE

Error m_Q in reserve is assumed as a composition of the at-well and inter-well errors weighted with modelling error factor marked as m_a , m_i and W_M respectively:

$$m_Q = W_M[m_a^2 + m_i^2]^{\frac{1}{2}}$$

The relative error m_Q in reserve calculated is interpreted as an over estimation factor of the true reserve to avoid problem of m_Q higher than 100%. The relative error relating to original reserve in place estimated can be calculated as $m_{QO} = \pm m_Q / (1 + m_Q)$.

The components of error are as follows:

1.1. The at-well error being characteristic for parameters derived in separate wells is composed from errors of main isovol parameters as porosity, water saturation and net pay weighted with lithological factor marked by m_p , m_s , m_h and W_L respectively:

$$m_a = [(m_p^2 + m_s^2 + m_h^2)W_L]^{\frac{1}{2}}$$

The weighting empirical factor W_L taken arbitrarily from Table I determined by consultations with specialists of great experience is characteristic to rock type of reservoir.

The absolute error of effective porosity based on publications and own experience being at disposal is one porosity per cent, therefore $m_p = 100/PHI[\%]$. At reservoirs of low porosity ($PHI < 2\%$) the relative error of porosity is considered as much as 50%.

The error of original hydrocarbon saturation using Fig.1 derived from analysis of Archie-equation can be calculated by water saturation S_w of formation:

$$m_s = 100\{\text{value taken from Fig.1}\}/(100 - S_w^{[\%]})$$

Table I

Matrix material \ Clay (silt) content	Negligible (<5 %)	Corrective (5-20 %)	Significant (>20%)
	Lithological Factors W_L		
Sandstone	1.0	1.5	2.0
Conglomerate or breccia	1.5	1.8	2.1
Carbonate of double porosity	1.8	2.0	2.3
Carbonate of secondary porosity	2.2	2.3	2.5
Metamorphic or basement rock	2.5	2.7	3.0

The error m_h of net pay is influenced by error of total thickness h_{to} considered to be $e=1m$ (if unit of 'h' other than meter, 'e' is to be converted) weighted with relative net pay h/h_{to} :

$$m_h = 100[e/(h/h_{to})]/h$$

The error calculation needs mean values of errors derived at each well. They can be averaged weighting with area (mapping the values) or net pay but, in the worst case, the error can be calculated using mean parameter values of the reservoir.

1.2. The inter-well error m_i being characteristic for space between wells including uncertainty of mapping is assumed to be determined by the shape of reservoir and the degree of tectonism as found in Table II.

1.3 The modelling error factor W_M characterising 'gap' between the geological, petrophysical or depletion (etc.) models used and the true reservoir conditions can be confined by the quality of information originated from separate sources being at disposal and accordance among them. Component factor values for the well information including core analysis, logging and production test as well as maturity of the field were arbitrarily estimated and tabulated based on professional experiences of the authors and skilled specialists.

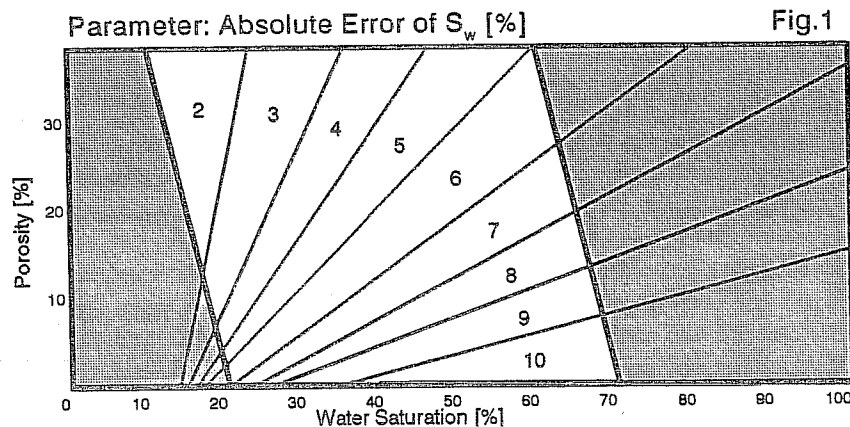


Table II

Type of Reservoir \ Tectonics	No	Recreatable	Disturbed
	Inter-Well Error m_i [%]		
Plain Sandstone	5	7	10
Anticline with more maximum	7	10	13
Turbidite, Channel Sediment	10	12	17
Lithological Trap	9	11	16
Blocked Structure	--	12	20

'Degree of accordance' among information available is ranged from 'accordance' to 'unresolvable contradictions' yielding weighting factor values as much as 0.8 and 1.4 respectively.

2. ERROR IN RECOVERABLE RESERVE

At the beginning of production the error of recoverable reserve is bigger by additional error m_{Qra} than that of the original reserve. After longer production period recoverable reserve predictable by production history becomes more independent from original one, moreover, its error can be considered negligible at normal technical abandonment of production. Therefore the error m_{Qr} of recoverable reserve depends on reserve q has been depleted and reserve q_a depletable by abandonment too:

$$m_{Qr} = [1 - q/q_a][m_{Qo}^2 + m_{Qra}^2]^{1/2}$$

The additional error m_{Qra} is based on weighted uncertainty of reservoir permeability m_K defined with porosity and saturation error:

$$m_K = 1.5[W_L(m_p^2 + m_s^2)]^{1/2}$$

The weighting factors of basic error tabulated show the effect of date of estimation (the maturity of the field); production technology applied; natural water inflow expectation; quality of production project; and quality of economic analysis.

3. CONCLUSION

The method has been developed focusing attention on technical aspect of reserve projection by subjective judgments based on experience and knowledge. It is very simple one, easy to perform, in spite of that reserve estimation is a fairly complicated task.

Results of the method let the evaluators and the management compare different fields and different conditions.

AN OPTIMAL METHOD FOR AVERAGING THE ABSOLUTE PERMEABILITY¹

Thierry Gallouët

Département de Mathématiques
Université de Savoie,
73011 Chambéry, France

Dominique Guérillot²

Division Gisements
Institut Français du Pétrole,
92506 Rueil Malmaison, France

I. INTRODUCTION

Improving the recovery in hydrocarbon reservoirs demands a very detailed knowledge of the subsurface porous media and, in particular, of the spatial variations in their properties. The means available for analysing and modeling these often complex variations are increasingly varied. However, accounting for this complexity in the numerical simulations of the fluid flows in the porous

¹Supported by the "Fonds de Soutien aux Hydrocarbures - COPREP", joint project IFP-ELF

² now seconded to ELF-U.K. Geoscience Research Center, 114A Cromwell Road, London SW7

media still remains. Discretized models cannot take into account heterogeneities of intermediate scale (decimetre to decametre) for reasons of memory size and calculation time of present-day computers. One of the practical problems faced by the user of a reservoir model is the following:

"How to average the physical quantities available so that the 'simulator' best reconstructs the real behaviour of the reservoir ?"

Note that this problem is different from the problem entitled *equivalent homogeneous medium* in so far as the attempt is not to model the structure of the reservoir by a continuous medium, but by a discrete structure, directly usable by the 'simulators'.

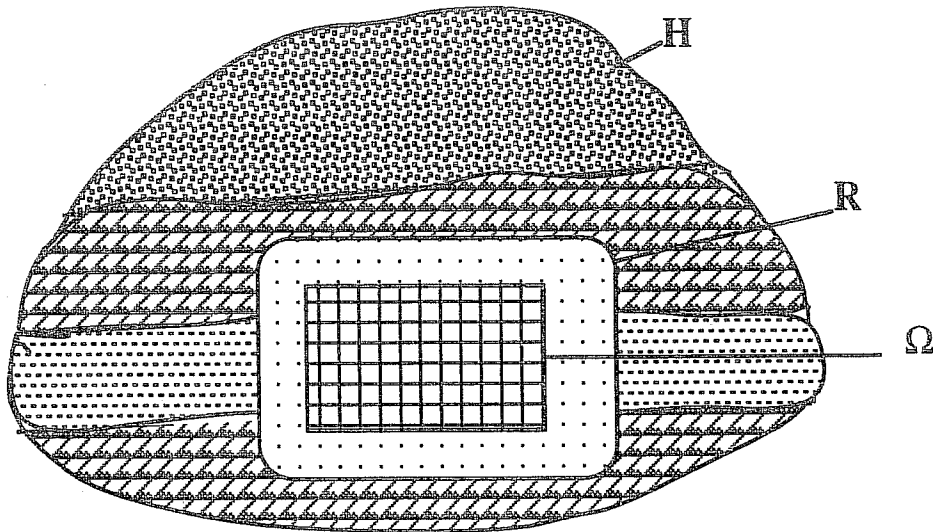
This general problem is a vast one. Among the physical quantities that have to be averaged, we shall focus here only on the absolute permeability.

II. PROPOSED METHOD

As proposed by Marle: "Let us consider a heterogeneous porous medium H (see next figure) in which an incompressible fluid flow takes place and replace a part Ω of this medium by a homogeneous medium with characteristics such that the overall flow is disturbed as little as possible".

It appears that the very definition of an equivalent permeability demands assumptions on the type of flow to be reconstructed to return to a local problem over a region R containing Ω , and requires the introduction of a criterion defining the information which is to be preserved.

We propose the following method:



(1) To define an average permeability which is independent of the solution over the whole domain H , a family of pressure fields P is considered, whose gradient is constant over H :

$$P(x) = \lambda \cdot x \text{ with } x=(x_1, x_2, x_3)^t \text{ and } \lambda=(\lambda_1, \lambda_2, \lambda_3)^t$$

This hypothesis implicitly presumes a large distance from any well. Other families of pressure fields could be selected for flows in their neighbourhood.

(2) A coupling is assumed on the edge of R between this *average* pressure P and the *local* pressure in R .

These hypotheses serve to return to the resolution of the following local problem (depending on parameter λ): "Find p and q such that:

$$\begin{aligned} q &= -k/\mu (\text{grad } p - \rho g) \text{ and } \text{div } q = 0, \text{ on } R \\ p &= \lambda \cdot x, \text{ on } \delta R, \end{aligned}$$

where the permeability tensor k is the only parameter here characterizing the porous medium, and the viscosity μ and the density ρ characterizing the fluid "

Since this problem is linear, it is necessary, in practice to solve d ($d=1, 2$ or 3) local problems to calculate the average matrix K_m by using the following criterion:

K_m is such that $J(K_m) \leq J(K)$,

$$\text{with: } J(K) = \int_D \left\{ \int_{\delta\Omega} [(Q-q) \cdot n]^2 d\sigma \right\} d\lambda,$$

where $D = \{\lambda \text{ such that } \lambda_1^2 + \lambda_2^2 + \lambda_3^2 = 1\}$, $K = k$ on $R \setminus \Omega$,

$$\begin{aligned} Q &= -K/\mu (\text{grad } P - \rho g) \text{ and } \text{div } Q = 0, \text{ on } R \\ P &= \lambda \cdot x, \text{ on } \delta R, \end{aligned}$$

and $n = (n_1, n_2, n_3)^t$ is the vector normal outside to the boundary.

A physical interpretation: try to minimize the square of the differences between local q and average Q filtration velocities, by averaging the differences with respect to all directions λ of the average flow.

Note that it is not assumed *a priori* that the average matrix K_m is symmetrical.

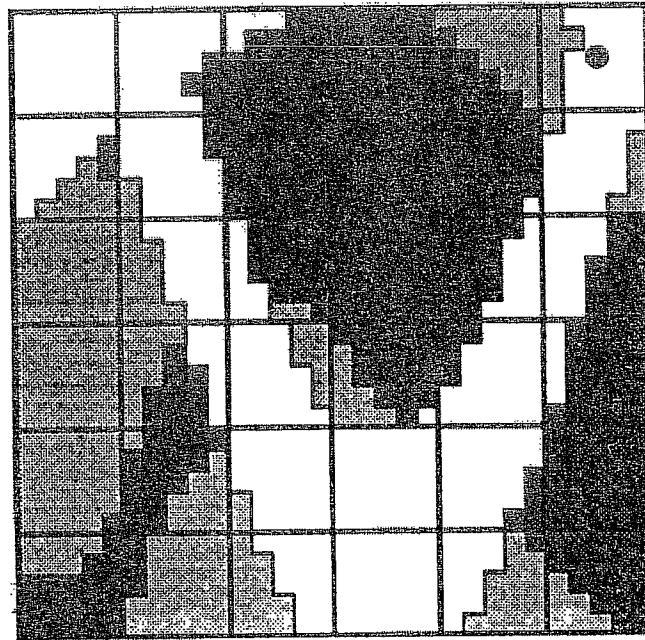
Solving this minimisation problem analytically gives the expression of the coefficients of the matrix K_m :

$$K_m \ddot{u} = - \frac{1}{\text{mes } \Omega} \int_{\delta\Omega} q_{ji}^2 \cdot n_i^2 d\sigma$$

where $q_1 = (q_{11}, q_{12}, q_{13})^t$ is the filtration speed solution of the local problem with $\lambda = (1, 0, 0)^t$, q_2 with $\lambda = (0, 1, 0)^t$ etc.

III. APPLICATION

Applying this method to an example published by White and Horne, 1987, and also used by Corre, and Samier, 1990 (here $d=2$ and $R=\Omega$) (see Figure below) gives the results on the following table:



■ $k = 0.10 \text{ D}$

■ $k = 1.0 \text{ D}$

□ $k = 10.0 \text{ D}$

10. 0.	6.97 -1.08	1.32 1.20	0.1 0.	0.5 -0.04	5.34 0.21
0. 10.	-0.71 7.10	1.13 1.25	0. 0.1	-0.04 0.54	6.51 7.43
5.05 0.56	6.69 2.16	0.1 0.	0.1 0.	0.76 0.66	5.67 -0.97
0.54 5.28	1.37 8.15	0. 0.1	0. 0.1	0.66 0.76	-1.2 7.35
1. 0.	4.60 -0.64	2.27 -0.69	0.1 0.	2.58 0.99	3.4 0.56
0. 1.	-0.30 5.88	0.60 2.71	0. 0.1	0.90 3.25	0.34 4.52
1. 0.	2.55 -0.60	6.25 0.34	0.93 0.52	6.96 -0.72	0.86 0.72
0. 1.	-0.53 2.97	0.44 7.77	0.52 0.93	-0.57 8.08	0.98 1.1
0.92 -0.06	0.37 0.22	8.44 1.01	10. 0.	6.96 -0.72	0.1 0.
-0.06 0.92	0.23 0.37	0.65 9.13	0. 10.	-0.57 8.08	0. 0.1
0.27 0.14	0.75 -0.10	4.51 -0.65	10. 0.	3.72 0.99	0.26 -0.14
0.11 0.26	0.06 0.90	-0.34 5.53	0. 10.	0.90 4.20	-0.14 0.26

Each cell of this table corresponds to the averaged matrix obtained on the coarse mesh. If one wants a symmetrical matrix, it averages the 2 extra-diagonal

coefficients. A 9-point finite volume scheme allows to take into account these unsymmetrical extra-diagonal coefficients.

Other tests have been done to (1) study the influence of choosing different overlapping R domain around the macro-cells, (2) compare the pressure and saturation contours from the microlevel and macrolevel simulations using different maps of heterogeneous permeability distribution.

IV. CONCLUSIONS

A new method for averaging the absolute permeability in 3 D is presented briefly. This method:

(1) gives a rigorous formalism for the practical problem faced by the user of a fluid flow simulator who wants to loose as little as possible his available information on the reservoir heterogeneities. Here, the error on the filtration speed is minimized (and even, it is possible to make *a posteriori* checks of this error),

(2) allows to consider 2 different supports: R which size should be linked to the correlation lengths of the absolute permeability and Ω which is often chosen as the reservoir grid cell;

(3) can be extended to take into account the neighbourhood of wells.

V. REFERENCES (short list)

Samier, P., 1990, A Finite Element Method for Calculating Transmissibilities, Second European Conference on the Mathematics of Oil Recovery, Editions Technip, Arles, France.

White, C.D. and Horne, R.N., 1987, Computing Absolute Transmissibility in the Presence of Fine-Scale Heterogeneity, SPE 16011, presented at the Ninth Symposium on Reservoir Simulation, San Antonio, Texas.

FRACTAL ANALYSIS OF CORE PHOTOGRAPHS WITH APPLICATION TO RESERVOIR CHARACTERIZATION

H. H. Hardy

Conoco
Ponca City, OK

I. INTRODUCTION

This article describes the one- and two-dimensional statistical character of rock property distributions. This character is used to produce statistical distributions of reservoir properties between wells at the reservoir scale.

At present, no interwell data exists at the scale needed to create reservoir property distributions for reservoir simulations. We must, therefore, try to deduce this information indirectly. Analyzing data from several sources gives us more confidence in our conclusions than any single data set. For this reason, this paper addresses the analyses of data from core photos, outcrop photos, and horizontal well logs.

Hewett¹ demonstrated that vertical well logs have a fractal structure called fractional Gaussian noise (fGn). He inferred the horizontal fractal character is different based on miscible flow data and seismic data. The horizontal character he assumed is called fractional Brownian motion (fBm). The present study indicates the statistical structure is not fBm, but fGn in both vertical and horizontal directions.

II. DATA ANALYSES

Core photos are analyzed to define "models" of reservoir property distributions. Core photos only capture light reflectance. Light reflectance is not a direct measure of the

reservoir properties needed for reservoir simulation (e.g., porosity or permeability). Care must be taken in lighting conditions, camera location, film speed, and the like. For outcrop photos, vegetation, shadows, and weathering further complicate photo analysis. Nevertheless, geologists have long used the visual descriptions (light reflectance) of outcrops and core photos to help define geologic trends and depositional units.

Cores were slabbed and polished smooth. The cores were oriented so that bedding planes were horizontal, and core photos were taken. The core photos (e.g., Figures 1a, 2a, and 3a) were digitized. Digitization produces an array of numbers which capture the light intensity on the photo at each "point" on the photo. Once light reflectance is reduced to a set of numbers, many statistical tests can be made. One- and two-dimensional statistical tests were made for this study.

The one-dimensional tests were the same as those used by Hewett¹ for vertical well logs. These were a variogram, Fourier transform, and RS analyses. These were applied to traces parallel, perpendicular, and at 45 degrees to bedding planes in the core photos. Examples of these techniques applied to a horizontal trace are shown in Figure 4.

These tests indicated fGn in for all three directions. The major difference in the vertical and horizontal directions was the total variance of the sample values rather than the fractal character. For example, in Figure 1a, both vertical and horizontal traces are fGn with $H=0.8$. The standard deviation of traces in the vertical direction is twice that of traces in the horizontal direction.

In addition to the one-dimensional tests, two-dimensional Fourier transforms were taken of the photos. Two-dimensional amplitude and phase arrays result. The amplitude arrays are used to calculate the spectral density array for a photo. In order to try to capture the full two-dimensional description, an equation was fit to this two-dimensional spectral density. The result was the following:

$$SD(\omega_x, \omega_y) = A \left[\frac{\delta(\omega_x)}{|\omega_y|^\alpha} + \frac{B}{|\omega_x^2 + \omega_y^2|^\beta} \right] \quad (1)$$

$$\alpha = 2H - 1, \quad \beta = H, \quad \text{and} \quad 0.5 < H < 1.0$$

$$\delta(\omega_x) = [1 \text{ if } \omega_x = 0, \text{ zero otherwise}]$$

If this equation is a good description of core photos, varying the parameters in this equation should produce other core photos. Indeed, this was found to be the case.

Figures 1b, 2b, and 3b were generated using Equation 1. Comparing these to core photos, Figures 1a, 2a, and 3a show that the computer-generated photos are indeed similar to many core photos.

The details of these analyses and the reconstruction of the core photos can be found in Hardy².

The one-dimensional analysis was also applied to the outcrop photo along the traces highlighted in Figure 5. The results of this study was also fGn in the vertical and horizontal directions.

The one-dimensional analysis applied to a neutron porosity log from a horizontal well also gives fGn. Crane and Tubman³ have published similar results for other horizontal wells. Figure 6 shows the similarity of horizontal well data with fGn rather than fBm. In this figure, fGn and fBm of $H=.8$ is plotted for comparison with the actual horizontal well data. The "smoothness" of fBm is not apparent in the horizontal well trace.

III. GENERATING WELL TO WELL CROSS SECTIONS

The spectral density analysis can be used to produce well-to-well cross sections using porosity log data. The technique is based on the observation that the spectral density equation, Equation 1, is made up of two parts. The first part produces "layers;" the second produces "splotches." For example, Figure 2b has $B \ll 1$ so that the first term in Equation 1 dominates. Figure 3b has $B \gg 1$ so that the second term dominates. Figure 2b is mostly "layers" whereas Figure 3b is mostly "splotches."

Well-to-well cross sections are generated by using linear interpolation between the wells to generate the layers. "Splotches" (noise) are added using Equation 1 with $B \gg 1$. H is set to the value found from analyzing the vertical well data. The amount of noise added is determined by the difference between the two well log readings. The details and result of this procedure are described by Beier and Hardy⁴. Crane and Tubman³ have generated cross sections with fGn noise but conditioned the cross section to the well data by the same technique used by Hewett¹ for fBm. The procedure described by Beier and Hardy⁴ is different and is based on our success of producing computer forgeries of core photos.

REFERENCES

1. Hewett, T. A.: "Fractal Distributions of Reservoir Heterogeneity and Their Influence on Fluid Transport," SPE paper 15386 presented at the 1986 SPE Annual Technical Conference and Exhibition, New Orleans, Oct. 5-8.
2. Hardy, H. H.: "The Fractal Character of Photos of Slabbed Cores," to appear in Mathematical Geology.
3. Beier, R. A. and Hardy, H. H.: "Comparison of Different Horizontal Fractal Distributions in Reservoir Simulations."
4. Crane, S. D. and Tubman, K. M.: "Reservoir Variability and Modeling With Fractals," paper SPE 20606 presented at the 1990 SPE Annual Technical Conference and Exhibition, New Orleans, LA, September 23-26.

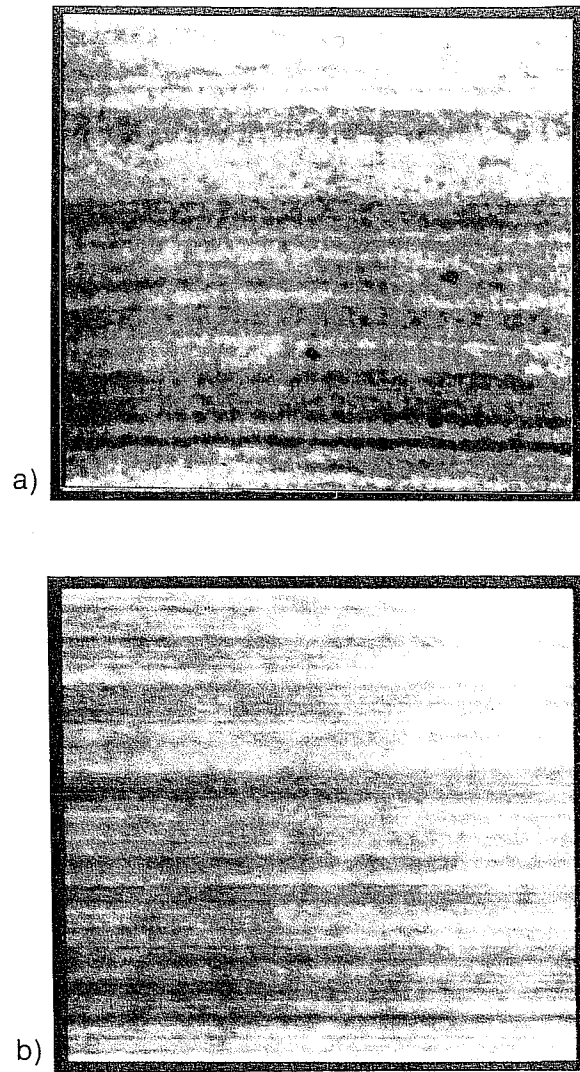


Figure 1. a) Core photo and b) computer generated core photo.

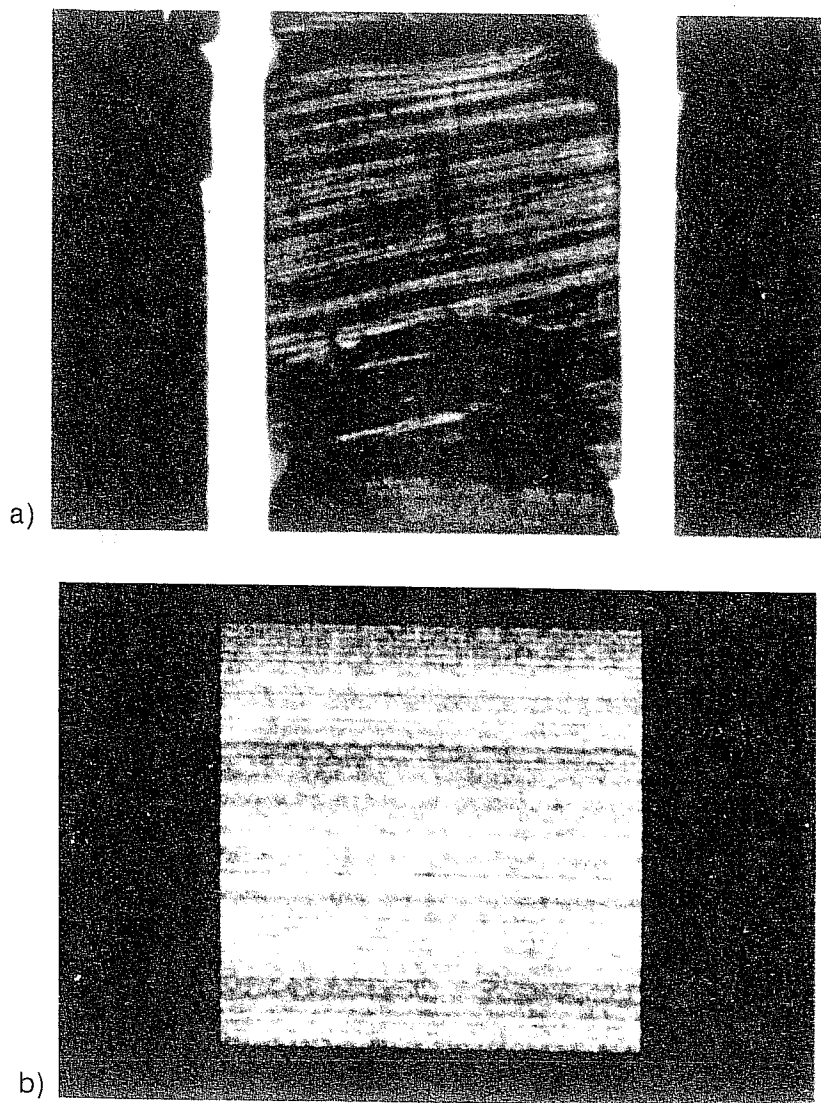


Figure 2. a) Core photo and b) computer generated core photo.

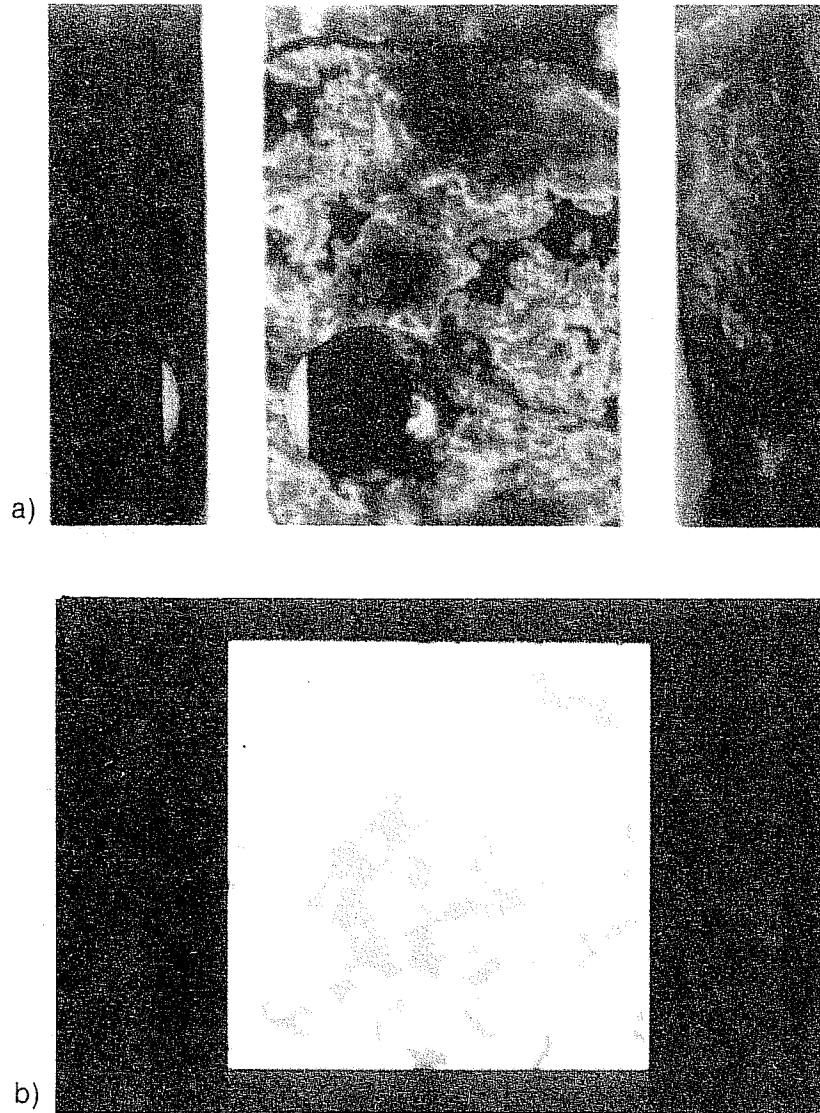


Figure 3. a) Core photo and b) computer generated core photo.

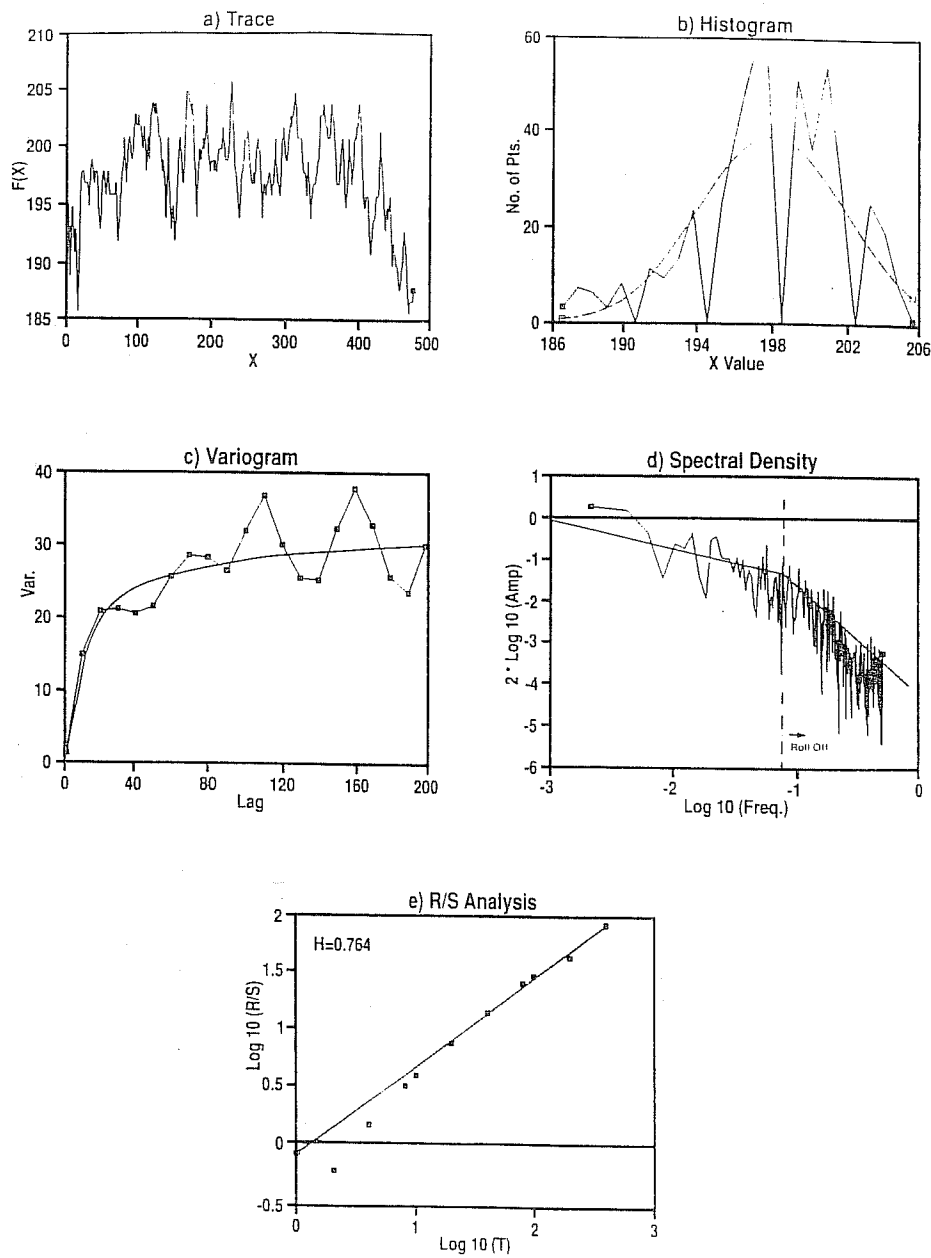


Figure 4. One dimensional statistical analysis applied to a horizontal trace: a) trace, b) variogram, c) spectral density, d) RS analysis, e) histogram.

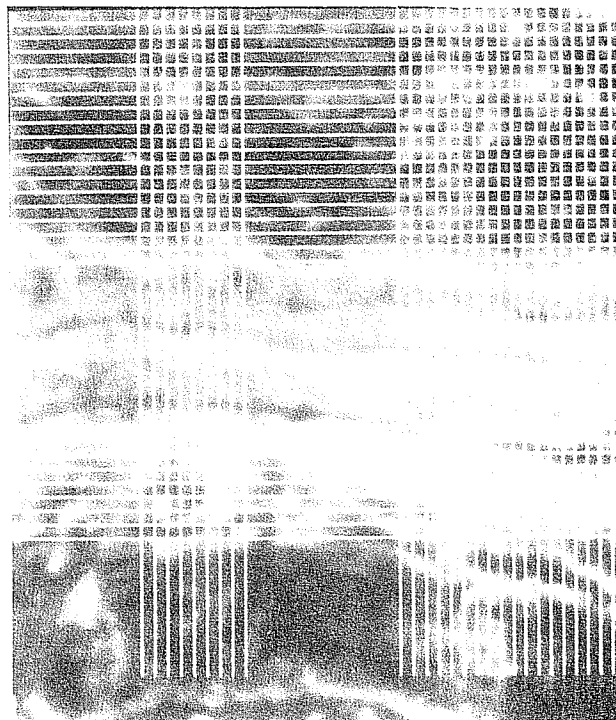
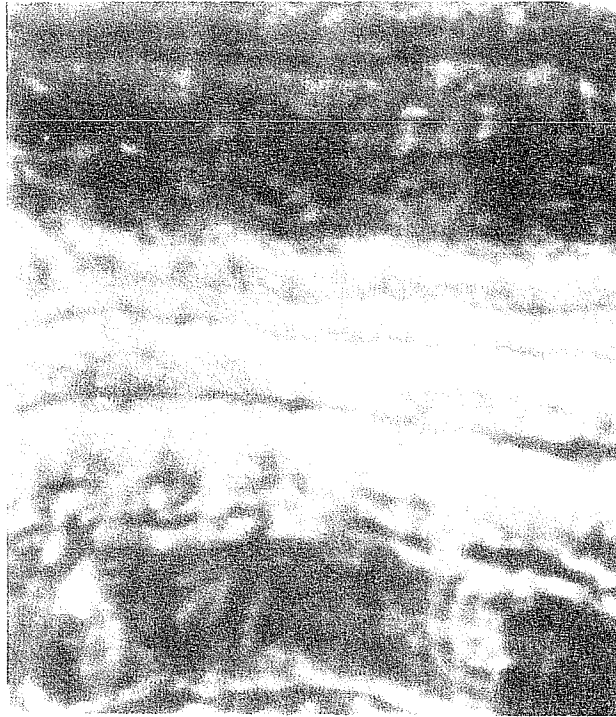


Figure 5. Outcrop photo showing traces analyzed.

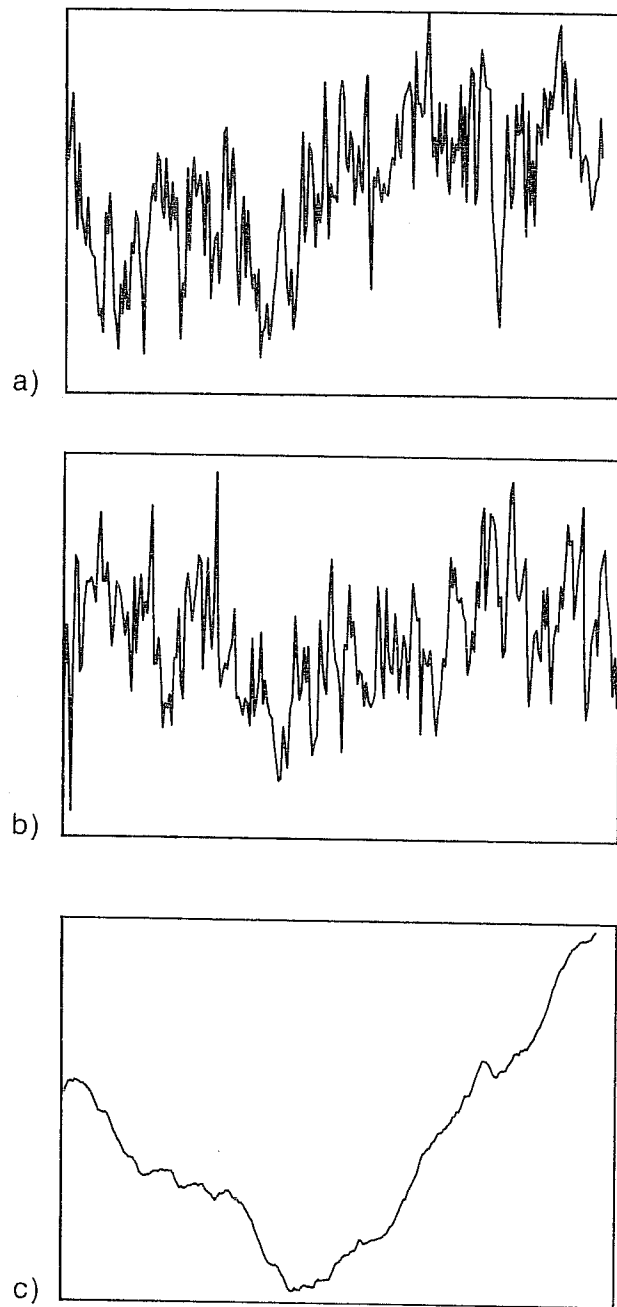


Figure 6. a) fGn, b) horizontal well, c) fBm.

ELECTROMAGNETIC OIL FIELD MAPPING FOR IMPROVED PROCESS MONITORING AND RESERVOIR CHARACTERIZATION¹

J. R. Waggoner
A. J. Mansure

Division 6253
Sandia National Laboratories
Albuquerque, NM

Electromagnetic (EM) techniques are being developed to monitor oil recovery processes and improve overall process performance. Just as seismic surveys generate acoustic waves to detect changes in sonic velocity, and then infer rock properties, EM surveys generate electromagnetic fields to detect changes in electrical resistivity, and then infer fluid properties. The potential impact of the EM survey is very significant, primarily in the areas of locating oil, identifying oil inside and outside the pattern, characterizing flow units, and pseudo-real time process control to optimize process performance and efficiency.

Since a map of resistivity is of no direct use to a reservoir engineer, an essential part of the EM technique is understanding the relationship between the process and the formation resistivity at all scales, and integrating this understanding into reservoir simulation. This abstract discusses the process we have developed for integrating EM measurements into reservoir characterization and simulation.

1. CORE SCALE PETROPHYSICS

To interpret steamflood resistivity, it is necessary to distinguish between the various fluid zones (steam zone, hot condensate zone, cold condensate zone, etc.) of a steamflood (Mansure and Meldau, 1990). Laboratory and field examples have demonstrated that for clean sands, Archie's law, and for shaly sands, Waxman-Smiths and dual-water models, can be used to understand and interpret steamflood resistivity (Mansure; et al., 1990). There are of course physical effects, such as chemical reactions, changes in wettability and formation

¹ Work performed at Sandia National Laboratories under DOE contract number DE-AC04-76DP00789.

factor, etc., that are not included in these petrophysical models. However, these effects appear to be less important than establishing proper estimates for temperature, saturation, salinity, and clay parameters. For a typical California heavy-oil steamflood like Kern River, steamflooding has been observed to lower formation resistivity a factor of about 3. As little as 3% clay can have a significant effect because of the low salinities frequently encountered in steamfloods.

2. COUPLING PETROPHYSICAL KNOWLEDGE AND RESERVOIR SIMULATION

To utilize the petrophysical insights described above, including Archie's Law, clay effects, and thermal effects, a post-processor named RESIST was written which calculates the electrical resistivity of each simulation grid block. The inputs to RESIST are both simulation-derived variables, such as saturation, porosity, and temperature, and user-defined constants, such as saturation and porosity exponents and clay effect parameters. The post-processing approach requires that the clay effects do not affect fluid flow, which is a reasonable assumption when the percentage of clay in the reservoir is low.

One additional RESIST input parameter is the water salinity, which is used along with temperature to estimate the water resistivity from published correlations (Arps, 1953). Since water salinity is not typically monitored in non-compositional simulators, a post-processor named TRACK was written to track multiple components within the aqueous phase. Again, it is required that the component concentrations not affect the aqueous phase flow properties. Knowing component concentrations and salinity, it is possible to mix the components and estimate the salinity of the mixture.

The post-processing approach briefly described allows electrical resistivity to be estimated for each grid block without substantial modification to the reservoir simulator. Since both TRACK and RESIST are stand-alone programs, they can be run multiple times with the same simulation data as input to study sensitivities to clay and multicomponent effects. Reducing the number of simulations required and interfacing with existing simulators are two of the major advantages of the post-processing approach. This triad of programs is named ORRSIM, the Oil Recovery/Resistivity Simulation System.

3. EFFECT OF HETEROGENEITY AND ANISOTROPY ON EM TECHNIQUE

The geology of a reservoir is not homogeneous at the scale of resolution of EM measurements or the grid scale of a reservoir simulator. It is thus necessary to understand how the resistivity of rocks average to give bulk or grid-scale resis-

tivity (Mansure, 1990). The bulk-averaged resistivity of a heterogeneous material is a function of the direction of current flow relative to any structure of the material, resulting in a bulk material that may be electrically anisotropic. Failure to recognize the importance of the direction of current flow can lead to significant errors in interpreting EM measurements, because the response of the bulk rock may depend upon the direction the EM measurement probes the rock. The bulk resistivity of rock also depends upon both the average and distribution of rock properties. Merely plugging average saturation into Archie's law can give resistivities that are off by 50% or more.

4. APPLICATION OF ORRSIM TO EM DATA INTERPRETATION

ORRSIM is a forward model following the path from reservoir description to reservoir simulation to TRACK and to RESIST to produce a resistivity map of the reservoir (path A on Fig. 1). Since the intent of the program is to interpret EM-derived resistivity in terms of reservoir parameters, ORRSIM can also be used in an iterative mode. After generating a good geologically-based reservoir description, ORRSIM will predict a process-derived resistivity map. Qualitative, or perhaps even quantitative, comparison with the EM-derived resistivity map may suggest ways to alter the reservoir description, the process simulation parameters, or TRACK and RESIST input variables. After making the changes, the map generated by a new ORRSIM run should yield a better match to the EM-derived map. This iteration can continue until a desired match is achieved.

REFERENCES

- Arps, J.J., (1953). "The Effect of Temperature on the Density and Electrical Resistivity of Sodium Chloride Solutions," Journal of Petroleum Technology, Section 1 pp 17-22, October; Trans. AIME, vol. 198.
- Mansure, A.J., to be published, Parameterizing and Block-Averaging Electrical Characteristics of a Reservoir: an Essential part of Electrical/Electromagnetic Evaluation of Production Processes, Trans. 1st Annual Archie Conf., 1990, AAPG.
- Mansure, A.J., and R.F. Meldau, 1990, Steam-Zone Electrical Characteristics for Geodiagnostic Evaluation of Steamflood Performance, SPE Formation Evaluation, 5, 3, 241-247.
- Mansure, A.J., R.F. Meldau, and H.V. Weyland, 1990, Field Examples of Electrical Resistivity Changes During Steamflooding, 65th Annual SPE Meeting, New Orleans, SPE 20539.

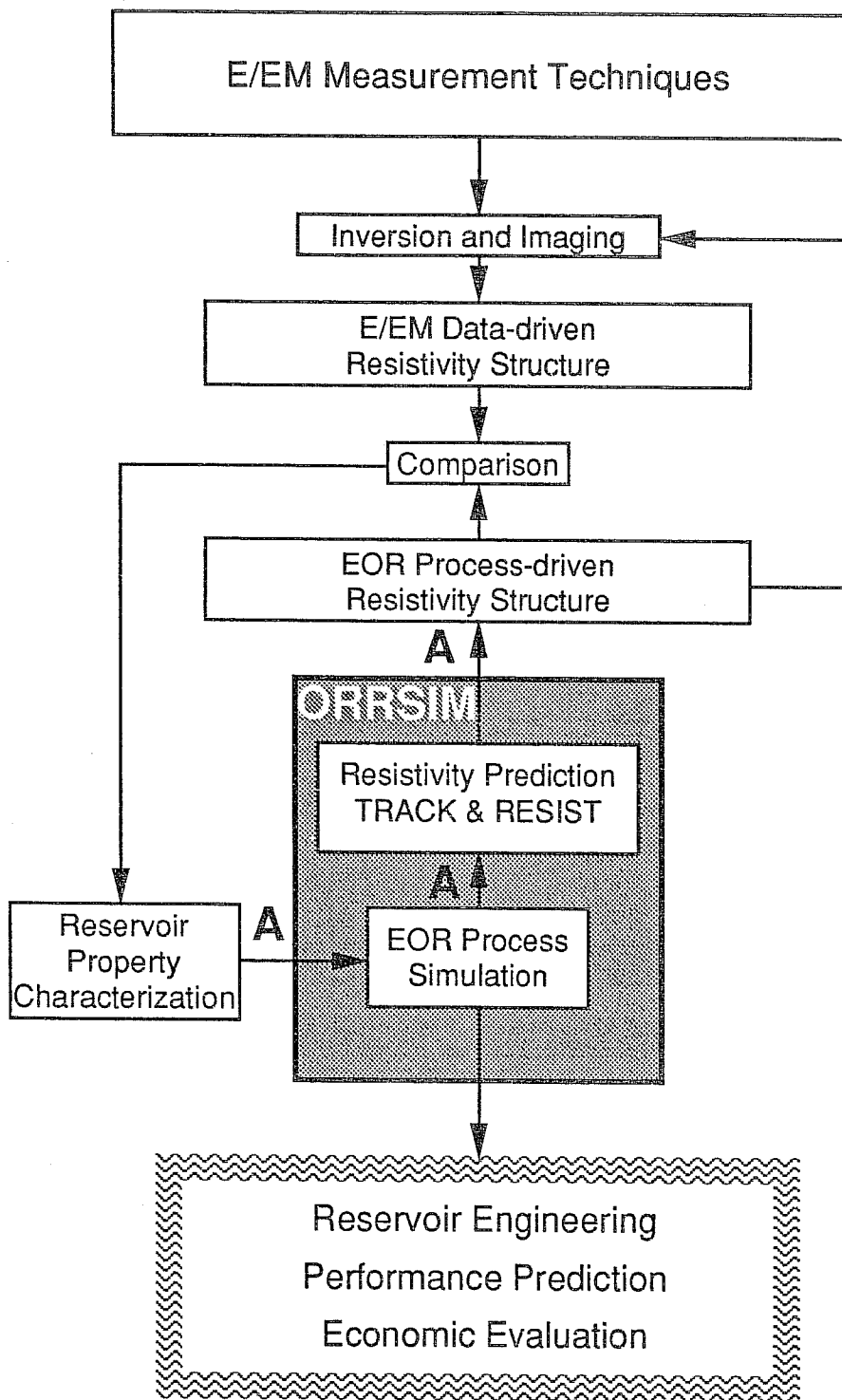


Figure 1: Electromagnetic (EM) Project Flowchart

RESERVOIR SIMULATION OF FLUVIAL RESERVOIRS: TWO PROGNOSTIC MODELS

Kelly Tyler
Adolfo Henriquez

Statoil
Stavanger, Norway

I. INTRODUCTION

Fluvial reservoirs are specially difficult to model in an offshore situation and in a predevelopment phase, as the sandbodies are rarely correlatable when the distance between wells may be kilometers. The main challenge has been to simulate hydrocarbon bearing isolated channels imbedded in an impermeable matrix which honors (i) the known data at the wells, (ii) the presence or absence of channels, their direction and thickness, (iii) outcrop data (thickness to width ratio) and (iv) seismic data (top and bottom of reservoir or other intrareservoir reflectors).

The sophisticated programs to model these types of reservoirs represent a large step forward in modelling medium-scale heterogeneities and away from the layered or zoned concepts. However, there exist several drawbacks (1):

1. The input data is difficult to obtain
 - a. The probability distribution of channel orientation is generally deduced from dipmeter data. These measurements are local, and as the channels meander or are 'braided', the main direction is lost.
 - b. The thickness from log data is not unambiguous, as the channels are stacked or eroded.
 - c. The width to thickness ratio, generally from analog outcrop data or other more densely drilled fields, can vary for different interpreters of the data. In addition, the literature does not (or can not) record parameters like compaction, avulsion or subsidence rates, which are essential to the stacking or spreading of the channels (5).
2. The geological model loses many of its details when being transferred to the coarser grids of the reservoir simulation model.
3. The geological simulation is generally computer-intensive.
4. It is difficult to integrate sedimentological understanding ('geological intelligence') developed by the geoscientists through their experience.

In spite of all of these challenges, which are being tackled, the status of modelling fluvial reservoirs is much more advanced now than just a few years ago. There is, however, a need for simple models, which capture some of the important features of fluvial reservoirs and which can be simulated quickly. Two such models are presented here. The net/gross ratio (NG) is one of the few geological parameters which can be trusted when few wells are drilled. Therefore, these models rely mainly on this parameter. The stochastic simulation model described in Augedal et al. (2) and Clementsen et al. (3) has been used to verify the two proposed models.

II. HOMOGENEOUS MODEL

A homogeneous model, with all cells having an average net/gross ratio and transmissibility can be used to approximate the upper limits for recovery and water breakthrough. The transmissibility multipliers (TM) should be a function of the area of the common face of the two blocks occupied by sand. This common area depends on the ratio of sand and shale in each block, and it can be shown that the average is the average net/gross ratio (NG) for the region. This assumption has been tested with the stochastic simulation model, using several net/gross ratios, channel widths, and varying grid size, and has been verified within 2%.

In testing the homogeneous model with a standard reservoir simulator, TM in the vertical direction was the average generated by the stochastic model. The results are shown in Table I.

The following arguments suggest methods to enhance the homogeneous model. Simple arguments show that the effect of channel orientation can be implemented in the approximation of TM in the following manner.

$$TMX(\Theta) = NG \times (\alpha - (1 - \alpha) \sin \Theta) \quad (1)$$

In the y-direction, $\sin \Theta$ is replaced with $\cos \Theta$, where Θ is the angle between the channel and the x-axis. α is a measure of the channel connectivity perpendicular to the channel direction and is of the type as the 'interconnectedness ratio' and 'average fractional contact - K' described in references 4 & 5.

In a geometric model with regular packing of channels (4), K may be approximated by:

$$K = 0 \text{ for } NG < 0.5 \text{ AND } K = 2 \times NG - 1 \text{ for } NG > 0.5 \quad (2)$$

In reservoirs generated with the stochastic model, K is approximately equal to NG. A realistic value of connectivity may then be $K(\text{regular packing}) < \alpha < K(\text{stochastic model})$. Connectivity in a fluvial reservoir generated by Bridge and Leeder (4) is included in figure 1.

Figure 2 shows TM in the x-direction from equation 1 and from the stochastic model for varying NG and channel orientation.

This simplified model is suited for sensitivity studies, such as testing fluid and relative permeability data, but does not reflect the geological detail of the reservoir. A heterogeneous model is proposed for this purpose.

III. HETEROGENEOUS MODEL

This model distributes NG for the individual grid blocks and then TM can be calculated as a function of NG.

It is expected that, with a fine grid system with NB number of grid blocks, that $NG \times NB$ blocks will be filled with sand, and $(1 - NG) \times NB$ blocks will be full of shale (no sand) where NG is the average net/gross of the reservoir. The slope of such a frequency distribution of sand content in the grid blocks is $m = 2 \times NG \times NB - NB$.

With a coarse grid, the distribution is flat with a slope of 0; all grid blocks have the same NG. With a realistic grid system, the slope of the distribution lies between these extremes.

$$m = NG \times NB - 0.5 \times NB \quad (3)$$

Several reservoirs were simulated using the stochastic reservoir simulator with varying NG. The frequency of NG in the the grid blocks was fitted with a straight line with slope $m = 0.93 \times NG \times NB - 0.46 \times NB$ (fig. 3). Thus the approximation made with equation 3 is suitable.

The y-axis intercept, y_0 , is found by considering that the integral of the frequency distribution is NB. A simple calculation shows that the intercept is

$$y_0 = -0.5 \times NB \times NG + 0.27 \times NB \quad (4)$$

The simulations used before are fitted with the equation $y_0 = -0.43 \times NB \times NG + 0.30 \times NB$ (fig. 3).

$$TMX(i,i+1) = 2 \times NG_i \times NG_{i+1} / NG_i + NG_{i+1} \quad (5)$$

Equation 5 is used to calculate TMX and similarly TMY and TMZ. This equation was verified with a fit for the transmissiblity multipliers. The regression coefficients are 0.95, 0.95 and 0.64 for the x-, y-, and z-directions respectively (fig. 4). The fit is not as good in the z-direction due to excess sand bodies generated in the stochastic model (1). A program using the package SAS was developed to generate grid block properties using equation 5.

The reservoirs were simulated with a black oil simulator and compared with reservoir realizations generated with the stochastic simulator. The results are shown in Table I and show good agreement.

IV. CONCLUSIONS

Two very simple models have been used for fluvial reservoirs in a standard reservoir simulator and have been verified using an advanced stochastic simulator. The recovery factors and breakthrough times were similar. Proper representation should be done with sophisticated

geostatistical programs developed to tackle this challenge, but at a predevelopment phase, simple, naive models are useful.

REFERENCES

1. Henriquez, A., Tyler, K., and Hurst, A.: "Characterization of Fluvial Sedimentology for Reservoir Simulation Modeling", *Formation Evaluation* (1990), Vol 5, 211-216.
2. Augedal, H.O., Stanley, K.O. and Omre, H.: "SISABOSA, a program for stochastic modelling and evaluation of reservoir geology", presented at the Conference on Reservoir Description and Simulation with Emphasis on EOR, Oslo, September 1986.
3. Clementsen, R., Hurst, A.R., Knarud, R., and Omre, H., "A Computer Program for Evaluation of Fluvial Reservoirs", presented at the IIInd International Conference on North Sea Oil and Gas Reservoirs, Trondheim, 1989 and references there in.
4. Bridge, J.S. and Leeder, M.R. : "A simulation model of alluvial stratigraphy", *Sedimentology* (1979), Vol 26, 617-644.
5. Allen, J.R.L. : "Studies in fluvial sedimentation: an elementary geometrical model for the connectedness of avulsion-related channel sand bodies", *Sedimentary Geology* (1979), Vol 24, 253-267.

COMPARISON OF THE MODELS		
MODEL	PRODUCTION TIME (Years)	RECOVERY %
STOCHASTIC	9.80	44
HOMOGENEOUS	8.40	48
HETEROGENEOUS	9.60	43

Table I. Comparison of results using a numerical reservoir simulator with input from the stochastic, homogeneous, and heterogeneous models.

"AVERAGE FRACTIONAL CONTACT" FOR VARYING NET/GROSS RATIOS

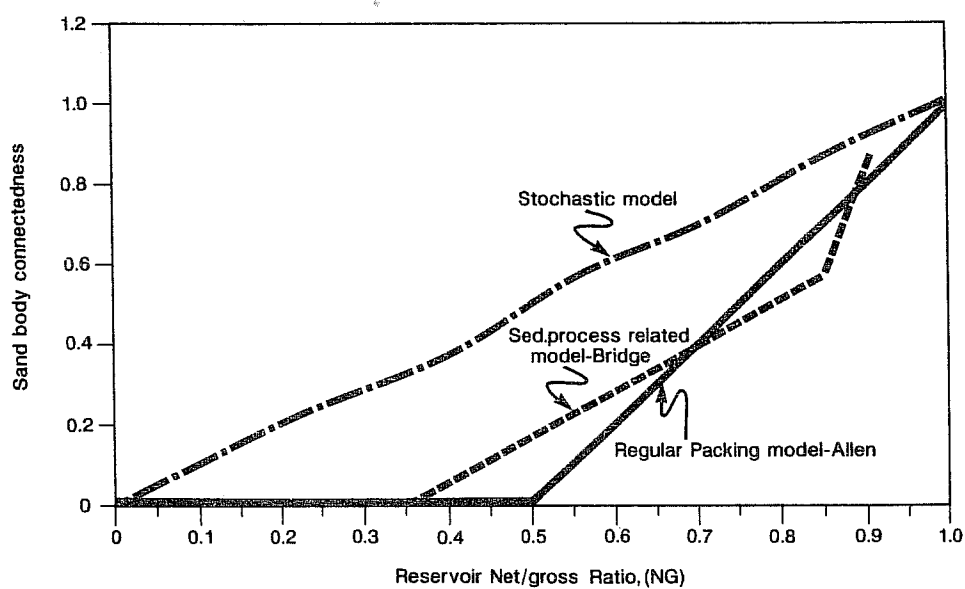


Fig. 1. Sand-body connectedness as calculated by different models. Taken from Henriquez et al. (ref. 1).

TMX CALCULATED FROM EQUATION (1) AND STOCHASTIC MODEL

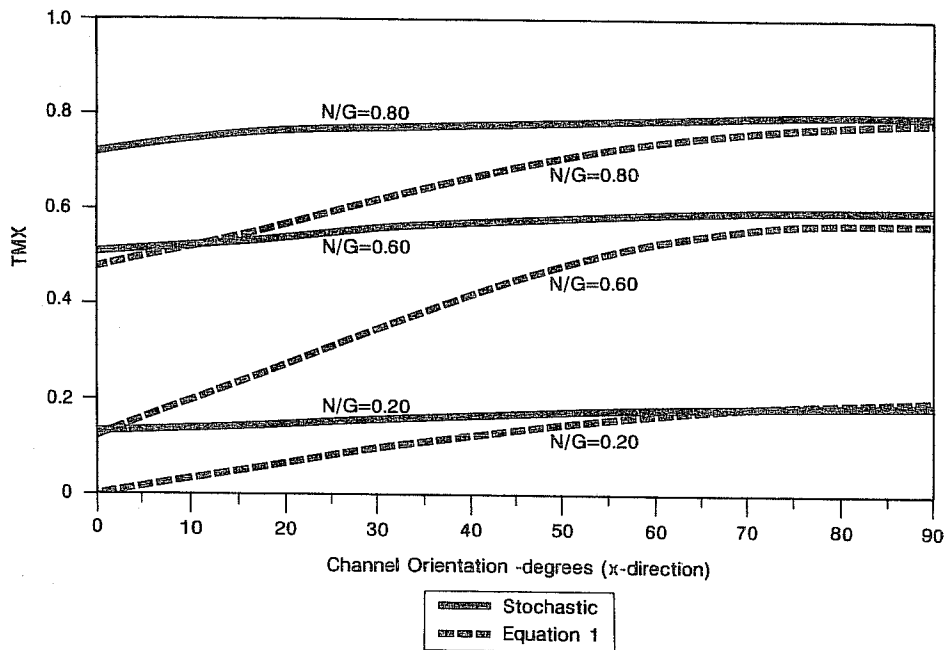


Fig. 2. TMX versus channel orientation, Θ , calculated from equation 1 and the stochastic model. α in equation 1 is derived from equation 2. When the channels are oriented along the y-axis (0°), the stochastic model is unable to calculate the $TMX=0$. Generally, the stochastic model overestimates transmissibility.

PARAMETERS FOR NET/GROSS DISTRIBUTION 750 GRIDBLOCKS

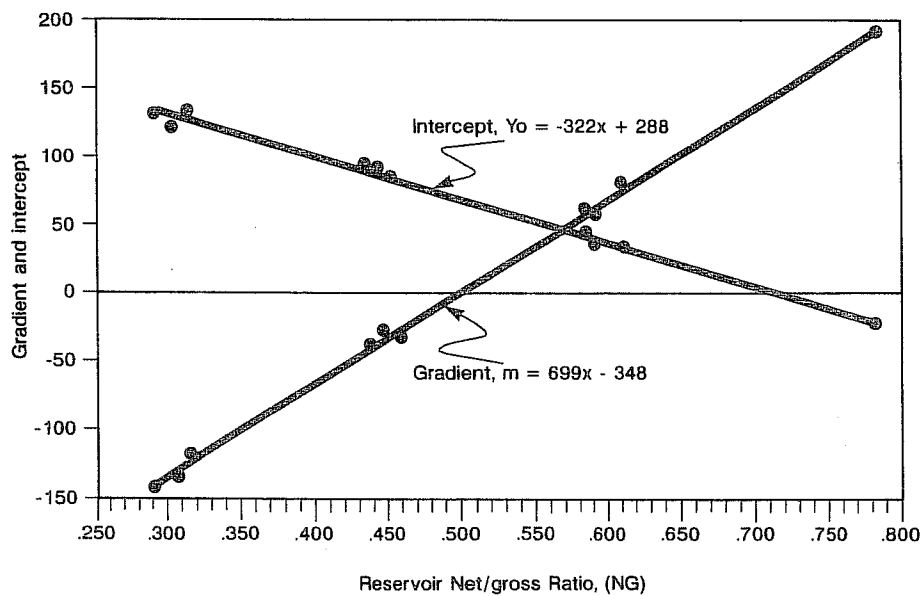


Fig. 3. Calculation of the parameters m and y_0 , as a function of reservoir net/gross ratio, which are used in the distribution of NG in grid blocks.

FITTING OF TRANSMISSIBILITY MULTIPLIERS

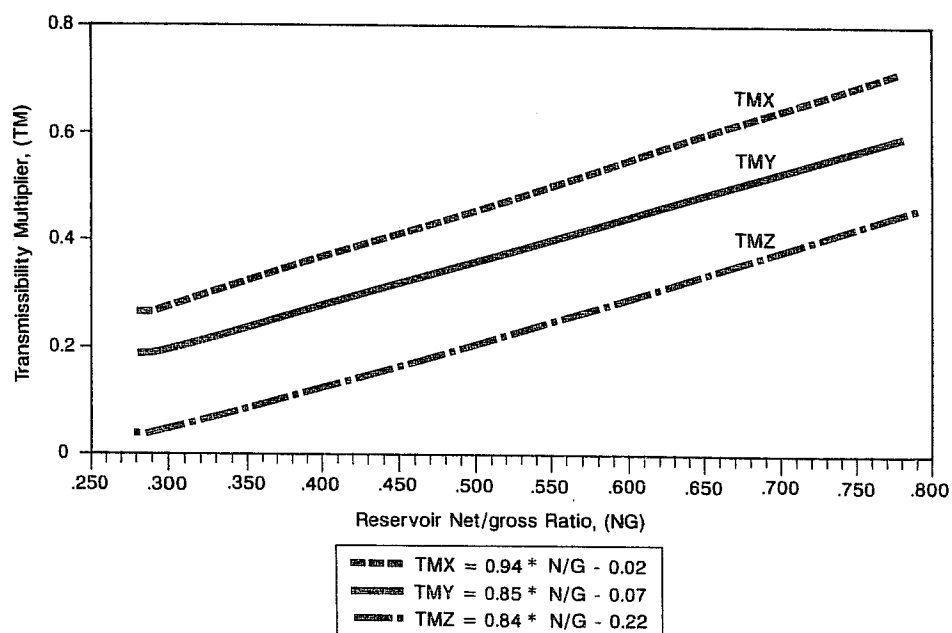


Fig. 4. Transmissibility multipliers from the stochastic model plotted as a function of reservoir NG. The regression coefficients are 0.95, 0.95 and 0.64 for TMX, TMY and TMZ, respectively.

SCALE-UP OF TENSORIAL EFFECTIVE PERMEABILITY TO DETECT ANISOTROPY THROUGH MFP MEASUREMENTS

Yngve Aasum
Ekrem Kasap
Mohan Kelkar

The University of Tulsa

I. INTRODUCTION

In optimizing recovery and production for a field scale study, numerical simulations are more cost effective than lab experiments . Field development and reservoir management practices require large scale numerical simulations. Although the development of more powerful computers and simulation techniques allows us to use very fine grids and include rather detailed features, the size of a simulation grid-block in a field scale numerical simulation is in the order of several hundreds of feet, which is much larger than the scale of inter-well scale laminations and cross-beddings. For these simulation blocks the heterogeneities can only be accounted by calculating an effective permeability . An *effective* permeability is one which preserves the fluid flux-potential drop quotient between a heterogeneous block and an equivalent (same size, geometry and fluid viscosity) homogeneous block.¹ An analytical method to calculate the effective permeability is required, because of its generality and ease in inserting into numerical simulators.

Simulation results indicate that not only the magnitudes of permeability heterogeneities but also their locations and positions will alter the calculated effective permeability. The positions and locations will cause fluid flow direction to diverge from the direction of applied pressure gradient. This phenomenon should be included in effective permeability calculations by calculating the effective permeability in tensorial form.

In this study we developed an analytic method to calculate effective block permeabilities as a full tensor based on geometry, block size, local permeabilities and the location of heterogeneities within the simulation block. This method can be applied to Mini-Field-Permeameter (MFP) measurements to detect the anisotropy in outcrop formations, thereby improving reservoir descriptions.

II. DISCUSSION

Mini-Field-Permeameters (MFP) have been intensively used to characterize inter-well scale heterogeneities of analog outcrop formations. Permeability anisotropy, however, cannot be detected with MFP, because a MFP often measures the permeability on a scale that is much smaller than the scale of lamination and cross-bedding which are considered to be prime cause for anisotropy. Therefore, a method to detect the cross-bedding and the permeability anisotropy from MFP measurements is needed for better description of outcrop analogs.

Non-uniform distributions of heterogeneities causes a transverse pressure gradient which results in a cross-flow or redirection of flow within the block, Fig. 1. The numerical simulation of flow in such a block also indicates flow redirectioning, although applied pressure gradient is unidirectional, Fig. 2. This flow redirectioning can be accounted by calculating the effective permeability as a tensor, because non-zero off-diagonal elements of the permeability tensor show similar effects on velocity field (mean flow direction is being different from the applied pressure gradient).

An analytical effective permeability calculation method is developed to account for the cross-flow caused by the transverse pressure gradient. First, we assume the extreme cases, no-crossflow and vertical equilibrium, hold, then the transverse pressure gradient is calculated by averaging those two limits. Because of the lengthy derivations of equations, for the analytical equations we refer to the research reports of TUPREP at the University of Tulsa.²

A series of numerical simulations were also conducted for various cases of local permeabilities. The effective permeability tensors calculated with the analytical method and from the numerical simulations are compared in Fig.'s 3-6. Also shown in Fig.'s 3-6 are the local permeabilities used in the calculations. The comparison indicates an excellent agreement between the numerical simulation results and the analytical method calculations.

The analytical method is applied to MFP measurements in San Andres, Algerita Outcrop to detect permeability anisotropy and existing cross-bedding. The analytical method employs the measured point permeabilities and their locations to calculate the effective permeability tensor for consecutively expanding scales. Figure 7 shows a grainstone permeability field obtained by 16x16 ft measurements.³ Figure 8 shows the calculated permeabilities during scale-up process. The final permeability tensor indicates that the principal directions of permeability are very close to the horizontal and the vertical directions and there exist approximately an anisotropy ratio of 4 between horizontal and vertical permeabilities.

The method applied to a generic cross-bedded permeable media, shown in Fig. 9, to test the method's ability to detect the cross-bedding. Only two permeability values are used in the generic cross-bedded flow field, dark cells =20 md and light cells=1000 md. The calculated effective permeability tensor follows;

$$k = \begin{bmatrix} 304 & -209 \\ -209 & 304 \end{bmatrix}$$

which compares with expected effective permeability tensor obtained by calculating the principal direction permeabilities⁴ in the parallel and perpendicular directions to cross-bedding, then applying a coordinate rotation procedure.

$$k = \begin{bmatrix} 275 & -235 \\ -235 & 275 \end{bmatrix}$$

The analytical method calculates the cross-bedding angle correctly (45°), because symmetrical tensorial elements in a cross-bedded medium will only come from 45° cross-bedding angle. The method calculates permeabilities in the principal directions as

$$k = \begin{bmatrix} k_p=513 & 0 \\ 0 & k_s=95 \end{bmatrix}$$

which compare with the results of simple calculations of parallel and serial beds model as

$$k = \begin{bmatrix} k_p=510 & 0 \\ 0 & k_s=39 \end{bmatrix}$$

Where k_s and k_p refer to permeabilities in the serial and parallel directions of cross-bedding and all permeabilities are in md.

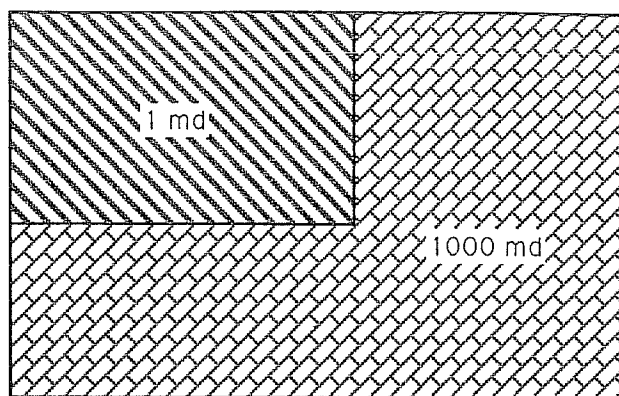
III. CONCLUSIONS

- 1- By using transverse pressure gradient an analytic method is developed to account for the effects of asymmetrically located heterogeneities

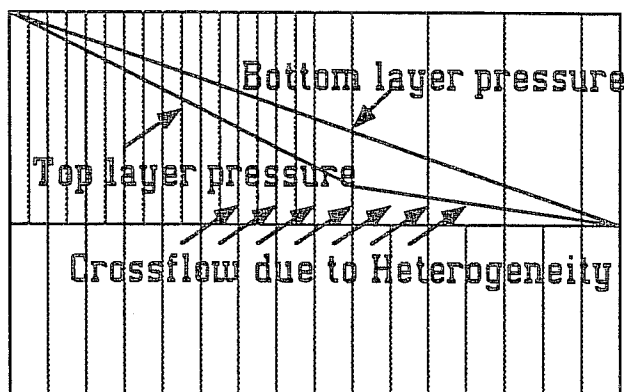
- 2- The effective permeabilities from the analytic method and detailed numerical simulations are in excellent agreement
- 3- By using scale-up procedures analytic method is able to capture the anisotropy in San Andres Grainstone formations. For the scale studied the anisotropy ratio was about 4.
- 4- Some additional work is needed for cross-bedded media, since the preliminary work we reported here is promising. Although the permeability in serial principal direction was off, the parallel direction permeability was almost exact and the cross-bedding angle was captured correctly (45°).

VI. REFERENCES

1. Kasap E. and Lake W. L.: "Calculating the Effective Permeability Tensor of a Gridblock," SPE Formation Evaluation, June 1990, 192-200.
2. Yngve, A., Kasap, E., Kelkar, M. "Effective Properties of Reservoir Simulator Grid Blocks," Status Report TUPREP, Research Report 5, March 11, 1991.
3. Lucia, F. J., Senger, R. K., Fogg, G. E., Kerans, C., Kasap, E. "Scales of Heterogeneity and Fluid Flow Response in Carbonate Ramp Reservoirs: San Andres Outcrop, Algerita Escarpment, New Mexico," paper SPE 22744 will be presented in 1991 SPE Annual Technical Conference and Exhibition, October 6-9, Dallas, Texas.
4. Kasap E. and Lake W. L.: "Dynamic Effective Relative Permeabilities for Cross-Bedded Flow Units," paper SPE 20179, Proceedings of SPE/DOE Seventh Symposium on Enhanced Oil Recovery, Tulsa, OK, April 22-25, 1990.



(a)



(b)

Figure 1. a) A Simulation Grid-Block with Megascopic Heterogeneities b) Schematic Pressure Distribution In the Block.

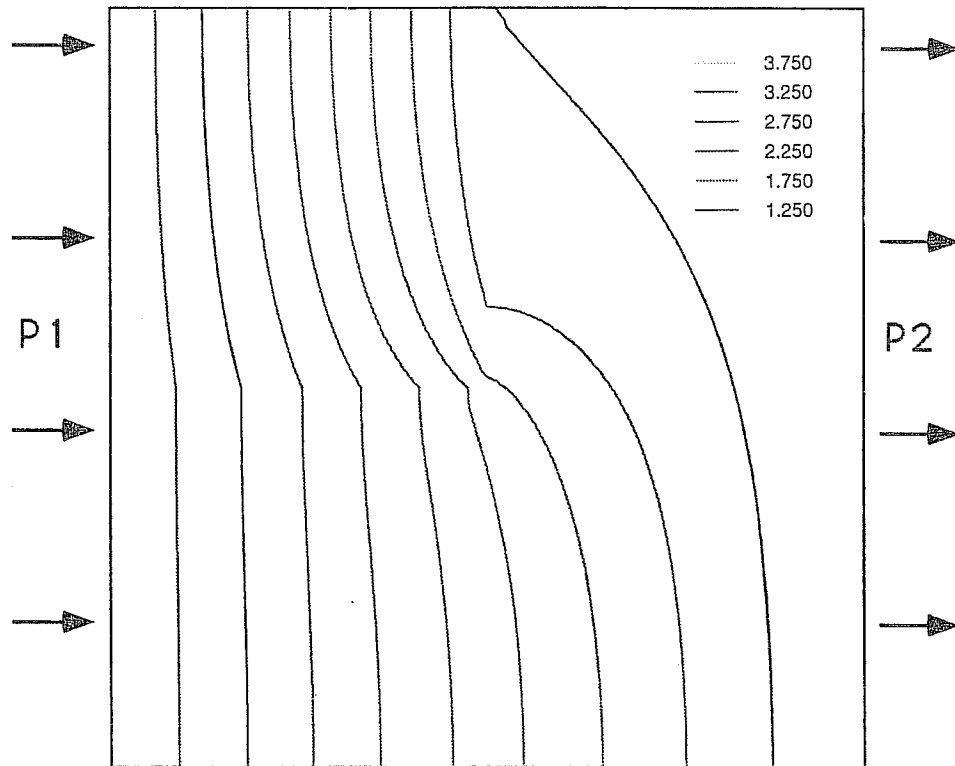


Figure 2. Pressure Contours from the Numerical Simulation of Flow in the Permeability Field Shown in Fig. 1-a. Pressures Are in atm. and Horizontal Boundaries are Sealed, $P1 > P2$

1	0.	1000	0.
0.	1	0.	1000
1000	0.	1000	0.
0.	1000	0.	1000

(a)

Analytic Method	
593	-74
-74	593
Numerical Method	
592	-88
-88	592

(b)

Figure 3. Comparison of Effective Permeability Tensors Calculated by Analytical and Numerical Methods. a) Isotropic Local Permeabilities (md) b) Calculated Effective Permeability Tensors (md)

1	0.	1000	0.
0.	.1	0.	100
1000	0.	1000	0.
0.	100	0.	100

(a)

Analytic Method	
523	-14.5
-14.5	65
Numerical Method	
531	-14.4
-15.3	64

(b)

Figure 4. Comparison of Effective Permeability Tensors Calculated by Analytical and Numerical Methods. a) Anisotropic Local Permeabilities (md) b) Calculated Effective Permeability Tensors (md)

1	.1	1000	100
.1	1	100	1000
1000	100	1000	100
100	1000	100	1000

(a)

Analytic Method	
581	-42
-42	581
Numerical Method	
577	-34
-34	577

(b)

Figure 5. Comparison of Effective Permeability Tensors Calculated by Analytical and Numerical Methods. a) Isotropic Local Tensorial Permeabilities (md) b) Calculated Effective Permeability Tensors (md)

1	.1	1000	100
.1	.1	100	100
1000	100	1000	100
100	100	100	100

(a)

Analytic Method	
493	-37
-42	62
Numerical Method	
501	-34
-44	61

(b)

Figure 6. Comparison of Effective Permeability Tensors Calculated by Analytical and Numerical Methods. a) Anisotropic Local Tensorial Permeabilities (md) b) Calculated Effective Permeability Tensors (md)

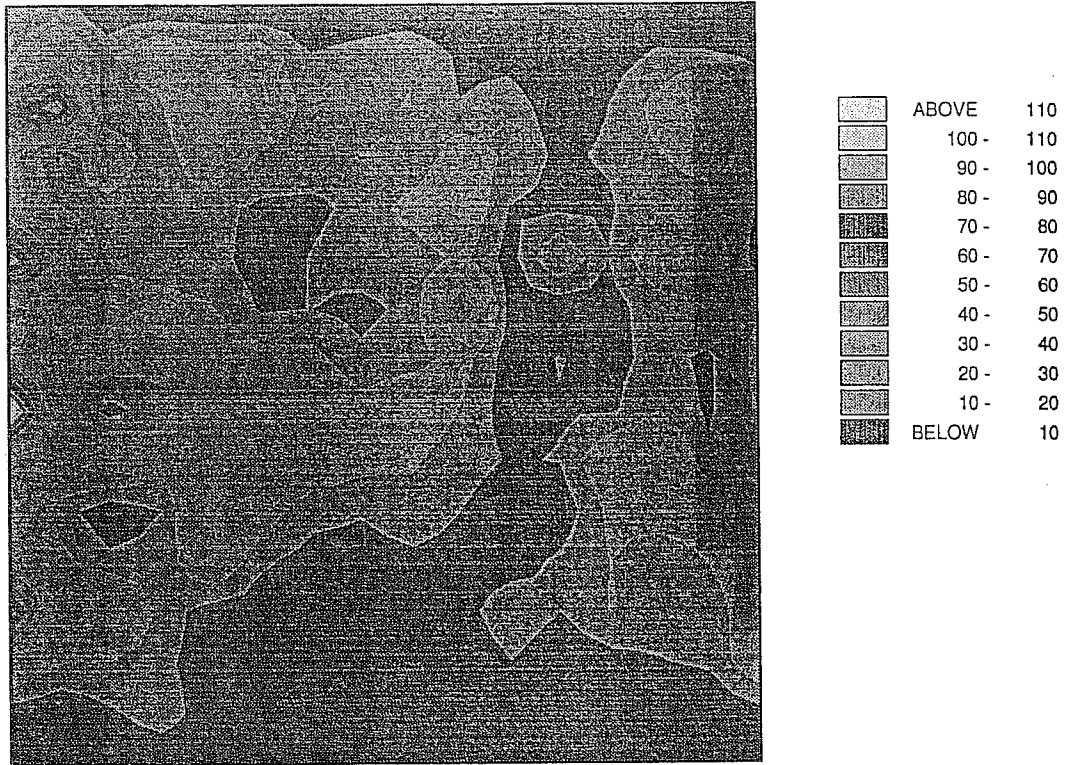
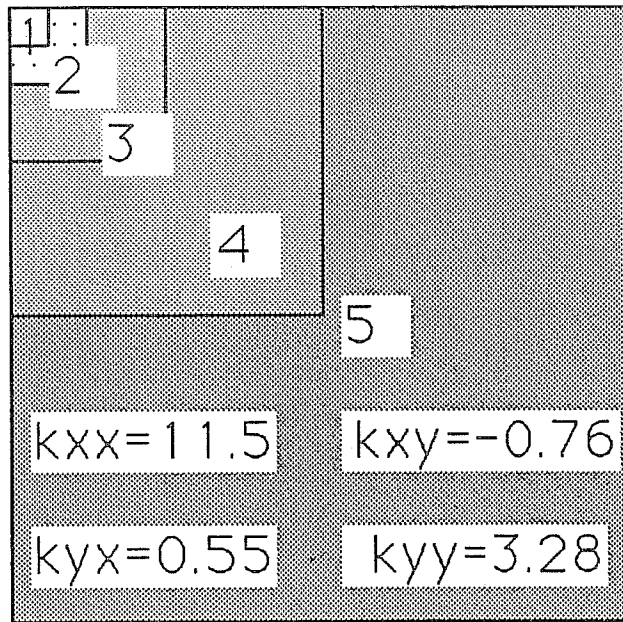


Figure 7. Grainstone Permeability Field, 16X16 MFP Measurements on San Andres Carbonate Outcrop, Algerita, New Mexico.



(a)

14.7	(1)	0.	19.73	(2)	0.61
0.		14.7	0.56.		19.16
19.1	(3)	-1.17	16.64	(4)	-1.04
-0.11.		13.45	0.16.		9.71

(b)

Figure 8. Scaling-Up of a Grainstone Permeability Field (16x16) Shown in Fig. 7 from San Andres Carbonate Outcrop, Algerita, New Mexico. a) Five Scales and the Final Permeability Tensor. b) Permeability Tensors at the Upper Left Corner for Other Scales.

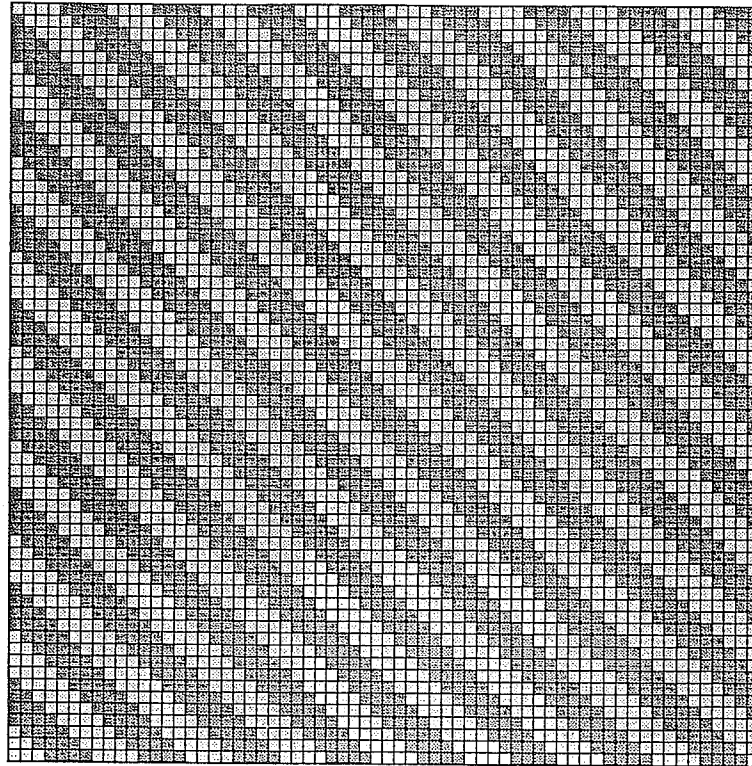


Figure 9. Generic Cross-Bedded Permeable Medium 64x64.
Only Two Permeability Types, Dark Cells= 20 md,
Light= 1000 md.

DEFINING WATER-DRIVE GAS RESERVOIRS: PROBLEMS IN
DATA ACQUISITION AND STRATEGIES IN EVALUATION.

William M. Colleary
John R. Hulme
Saad M. Al-Haddad

Colorado School of Mines
Golden, Colorado

Gas Research Institute
Chicago, Illinois

This paper presents the steps which must be taken, and discusses the data necessary, to identify water-drive gas reservoirs, and addresses the importance of making this determination. This work presents the interim results of a research project presently underway at the Colorado School of Mines, and funded through the Gas Research Institute (GRI).

A comprehensive search for water-drive reservoirs was conducted throughout the continental United States, with emphasis on the Rocky Mountain and Mid-Continent regions. This search included a review of geologic and engineering literature, contacts with operating companies, and search through the Petroleum Information (TM) Production and Historical Databases.

Early identification of water-drive commences with detailed geologic appraisal of a reservoir, and provides the data necessary and time scale to develop and evaluate alternate programs for maximizing recovery of reserves through field development, completion and operations, and management of produced water. One traditional production strategy calls for high production rates to "out-run" encroaching water, often leaves a significant amount of unrecoverable gas within the reservoirs. Alternative strategies are proposed.

The identification of pressure support within a reservoir is the most reliable engineering method to determine the presence of water-drive. To verify this, a complete pressure history, along with gas composition, is needed to construct P/Z plots. An example of a classic strong water-drive is shown in Figure 1, from a Delaware Basin Field in West Texas. Pressure data should be collected for each individual well, since the water-drive often only appears in certain wells in the field. As an example, Figures 2 and 3 were taken from wells less than one mile apart in another West Texas Field. Figure 2 shows a volumetric depletion, whereas Figure 3 shows water-drive pressure support.

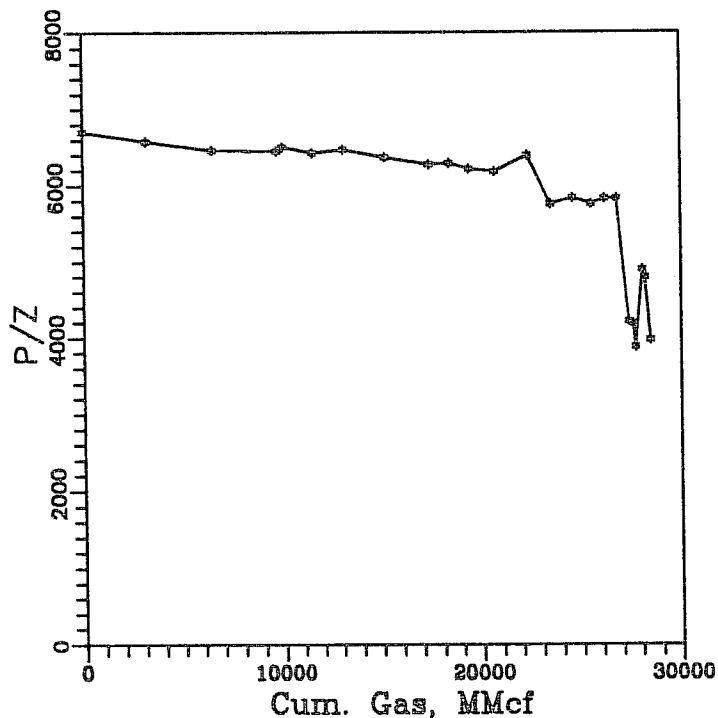


Figure 1. P/Z plot of deep Delaware Basin Reservoir illustrating strong water-drive support.

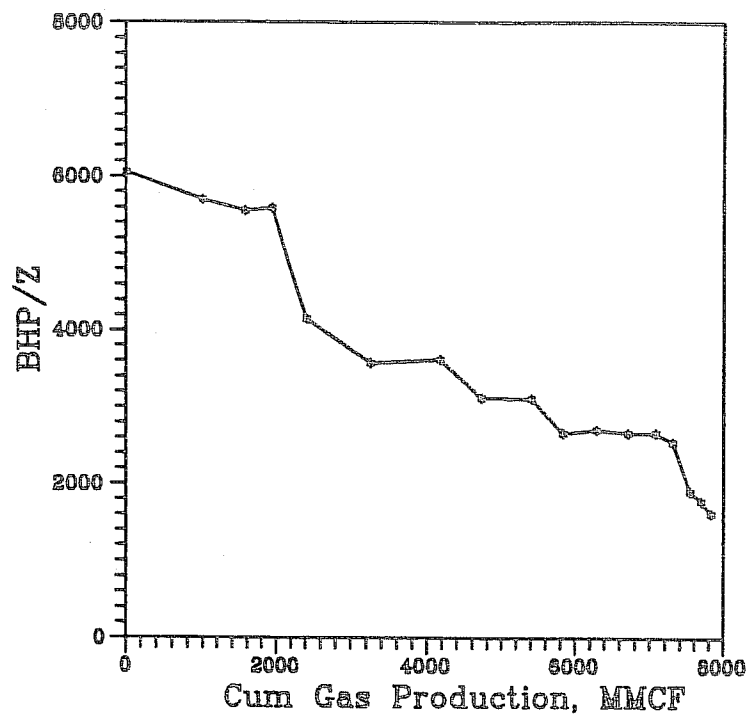


Figure 2. P/Z plot of West Texas Well showing volumetric depletion.

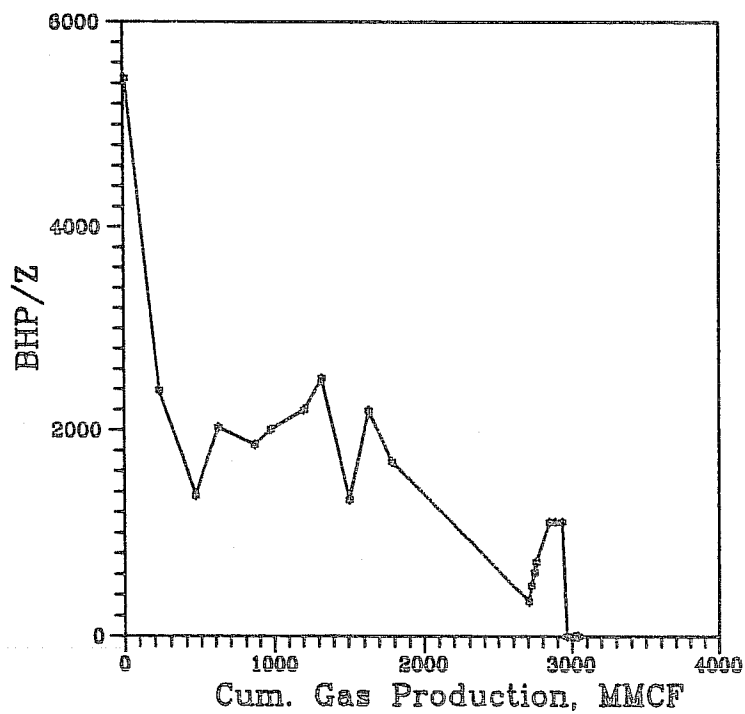


Figure 3. P/Z plot of West Texas Well showing pressure support.

Comprehensive production histories are also important in investigating future reservoir management strategies through reservoir simulation. These data should include water, gas, and condensate production, and water injection volumes, if any. Complete workover and completion records, with any production logging surveys are also available.

Important clues to the internal architecture of the reservoir can only be obtained through the analysis of well-by-well production histories. The existence of permeability barriers, such as small-scale sealing faults, or facies changes, which affect reservoir behavior, can be identified, and the geologic interpretation may be confirmed. Pressure data should also be taken throughout the life of the well, since a straight line depletion does not assure a closed system. "Many curves show a rapid decline in the early stages of production after which they flatten out." (Bruns, Fetkovich, Meitzen, SPE #898, March 1965). An example of this is shown in Figure 4, from a Gulf Coast Region reservoir in Texas.

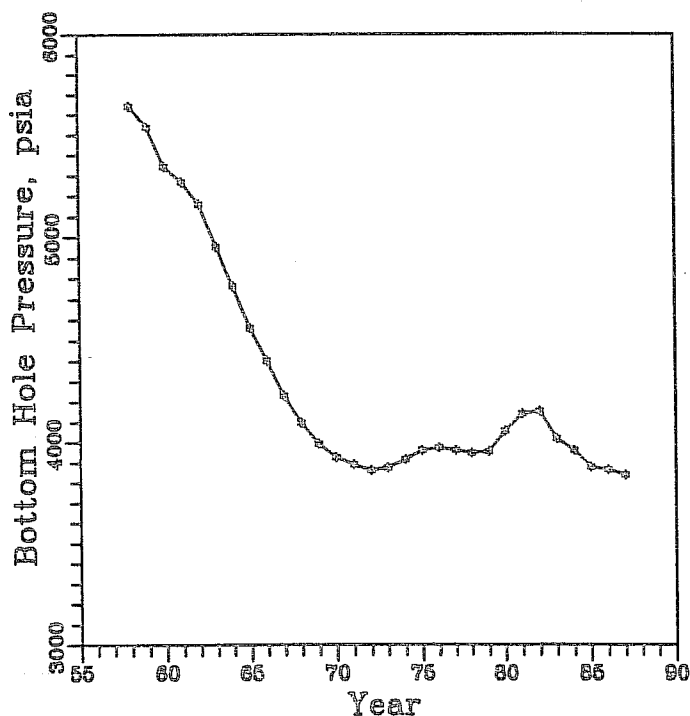


Figure 4. Pressure versus time plot of Texas Gulf Coast Field.

The primary problem encountered in any analysis is the incomplete or total lack of pressure data. In various regions, reporting of reservoir pressures is not required by regulatory agencies, and many operators do not recognize the economic value of such data. In such cases, the possibility of water-drive would not be considered until wells show an increase in water production. This would occur, generally, at a later stage in the life of the reservoir, when it is too late to carry out the most effective management strategies. As water production begins, it may rise sharply, causing problems if there has been no preparation for water disposal. An example of such a sharp increase is shown in Figure 5, from a field in the San Juan Basin of New Mexico.

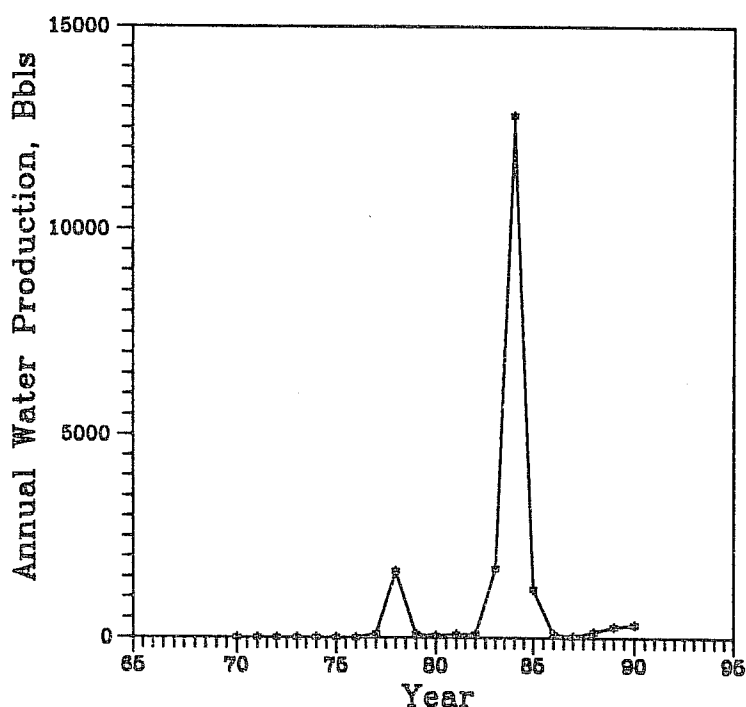


Figure 5. Plot of water production of a San Juan Basin Field, NM.

In conclusion, the early recognition of water-drive in gas reservoirs is critical to maximizing recovery of natural gas reserves from the reservoir. This recognition can be achieved when the detailed reservoir geologic description and classic reservoir engineering methods are integrated to provide the data necessary for the development of an effective management strategy. Detailed pressure data, fluids production histories, compositional analyses, open hole and production logging, and completion data are essential for such early recognition.

RENORMALIZATION: A MULTILEVEL METHODOLOGY FOR UPSCALING.

Alistair Jones, Peter King, Colin McGill and John Williams

*BP Research,
Sunbury Research Centre, Chertsey Road,
Sunbury-on-Thames,
Middlesex, TW16 7LN, U.K.*

1. Introduction.

Reservoir descriptions are invariably generated on a fine scale, in part reflecting the scale of the input information. Reservoir performance simulators require input on a much coarser scale for manageable computation. The averaging process for changing scale — upscaling — is complicated, particularly for a property like permeability which is non-additive. The purpose of our poster is to describe the renormalization approach to upscaling and to give some impression of the wide range of problems that can be tackled using such an approach. In this note we outline the renormalization strategy and describe a simple implementation of the rescaling procedure. This is followed by some illustrative examples and a brief look towards the future.

Our principal aim in reservoir characterization is to determine the large-length-scale flow behaviour of the reservoir (i.e. at the scale of a simulator grid-block). For clarity, we focus on the determination of effective permeability. The main difficulty lies in the interdependent influences of permeability heterogeneities on many length scales. In essence the renormalization strategy tackles such problems via a multilevel or hierarchical approach. At each stage the current grid is divided up into cells, each consisting of a number of grid-blocks, and the effective permeability of each cell determined. These cells then become the grid-blocks of the next coarser grid. In effect, repeated application of the rescaling operation captures successively the effects of increasingly larger-scale heterogeneities on the large-scale flow behaviour of concern: as explicit reference to permeability heterogeneities on a given scale is eliminated by rescaling; their influence is carried forward implicitly in the coarse grid parameters (i.e. renormalized permeabilities).

The renormalization approach is remarkably accurate, efficient and robust — by robust we mean that it can be successfully applied to a wide variety of heterogeneous problems. Its power comes from choosing an appropriate rescaling prescription.

2. Rescaling Prescriptions.

Whenever possible, it is advantageous to maintain a 1:2 ratio in length scales between successive grids: this entails using $2 \times 2 \times 2$ unit cells as shown in Figure (1). In order to calculate the cell effective permeability in a given direction we set constant pressures over the inlet and outlet cell boundaries and no flow through the other boundaries, and then replace the cell by a network of transmissibilities or equivalent resistors (using the analogy between Darcy's Law and Ohm's Law). Using simple resistor transformations we can find the equivalent network resistance and hence the effective permeability [1,2]. We can then 'rotate' the boundary conditions and repeat the procedure to obtain the cell effective permeabilities in the other directions. The main elements are outlined schematically in Figure (1) for both uniform and radial flow; standard transformations are used for the latter to map from a radial sector grid to a cartesian computational grid (non-uniform grid spacings are easily handled).

The choice of small cells renders the calculations extremely efficient with, under most circumstances, remarkably little loss in accuracy. In comparison with full numerical simulation 100 to 1000-fold speed-ups are not atypical, with errors usually less than 10 %.

3. Representative Examples.

In Figure (2) we indicate how renormalization can be used for upscaling. The problem is to reconcile core data with results from a well-test via a plausible reservoir description. The approach is to generate stochastic realizations of the large scale reservoir architecture (lithofacies) using SIS (Sequential Indicator Simulation) [3], taking facies abundance from well data and estimating dimensions/spatial correlations from analogue data. The permeability distribution within each lithofacies is simulated by using SGS (Sequential Gaussian Simulation) [4], using core data as input together with estimated spatial correlations. These permeability distributions are upscaled using renormalization to the scale of the grid-blocks used in the SIS simulation. This yields a full permeability grid at that scale, which is then renormalized to obtain the final effective permeability values for comparison with the well-test. The final agreement is good given the various assumptions made in producing the reservoir description.

In Figure (3) we give an example of an application to an idealised 2D fracture network. The model consists of a set of orthogonal fractures resolved onto a 200 by 200 grid. The fractures are assigned different conductivities in the horizontal and vertical directions and the macroscopic

flow direction is assumed to be horizontal. The fracture network can be treated as an analogue resistor network and a large cell renormalization technique [2,5] used to determine the effective permeability. In 2D it is possible to obtain essentially exact results as confirmed by the agreement between the results obtained using either the full network or the backbone (those fractures carrying the flow). These results can be obtained at a fraction of the cost of a conventional numerical solution.

4. Concluding Remarks.

The renormalization technique provides a powerful approach to the general problem of upscaling. In many instances simple small cell schemes yield very accurate results at minimal computational expense. In those cases where the small cell schemes are less satisfactory (usually when there is significant macroscopic flow tortuosity) other options are available. One option is to use a large cell approach (as in the fracture example above); another is to improve the small cell approach by combining it with a multi-grid approach [6]. The latter has so far received little attention in the literature.

We believe that the most promising path to the solution of many difficult upscaling problems lies in further development of renormalization and multi-level methods.

Acknowledgements.

The authors would like to thank the British Petroleum Company plc. for permission to publish this note.

References.

- [1] King P R, *Transport in Porous Media*, 4, p37 (1989)
- [2] Williams J K, in 'Mathematics of Oil Recovery', Oxford UP (1991)
- [3] Journel A G and Alabert F G, *J.P.T.* p212 (Feb 1990)
- [4] Verly G, presented at EAPG Conf. (Florence) (1991)
- [5] Frank D J and Lobb C J, *Phys. Rev. B* 37, p302 (1988)
- [6] Brandt A, in 'Multigrid Methods', Marcel Dekker (1988)

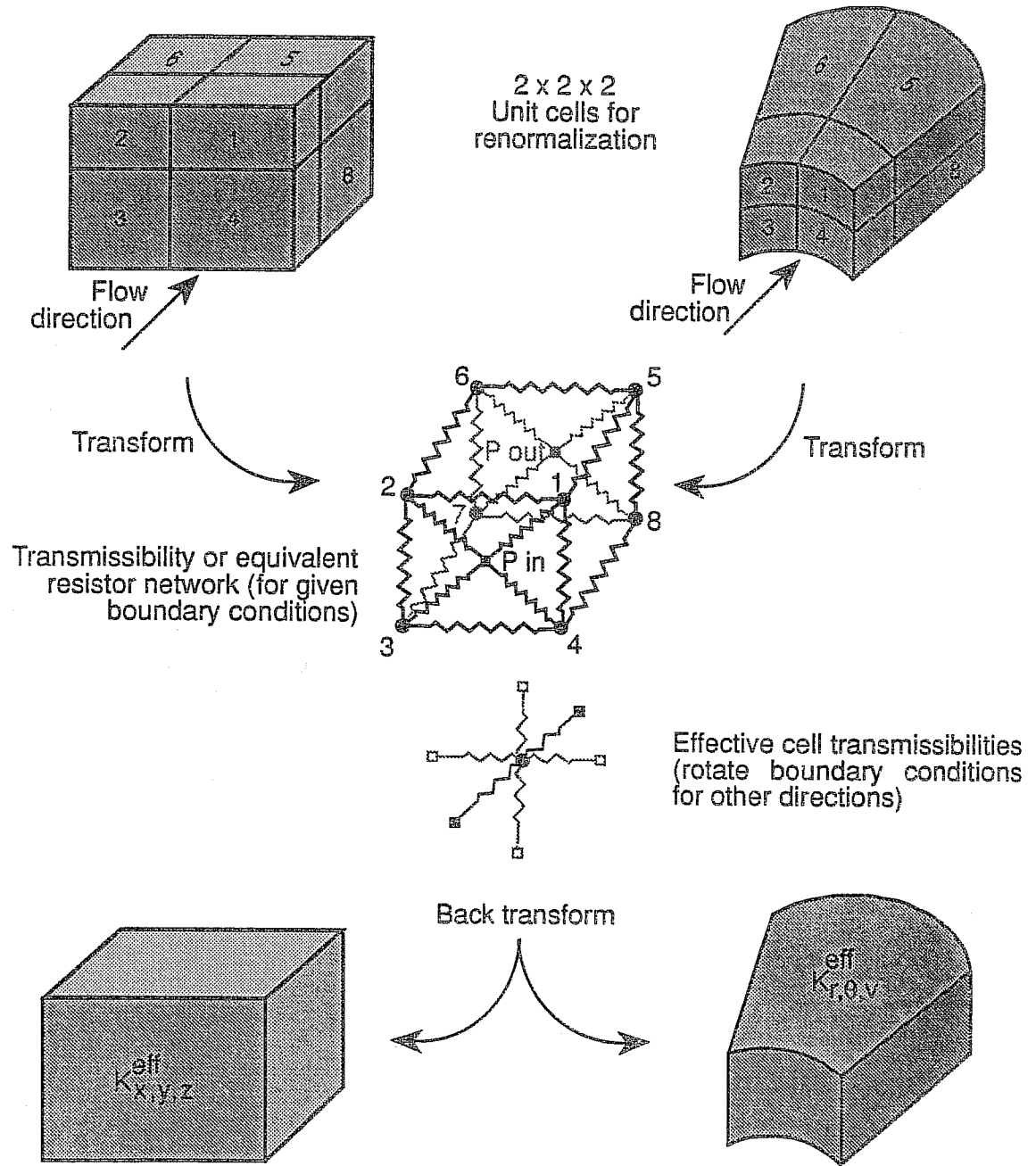
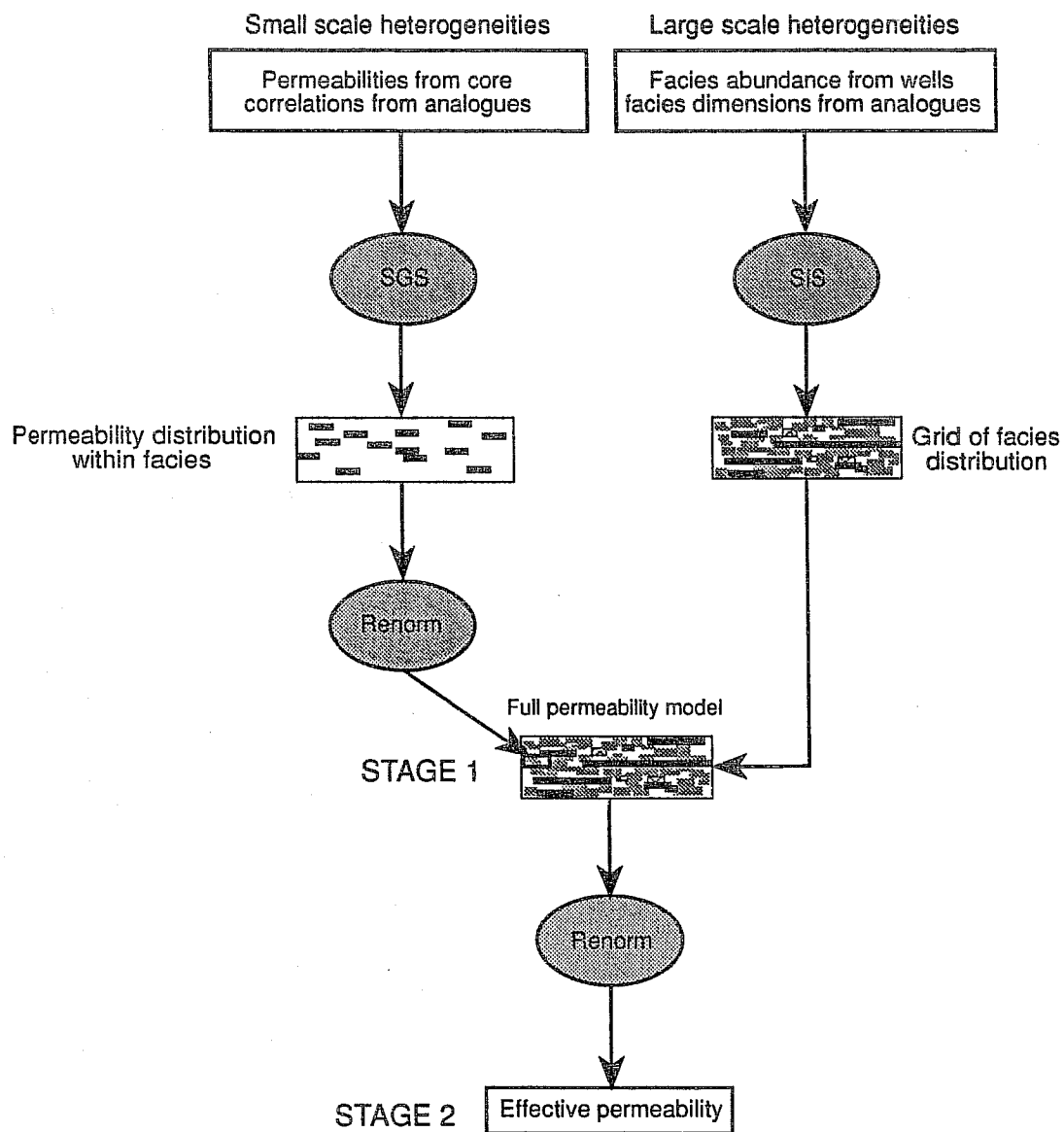


Fig 1. SMALL CELL RESCALING

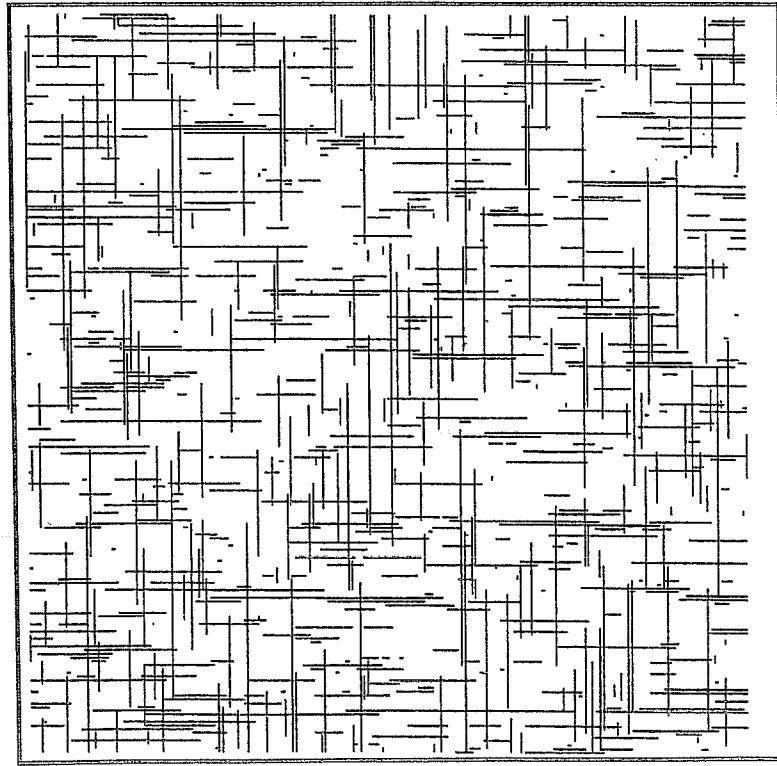
RCS 32517



STAGE 1	Facies	Kh	Kv/Kh	% abundance
	1	53.8	0.44	45
	2	11.2	0.12	21
	3	2.4	1	14
	4	0.001	1	13
	5	0.001	1	4
	6	13.0	1	3
STAGE 2	Effective Kh = 16.9 Kv = 1.3 Well test k = 22			

Fig 2 EXAMPLE OF USE OF UPSCALING

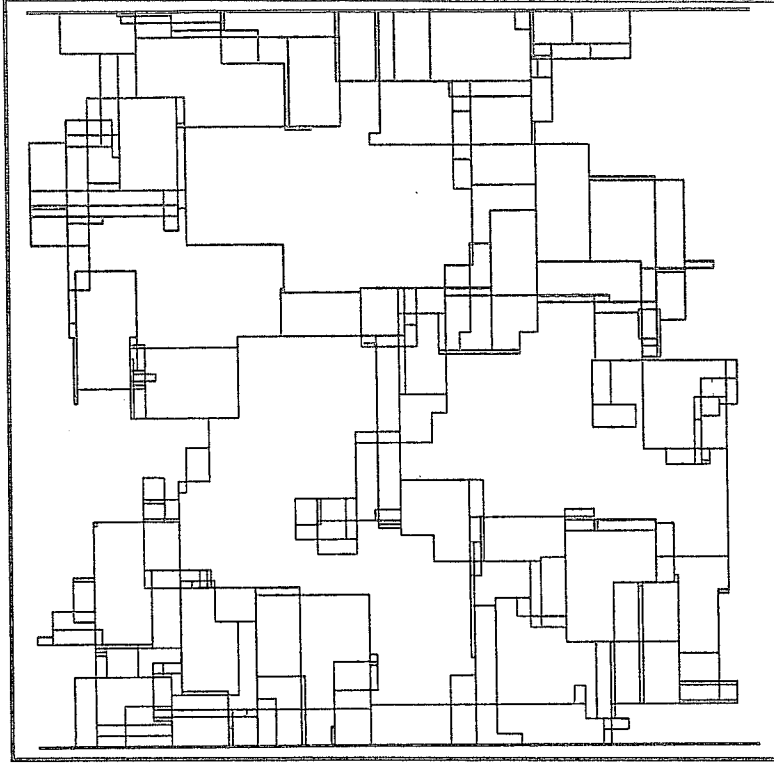
RCS 32518



Fracture $K_h = 10.0$

Fracture $K_v = 1.0$

Effective $K_h = 0.1005$



Permeable Backbone

Effective $K_h = 0.1005$

Fig 3 UPSCALING FOR FRACTURED MEDIA
RCS 32536

Estimating Effective Permeability: A Comparison of Techniques

Colin McGill, Peter King & John Williams

*BP Research,
Sunbury Research Centre, Chertsey Road,
Sunbury-on-Thames, Middlesex, TW16 7LN, U.K.*

1 Introduction

Effective permeability is an important control on the behaviour of reservoir models. With the advent of multi-million block stochastic models, calculating effective permeability assumes an even greater importance. A number of different techniques for evaluating this quantity have been developed by various workers. This paper presents a quantitative comparison of these methods. We begin by providing a brief description of the methods to be studied.

2 Simple Methods

It is useful to divide the methods for estimating effective permeability, k_{eff} , into two groups: those that consider only the *frequency* distribution of permeabilities, and those that also allow for the *spatial* distribution. The techniques described in this section belong to the first category.

2.1 AVERAGES

It is common practice to use averages as estimates of k_{eff} . The most general form is the *power average* advocated by Deutsch (1986):

$$k_{\text{eff}} = \left\{ \int p(k) k^{\omega} dk \right\}^{1/\omega} \quad (2.1)$$

where $p(k)$ is the frequency distribution of permeabilities. In this formulation, the arithmetic, geometric and harmonic means may be represented by choosing ω to be 1, 0, and -1 , respectively. The difficulty with using the power average is that the choice of ω depends upon the spatial distribution of permeabilities. Only the arithmetic, harmonic and geometric means will be used in this study. A full commentary on the power average can be found in McGill, Williams & King (1991)

2.2 PERTURBATION THEORY

Perturbation theory assumes that the permeability is roughly constant with only small deviations from the mean. Standard theory performs a Taylor series expansion in the parameter $\delta k \equiv (k - \bar{k})/\bar{k}$ up to order δk^2 , where \bar{k} is the mean permeability. This yields

$$k_{\text{eff}} = \bar{k}(1 - \overline{\delta k^2}/D), \quad (2.2)$$

where D is the number of dimensions (2 or 3). This has been extended by King (1987) to include more terms in the Taylor expansion:

$$k_{\text{eff}} = k_g \exp(\sigma_g^2 [1/2 - 1/D]) \quad (2.3)$$

where k_g is the geometric mean of the permeabilities and σ_g^2 is the variance of the logarithm of the permeabilities. Recently, Noetinger (1990) has shown that King's results are exact for an uncorrelated medium with a log-normal distribution of permeabilities.

2.3 EFFECTIVE MEDIUM THEORY

This is an example of a mean field theory. It assumes that any region of permeability behaves as if embedded within the average medium. This problem may be solved analytically. By demanding that the sum of the permeability regions reproduces the average medium a self-consistent solution may be found. This constraint produces the integral equation (Kirkpatrick 1973)

$$\int \frac{p(k)(k - k_{\text{eff}})}{(D - 1)k_{\text{eff}} + k} dk = 0. \quad (2.4)$$

3 Better Estimates

The techniques discussed above have two main restrictions. They do not take the spatial distribution of permeabilities into account and they can deal only with scalar (isotropic) permeabilities. The techniques discussed in this section can address both these considerations, although the formulations considered here are restricted to permeability tensors which have diagonal components only. While this is a common assumption in reservoir engineering studies, some authors (e.g., White & Horne 1987) claim that the full tensor nature of the permeability must be taken into account.

3.1 LAYER AND COLUMN ESTIMATES

These techniques are quick and allow bounds to be placed on each component of effective permeability. Note that even if the permeability is locally isotropic, the spatial distribution of permeabilities will in general mean that k_{eff} will be anisotropic.

The column technique divides the region into one-dimensional columns in the direction of flow. By assuming that no flow is allowed between columns, an estimate of effective permeability is readily constructed. This is an underestimate of the permeability since inter-column flow is restricted. In contrast, the layer method breaks the region down into a series of layers perpendicular to the flow direction. The effective permeability of each layer is given by the arithmetic mean of the permeabilities in the layer. The layer permeabilities can then be combined by taking their harmonic mean. This produces an overestimate of effective permeability since inter-column flow is unimpeded.

3.2 RENORMALISATION

Renormalisation is a quick yet sophisticated method for calculating effective permeabilities (King 1989). The technique works by dividing the grid into $2 \times 2 \times 2$ sub-blocks. The effective permeability of each sub-block can be calculated analytically, yielding a new grid with 8 times fewer blocks. The process can be repeated again and again until only one block remains. This block has the effective permeability of the original grid. Renormalisation is discussed in detail by Jones, King, McGill & Williams elsewhere in this volume.

3.3 NUMERICAL SOLUTION

It is possible to obtain the 'exact' effective permeability by solving the flow equations (Darcy's law plus conservation of mass) numerically. This technique is much slower than the others discussed here but it does provide the yardstick by which others may be judged. Full details may be found in Begg & King (1985).

3.4 RESISTOR NETWORK METHODS

It is an interesting and useful observation that the discretised form of the flow equations can be cast in the form of a resistor network. In two dimensions, the resistor network can be manipulated using the star-triangle transformation. The result is a single resistor which can be interpreted as an effective permeability. This is an *exact* solution for effective permeability, in full agreement with the numerical answer. However, the technique is much faster than the conventional numerical solution. Full details can be found in Williams (1991).

4 Comparison of methods

The methods described above were used to evaluate the effective permeabilities for several permeability data sets, all generated using the Sequential Gaussian Simulation (SGS) technique (Verly 1991). SGS produces output with normal scores (normally distributed with a mean of zero and variance of one). This may be mapped into a log-normal distribution of permeabilities by using a transformation of the form:

$$k = k_g \exp(\sigma_g \phi), \quad (4.1)$$

where ϕ is the normal score value, k_g the desired geometric mean of the permeability distribution and σ_g is the desired variance in logarithm of the permeabilities.

For the first test, an uncorrelated field was generated and converted to permeabilities using σ_g values of 0.1, 0.5, 1.0, 2.0 and 3.0. k_g was taken to be 100 throughout. The results of applying the different methods are shown in Table 1.

Method	k_{eff} $\sigma_g = 0.1$	k_{eff} $\sigma_g = 0.5$	k_{eff} $\sigma_g = 1.0$	k_{eff} $\sigma_g = 2.0$	k_{eff} $\sigma_g = 3.0$	CPU s
Arithmetic Mean	100.52	113.39	164.68	727.45	7928.22	0.13
Geometric Mean	100.02	100.12	100.24	100.47	100.71	0.13
Harmonic Mean	99.52	88.25	60.19	12.77	1.10	0.13
Standard P.T.	100.02	97.47	27.05	—	—	0.17
Extended P.T	100.02	100.12	100.24	100.47	100.71	0.21
E.M.T.	100.02	100.15	100.41	100.95	101.31	1–4
Column Estimate	99.53	88.50	61.53	16.33	3.21	0.14
Layer Estimate	100.51	112.73	161.23	573.27	3234.43	0.16
Renormalisation	99.94	98.12	93.34	80.15	66.37	0.65
KEFF	99.84	96.21	87.96	71.40	56.68	50–180
Resistor Network	99.84	96.21	87.96	71.40	56.68	4.91

Table 1. The results of applying the methods for calculating effective permeabilities discussed above to datasets with increasing variability. It should be noted that for small σ_g virtually any method will give an acceptable answer. However, as σ_g increases, only the renormalisation method gives an acceptable answer. The last two methods are assumed to represent the correct answer. — indicates a negative value.

As can be seen from Table 1, for small σ_g virtually any method will give an acceptable answer. As the variability increases, however, renormalisation alone of all the approximate methods yields an acceptable answer. Note that renormalisation is about 200 times faster than KEFF for this grid of 250×40 points.

The second test was designed to show the influence of lateral correlations on the resulting effective permeabilities. Data sets with a vertical correlation length of 4 grid points and horizontal correlation lengths of 0, 5, 25, 125 and 625 grid points were generated. They were converted to permeabilities using $k_g = 100$ and $\sigma_g = 2$. The results are shown in Table 2. Note that for the simple methods only a value of the isotropic k_{eff} can be obtained whilst the other

Method	k_{eff} $l_c = 0$	k_{eff} $l_c = 5$	k_{eff} $l_c = 25$	k_{eff} $l_c = 125$	k_{eff} $l_c = 625$	CPU s
Arithmetic Mean	724.47	732.93	654.04	916.61	438.12	0.10
Geometric Mean	100.47	97.81	109.45	143.50	97.49	0.16
Harmonic Mean	12.77	12.22	14.88	25.91	13.05	0.13
Standard P.T.	—	—	—	—	—	0.17
Extended P.T	100.47	97.81	109.45	143.50	97.49	0.21
E.M.T.	100.95	98.68	111.06	142.69	105.02	2

Method	k_h $l_c = 0$	k_h $l_c = 5$	k_h $l_c = 25$	k_h $l_c = 125$	k_h $l_c = 625$	CPU s
Column Estimate	14.23	14.75	24.20	66.73	213.70	0.14
Layer Estimate	504.60	415.42	386.05	749.60	414.28	0.16
Renormalisation	78.95	87.15	193.36	473.87	323.05	0.65
Resistor Network	69.40	86.52	177.10	416.45	321.97	4.91
KEFF	69.40	86.51	177.07	416.40	322.00	~ 100

Method	k_v $l_c = 0$	k_v $l_c = 5$	k_v $l_c = 25$	k_v $l_c = 125$	k_v $l_c = 625$	CPU s
Column Estimate	19.18	22.77	29.42	35.03	15.15	0.14
Layer Estimate	652.77	607.29	450.01	269.33	34.29	0.16
Renormalisation	81.17	80.81	50.78	48.11	15.55	0.65
Resistor Network	72.34	80.98	57.82	55.53	15.69	4.91
KEFF	72.34	80.98	57.82	55.54	15.70	~ 100

Table 2. The results of applying the different methods for obtaining k_{eff} to datasets with increasing correlation lengths. Note again that only renormalisation produces results in accord with the exact results.

methods can provide values for both k_h and k_v . Since the correlation lengths are anisotropic it is expected that these should now be different.

Before comparing the methods, it is instructive to note that the bounds on permeability given by the column and layer estimates converge to the correct solution as the correlation length increases. This is because for infinite correlation length the system is layered; in this limit the column and layer estimates become *exact*. Table 2 also indicates that correlation has little effect when the correlation lengths are much smaller than the size of the system. In this limit, the system behaves as though uncorrelated. Thus, the more approximate estimates can work well in the limits of small or infinite correlation. However, in the intermediate regime, more sophisticated methods are needed.

Again the figures indicate that renormalisation gives quite impressive results. Typically, renormalisation gives results which are correct to within 10–20% whilst taking only five times as much CPU as a straight average. The time taken is at least two orders of magnitude less than the numerical solution. Although we have not performed experiments on larger systems here, this impressive speed ratio can be expected to improve with system size.

The impressive performance of renormalisation has also been noted by other authors (e.g., Grindheim & Aasen 1991). A more complete comparison can be found in McGill, Williams & King (1991).

Acknowledgements

The authors would like to thank the British Petroleum Company plc for permission to publish this paper.

References

- Begg, S.H. & King, P.R. (1985) *SPE* 13529
- Deutsch, C. (1986) *SPE* 15991
- Grindheim, A.O. & Aasen, J.O. (1991) Presented at *Lerkendal Petroleum Engineering Workshop*, Trondheim.
- King, P.R. (1987) *J.Phys.A*, **20**, 3935.
- King, P.R. (1989) *Transport in Porous Media*, **4**, 37.
- Kirkpatrick, S. (1973) *Rev. Mod. Phys.*, **45**, 574.
- Jones, A.D.W., McGill, C.A., King, P.R. & Williams, J.K. (1991) This volume.
- McGill, C.A., Williams, J. K. & King, P.R. (1991) In preparation.
- Noetinger, B. (1990) Submitted to *Transport in Porous Media*.
- Verly, G.W. (1991) Presented at *EAPG Conference*, Florence.
- White, C.D & Horne, R.N. (1987) *SPE* 16011
- Williams, J.K. (1991) in *Mathematics of Oil Recovery*, Oxford University Press

EARTH STRESS ORIENTATION
- A CONTROL ON, AND GUIDE TO, FLOODING DIRECTIONALITY
IN A MAJORITY OF RESERVOIRS

K J Heffer

BP Research, Sunbury, England

J C Lean

Imperial College of Science
Technology and Medicine
London

I. INTRODUCTION

This poster describes analysis of empirical field data relating to lateral directionality (anisotropy) in flooding of oil reservoirs. It tests the suggestion that anisotropy caused by the presence of natural fractures and faults in the reservoir is widespread. Although this has often been realised during the life of a flood, the influence of natural fractures is not always obvious nor anticipated.

In a network of existing natural fracture sets, any anisotropy in the present earth stresses will influence the distribution and orientation of fracture widths, either with or without injection; hence stresses can govern the anisotropy in fluid conductivity. Perhaps the best direct demonstration of this has been obtained from observations of microseismicity during water injection into jointed granitic geothermal reservoirs (Pine and Batchelor, 1984; Fehler, 1987). If fractures, natural or induced, are conductive over extensive areas of a reservoir, in which the local minimum principal stress axis is (sub) horizontal, then we anticipate that the preferred flooding directions would tend to be at small angles to the local present major horizontal principal stress axis (SHMAX).

The small inclination to SHMAX would be symptomatic of the involvement of extension, shear or hybrid shear fractures, a mixture of these fracture types or local variation of stress directions. The anticipated correlation between the anisotropies of flooding and horizontal stresses was indeed found for 36 field cases in Heffer & Dowokpor (1990). The database for that study has now been more than doubled and we report below the confirmation and further analysis of that correlation.

Other sources of flooding directionality, such as variations in interwell distances or offtake rates, large-scale pressure gradients or formation dip could distort anisotropy due to fractures. For the purposes of this study those other influences are again put aside in order to test the hypothesis of the influence of fracture. The existence of a correlation amidst these potentially conflicting influences on directionality could only strengthen the inference that stress orientation is a prime indicator for flooding directionality.

II. ANALYSIS

The relationship between the flood and stress anisotropies is tested for some 80 fields involving water floods, surfactant/polymer floods and gas floods across North America, the North Sea, Continental Europe, the Middle East and China, using data from both BP operations and the literature. As previously, preferred flood directions were determined by a consistent method, designed to be as objective as possible and utilising data on injected fluid breakthrough, tracer production, oil production response and multiwell pressure analysis. The methodology is to fit, by maximum likelihood, an ellipse representing variation of probability of breakthrough with azimuth to the observed data. It is described in detail in Heffer & Dowokpor, 1990. The preferred flooding direction is taken as the major axis of the fitted ellipse. Stress data were taken mainly from published maps, particularly Zoback et al. 1989, supplemented of course with any locally available data. In general there is an uncertainty of 20 to 30 degrees in stress azimuth measurements, except where more concentrated data has allowed this uncertainty to be reduced to 15°. Interpolation between published data points and local variability of stress direction within structures will further degrade the accuracy.

Figure 1 gives an example of the type of data. Water breakthrough in this group of neighbouring fields showed a strong NW-SE trend, in line with the local orientation of SHMAX.

The 80 field cases studied covered wide variations in reservoir characteristics, such as permeabilities, depths, thickness, lithologies, and tectonic setting. The large majority of cases involved flooding with water or water-based or WAG schemes. Some cases of just gas injection were also included. It is emphasised that no screening of cases was made other than for availability of data on both flood behaviour and local stress orientation.

III. RESULTS

The overall correlation between principal flooding and stress directions for all 80 cases is shown in Figure 2. A very strong trend of flooding in the direction of the major horizontal stress axis is seen; 80% of cases (64) have a deviation between these axes of less than 45 degrees. The data involved more than 1700 individual injector-producer pairs between which flood breakthrough was possible. Figure 3 shows the circular frequency of both "available" flooding directions (outer rose diagram) as well as those directions "taken" by the flood (inner rose diagram). Figure 4 shows directional variation in the proportion of those "available" paths along which breakthrough had actually occurred. It is seen that a significantly higher proportion of breakthrough has occurred along directions close to SHMAX. The probability of breakthrough parallel to SHMAX is interpreted as being approximately 50% greater than the probability in the orthogonal direction. Figure 5 is the "aggregate" ellipse which best fits all of the data: it confirms the trend of figure 4.

The success of the correlation despite variability in local stress orientations is attributed to the fact that averages of both stress and flooding directions are being compared for a given field.

The greater quantity of data in this study has allowed screening of different characteristics of reservoirs. In particular we have divided the cases into those which are deemed "naturally fractured" and those for which natural fractures are not a prominent feature of the reservoir description. Figure 6 shows the deviations of the major flood axes for the "naturally fractured" set of reservoirs: there is a peak at 0 degrees with side peaks at $\pm 15^\circ$. Figure 7 shows the aggregate ellipse of this set of data. Figures 8 & 9 record the results for reservoirs deemed to be "not naturally fractured".

There is little difference in the strength of the trend in either case. Work is currently in progress to determine whether the relative low in frequencies at precisely zero degrees in Figure 8 is meaningful.

Additionally, screening of other reservoir characteristics has indicated:-

- floods below 2000 ft deep show high anisotropy whilst those shallower than 2000 ft show hardly any anisotropy. This would be in accordance with expectations of fractures being responsible for the anisotropy if at greater depths the fractures are sub-vertical whilst at shallower depths they are sub-horizontal or shallow dipping. (Figures 10 to 13)
- floods in extensional tectonic regimes show much higher anisotropies than do those in compressional regimes (defined by maximum principal stress being sub-horizontal, i.e. strike-slip or thrust conditions). This is again in accordance with the involvement of fractures: extensional regimes are favourable for subvertical fractures parallel to SHMAX whilst compressional regimes tend to give vertical fractures striking approximately $\pm 30^\circ$ to SHMAX or thrust fractures with little lateral anisotropy. (Figures 14 to 19).

Two further results are contrary to the possibility that hydraulic fractures induced by injection are responsible for the correlation:

- the more permeable reservoirs show tighter clustering in flood directionality around SHMAX (figures 20 and 21) whilst less permeable reservoirs show greater directionality towards $\pm 30^\circ$ from SHMAX (figures 22 and 23).
- the strength of the correlation is much more marked for those cases in which well spacing is greater than 1000 feet. (figures 24 to 27).

The latter result also weighs against the possibility that the correlation is produced by sedimentary controls; conversely, directionality inherent in the depositional trends contrary to stress directions may destroy the correlation at smaller well spacings.

IV. CONCLUSIONS

Whilst full explanation of these results will require coupled numerical modelling of hydraulic and geomechanical processes, they are strongly indicative of the influence of natural fractures in flooding directionality. Whatever the explanation the study has strengthened the implication that local stress orientation measurements are immediate guides to the likely preferred directions of flooding in a reservoir, to which well patterns and development plans may be adjusted. It is also a pointer towards better understanding, and therefore better prediction of flooding processes.

V. REFERENCES

Heffer, KJ and Dowokpor, AB, (1990). Relationship between Azimuths of Flood Anisotropy and Local Earth Stresses in Oil Reservoirs, North Sea Oil and Gas Reservoirs II, Graham and Trotman.

Zoback, ML et al. (1989). Global Pattern of Tectonic Stress, Nature, 341 (6240), 291-298.

Fig 1. ORIENTATION OF WATER BREAKTHROUGH PATHS
AND PREFERRED PERMEABILITY DIRECTIONS

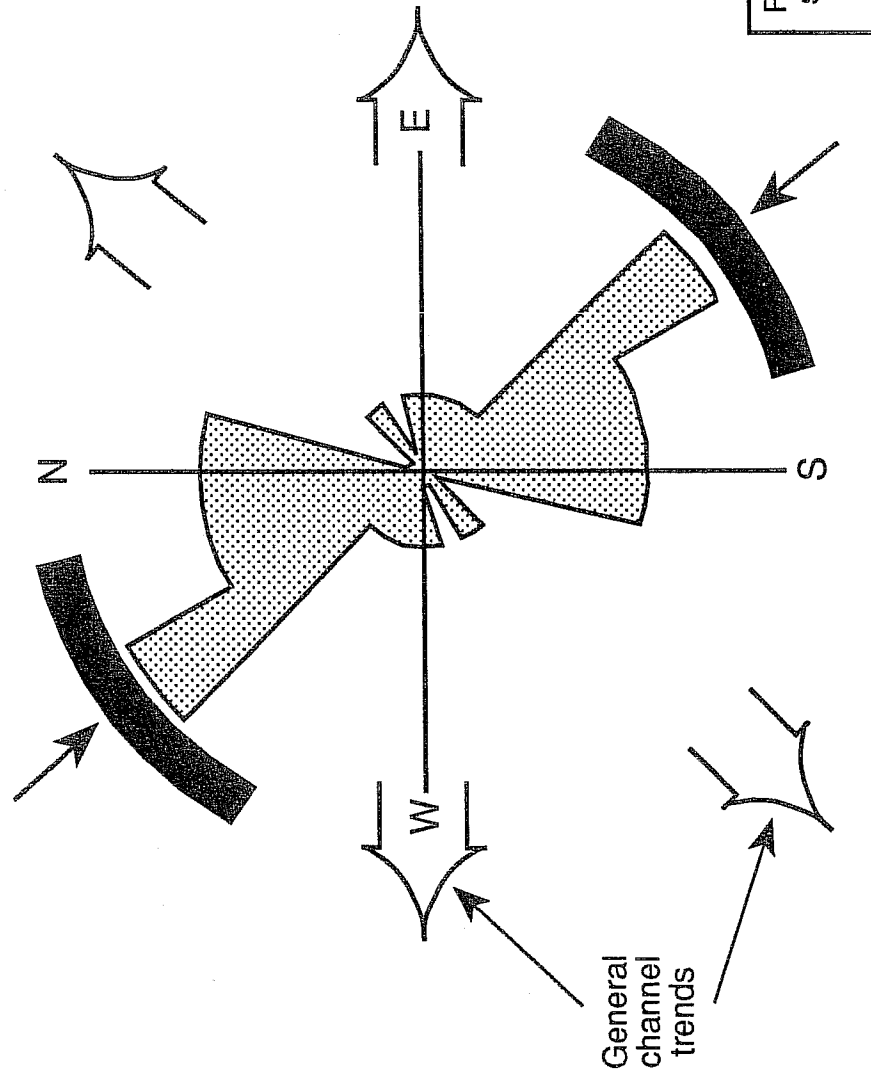


Fig 2. DEVIATION OF MAJOR FLOOD AXES FROM S_{Hmax}
- ALL CASES

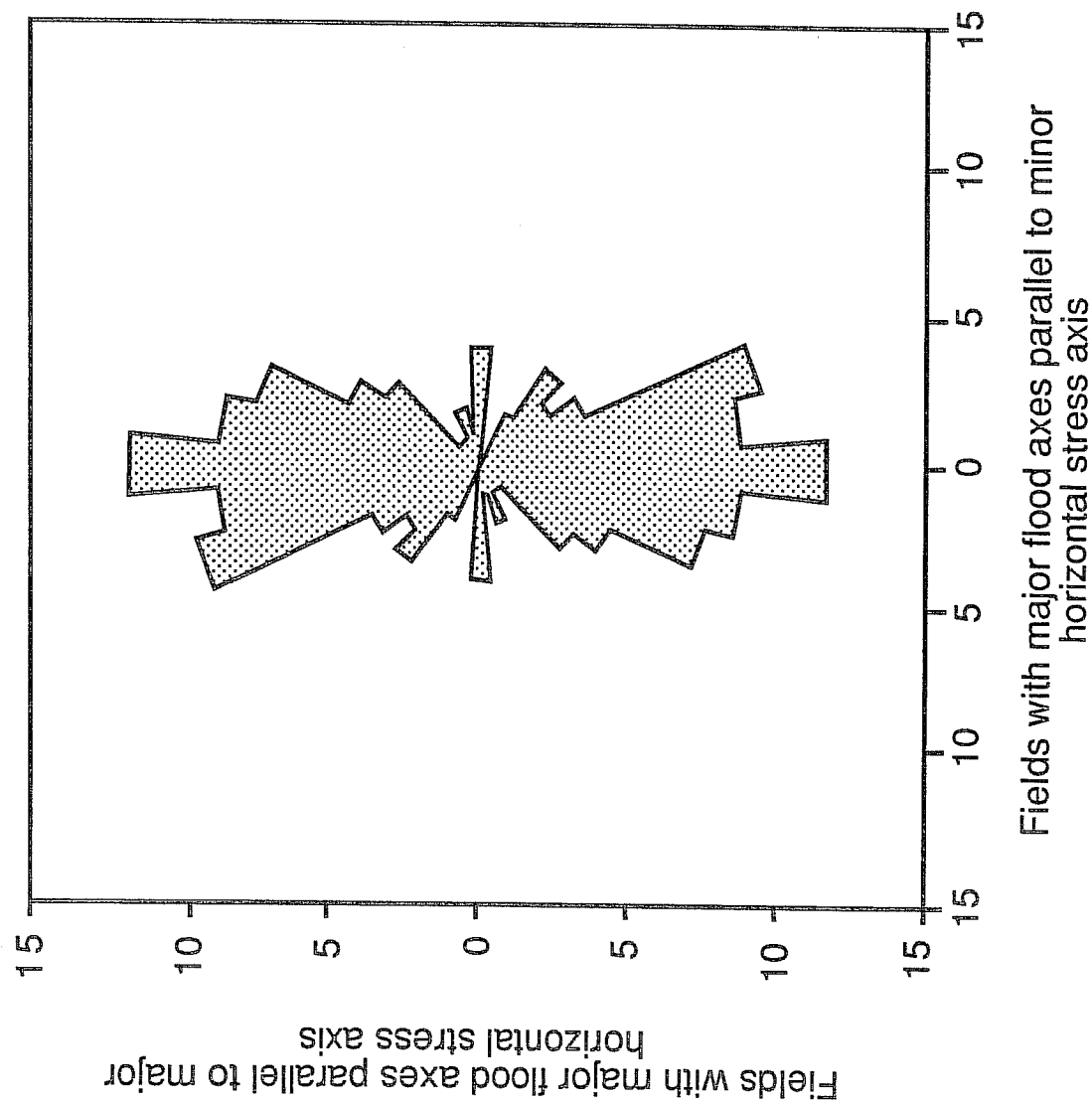


Fig 3. PROPORTIONAL BREAKTHROUGH
- ALL CASES

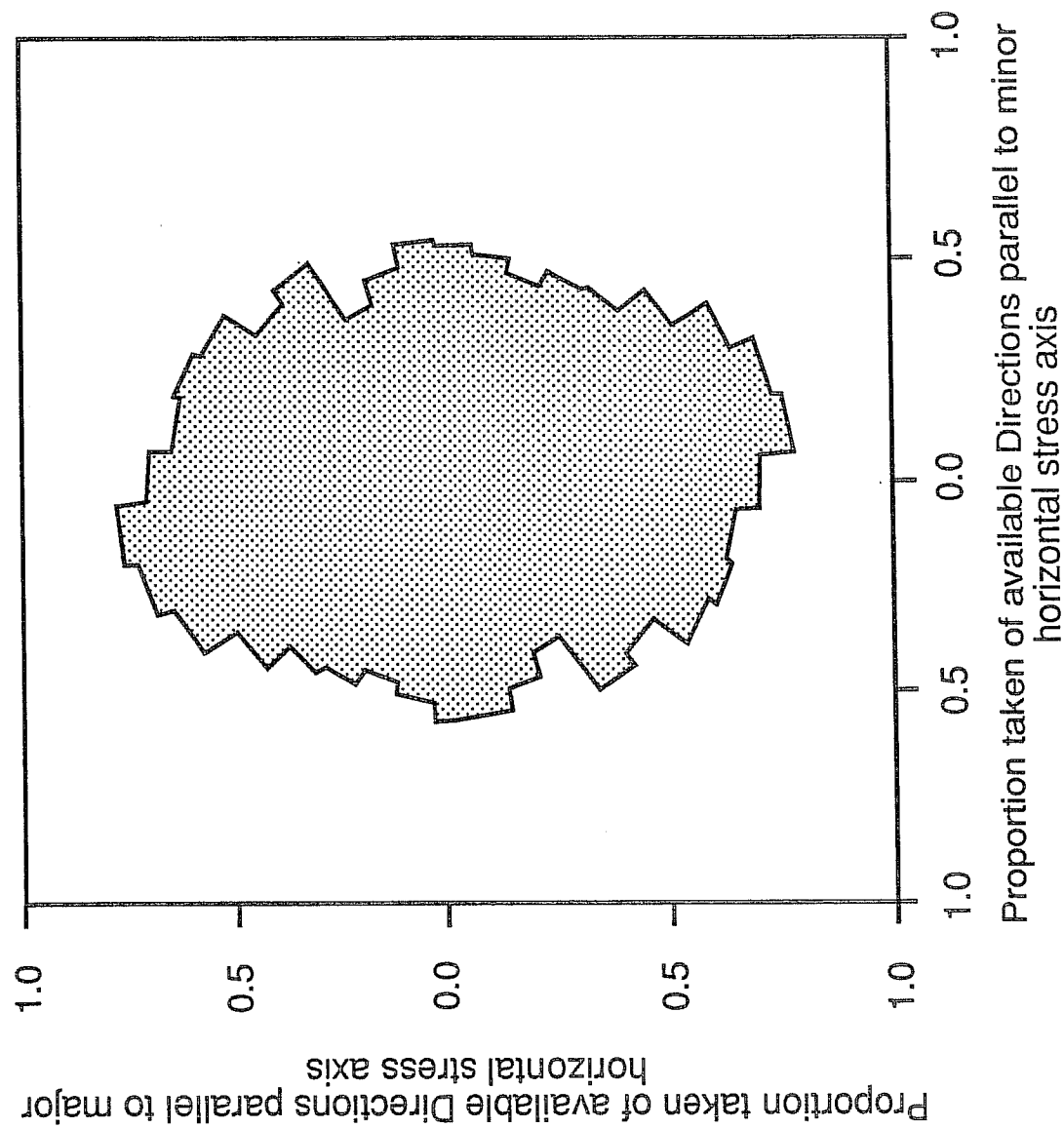


Fig 4. TAKEN AND AVAILABLE DIRECTIONS
- ALL CASES

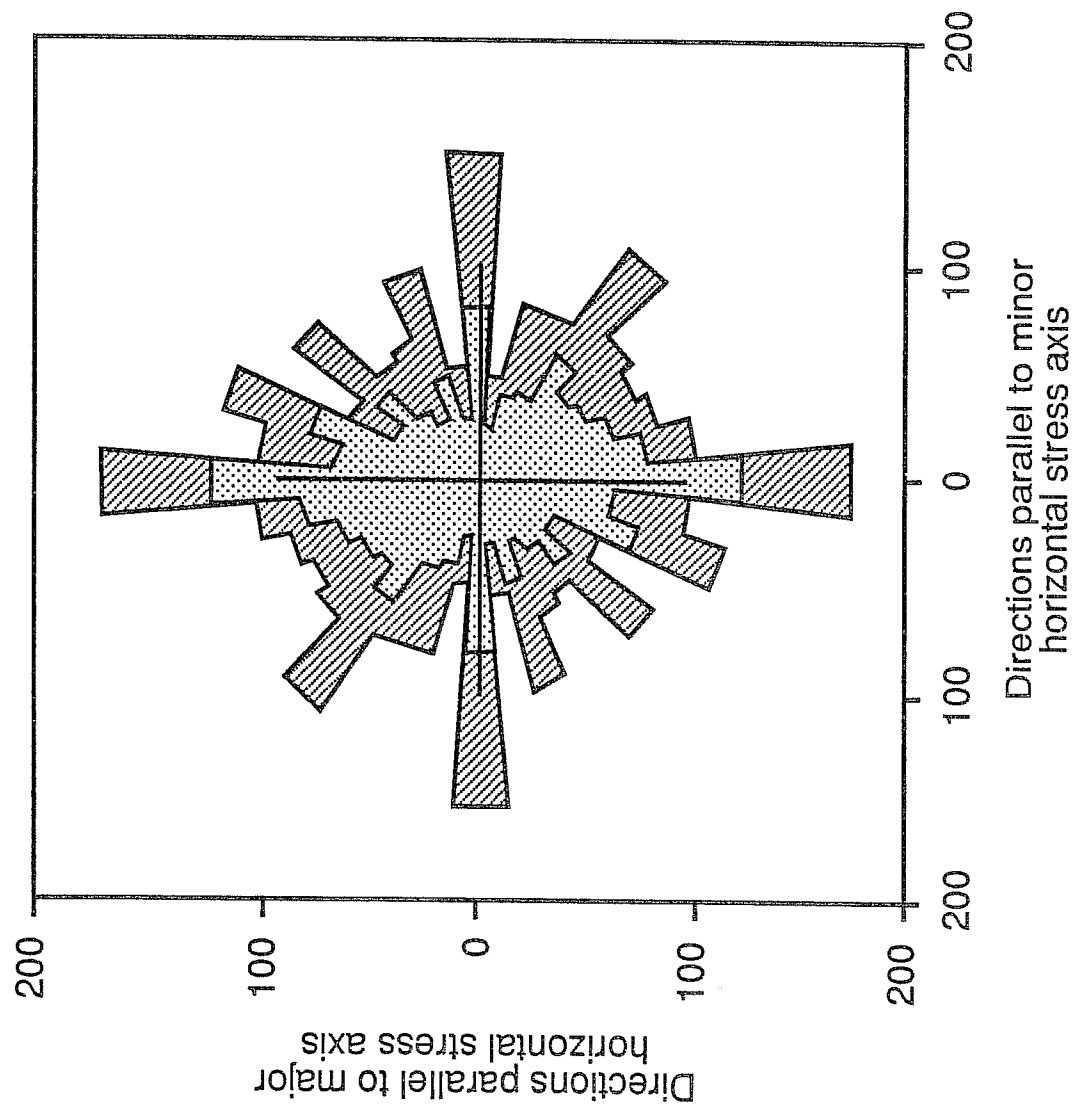


Fig 5. AGGREGATE BREAKTHROUGH PROBABILITY ELLIPSE
- ALL CASES

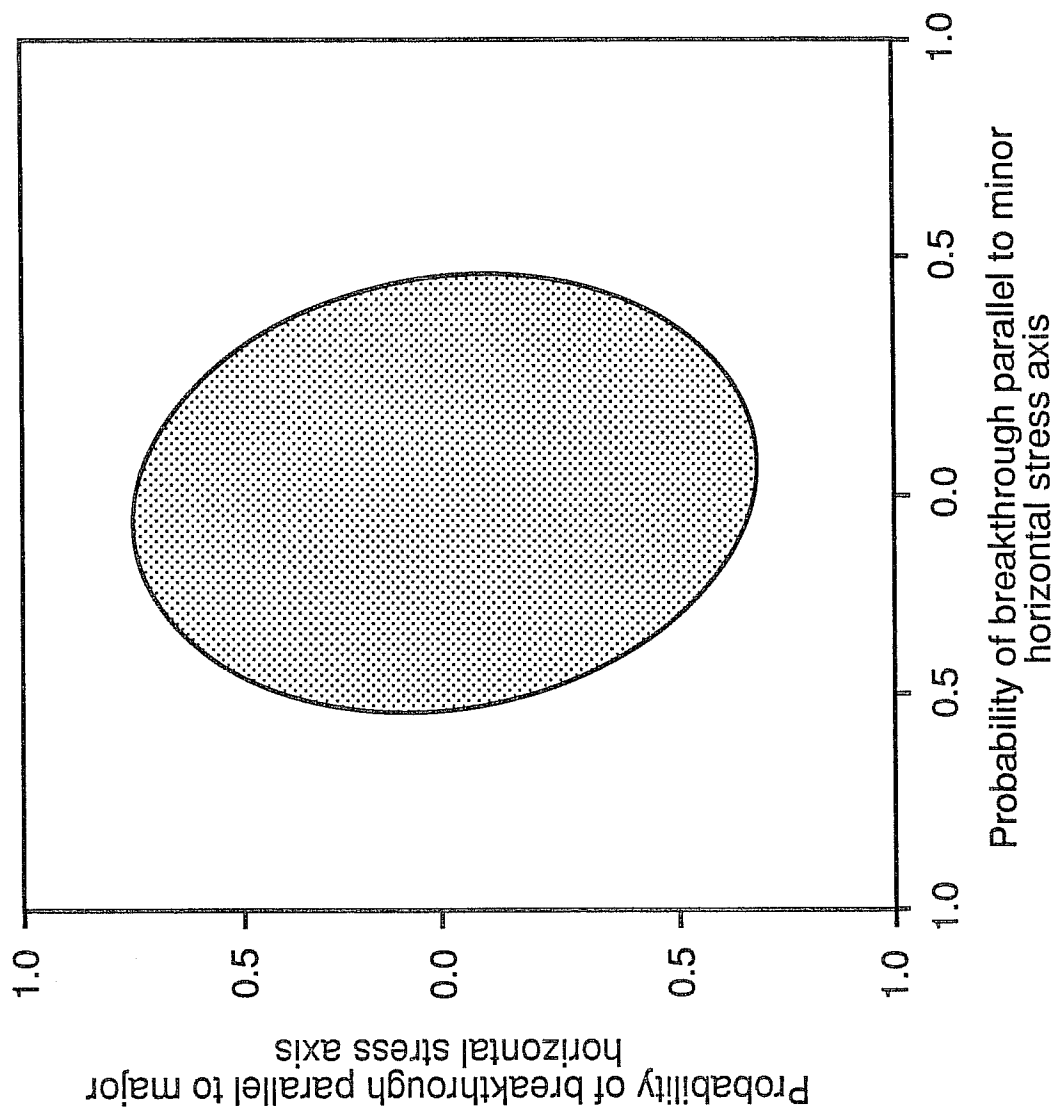


Fig 6. DEVIATION OF MAJOR FLOOD AXES FROM S_{Hmax}
- NATURALLY FRACTURED

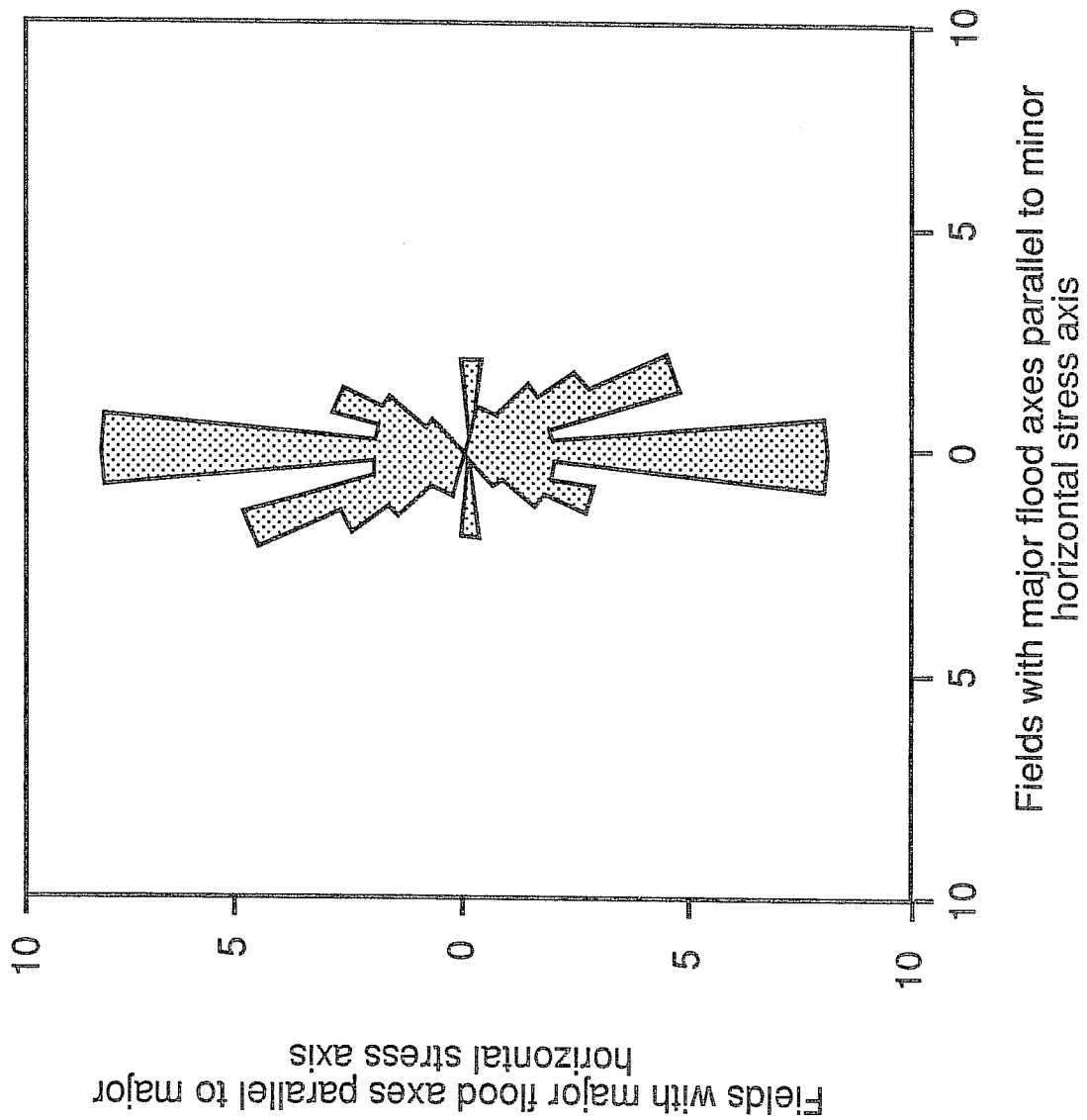


Fig 7. AGGREGATE BREAKTHROUGH PROBABILITY ELLIPSE
- NATURALLY FRACTURED

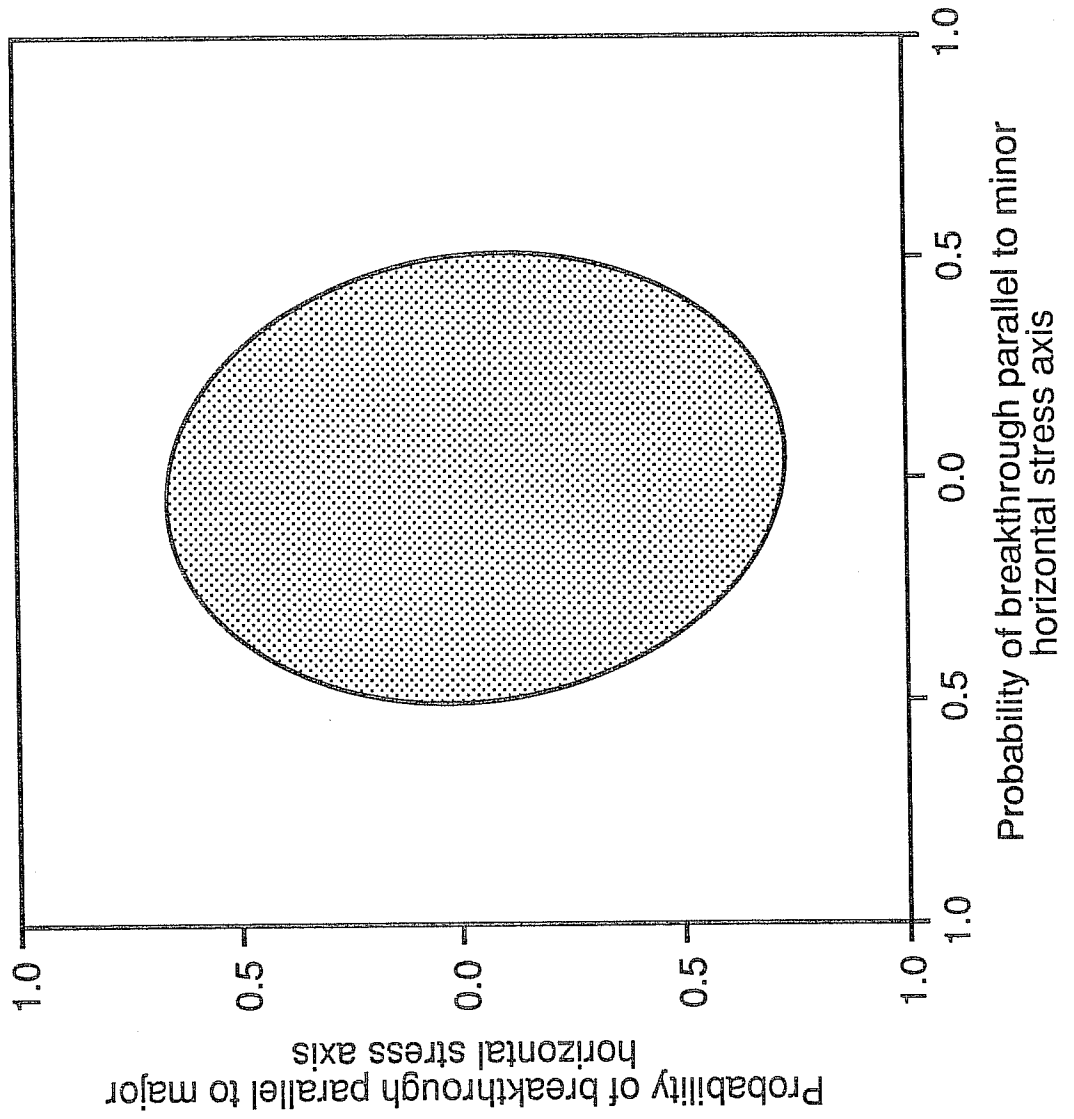


Fig 8. DEVIATION OF MAJOR FLOOD AXES FROM S_{Hmax}
- NOT FRACTURED

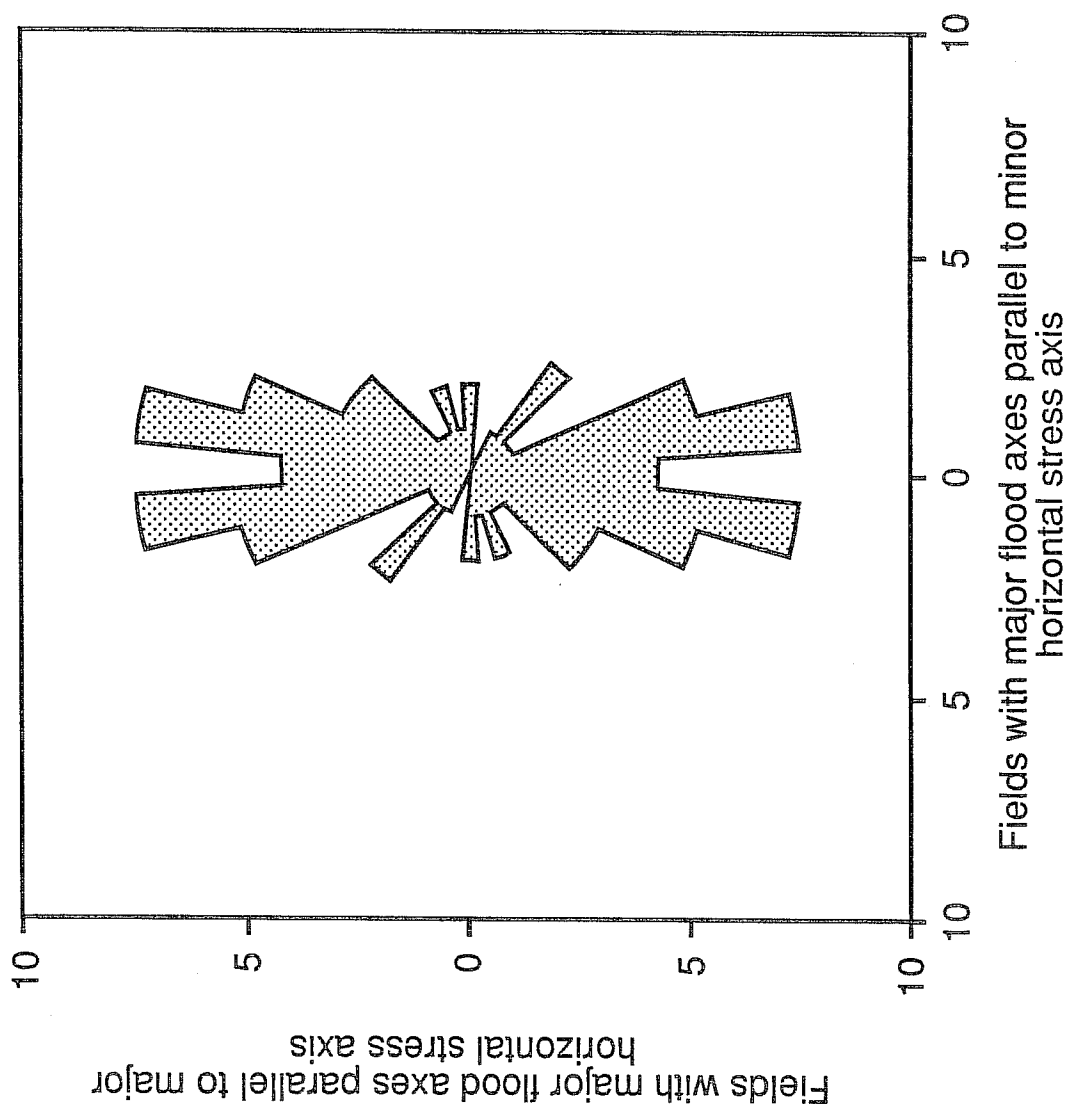


Fig 9. AGGREGATE BREAKTHROUGH PROBABILITY ELLIPSE
- NOT FRACTURED

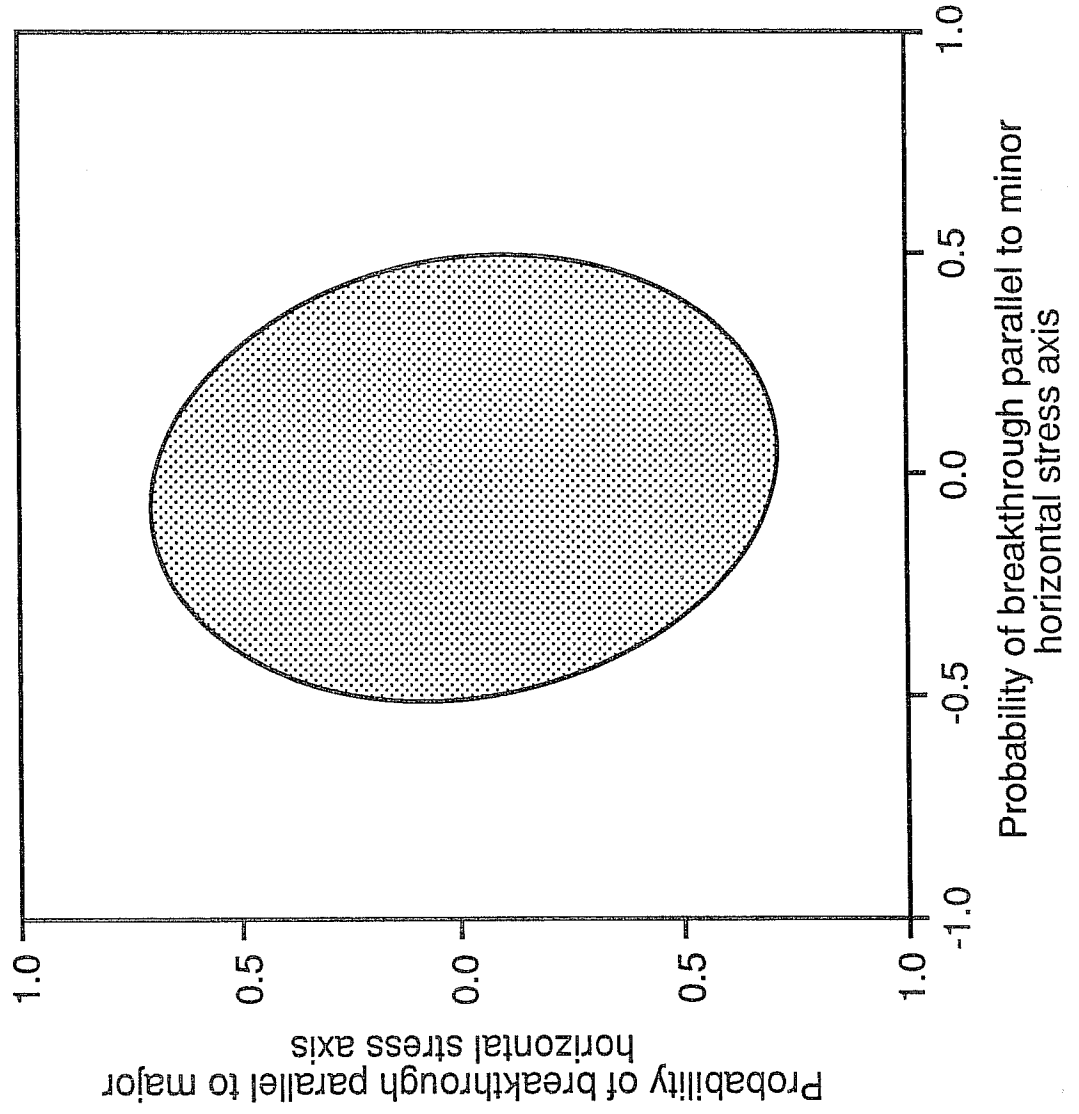


Fig 10. DEVIATION OF MAJOR FLOOD AXES FROM S_{Hmax}
- FLOODS BELOW 2000 ft

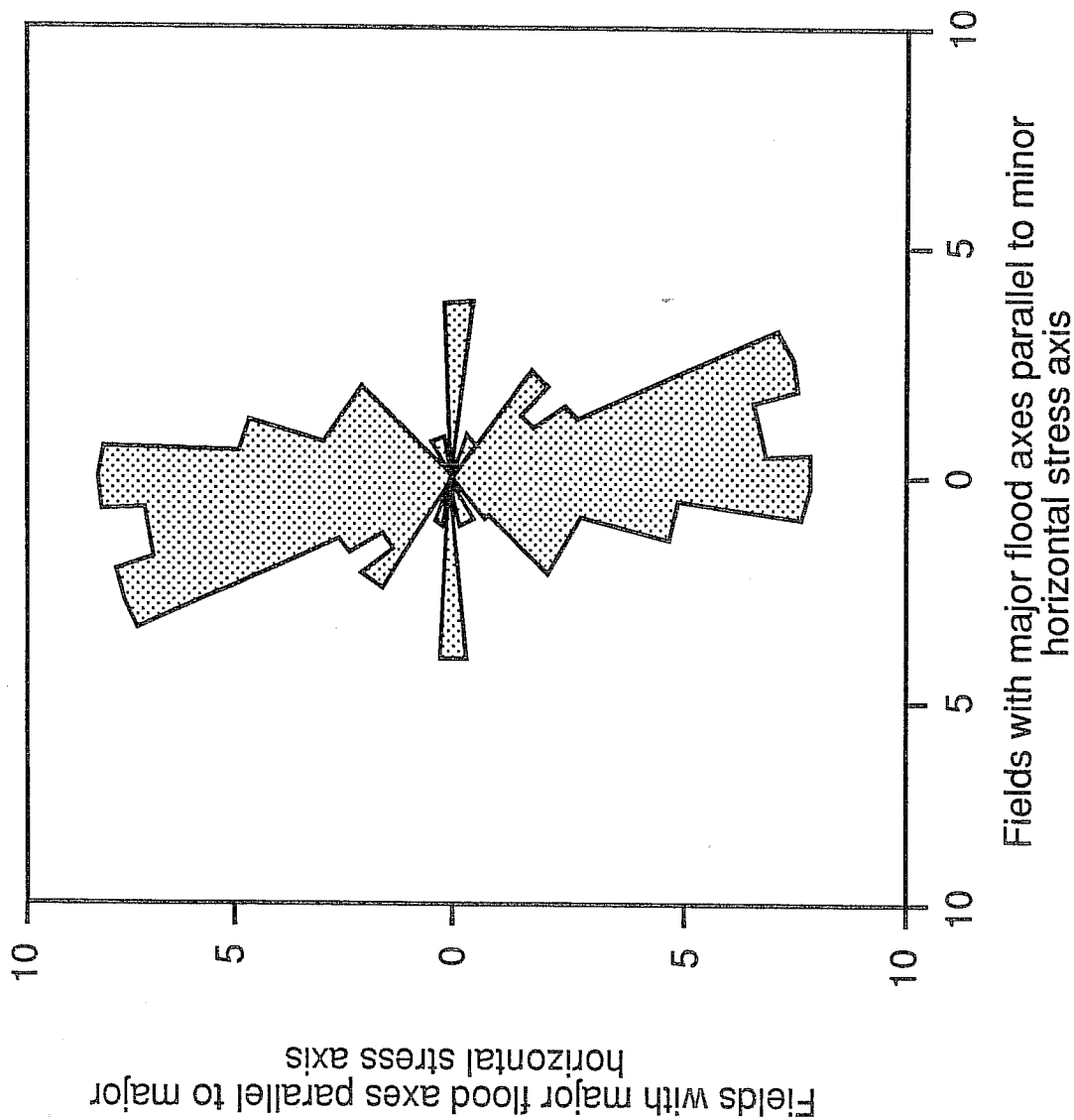


Fig 11. AGGREGATE BREAKTHROUGH PROBABILITY ELLIPSE
- FLOODS BELOW 2000 ft

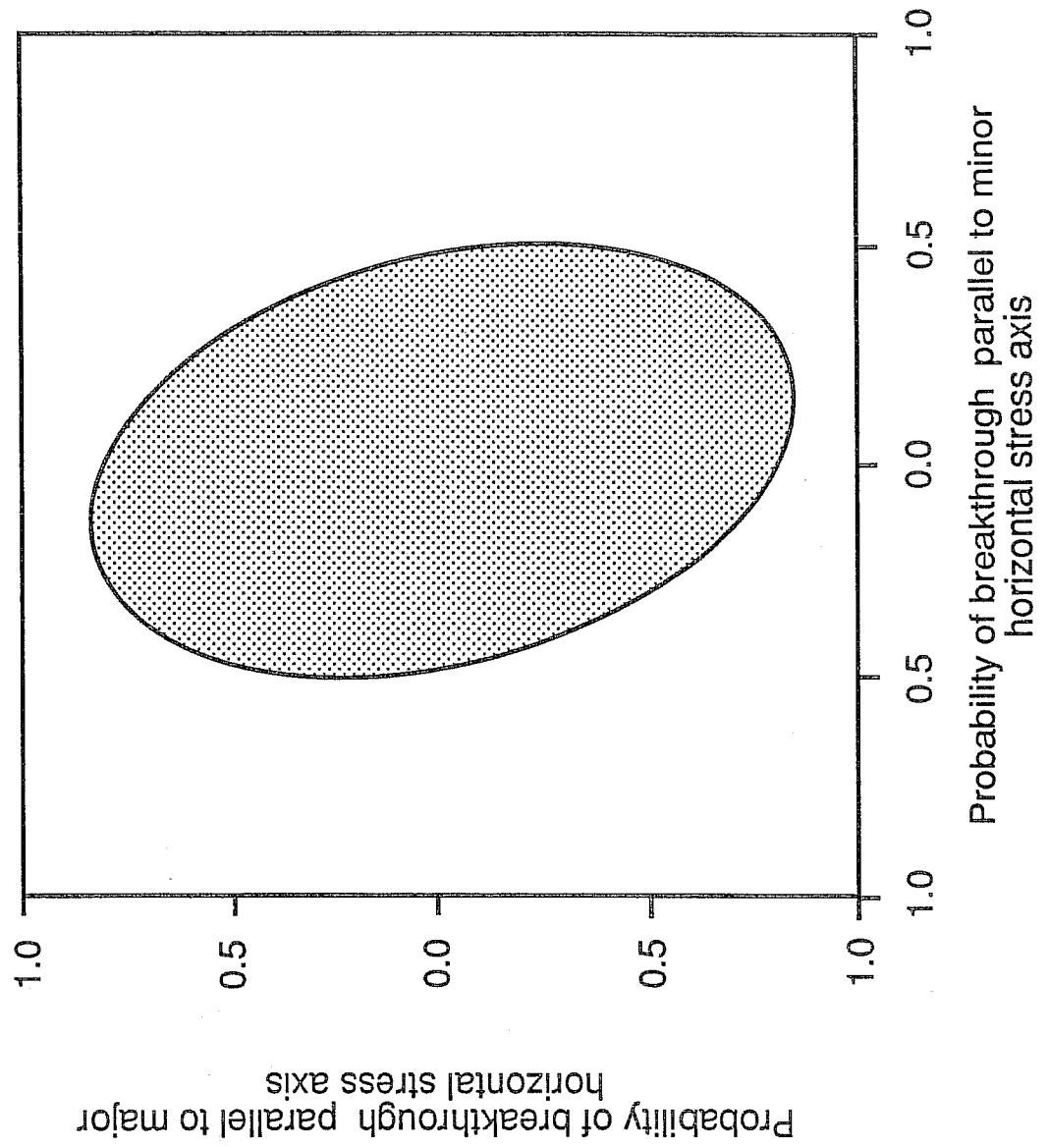


Fig 12. DEVIATION OF MAJOR FLOOD AXES FROM S_{Hmax}
- FLOODS ABOVE 2000 ft

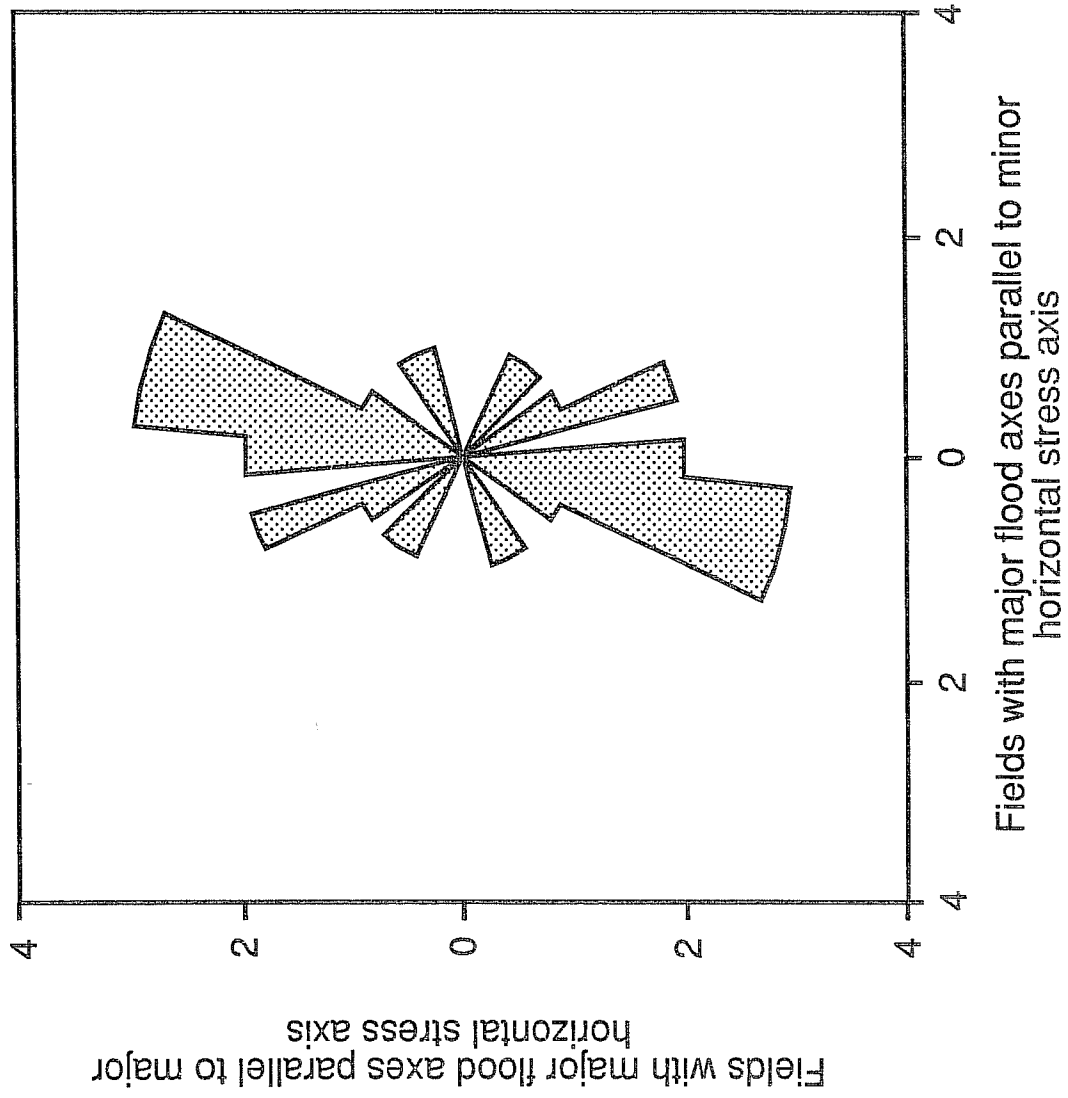


Fig 13. AGGREGATE BREAKTHROUGH PROBABILITY ELLIPSE
- FLOODS ABOVE 2000ft

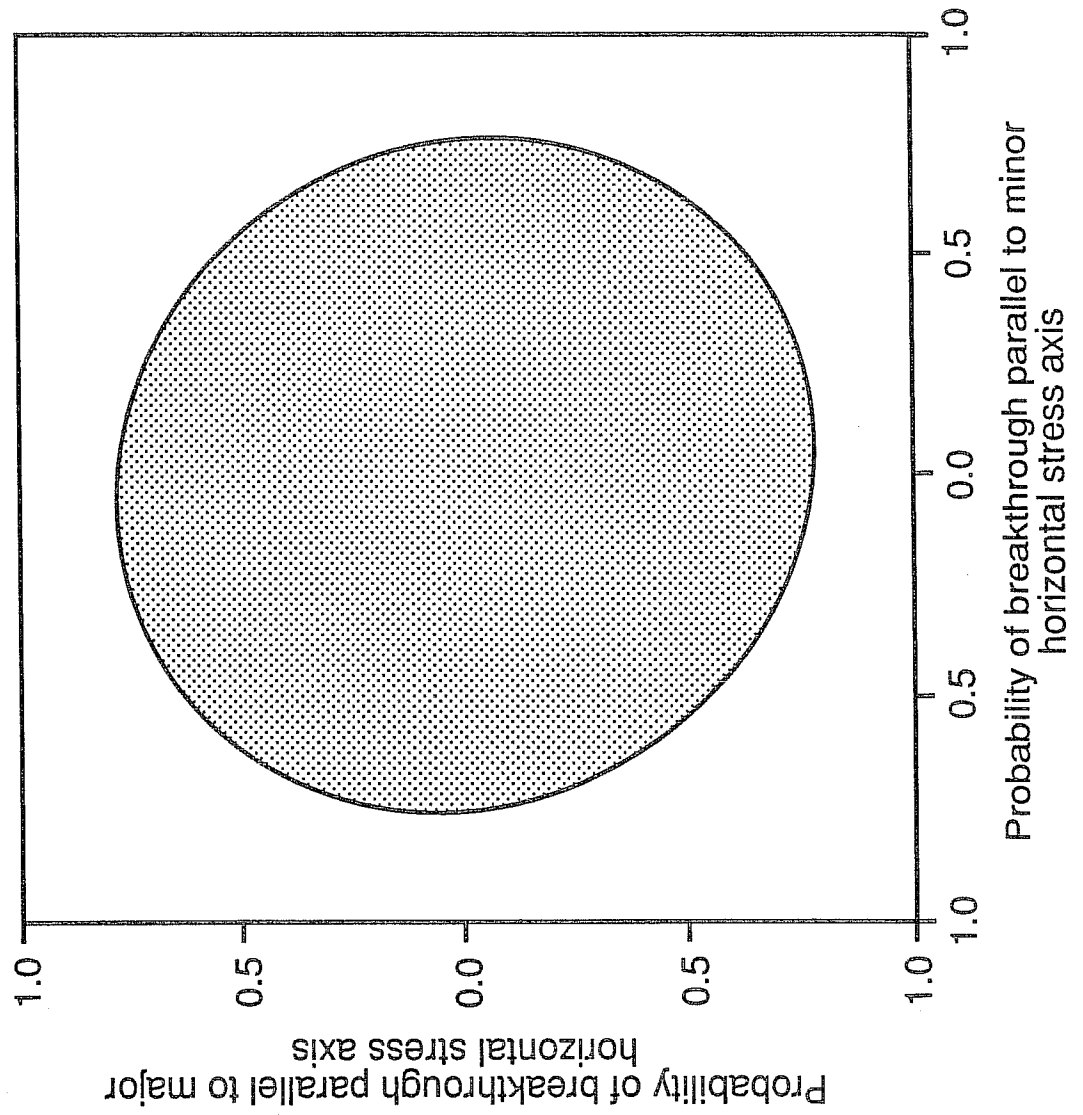


Fig 14. DEVIATION OF MAJOR FLOOD AXES FROM S_{Hmax}
- EXTENSIONAL REGIME

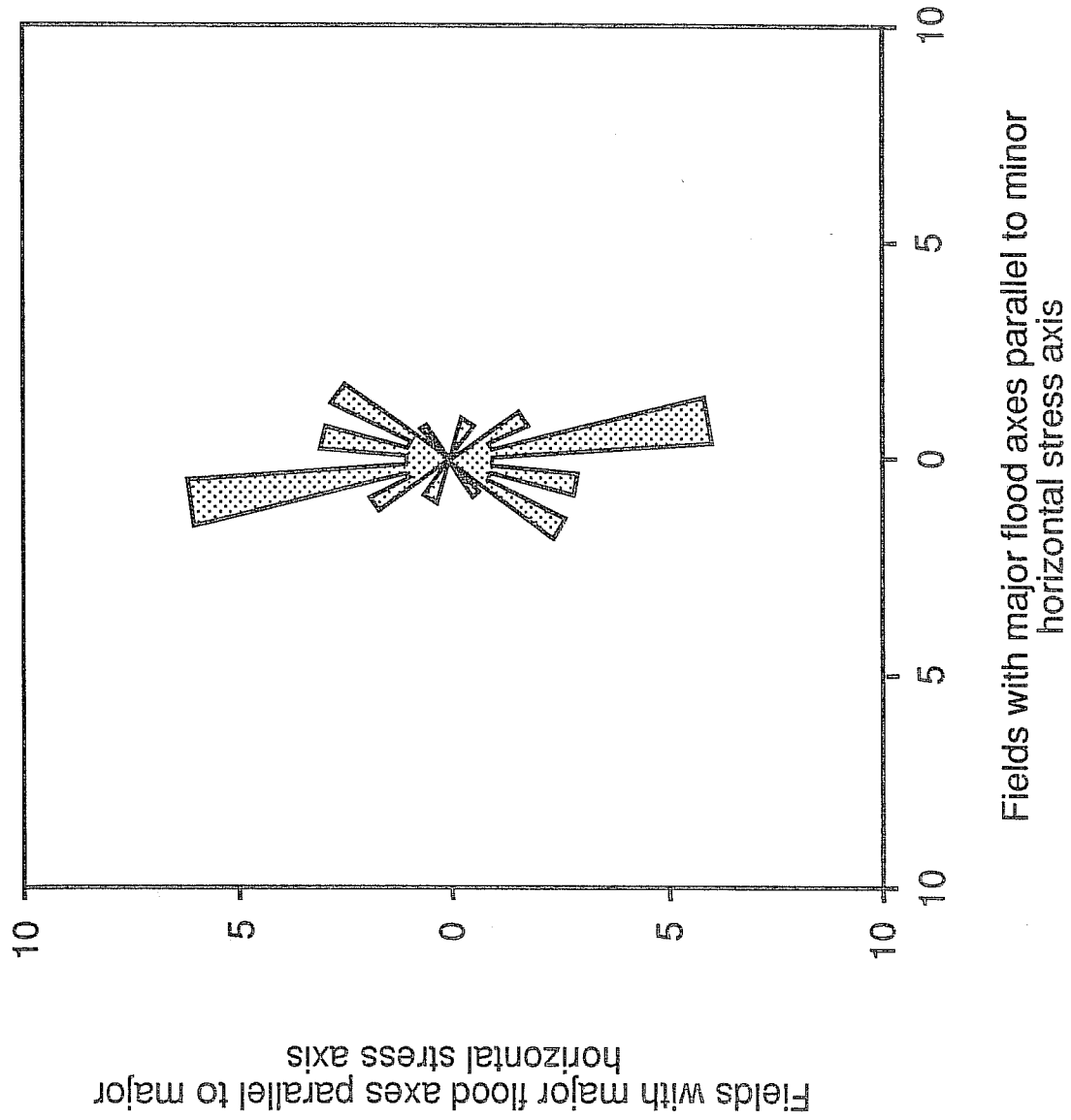


Fig 15. AGGREGATE BREAKTHROUGH PROBABILITY ELLIPSE
- EXTENSIONAL REGIME

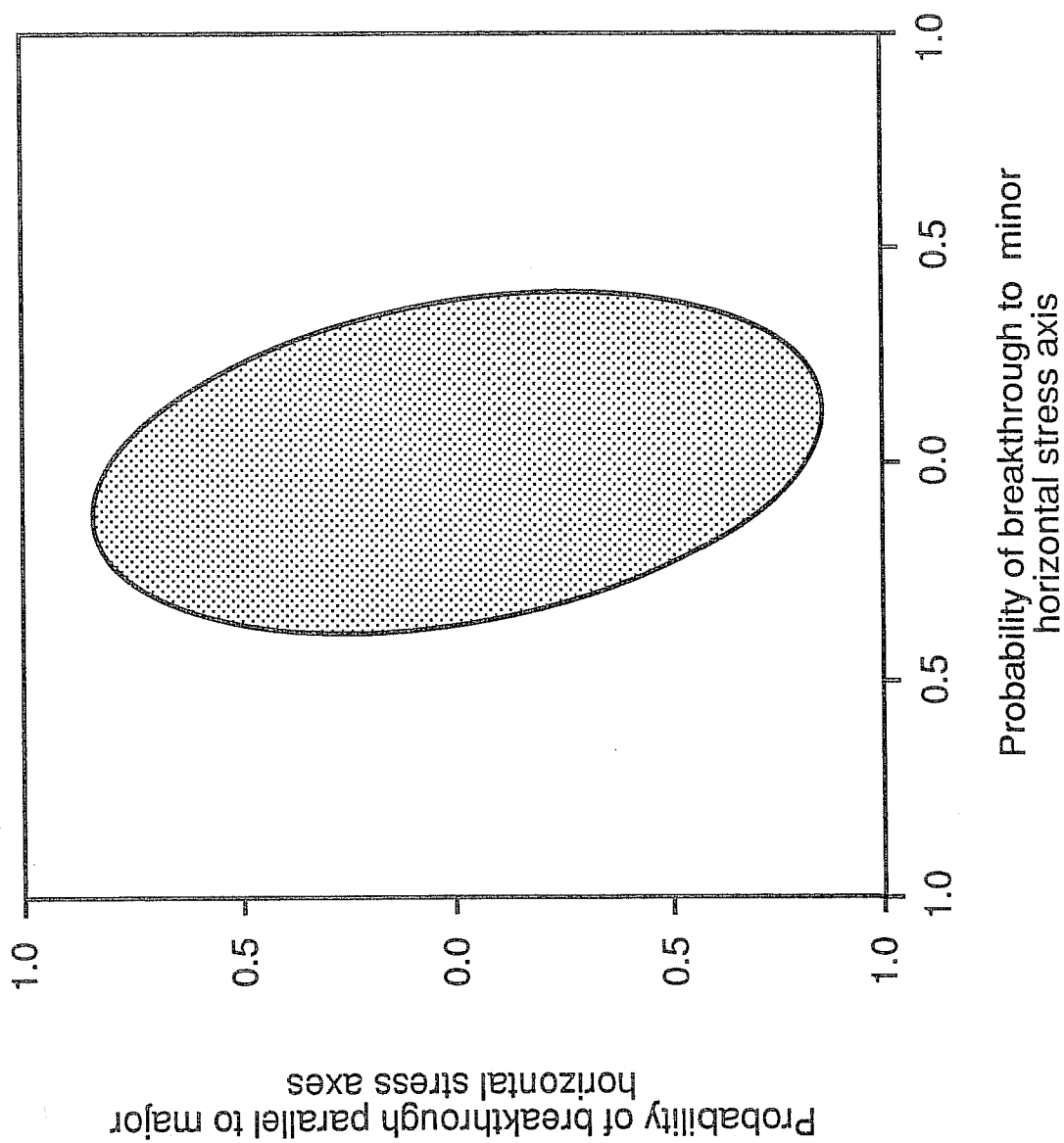


Fig 16. DEVIATION OF MAJOR FLOOD AXES FROM S_{Hmax}
- COMPRESSIONAL CASES

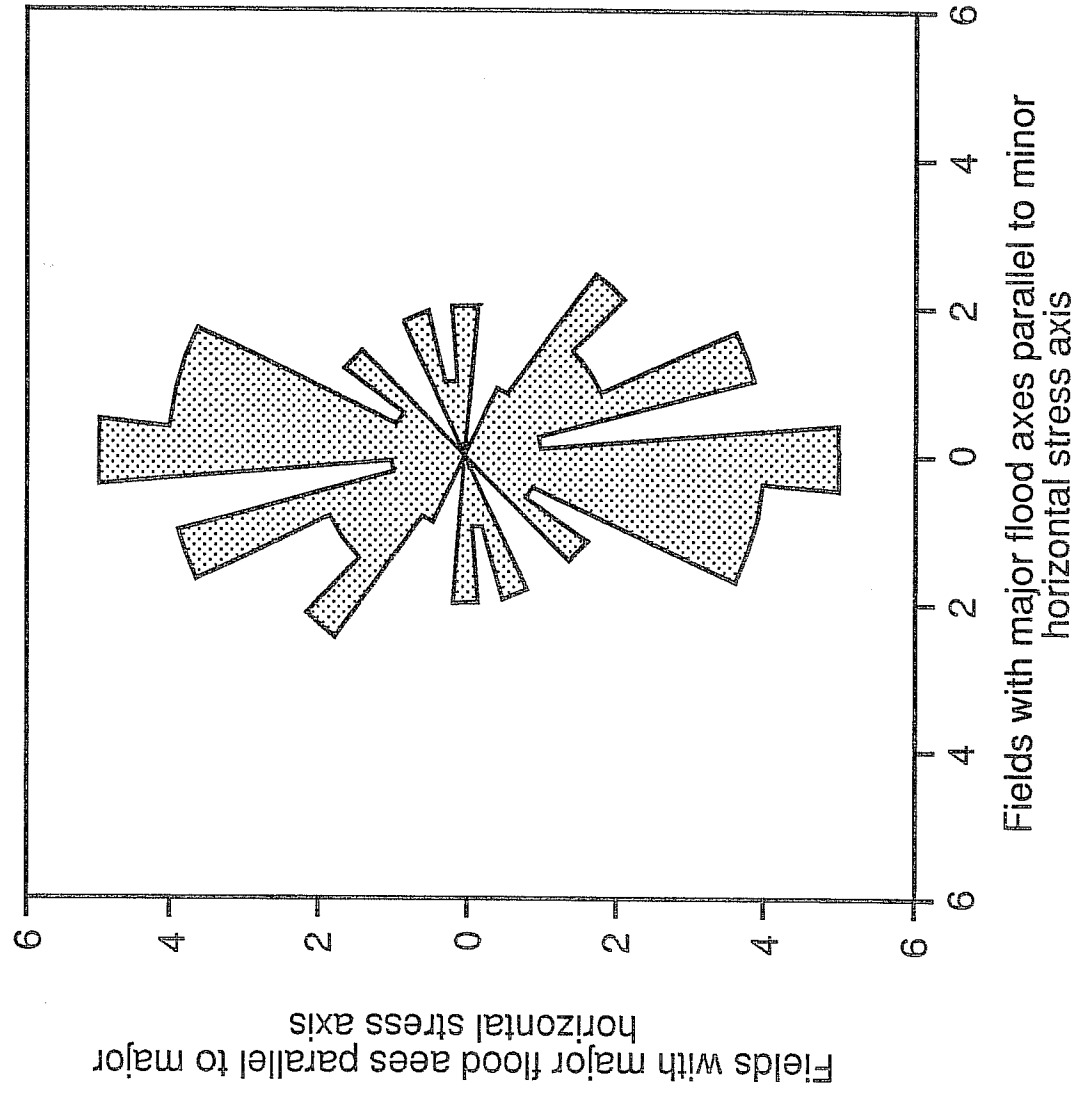


Fig 17. AGGREGATE BREAKTHROUGH PROBABILITY ELLIPSE
-COMPRESSIONAL CASES

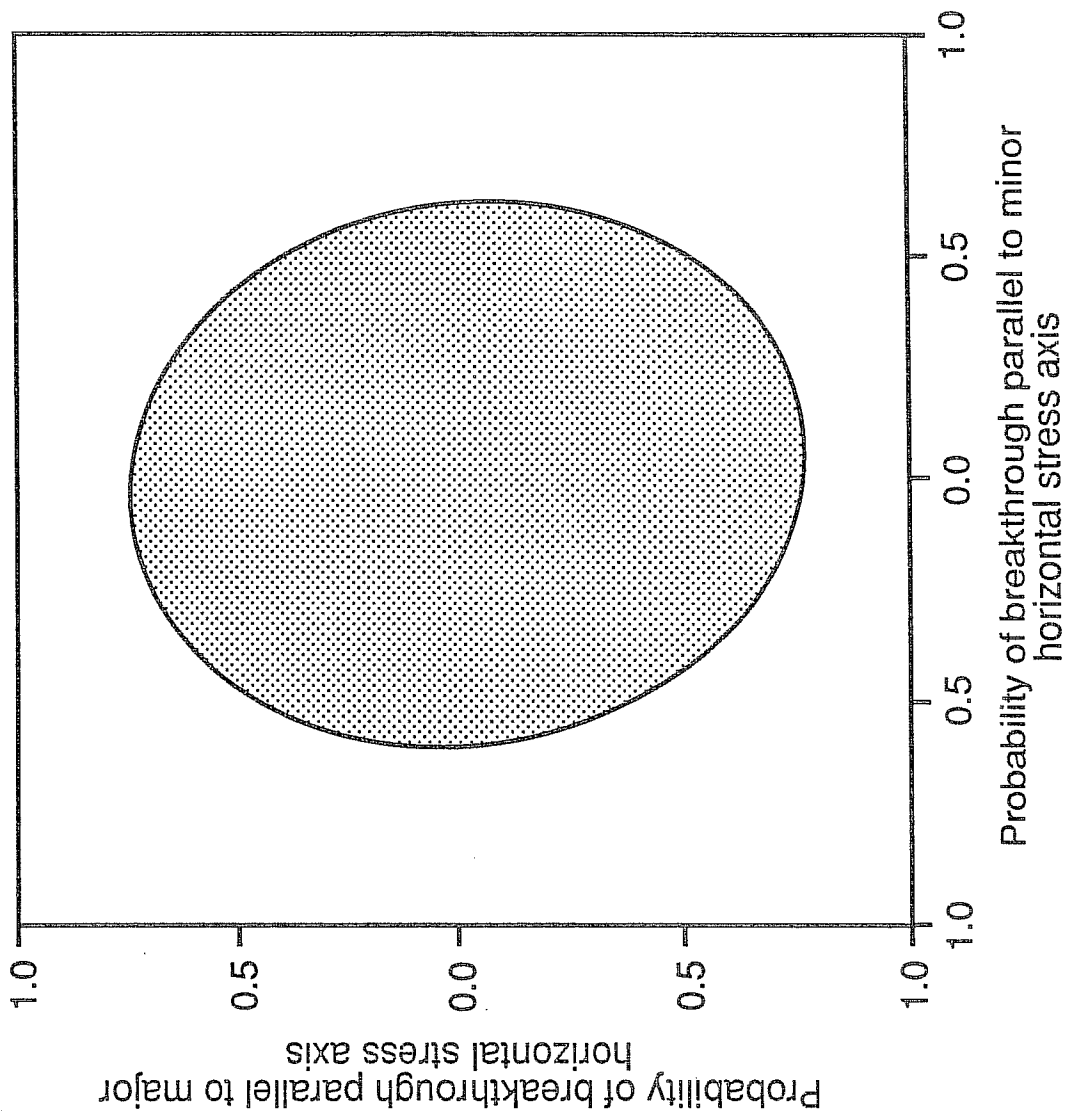


Fig 18. "EXTENSIONAL" REGIME

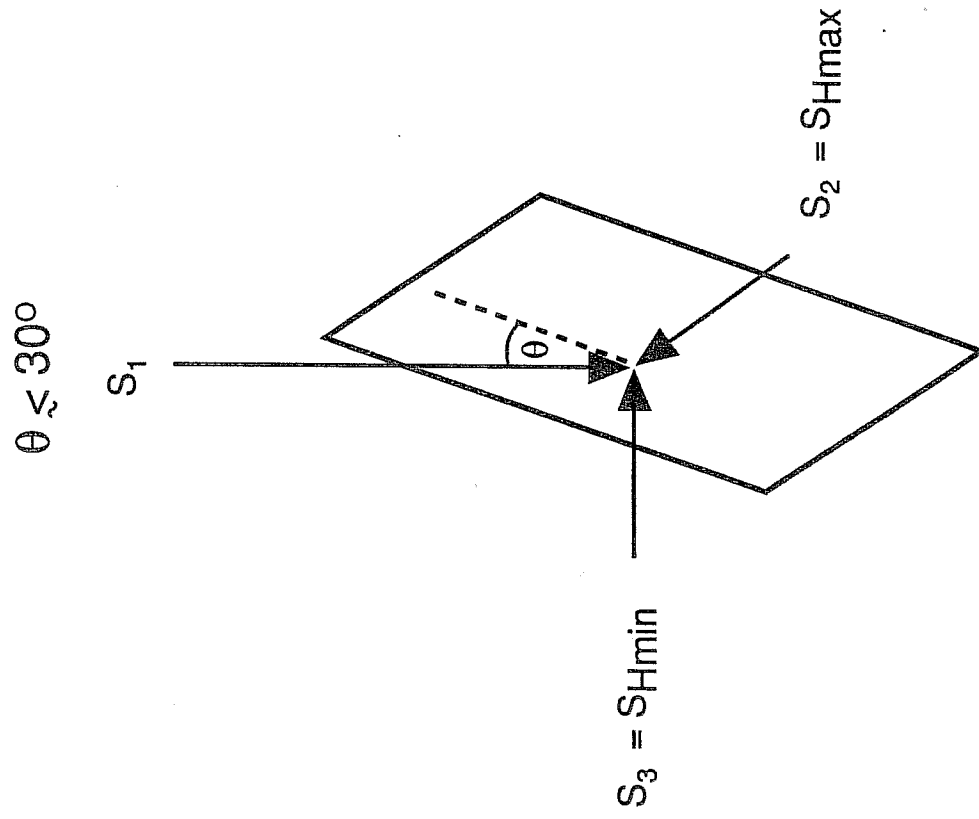


Fig 19. "COMPRESSIONAL" REGIME

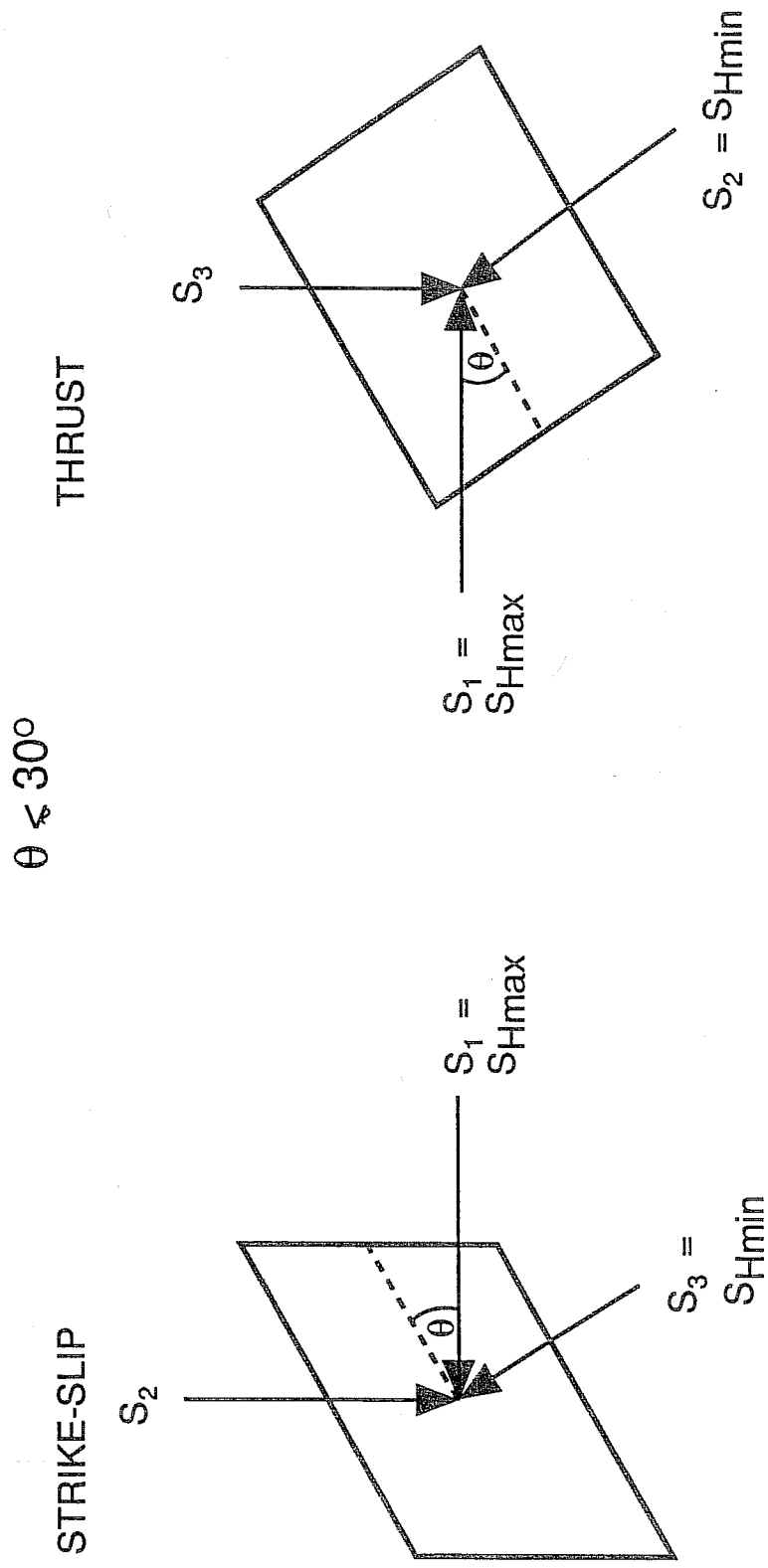


Fig 20. DEVIATION OF MAJOR FLOOD AXES FROM S_{Hmax}
 - PERMEABILITIES > 100mD

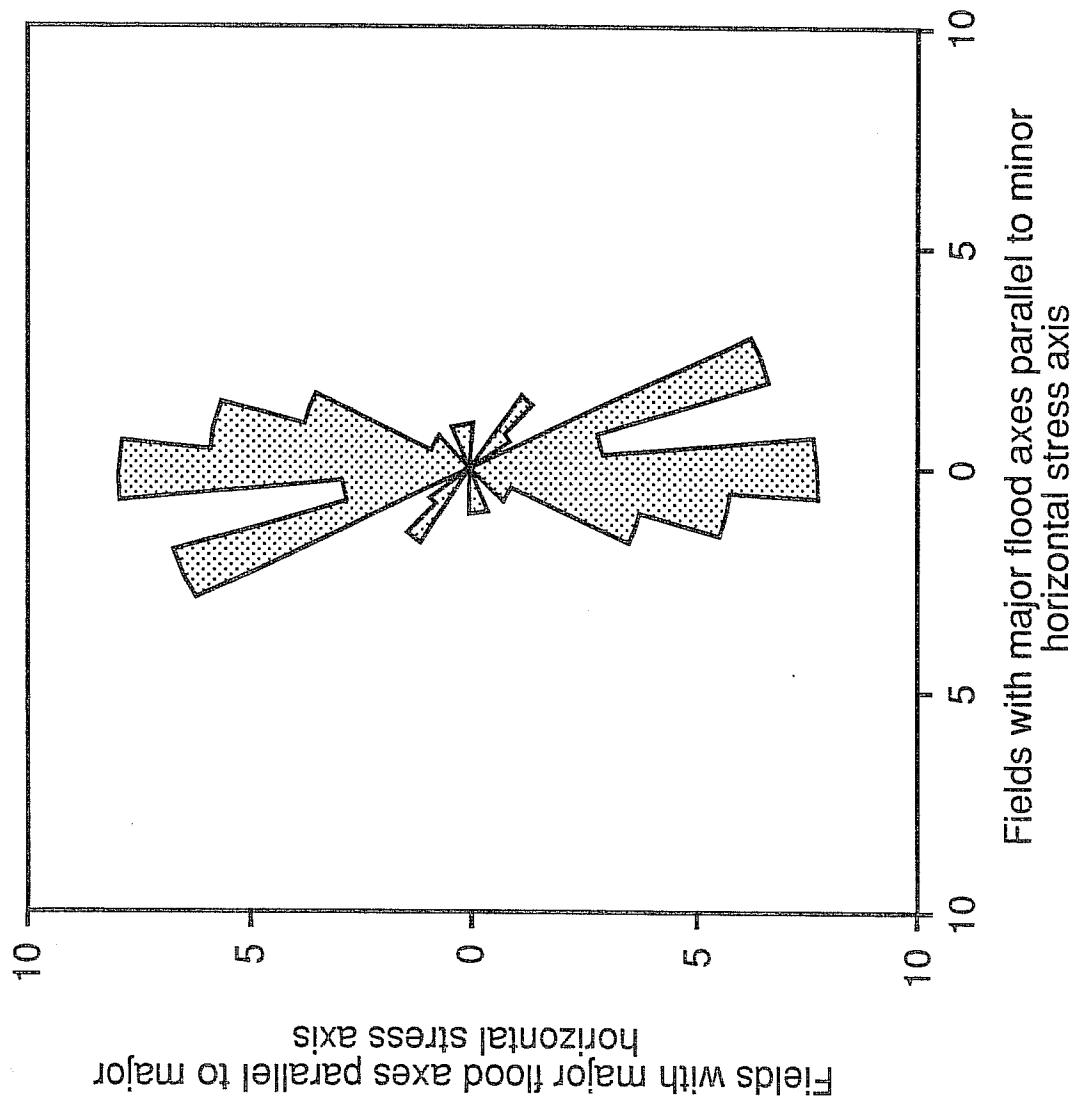


Fig 21. AGGREGATE BREAKTHROUGH PROBABILITY ELLIPSE
 - PERMEABILITIES > 100 mD

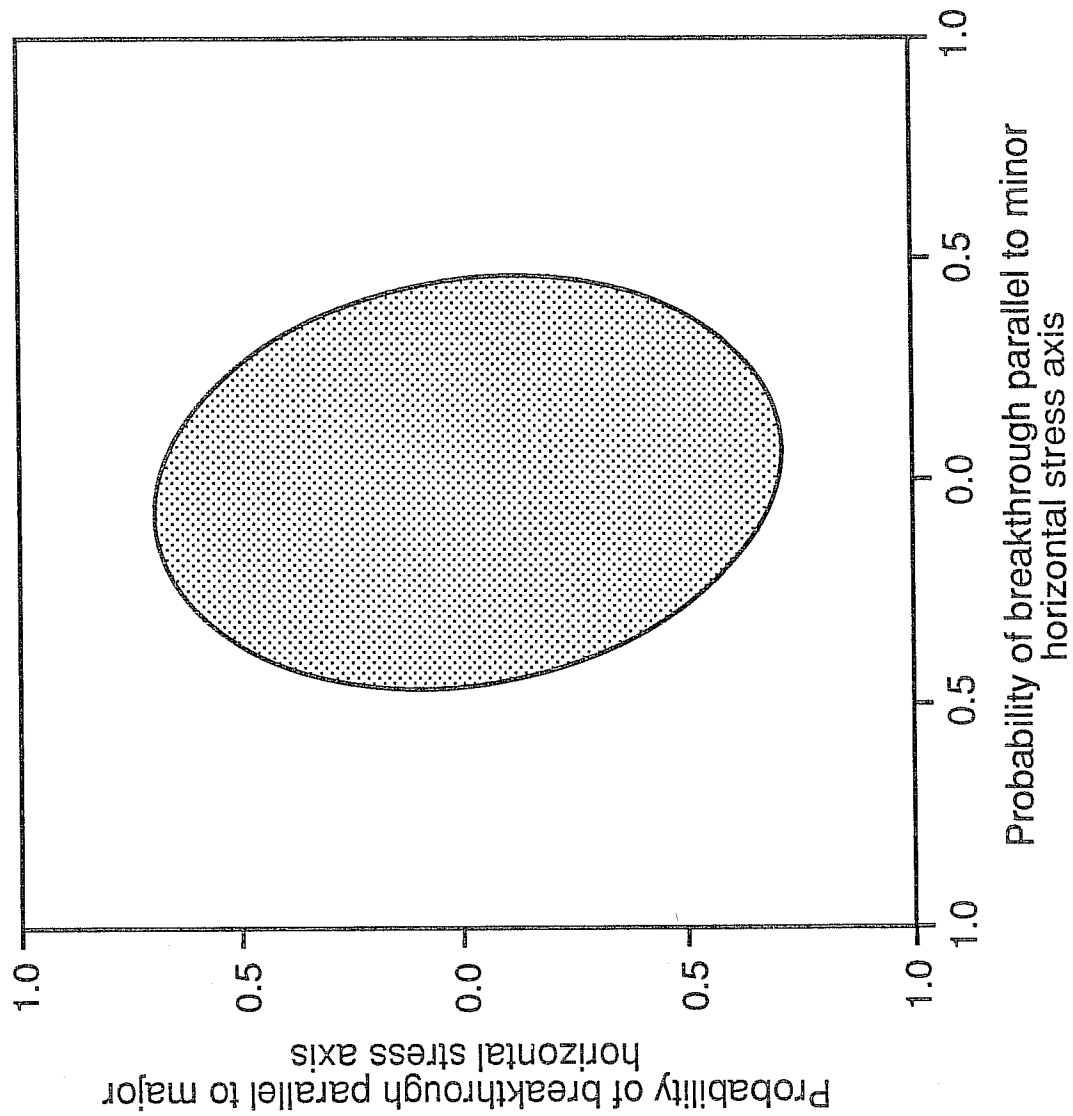


Fig 22. DEVIATION OF MAJOR FLOOD AXES FROM S_{Hmax}
 - PERMEABILITIES < 100 mD

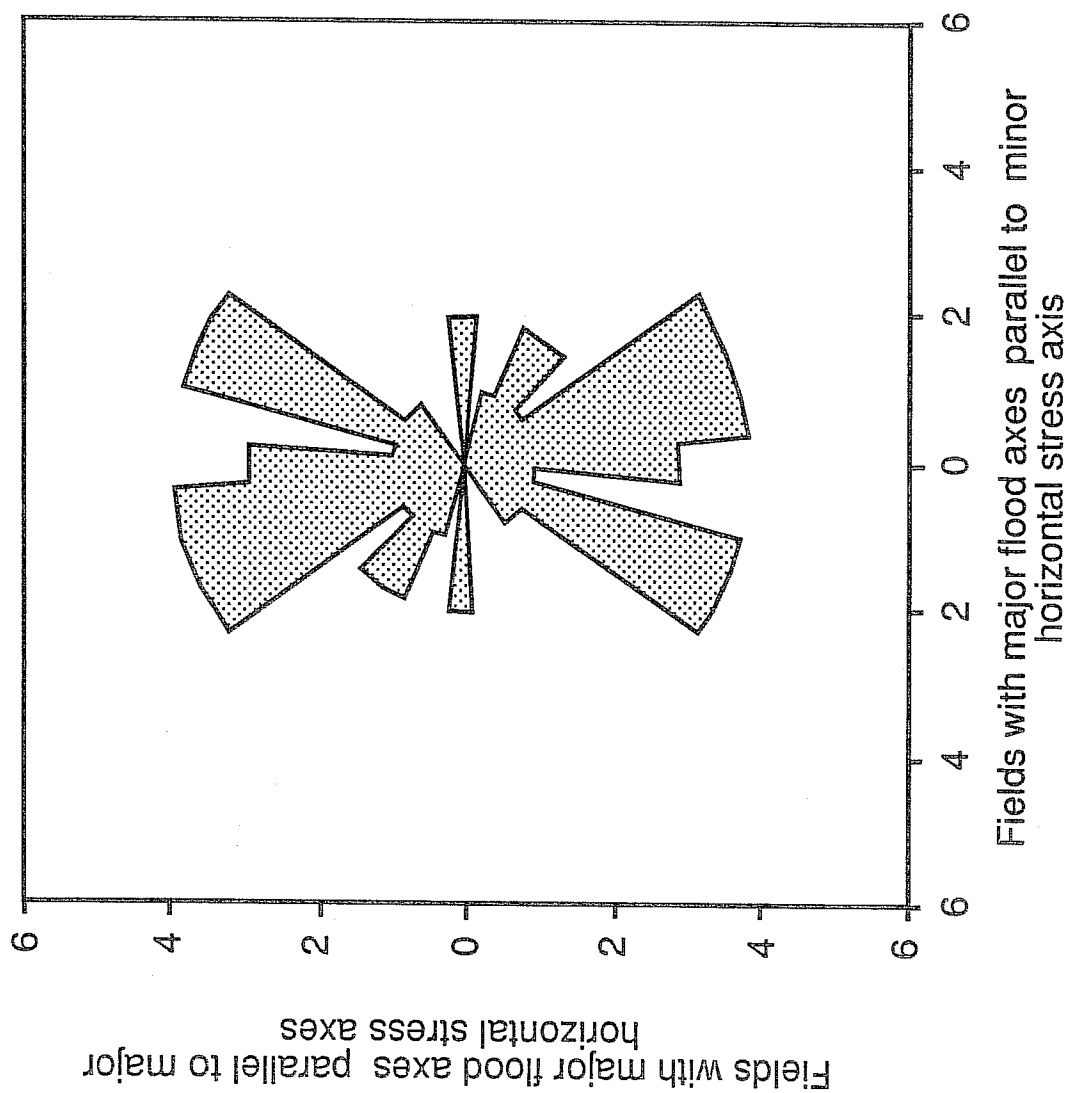


Fig 23. AGGREGATE BREAKTHROUGH PROBABILITY ELLIPSE
- PERMEABILITIES < 100 mD

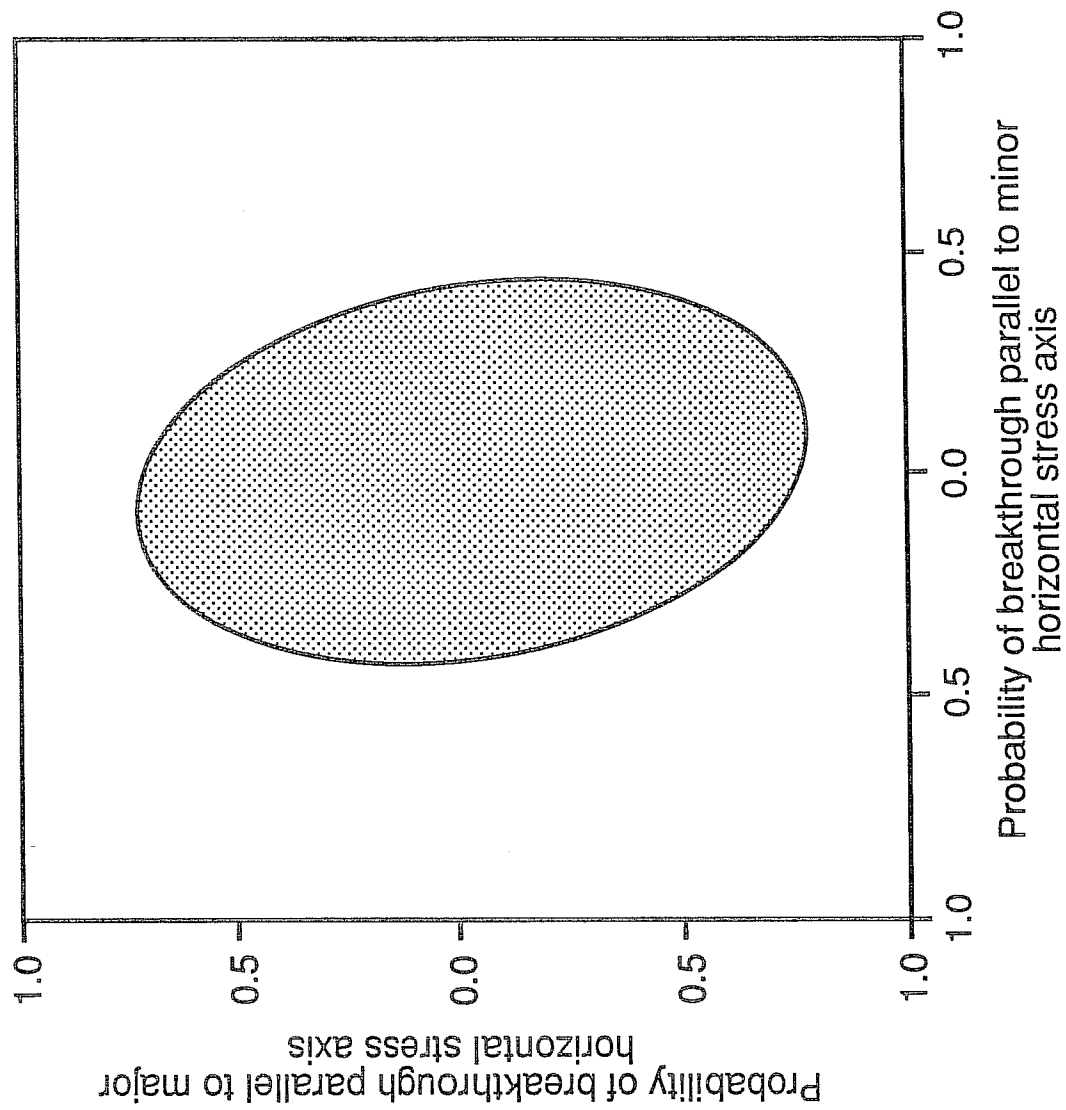


Fig 24. DEVIATION OF MAJOR FLOOD AXES FROM S_{Hmax}
 - SPACINGS < 1000 ft

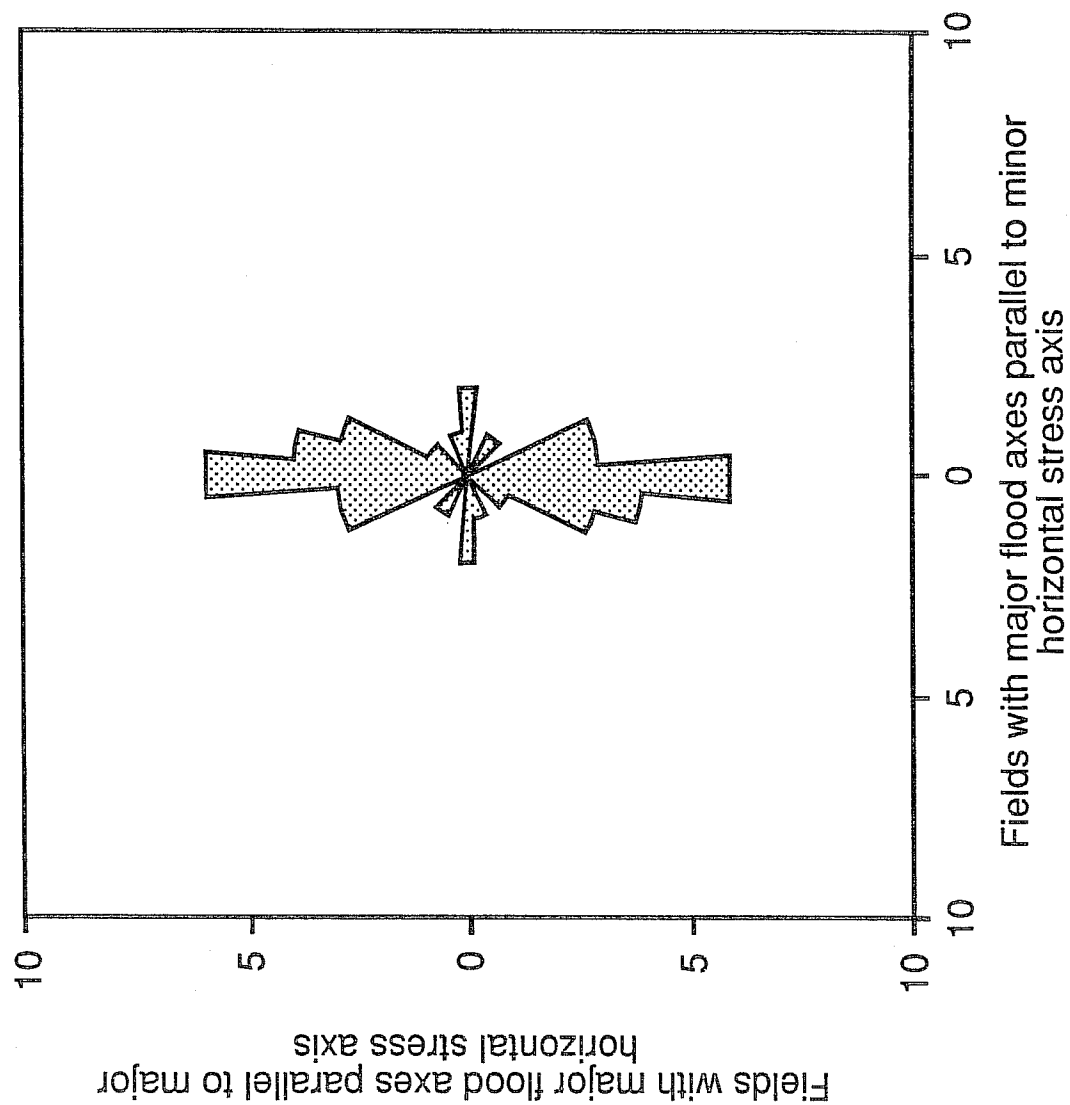


Fig 25. AGGREGATE BREAKTHROUGH PROBABILITY ELLIPSE
- SPACINGS > 1000 ft

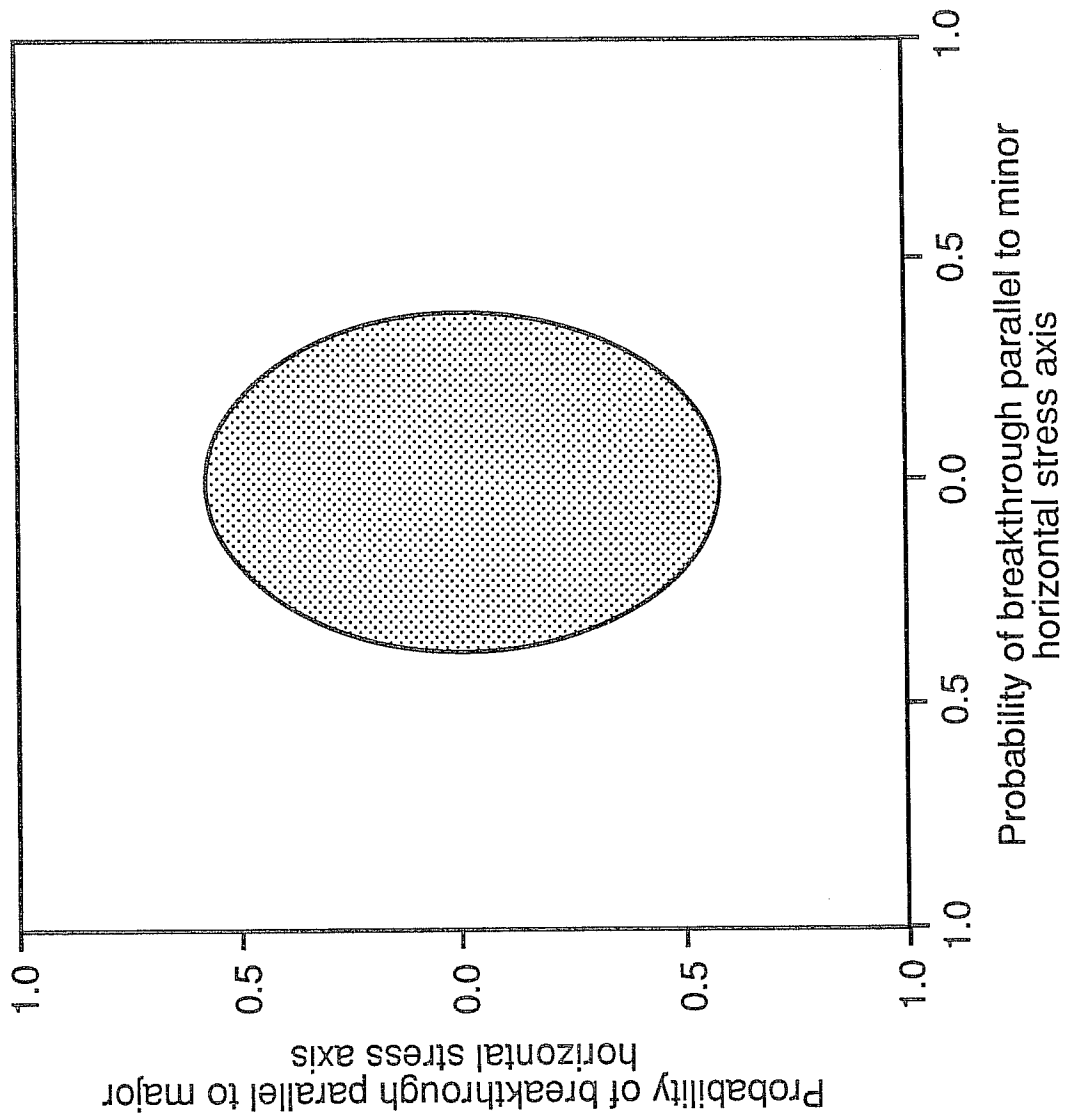


Fig 26. DEVIATION OF MAJOR FLOOD AXES FROM S_{Hmax}
 - SPACINGS < 1000ft

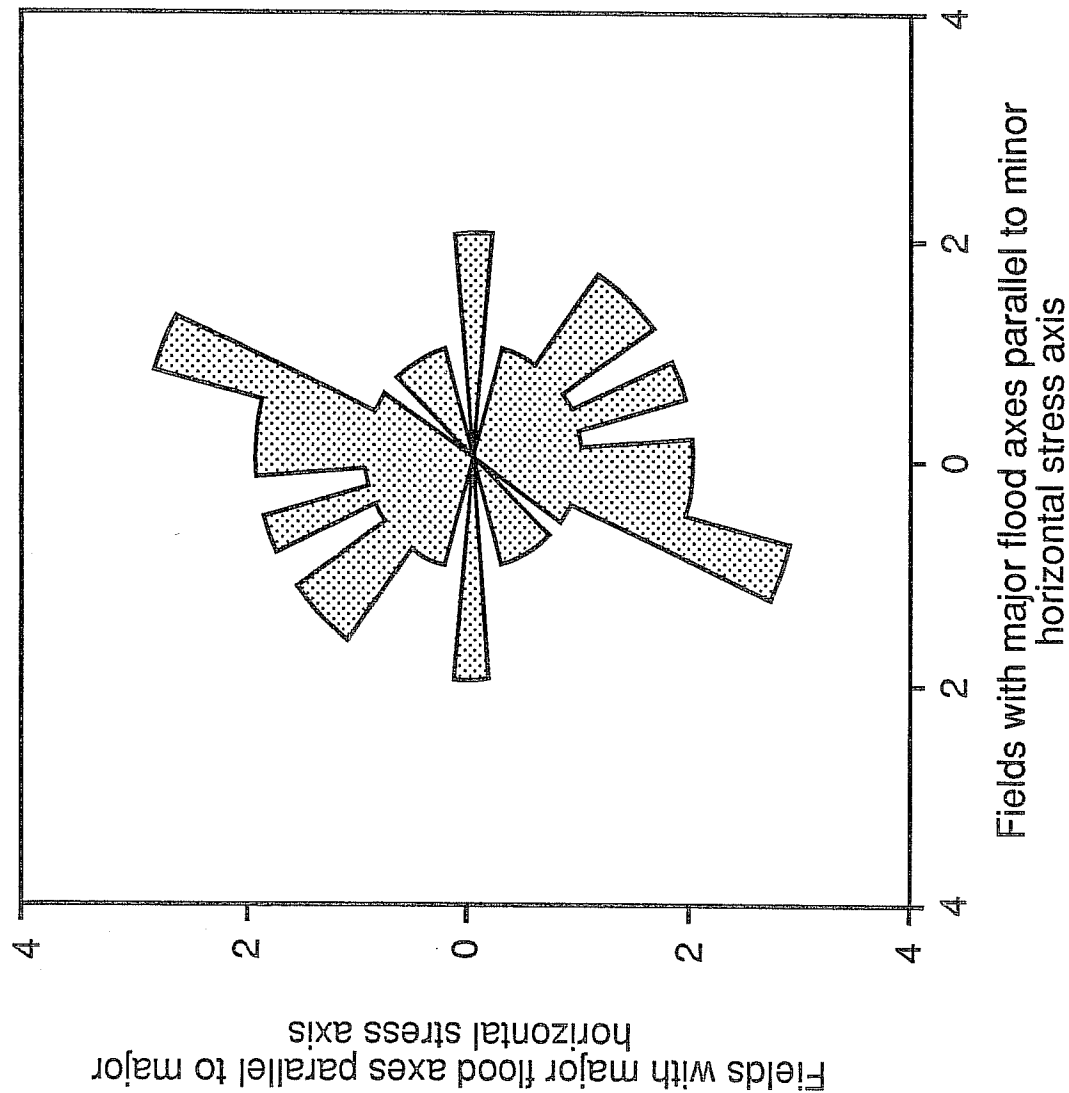


Fig 27. AGGREGATE BREAKTHROUGH PROBABILITY ELLIPSE
- SPACINGS < 1000ft

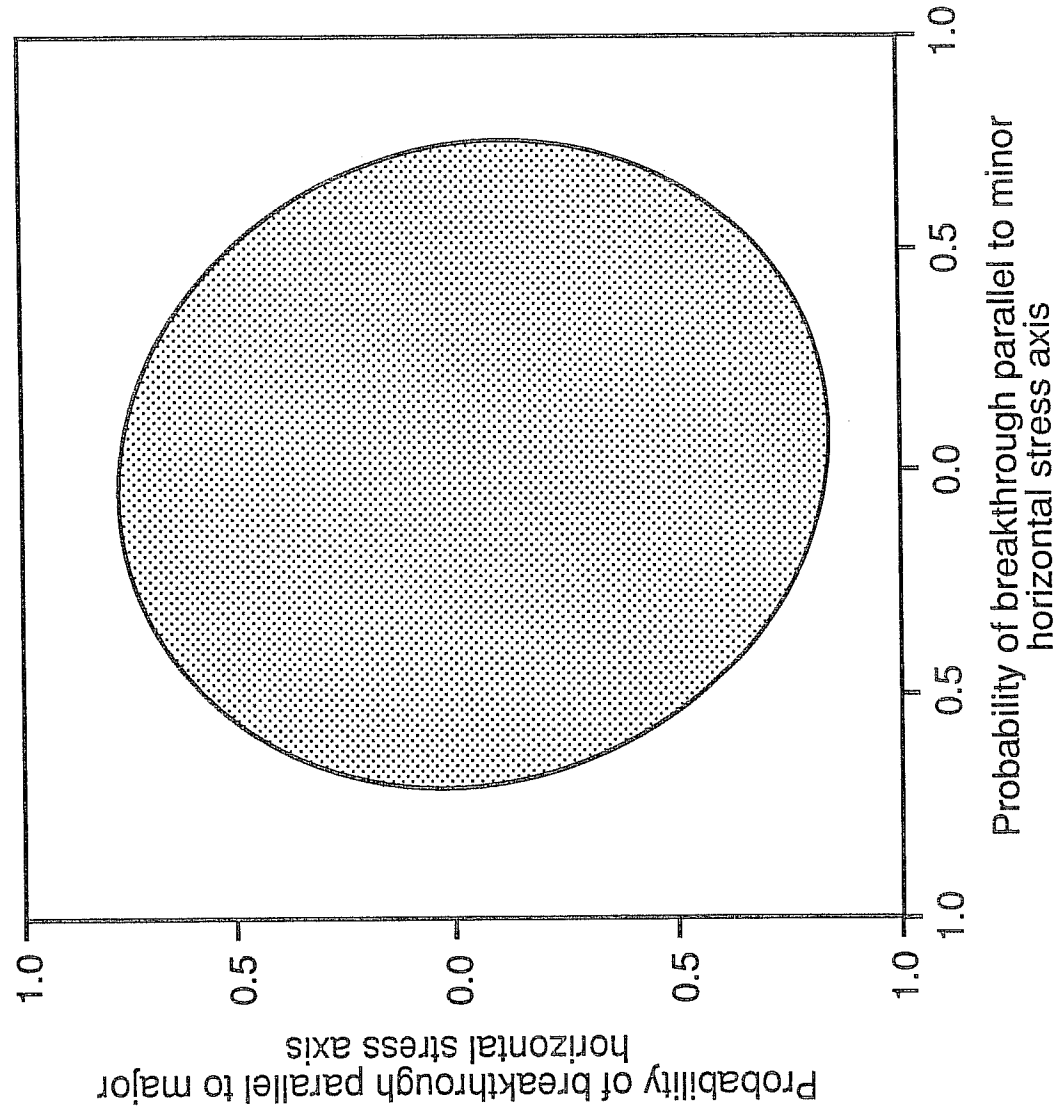


Fig 28. DEVIATION OF MAJOR FLOOD AXES FROM S_{Hmax}
- NON GAS FLOODS

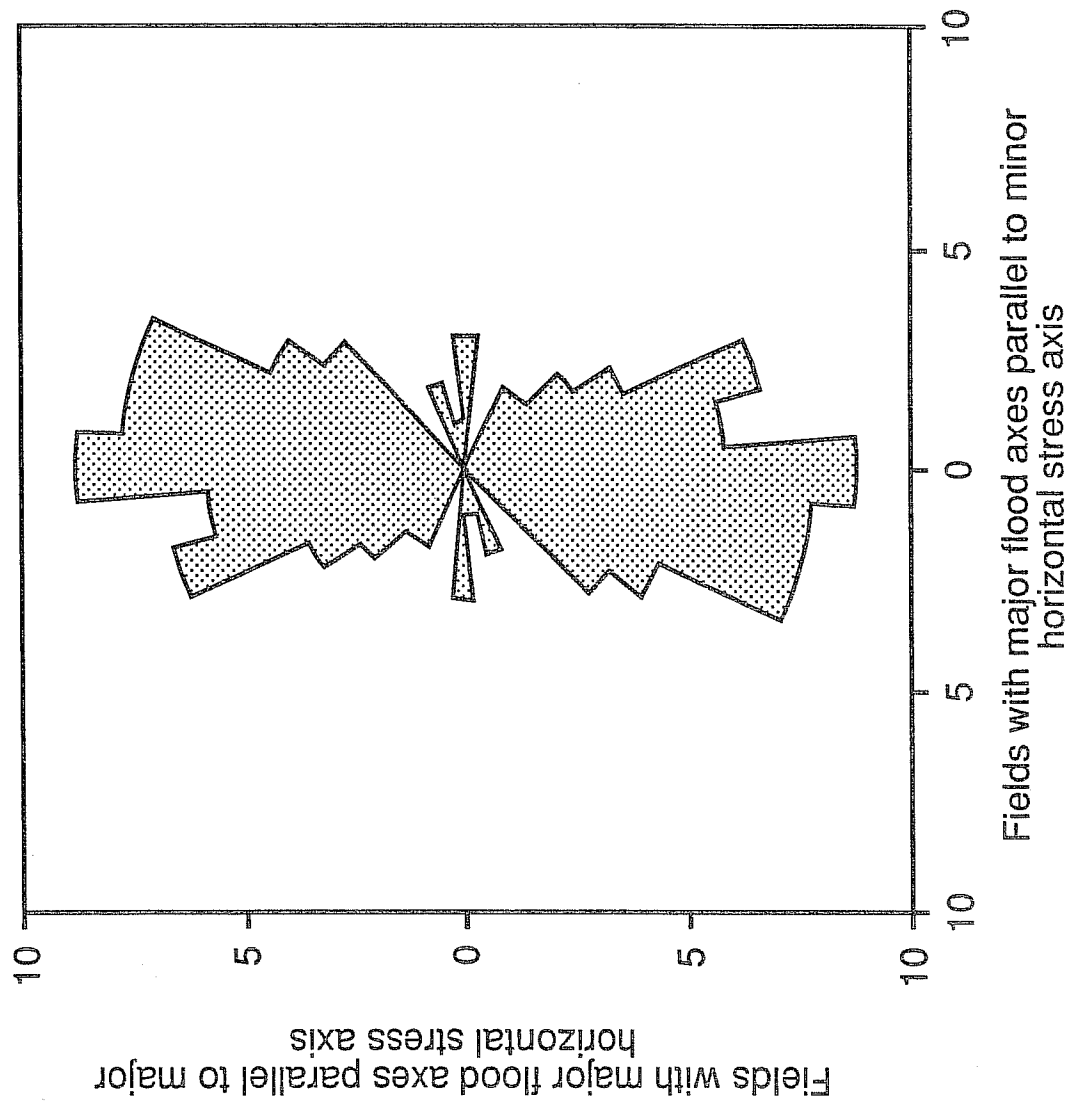


Fig 29. AGGREGATE BREAKTHROUGH PROBABILITY ELLIPSE
- NON GAS FLOODS

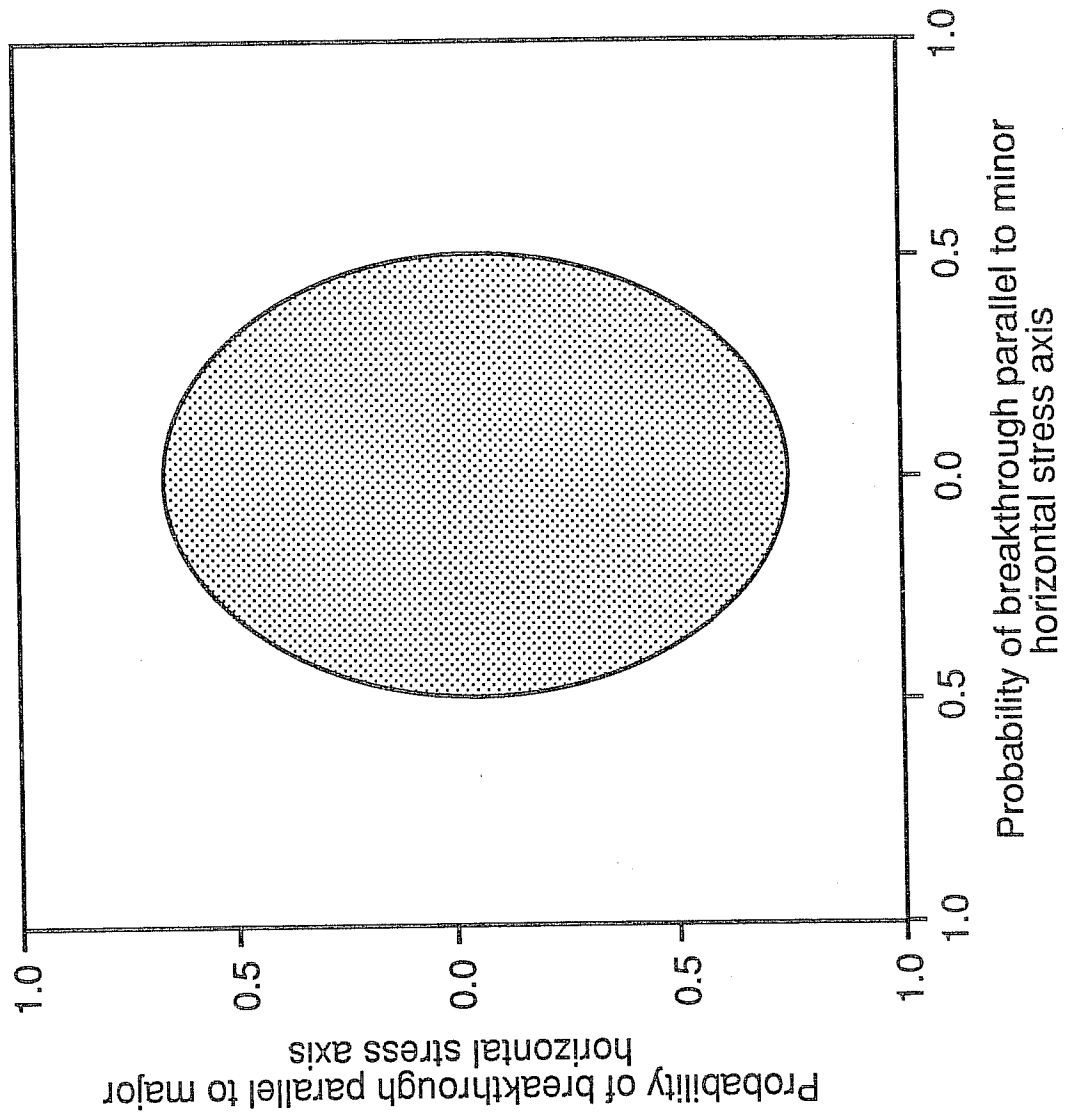


Fig 30. DEVIATION OF MAJOR FLOOD AXES FROM S_{Hmax}
- GAS FLOODS

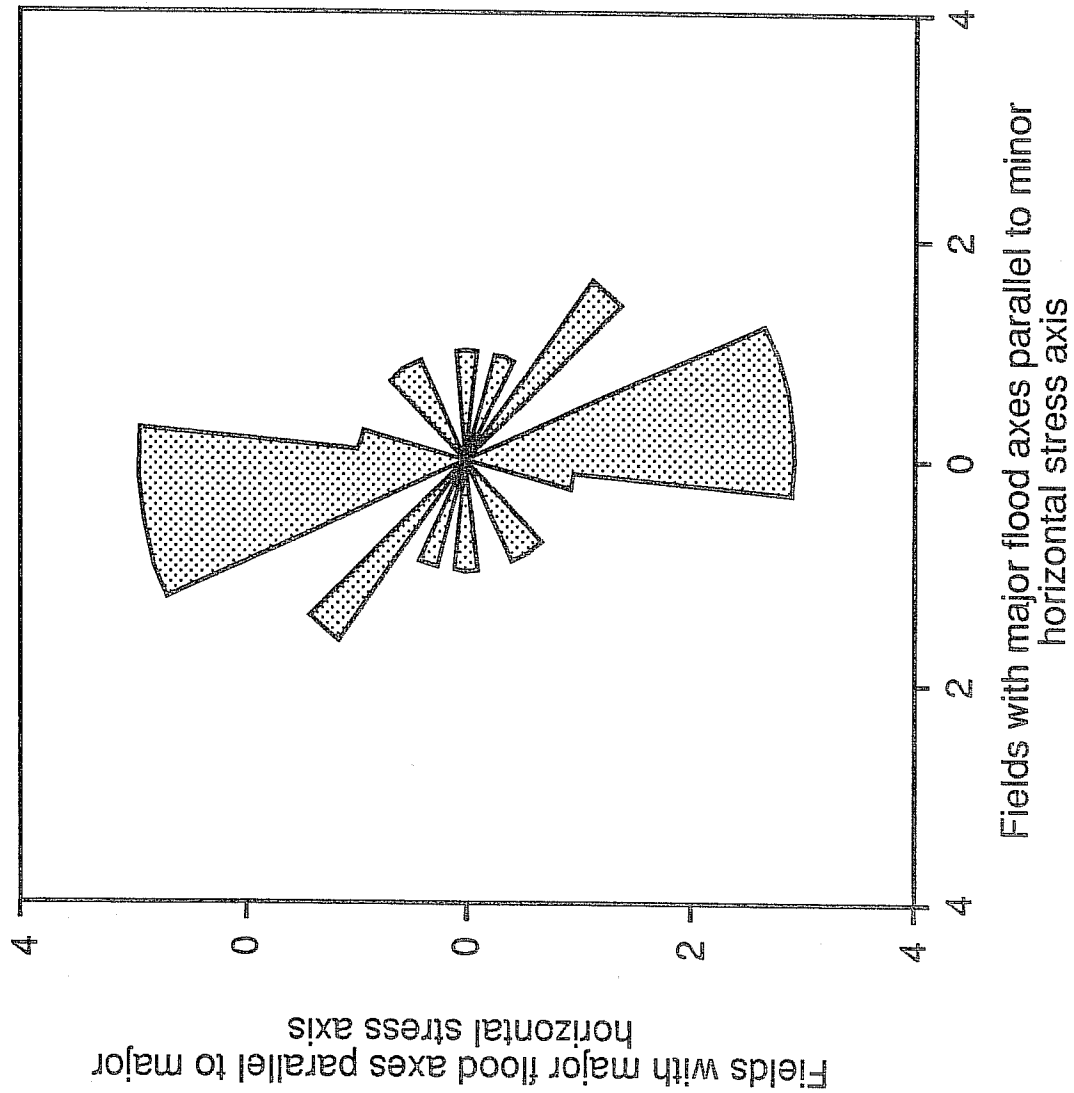


Fig 31. AGGREGATE BREAKTHROUGH PROBABILITY ELLIPSE
- GAS FLOODS

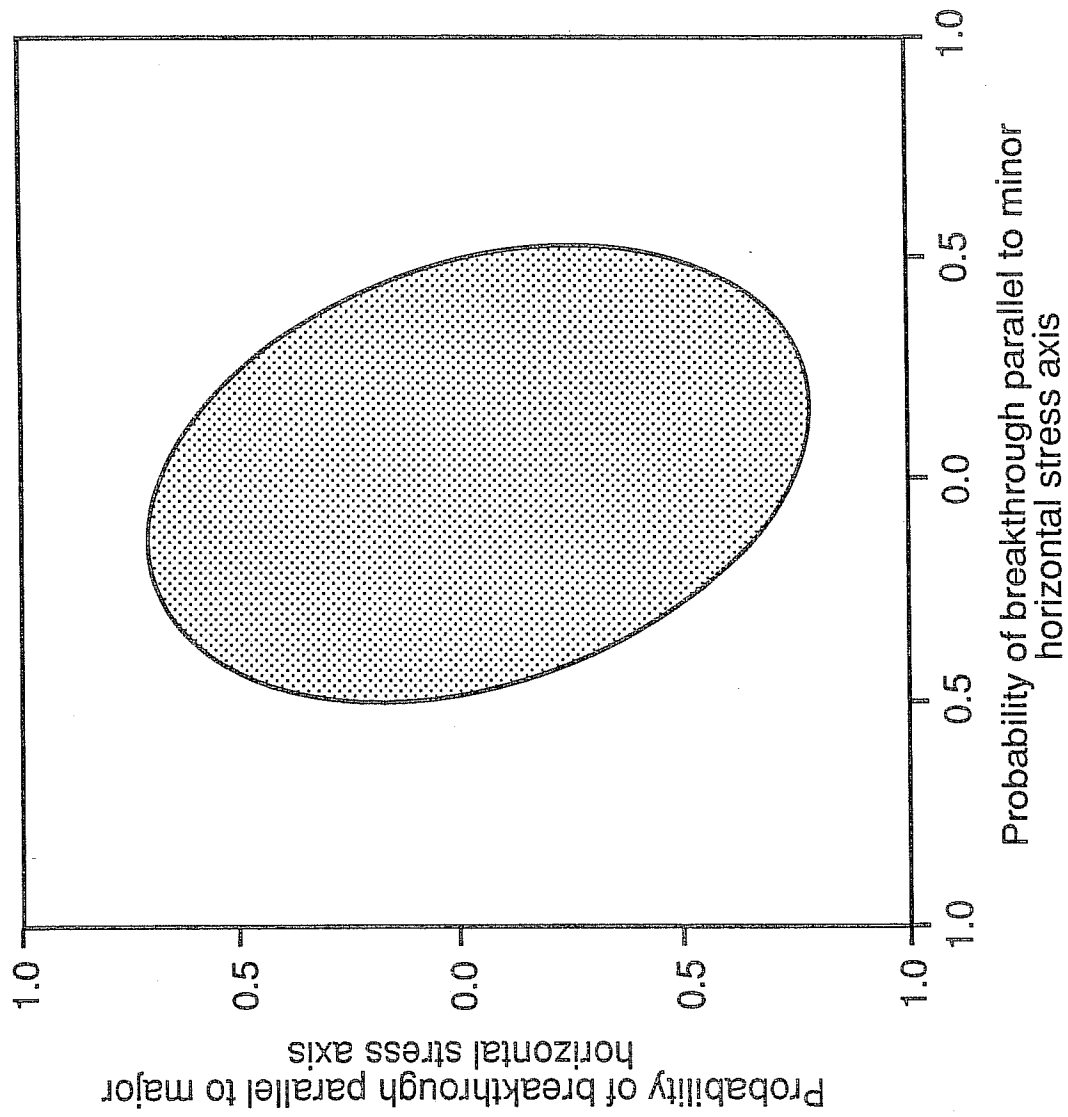
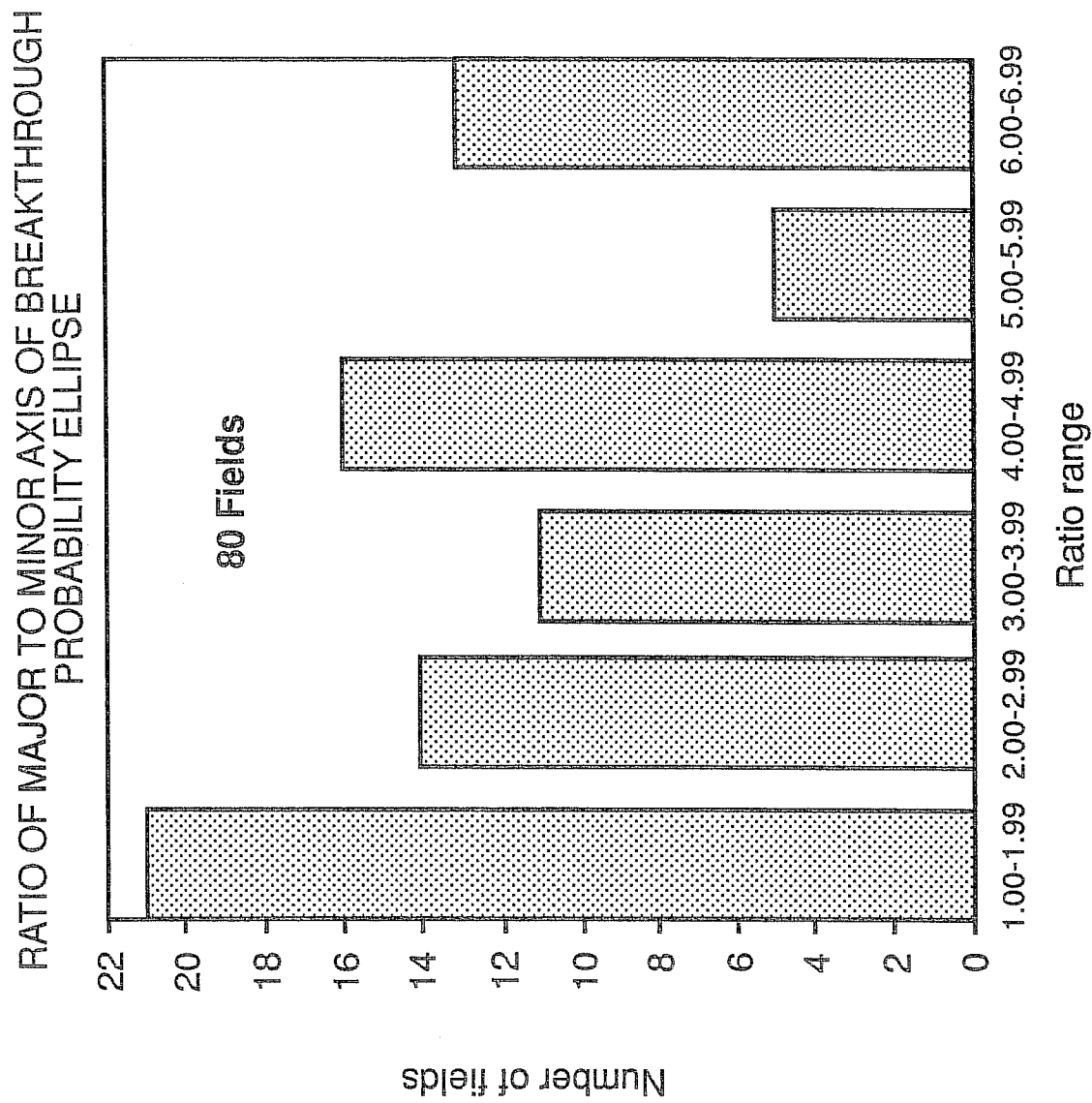


Fig 32. BREAKTHROUGH ANISOTROPY



THERMAL SIMULATION OF SHALLOW OIL ZONE
LIGHT OIL STEAMFLOOD PILOT
IN THE ELK HILLS OIL FIELD

Alan A. Burzlaff

ECL-Bergeson Petroleum Technologies, Inc.
Denver, Colorado

Bob R. Harris, Jr.

U. S. Department of Energy
Tupman, California

I. INTRODUCTION

A light oil steamflood (LOSF) pilot project has been operating since July 1987 in the Shallow Oil Zone (SOZ) at the Elk Hills oil field, Naval Petroleum Reserve No. 1, Kern County, California (Gangle et al., 1990). The SOZ is still largely under primary recovery and represents a potential 100 million barrel enhanced oil recovery target. The performance of the LOSF pilot project was duplicated using a single distillable component thermal simulator. The principle objectives of the simulation study were to develop a useful geologic and engineering model to screen other prospective SOZ steamflood areas, and to evaluate expansion of the current project.

II. RESERVOIR CHARACTERIZATION

The LOSF pilot project (Fig. 1) is located on the southeastern flank of the Elk Hills anticline. Steam is injected into the SS-1 sands of the Eastern SOZ at an average depth of 3000 feet. The beds dip at three to five degrees in the pilot area. Normal faulting is extensive throughout the LOSF pilot area (Fig. 2) and there is a confining fault (S fault) to the south whose 70 to 90 foot of displacement is believed to be an effective barrier to fluid movement. Other minor faults with five to thirty feet of displacement act as partial barriers or conduits depending on the degree of displacement and juxtaposition.

Seven discrete SS-1 sand members, designated the A, A1, B, C1, C2, D and E subzones (Fig. 3) have been identified in the steamflood area. During the course of this study, the subzones were further divided into 16 layers to incorporate the permeability variation of the SS-1 sands into the simulation models. The total interval is about 90 feet thick, with net sand thicknesses ranging from 50 to 70 feet. The porosity varies between 27 to 35 percent, and air permeabilities range from 100 to 2000 millidarcies. The average oil gravity in the project area is 27 degree API.

Petrophysical relationships developed in a previous study (Bergeson, 1989) were applied to the log and core data in the LOSF study area to calculate net thicknesses, porosities, initial water saturations and permeabilities for each of the 16 layers. Vertical permeability as a function of horizontal permeability, and relative permeability relationships were generated using conventional and special core analysis studies from wells in the surrounding area.

A 20 x 15 x 16 conventional black oil model was constructed which covered the LOSF pilot area as well as a significant area surrounding the patterns. The conventional model¹ was used to duplicate 11 years of pre-pilot primary production performance.

A significant improvement in the reservoir description was obtained as a result of this history match. The improved reservoir description included adjusting the pore volume to match observed production and pressure data, identifying the effectiveness of faulting in preventing fluid migration, and quantifying the distribution of oil, water and gas saturations prior to the initiation of enhanced recovery operations. This increased the confidence in the performance projections and provided useful operational information, such as identifying trapping of oil against faults.

III. LOSF PILOT PERFORMANCE

Pilot steam injection began in July 1987 with the commencement of steam injection into the D and E subzones of well 18N-3G. In November 1987, three additional steam injection wells were added to the pilot project. Between November 1987 and May 1988, steam injection was limited to the D and E subzones of the SS-1. In June 1988, the A, B, C1 and C2 subzones were completed with limited entry perforations to regulate steam injection into each subzone. After June 1988, all subzones were open to steam injection except for the A1 subzone which was felt to be gas saturated.

The pilot area oil production doubled within 6 months after the start of steam injection increasing from 400 BOPD to a peak rate of 850 BOPD. Oil production also increased significantly in producers outside the pilot area as a result of repressuring of the reservoir with steam, in situ generated carbon dioxide, and hot water. Oil production has subsequently declined in the pilot area as a result of operational problems, increasing watercuts, and severe formation damage.

¹ECLIPSE Black Oil Simulator

IV. THERMAL SIMULATION

A thermal simulation program², which models the flow of four components plus the energy associated with the system, was used to perform the steamflood simulation work. The four components are "heavy" oil, "light" oil, water and non-condensable gas. The model's light oil component is capable of being vaporized at increased temperature. Since the steamflood has not historically experienced particularly high temperatures, the use of a simulator with a single distillable component was suitable for this study.

A steamflood model of 2145 cells (11 x 15 x 13 layers) was constructed for a sector of the LOSF project area. This sector, shown in Fig. 4, was selected such that all four pilot injection wells would be included in the model area. In addition, a substantial portion of the responding area northeast of the pilot was included in the sector.

A satisfactory history match of the performance of this sector of the LOSF pilot was achieved with the steamflood model (Figures 5-6). Temperature profile surveys, run in several observation wells located in the pilot area, were also matched by the steamflood model (Fig. 7). A prediction of future pilot performance was made assuming a continued steaming operations scenario.

Steamflooding was compared to two alternative depletion scenarios, waterflooding and continued primary depletion. The waterflood and primary depletion scenarios were predicted using the history matched conventional model (Fig. 8). The major conclusions from the results of the steamflood model history match and the various prediction cases were:

1. The majority of the oil response has been due to waterflooding by the condensed steam. Steam distillation and distillate drive recovery mechanisms have been of secondary importance due to uneven thermal energy distribution and limited sustained steam zone temperatures in the pilot area (Fig 9).
2. The 'P' fault in the pilot area significantly affected the movement of steam and condensed hot water by restricting steam and heat flow to offsetting downdip producers.
3. Oil recovery from the LOSF pilot area, through September 1990, is estimated to be about 41 percent of the oil-in-place (OIP) at the beginning of steam injection (Fig. 10). Of this 41 percent, an amount of oil equal to approximately 14 percent of the OIP has been displaced outside of the pattern area. This amount of oil recovery is only about 5 percent greater than that predicted for a waterflood depletion scenario employing the same injection rates.
4. Based on the performance of the LOSF pilot, the predicted future performance from the steamflood model, and the price and cost projections provided by the

²Dynamic Reservoir Systems - Thermal (DRSTH), a product of Simtech Consulting Services, Inc.

Department of Energy, light oil steamflooding will not maximize economic oil recovery in the SOZ.

ACKNOWLEDGEMENTS:

We would like to acknowledge our appreciation of the Unit Management at the Naval Petroleum Reserve No. 1 for allowing publication of this paper. We also acknowledge the assistance provided by Vernon Breit and Joe Dosso of Simtech Consulting Services, Inc.

REFERENCES:

Bergeson & Associates, 1989, "Eastern Shallow Oil Zone Study - Fault Blocks 10, 11, 12, Phase IVA Report".

Gangle, F. J., Weyland, G. V., Lassiter, J. P., and Veith, E. J., 1990, "Light Oil Steamdrive Pilot Test at NPR-1, Elk Hills, California", SPE Paper #20032.

NAVAL PETROLEUM RESERVE NO.1

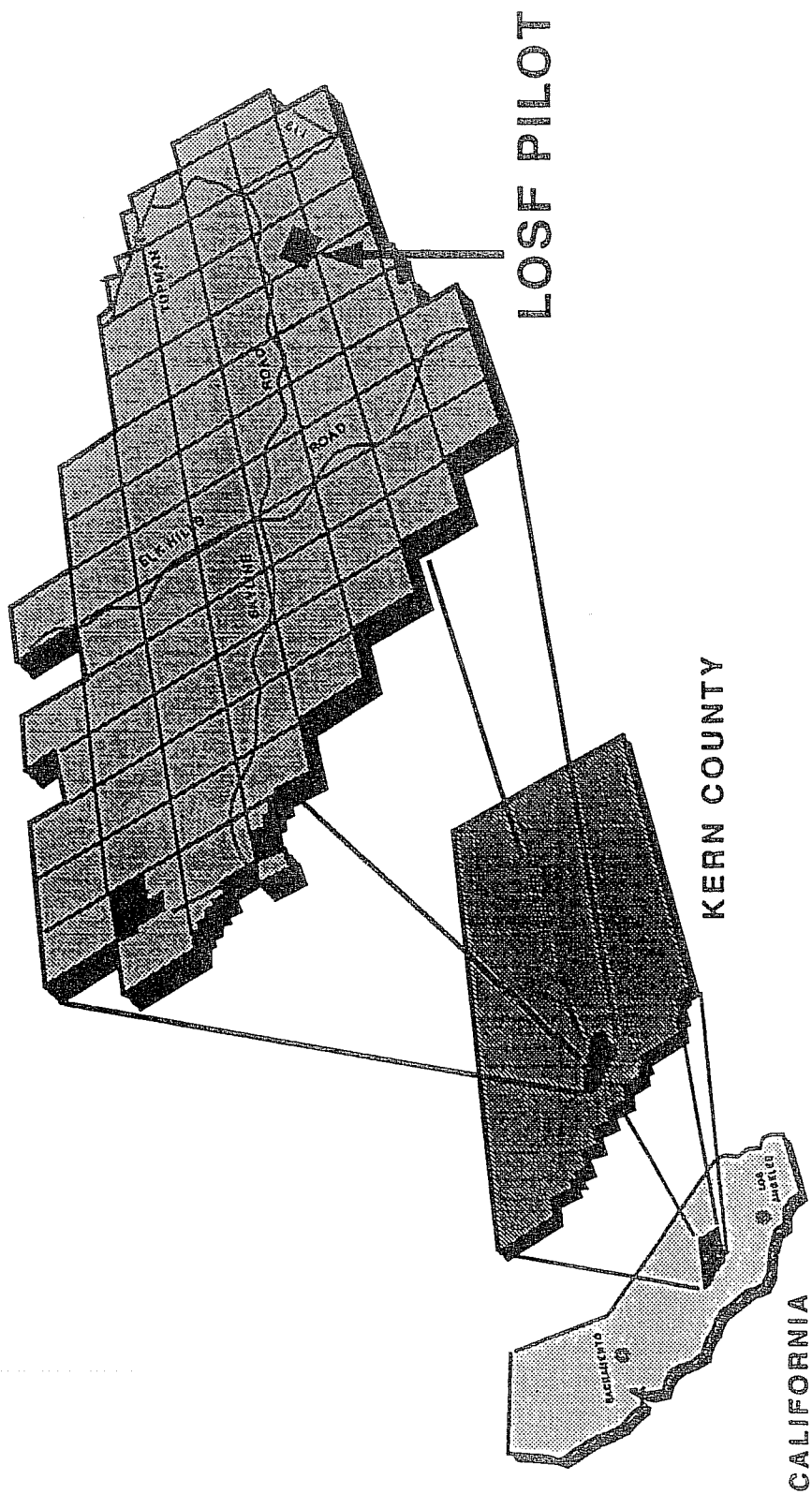


Fig. 1 - LOSF Pilot Area

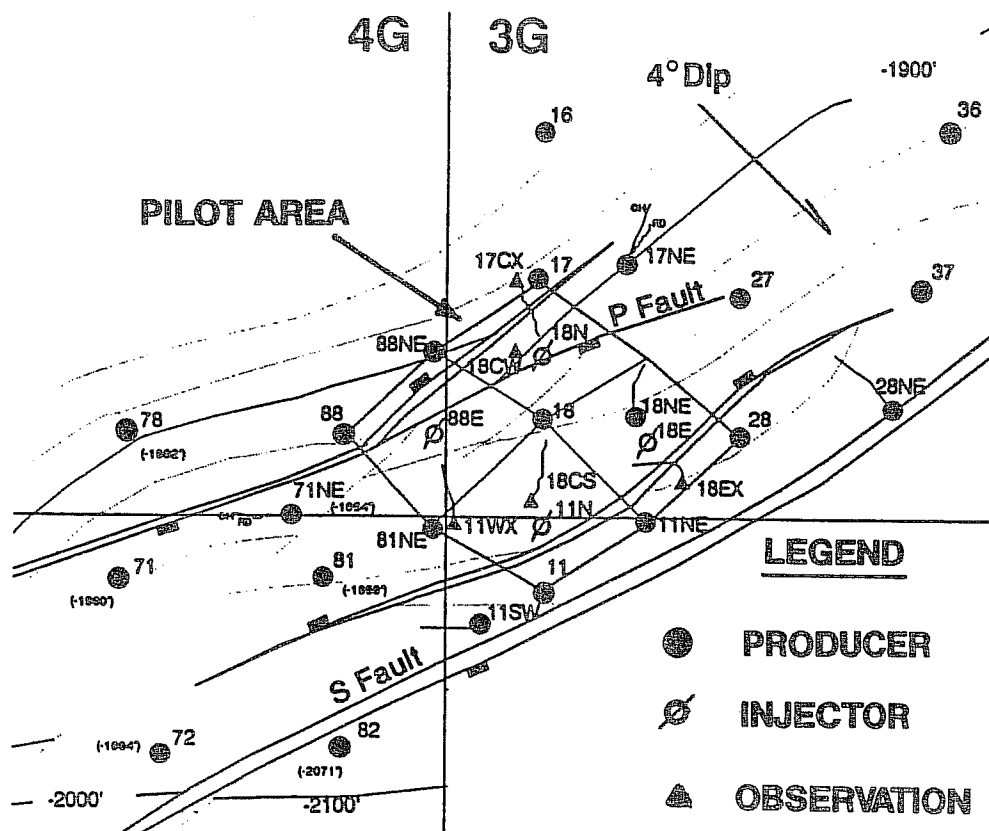


Fig. 2- Steamflood pilot area structure map and well configuration.

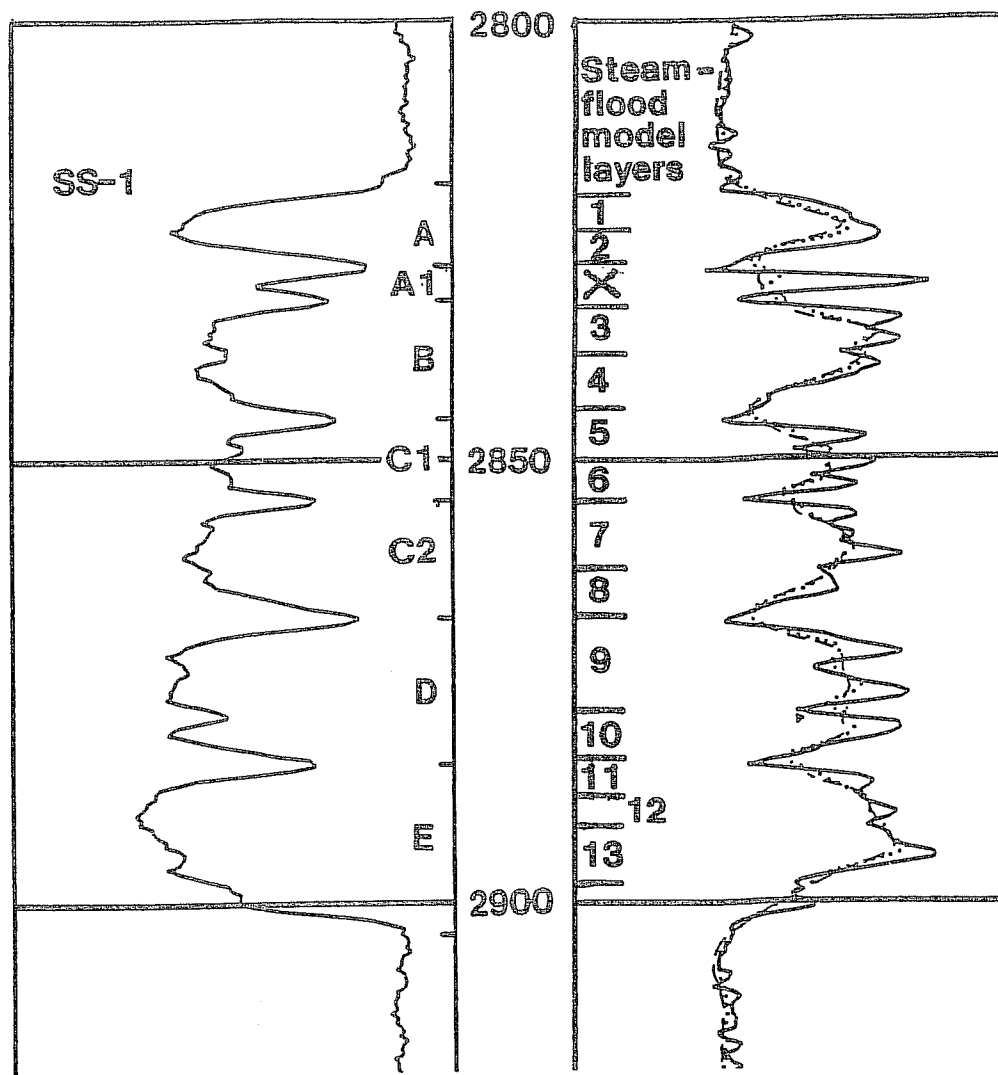


Fig. 3-Type log showing designated sand lobes, A through E.

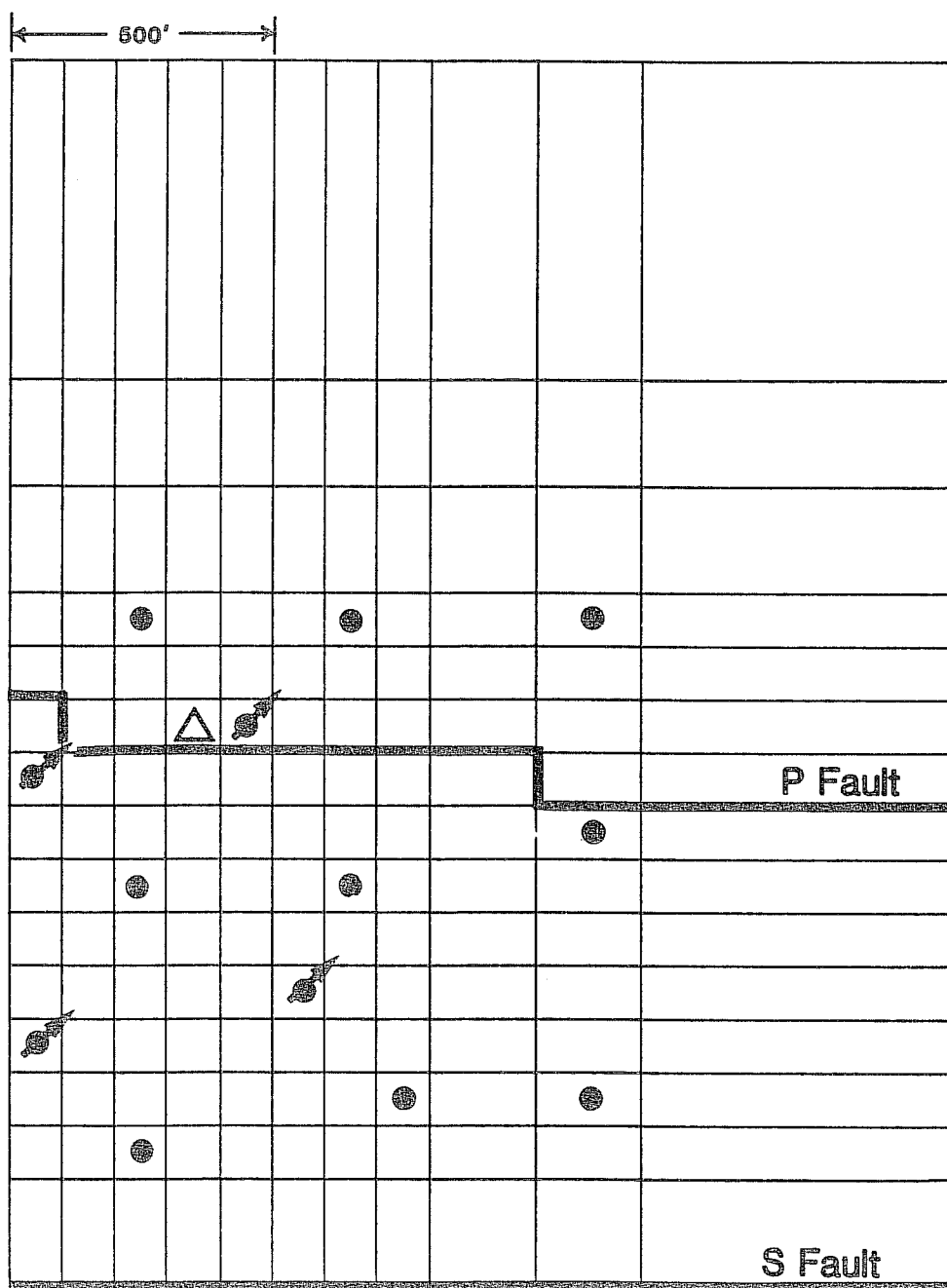
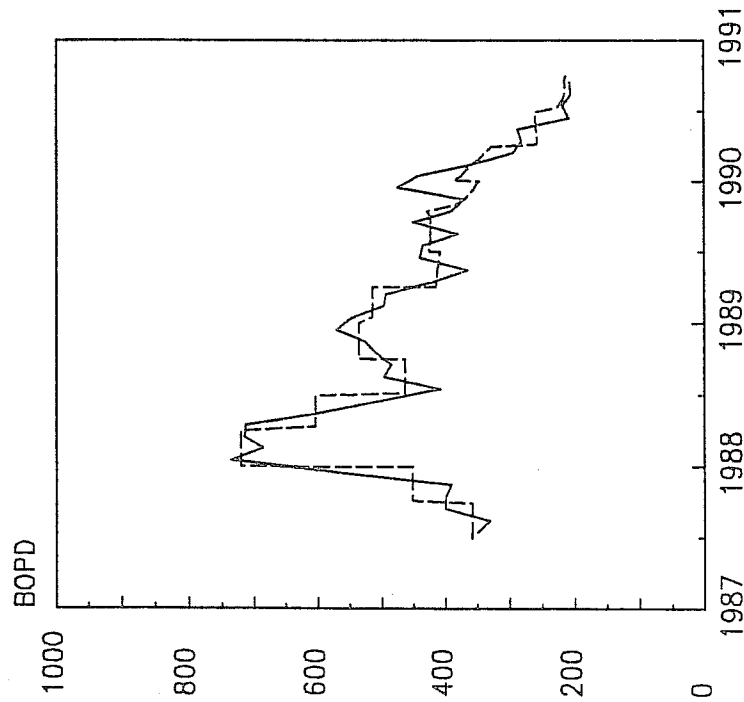


Fig. 4--Areal grid of steamflood model.

— OBSERVED OIL RATE
- - - HISTORY MATCH



**Fig. 5— Steamflood model
oil rate history match**

— OBSERVED WATERCUT
- - - HISTORY MATCH

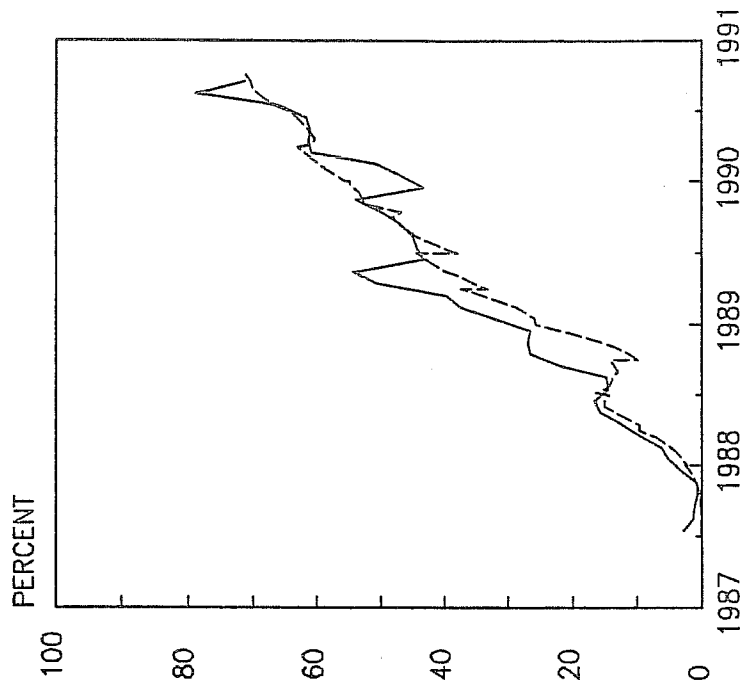


**Fig. 6— Steamflood model
watercut history match.**

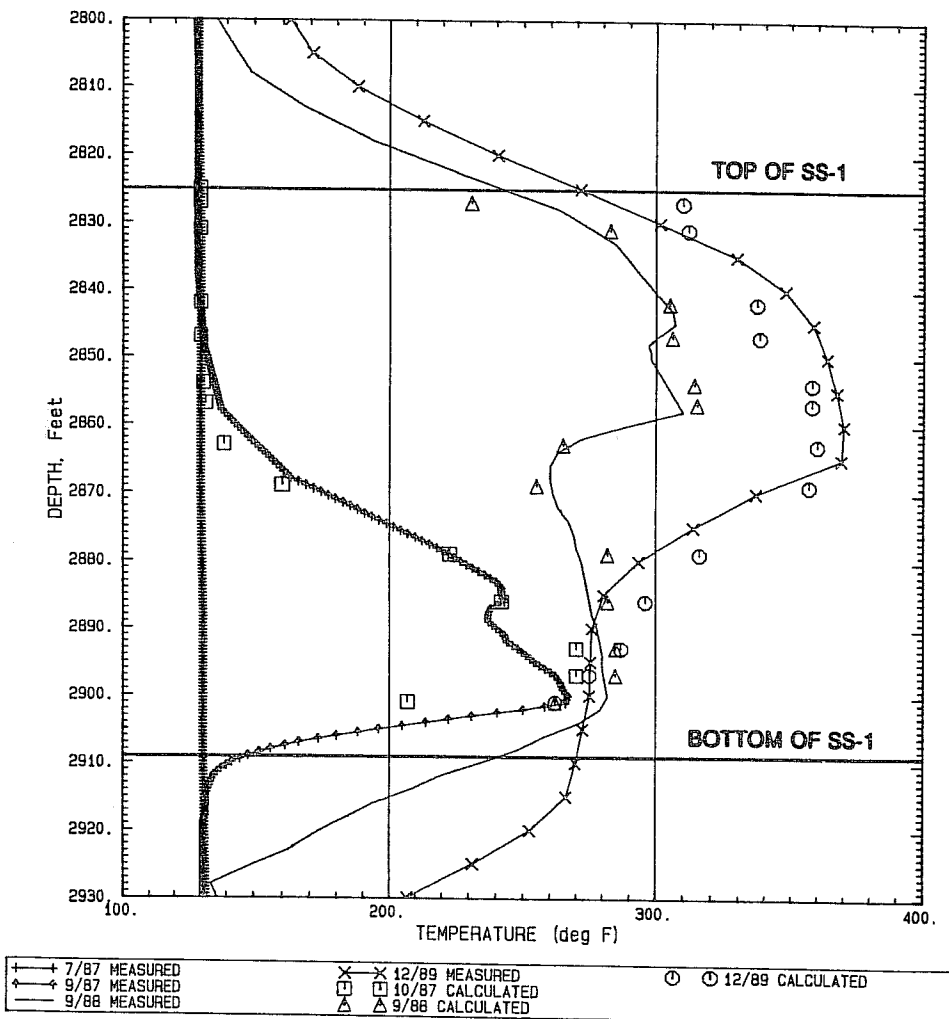


Fig. 7—Measured vs calculated reservoir temperatures—observation well 18CW.

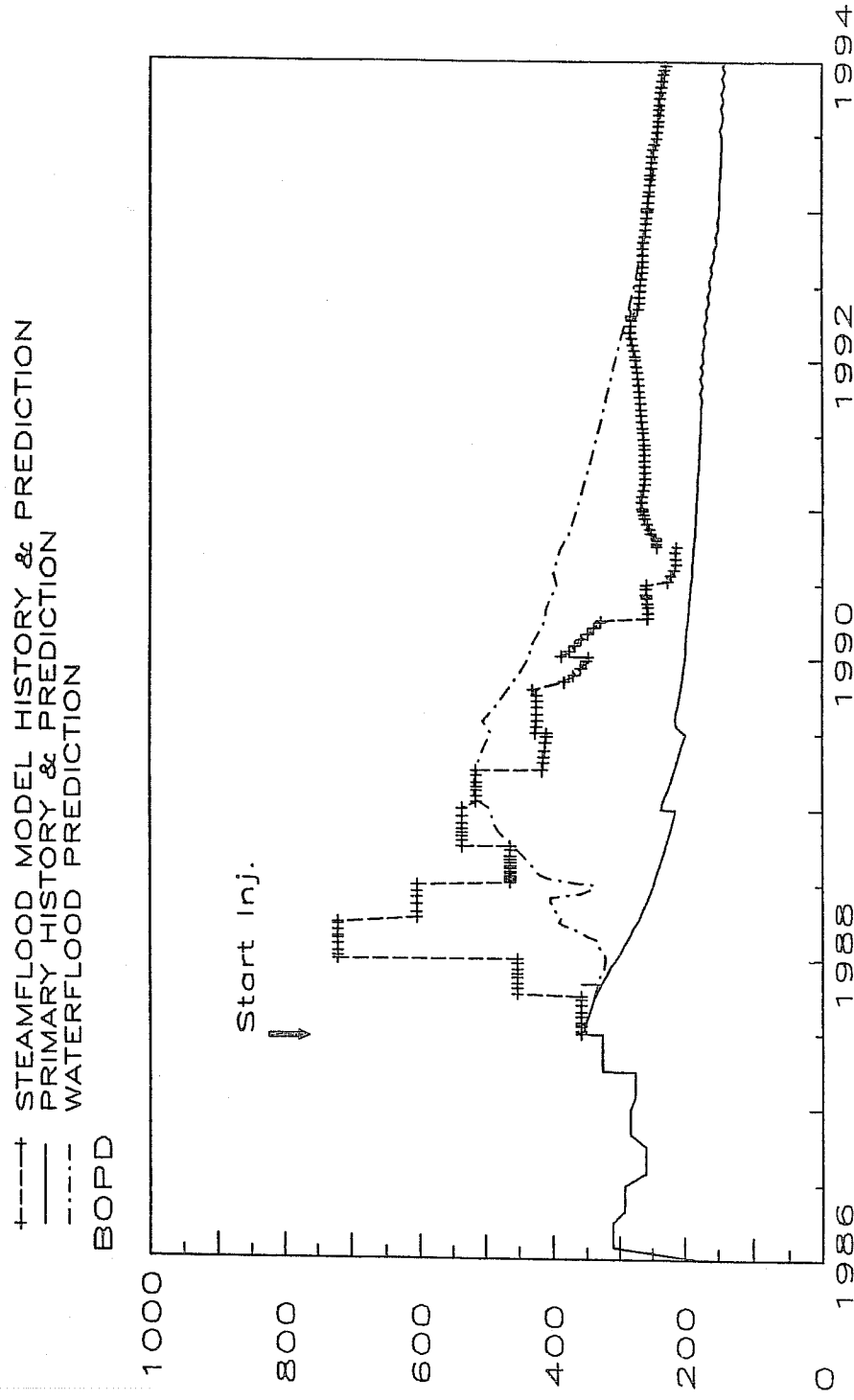


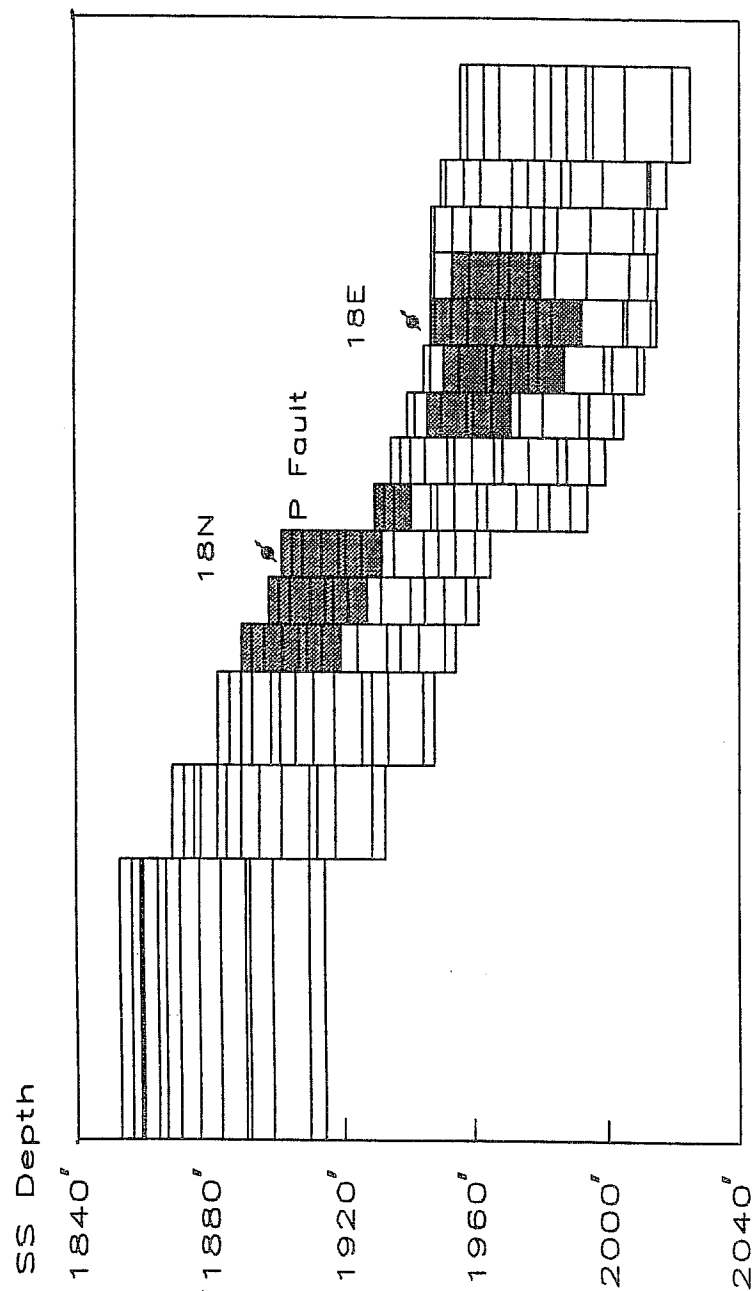


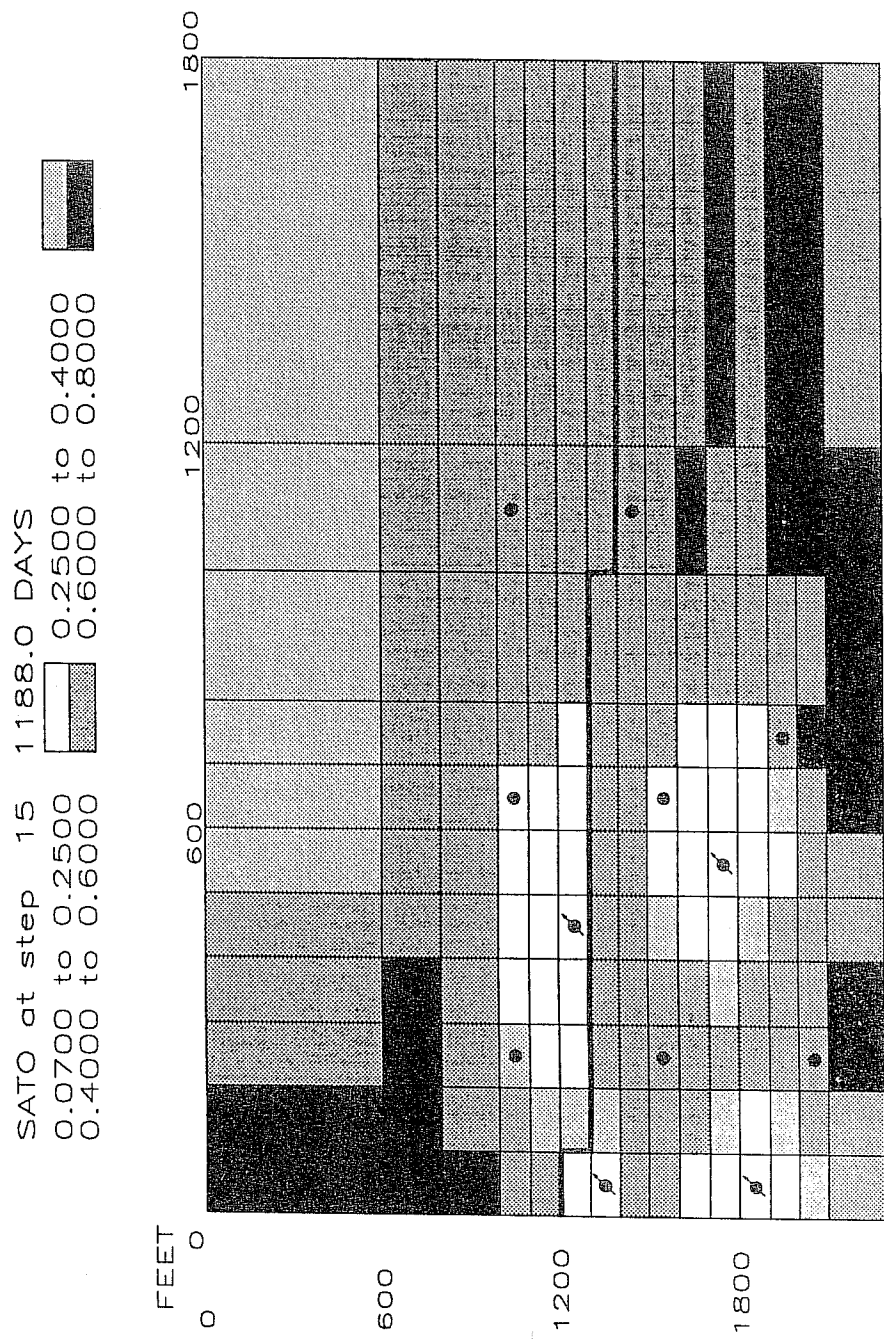
Fig. 8-Comparison of predicted oil rates for steamflood, waterflood, and continued primary depletion cases.

YSTM at step 15 1188.0 DAYS
 0 to 0.9000  0.9000 to 1.0000 



CROSS SECTION YZ Plane, X=5

Fig. 9-Distribution of steam mole fraction in the gas phase at end of history match.



AREAL SECTION, Z=5

Fig. 10-Oil saturation at end of history match, layer 5 (C1 subzone).

Reservoir and Haybarn fields (fig. 1).

Fining-upward fluvial channel sandstones are the best reservoirs. These sandstones rarely exceed 20 ft in aggregate thickness; porosity is about 20%, and permeability may be as high as 100-150 md. Coarsening-upward delta-front sandstones, which may be as thick as, and only slightly less porous (15-18%) than, the fluvial channel sandstones, have measured ambient permeabilities typically less than 50 md. Porosity, even when good (10-20%), may be partly to extensively occluded by pore-filling clays, especially kaolinite. Locally, 1-2 ft-thick delta-front sandstone units tightly cemented by Fe-bearing carbonate cement may serve as permeability barriers. Framework architecture of the fluvial-channel sandstones reveals laterally stacked, partly interconnected reservoirs 0.1-0.6 miles in lateral extent. Delta-front sandstones are vertically stacked and form isolated reservoir compartments that may be 1.5-4.5 miles wide.

Our study indicates that reservoir characterization of Fort Union sandstones reflects heterogeneity on the scale from outcrop to thin section. Although potential reservoir facies include sandstones deposited in fluvial channels, crevasse channels, crevasse channel/splay deposits, or as delta fronts deposits, plots of permeability/porosity/lithology-facies data indicate that sandstones from fluvial channels are most porous and permeable (fig. 2a,b). Thus, reservoir architectural complexities due to depositional environments, as well as petrophysical differences, are vital aspects to developmental strategies.

REFERENCES

- Flores, R.M., Keighin, C.Wm., and Keefer, W.R., 1990, Reservoir-sandstone paradigms, Paleocene Fort Union Formation, Wind River basin, Wyoming (abs.), Am. Assoc. Petroleum Geologists Bull., v. 74/8, p. 1323.
- Keefer, W.R., 1965, Stratigraphy and geologic history of the Uppermost Cretaceous, Paleocene, and lower Eocene rocks in the Wind River basin, Wyoming, U.S. Geol. Survey Professional Paper 495-A, 77p.
- Keefer, W.R., 1990, Cretaceous rocks in the Wind River basin, Central Wyoming (abs.), Am. Assoc. Petroleum Geologists Bull., v. 74/8, p. 1331.
- Pirner, C.F., 1978, Geology of the Fuller Reservoir Unit,

CHARACTERIZATION OF RESERVOIR HETEROGENEITY,
FULLER RESERVOIR AND HAYBARN FIELDS, PALEOCENE
FORT UNION FORMATION, FREMONT COUNTY, WYOMING

C. Wm. Keighin
R. M. Flores

U.S. Geological Survey
Denver, CO 80225.

A major concern in petroleum exploration and development is the detailed architecture (internal and hierarchical) of sandstone reservoirs in a field or basin-wide setting. This concern is due, in part, to the effects of architecture on fluid flow. Unifying models of reservoir architecture are seldom available because of the temporal and three-dimensional complexity of depositional systems (Keefer, 1965; 1990; Flores and others, 1990). Local and basinal scales of sandstone-reservoir heterogeneities can be recognized and classified in outcrops and subcrops. Outcrop studies provide information on grain size, internal structure, geometry, hierarchical arrangements, and continuity of reservoir sandstones. Subcrop investigations, including studies of core and geophysical logs, help extend mappability (lateral variability) and predictability of the geometry and architecture of reservoir sandstones in a basinal setting.

Fluvio-deltaic sandstones in the Paleocene Fort Union Formation, Fremont Co., WY, form shallow (approximately 2,500-5,000 ft in depth) discontinuous reservoirs for oil and gas in the Fuller Reservoir and Haybarn fields, Wind River Basin, Wyoming (Pirner, 1978; Robertson, 1984; Specht, 1989). These fields have yielded 1.79 million bbl of oil and 12.9 bcf of natural gas. An integrated investigation of these sandstones, utilizing facies descriptions from outcrops, wireline logs, cores, and petrographic examination of core samples, demonstrates a relationship between reservoir quality and facies architecture. These data also show that sandstone facies within the upper Fort Union Formation (Shotgun and Waltman Shale Members) are discontinuous across the Fuller

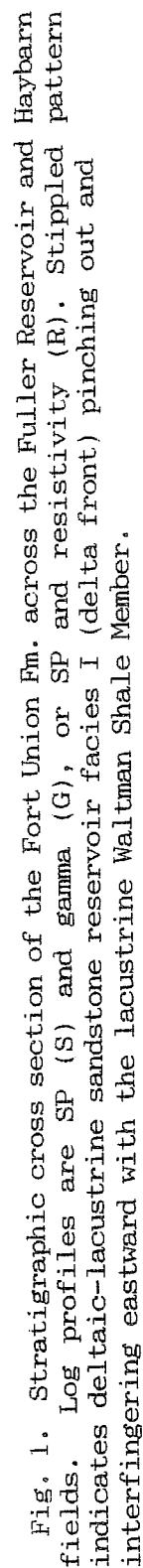


Fig. 1. Stratigraphic cross section of the Fort Union Fm. across the Fuller Reservoir and Haybarn fields. Log profiles are SP (S) and gamma (G), or SP and resistivity (R). Stippled pattern indicates deltaic-lacustrine sandstone reservoir facies I (delta front) pinching out and interfingering eastward with the lacustrine Waltman Shale Member.

Fremont County, Wyoming, in Wyoming Geological Assoc.
30th Ann. Field Conf. Guidebook "Resources of the Wind
River basin", Casper, WY, p. 281-288.

Robertson, R.D., 1984, Haybarn field, Fremont County, Wyoming:
An Upper Fort Union (Paleocene) stratigraphic trap,
Mountain Geologist, v.21, p. 47-56.

Specht, R.W., 1989, Fuller Reservoir, in Wyoming Geological
Assoc. "Wyoming oil and gas fields symposium, Bighorn
and Wind River basins", p. 178-180.

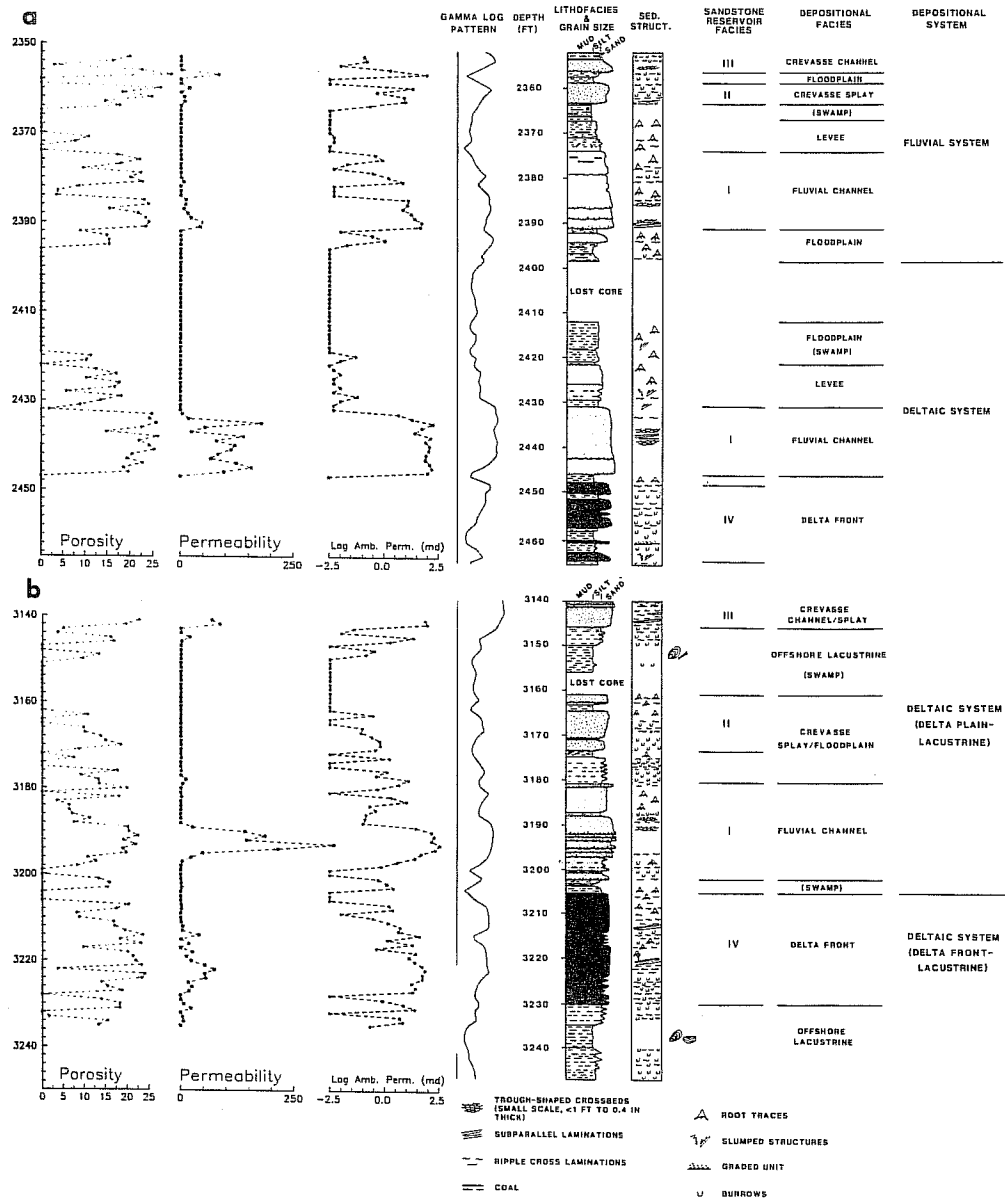


Fig. 2. Porosity-permeability data (measured on core plugs) plotted against various parameters, but especially depth (ft below surface), lithofacies, and depositional facies. Porosity/permeability values are closely related to the environment of deposition. (a) Northern Natural Gas #7-18 Federal 886 (SE NE SEC.18 36N 93W). Porosity values range between 3 and 25%; permeability (md) ranges between <0.01 and 179, but rarely exceeds 50 md. (b) Husky Oil Co. #8-19 Fuller Federal (SE NE SEC.19 36N 93W). Porosity values range between 3.6 and 24%; permeability (md) ranges between 0.01 and 339. Permeability above 100 md appears restricted to fluvial channel environments.

MICROSCOPIC TO FIELD-WIDE DIAGENETIC HETEROGENEITY
IN DELTAIC RESERVOIRS FROM BRAZIL: DESCRIPTION,
QUANTIFICATION AND INTEGRATION WITH OTHER
RESERVOIR PROPERTIES

Marco A. S. Moraes
PETROBRAS/CENPES/DIGER
Ilha do Fundão, Cid. Universitária
Rio de Janeiro RJ 21910 Brazil

Ronald C. Surdam
Department of Geology and Geophysics
University of Wyoming
Laramie WY 82071 U. S. A.

I. INTRODUCTION

The description and quantification of reservoir heterogeneity has achieved significant progress in recent years. Most of the new developments have been in the application of depositional models and stochastic models to reservoir characterization (Haldorsen, 1983; Weber, 1986; Fogg and Lucia, 1990; Haldorsen and Damsleth, 1990; Weber and van Genus, 1990). In most cases, the main objective has been to model depositional features. Diagenetic studies commonly do not include an evaluation of the heterogeneity resulting from diagenetic processes. Such heterogeneity, however, is typically observed at different reservoir scales and its detailed description is essential to achieve a complete and adequate spatial representation of the reservoirs.

Deltaic lacustrine sandstones produce hydrocarbons in more than a hundred accumulations in the Cretaceous rift basins of northeastern Brazil. These sandstones show a complex

diagenetic evolution that has been extensively documented by core, thin section and SEM studies in many different oil fields. Similarities observed in the depositional and diagenetic properties characterizing these reservoirs permitted the development of diagenetic models that can be used to improve reservoir quality evaluation and performance prediction.

II. GEOLOGIC SETTING

Deltaic reservoirs have been studied in the Potiguar and Recôncavo basins of northeastern Brazil (Fig. 1). The basins are onshore failed rift arms formed in Early Cretaceous and associated with the opening of the South Atlantic (Bertani et al., 1987; Milani and Davinson, 1988). The structural framework of the basins is characterized by deep asymmetrical grabens separated by internal highs (Fig. 2). Deltaic reservoirs commonly consist of a series of stacked delta-front sandstone bodies deposited in lows associated with growth faults (see Fig. 2). The sandstone bodies typically pinch-out away from the faults. Extensive and fairly continuous lacustrine shales commonly separate the reservoir beds. The sandstones are predominantly fine-grained, with medium- to coarse-grained sandstones appearing locally.

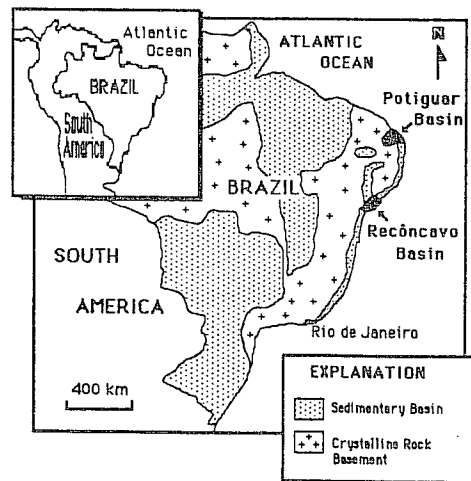


Fig. 1- Location of Potiguar and Recôncavo basins.

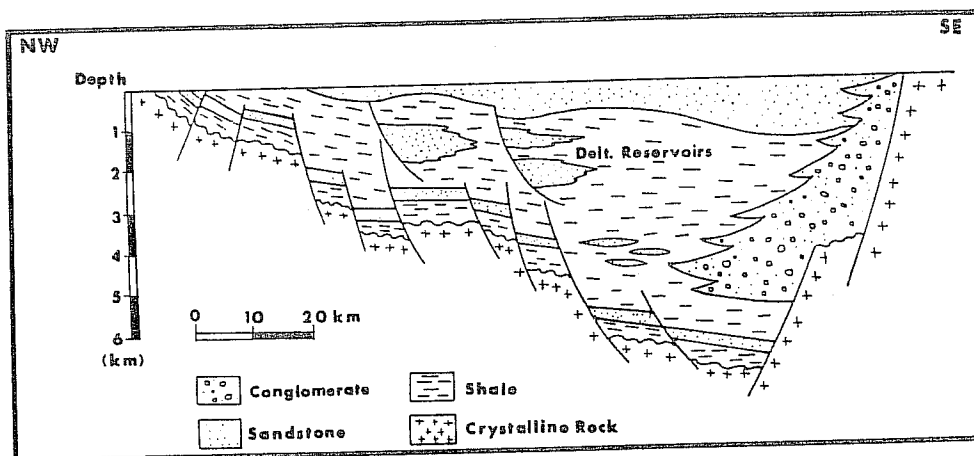


Fig. 2- Schematic geologic section of Recôncavo Basin showing main geologic features and the typical setting of deltaic reservoirs.

The petrographic characteristics and the diagenetic evolution of these rocks have been summarized by Becker (1984), Alves (1985), Anjos and Carozzi (1988) and Moraes (1991). Main diagenetic phases include, in an inferred temporal succession: 1. mechanical compaction, 2. quartz and feldspar overgrowths, 3. calcite precipitation, 4. dissolution of framework grains and calcite cement, 5. dolomite precipitation, and 6. chlorite formation.

III. MICROSCOPIC HETEROGENEITY

Burial and consequent diagenesis of these lacustrine sandstones produced strong pore modifications, not only in the geometry of individual pores, but also in the whole porosity structure of the sandstones. The evaluation of pore structure leads to a better understanding of fluid distribution, mobility and recovery at the microscopic level, where fluid properties are essentially controlled by capillary forces (Wardlaw and Cassan, 1979; Wardlaw, 1980).

Present porosity values in the main reservoir zones average 21% from petrophysical analyses, and 19% from thin-section determinations. At the microscopic scale, sandstone pore structure (Fig. 3) is characterized by discontinuous patches (islands) of small and badly connected reduced primary (RP)

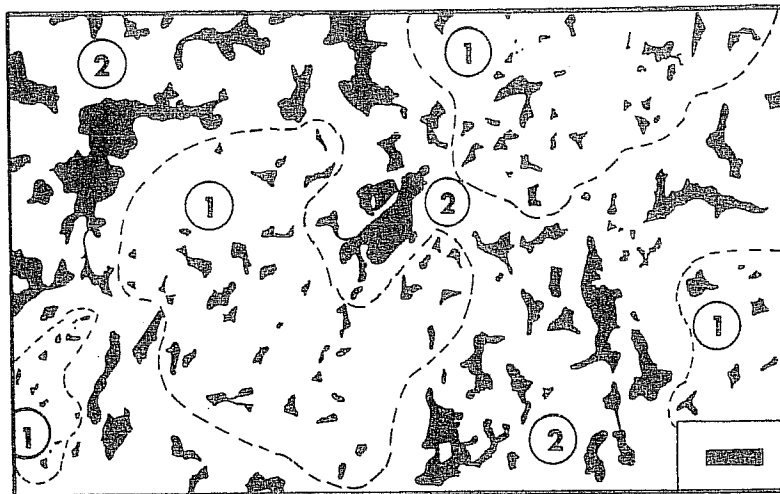


Fig. 3- Map obtained by tracing over a photomicrograph showing the typical pore geometry observed within a deltaic reservoir. 1- RP pores; 2- CD pores.

pores surrounded by a more continuous network of larger and better connected carbonate dissolution (CD) pores.

This type of pore structure is thought to strongly affect microscopic reservoir properties, particularly irreducible water saturation (S_{wi}), which is typically high (>30%) in the reservoirs (Fig. 4).

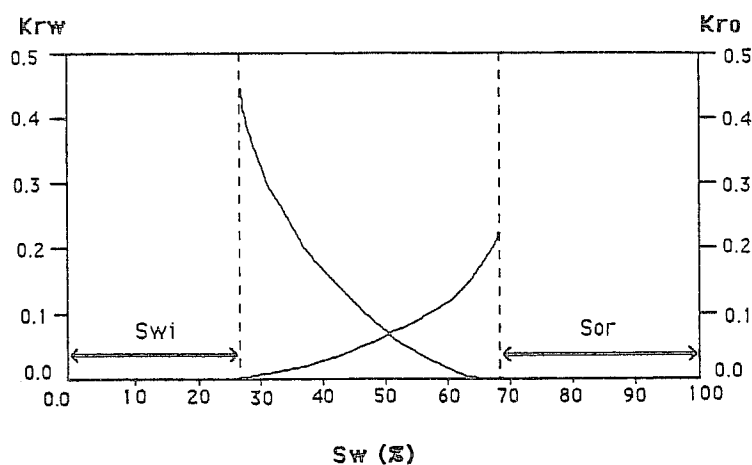


Fig. 4. Typical relative-permeability curve of deltaic reservoirs showing irreducible water saturation (S_{wi}) and residual oil saturation (S_{or}).

Part of the Swi can be attributed to the microporosity developed within authigenic clay (chlorite) aggregates, or intragranular pores formed by the partial dissolution of framework grains. However, high saturations are found also in sandstones with low clay content and relatively low intragranular porosity. Retention of water as a discontinuous phase within the islands of RP porosity whereas the oil fills the main (CD porosity dominated) pore system is inferred to be another important factor producing high irreducible water saturation (Table 1).

Factors Controlling the Occurrence of High (> 20%)
Irreducible Water Saturations in the Sandstone Reservoirs

Element	Critical Amount
Authigenic Clays (chlorite)	> 5% ^a
Intragranular and Moldic Pores	> 30% ^b
RP porosity	> 30% ^b

^a Percent of bulk rock volume (BRV)

^b Percent of total thin section porosity

Table 1. Factors affecting irreducible water saturation (Swi) in the sandstones.

IV. INTERWELL HETEROGENEITY

The relationships between diagenetic properties and depositional facies strongly influence reservoir performance at the interwell level. Diagenetic transformations can enhance, decrease or simply modify the nature of the contrasts inherited from the depositional environment. In the sandstones, dolomite and chlorite are the diagenetic elements which have a significant impact at the interwell scale.

Dolomite cement is observed concentrated along discrete stratification planes, a feature that increases permeability anisotropy and lowers the effective horizontal permeability (K_{eff}) of cross-bedded zones (Fig. 5).

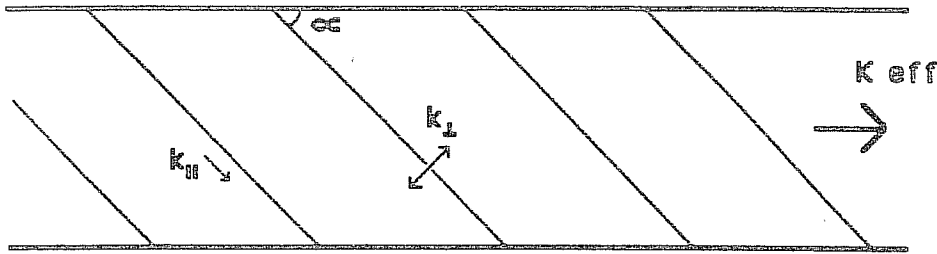


Fig. 5. Elements used for the calculation of effective directional permeability (K_{eff}) in a cross-bedded reservoir.

The dolomite effect was evaluated with data from the Serraria field, Potiguar Basin, using the following relationship (Weber, 1982):

$$\frac{1}{k_{eff}} = \frac{\cos^2 \alpha}{k_{\parallel}} + \frac{\sin^2 \alpha}{k_{\perp}}$$

Where:

α = foreset dip angle

k_{\parallel} = permeability parallel to the foresets

k_{\perp} = permeability normal to the foresets

The calculations indicate that a reservoir layer with 125 md of averaged plug horizontal permeability would have only 8.17 md of effective horizontal permeability if dolomite (> 5% of the bulk rock volume) and high-angle ($\alpha > 15^\circ$) cross-bedding are present.

Chlorite rims on framework grains were observed to reduce permeability in fine-grained sandstones, but had little influence on coarser grained sandstones (Fig. 6). This grain size dependent effect may change the permeability structure of the reservoirs because although deltaic reservoir units consist dominantly of fine-grained sandstones, narrow elongated zones composed of medium- to coarse-grained sandstones appear locally. Such coarser zones, which represent channel-mouth bar deposits, occur associated with the points where distributary channels fed into the delta-front (Alves, 1985; Moraes, 1991). If chlorite is present in both zones, it will have little influence on the coarser zones but will cause a significant permeability reduction in the fine-grained portion of the reservoir.

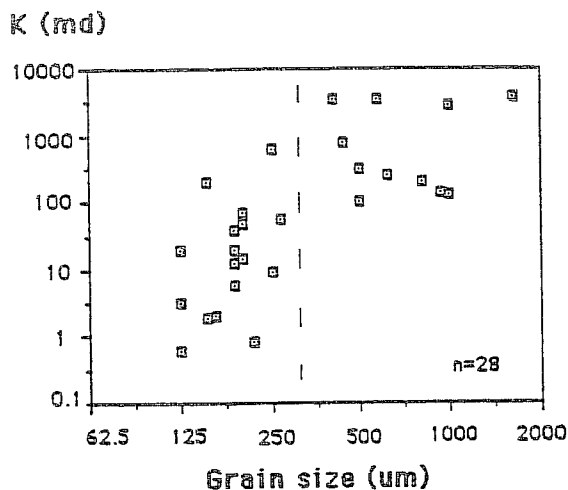


Fig. 6. Plot relating permeability to grain size in deltaic sandstone reservoirs.

Figure 7 illustrates the chlorite effect at the interwell level using an example from the Serraria field. The presence of such narrow high permeability zones encased in a moderate to low permeability region may cause strong irregularities (e. g., fingering phenomena) to develop at the fluid fronts.

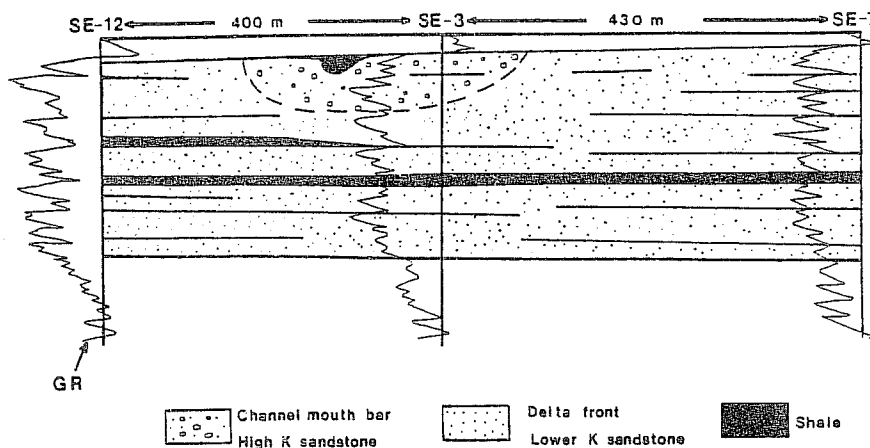


Fig. 7. Geologic section in the deltaic reservoirs of the Serraria field, Potiguar Basin, showing the location of a high permeability zone.

V. FIELD-WIDE HETEROGENEITY

Distribution of diagenetic elements at the field-wide scale is commonly related to both the depositional geometry and to the geological context of hydrocarbon trapping in the different reservoir types. Knowledge of reservoir heterogeneity at this scale serves as a guide for location of development wells and definition of production strategies. Field-wide water flooding and enhanced oil recovery (EOR) projects also will greatly rely on that kind of information.

The most significant diagenetic heterogeneity observed at the field-wide scale is the increase of carbonate cementation toward the outer boundaries of the sandstone accumulations (Anjos and Carozzi, 1988; Moraes, 1991). Such a carbonate cement distribution typically causes the occurrence of poorest reservoir quality in the outer portions of deltaic reservoirs (Fig. 8), and better reservoir quality toward the inner portions of the reservoir. In addition to the carbonate cement effect, the occurrence of narrow high permeability zones at the inner portion of the reservoir shown in Figure 8 is related to the lack of permeability reduction by chlorite in regions composed of coarser grained sandstones. The existence of such narrow high permeability zones at central portions in the reservoir will likely have a strong impact on fluid mobility at the field-wide scale.

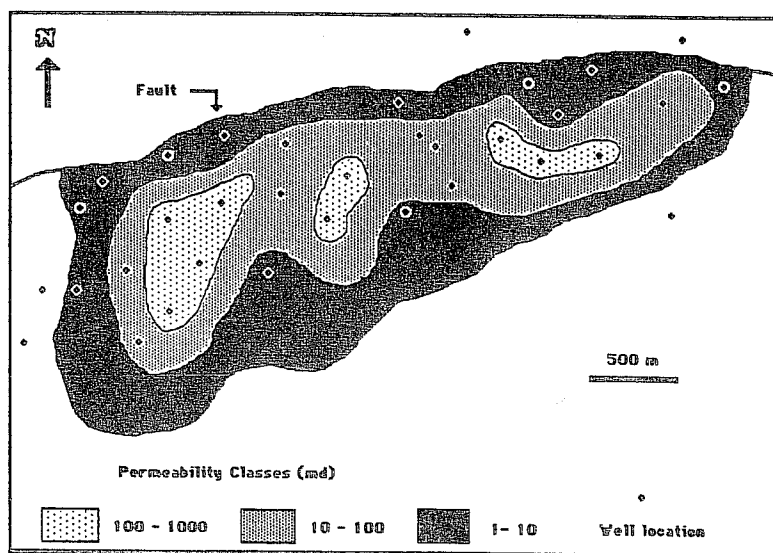


Fig. 8. Reservoir quality map of the deltaic reservoirs of Serraria field, Potiguar Basin.

VI. CONCLUSIONS

Diagenetic models can help to determine the critical aspects controlling fluid distribution and mobility at different reservoir scale levels. These diagenetic models are specially significant when viewed in a stratigraphic/sedimentologic framework. Integrating depositional and diagenetic characteristics at various scales permits a more accurate determination of effective properties used for performance prediction and numerical simulation of hydrocarbon reservoirs. Most of the patterns described herein were found to be repetitive in the lacustrine sandstone reservoirs of northeastern Brazil. Thus, the diagenetic models generated here are thought to have general applicability in the studied basins.

VII. REFERENCES

- Alves, A. C., 1985, Petrografia e diagênese dos arenitos reservatório da Formação Pendência (Cretáceo Inferior) na Campo de Serraria, Bacia Potiguar [unpubl. M.S. thesis]: Universidade Federal de Ouro Preto, Ouro Preto, Brazil, 143 p.
- Anjos, S. M. C. and Carozzi, A. V., 1988, Depositional and diagenetic factors in the generation of the Santiago arenite reservoirs (Lower Cretaceous): Araças oil field, Recôncavo Basin, Brazil: Jour. South American Earth Sciences, v. 1, p. 3-19.
- Becker, M. R., 1984, Petrologia e geologia de reservatório da unidade Catu 5, Grupo Ilhas, campo de Miranga, Bacia do Recôncavo [unpubl. M. S. thesis]: Universidade Federal de Ouro Preto, Ouro Preto, Brazil, 207 p.
- Bertani, R. T.; A. F. Apoluceno Netto and R. M. D. Matos, 1987, Habitat do petróleo e perspectivas exploratórias da Bacia Potiguar: Bol. Geoc. Petrobras, v. 1, p. 41-49.
- Fogg, G. E. and F. J. Lucia, 1990, Reservoir modeling of restricted platform carbonates: geologic/geostatistical characterization of interwell-scale reservoir heterogeneity, Dune field, Crane County, Texas: The Bureau of Economic Geology Report of Investigations no. 190, 66 p.
- Haldorsen, H. H., 1983, Reservoir characterization procedures for numerical simulation [unpubl. Ph.D. dissertation]: University of Texas, Austin, 147 p.

- Haldorsen, H. H. and E. Damsleth, 1990, Stochastic modeling: Jour. Pet. Technology, v. 42, p. 404-412.
- Milani, E.D. and I. Davison, 1988, Basement control and tectonic transfer in the Recôncavo-Tucano-Jatobá Rift, Brazil: Tectonophysics, v. 154, p. 41-70.
- Moraes, M. A. S., 1991, Multiscale diagenetic heterogeneity and its influence on the reservoir properties of fluvial, deltaic and turbiditic reservoirs, Potiguar and Recôncavo rift basins, Brazil [unpubl. Ph. D. dissertation]: University of Wyoming, Laramie, 176 p.
- Wardlaw, N. C., 1980, The effects of pore structure on displacement efficiency in reservoir rocks and in glass micromodels: Society of Petroleum Engineers of AIME Preprint SPE 8843, p. 345-352.
- Wardlaw, N. C. and J. P. Cassan, 1979, Oil recovery efficiency and the rock-pore properties of some sandstone reservoirs: Bull. Can. Pet. Geology, v. 27, p. 117-138.
- Weber, K. S., 1982, Influence of common sedimentary structures on fluid flow in reservoir models: Jour. Pet. Technology, v. 34, p. 665-672.
- Weber, K. J., 1986, How heterogeneity affects oil recovery, in Lake, L. W. and Carrol Jr., H. B. (eds.), Reservoir characterization, Orlando, Florida, Academic Press, p. 487-544.
- Weber, K. S. and L. C. van Genus, 1990, Framework for constructing clastic reservoir simulation models: Jour. Pet. Technology, v. 42, p. 1248-1253/1296-1297.

VARIABILITY IN CARBONATE RESERVOIR HETEROGENEITY AMONG JURASSIC SMACKOVER OIL PLAYS OF SOUTHWEST ALABAMA

Ernest A. Mancini
Robert M. Mink
Berry H. Tew
David C. Kopaska-Merkel
Steven D. Mann

Geological Survey of Alabama
Tuscaloosa, Alabama 35486-9780

The Upper Jurassic Smackover Formation is the most prolific petroleum reservoir in southwest Alabama (figs. 1 and 2). To date, 70 fields in this area have produced 258 million barrels of oil and condensate (fig. 3 and Table 1). These fields can be grouped into five distinct oil plays (fig. 4): the basement ridge play, the regional peripheral fault trend play, the Mississippi interior salt basin play, the Mobile graben fault system play, and the Wiggins arch complex play. Plays are recognized by basinal position, relationships to regional structural features, and characteristic petroleum traps. Within the basement ridge play, two subplays, the Choctaw ridge complex subplay and the Conecuh and Pensacola-Decatur ridge complexes subplay, can be distinguished based on oil gravities and reservoir characteristics. Similarly, two subplays, the Pickens, Gilbertown, and West Bend fault systems subplay and the Pollard and Foshee fault systems subplay can be recognized in the regional peripheral fault trend play. The plays are classified into three groups that differ in the scale, type, and range of reservoir heterogeneity (Table 2).

Lithologically, Smackover reservoirs include primarily grainstone, dolograinsone and crystalline dolostone. Pore systems in these reservoirs are dominated volumetrically by particle molds and intercrystalline pores. Moldic, secondary intraparticle, and

interparticle pores are a product of depositional fabric modified by diagenesis, whereas intercrystalline pores are created by fabric-destructive, nonselective dolomitization. The plays differ in reservoir characteristics and in the nature of heterogeneity as a result of depositional, diagenetic, and halokinetic processes. Reservoirs in the Choctaw ridge complex subplay are peritidal, nondolomitized to completely dolomitized, oolitic, peloidal, and oncoidal grainstone. Reservoir pore systems are dominated by molds of nonskeletal particles and by secondary intraparticle pores (partial molds). Heterogeneity is low, primarily because hydrocarbon accumulations are small and because the dominant reservoir type, grainstone with moldic and secondary intraparticle pore systems, forms large and homogeneous flow units. Reservoirs in the Conecuh and Pensacola-Decatur ridge complexes subplay are subtidal to supratidal, oolitic, oncoidal, intraclastic, and peloidal dolograins and dolopackstone, fenestral dolostone, quartz sandstone, and doloboundstone. The pore systems have substantial amounts of intercrystalline porosity; moldic and secondary intraparticle pores are also common. The variety of lithofacies and pore systems associated with the relatively small hydrocarbon accumulations result in moderate to high reservoir heterogeneity. Multiple reservoir zones are common. Reservoirs in the Pickens, Gilbertown, and West Bend fault systems subplay are peritidal, nondolomitized to completely dolomitized, oolitic, oncoidal, and peloidal grainstone. Reservoir pore systems are dominated by moldic and secondary intraparticle pores. Grainstone lithofacies are areally extensive and this, in combination with relatively well-developed moldic and secondary intraparticle pore systems, produces low reservoir heterogeneity. Reservoirs in the Pollard and Foshee fault systems subplay are subtidal to supratidal, partially to completely dolomitized, peloidal grainstone to wackestone and dolomitized boundstone. Reservoir pore systems are dominated by intercrystalline pores with a high percentage of moldic and secondary intraparticle pores. This subplay is characterized by a variety of reservoir lithofacies and pore systems and by multiple reservoir zones; therefore, heterogeneity is moderate to high. Due, however, to the generally higher reservoir pressures and relatively higher gravities of the liquids produced, hydrocarbon recovery is good. Reservoirs in the Mississippi interior salt basin play are peritidal, nondolomitized to completely dolomitized, peloidal and oolitic grainstone and packstone. In the northern part of this play, reservoir pore systems are dominated by oomolds and secondary intraooid pores, and in the southern part, pelmold and intrapeloid pores are the most important. Heterogeneity is low because the

particle-supported reservoir strata are widespread and have well-developed moldic pore systems. Reservoirs in the Mobile graben fault system play are peritidal, peloidal and oolitic dolograstone to dolowackestone and crystalline dolostone. Reservoir pore systems are dominated by intercrystalline pores. However, in the northern part of the play, moldic and interparticle pores are common. Heterogeneity is variable and ranges from low in the northern part of the play to high in the southern part. Reservoirs in the Wiggins arch complex play are subtidal to supratidal, peloidal, oolitic, oncoidal dolograstone and dolopackstone and crystalline dolostone. Intercrystalline pores dominate reservoir pore systems. Heterogeneity is high in this play due to the variety of reservoir lithofacies and because of the highly variable permeability distribution associated with the intercrystalline pore system which has a significant effect on producibility.

The distribution of Smackover depositional facies exerts the primary control on reservoir heterogeneity. In general, upper Smackover strata, which include the principal reservoirs, consist of stacked, cyclical, upward-shoaling, carbonate mudstone to grainstone, highstand parasequences that accumulated in a keep-up, shallow carbonate setting during progressive overall relative sea level fall (fig. 5). Relative sea level, as used here, approximates water depth. Depositional facies distribution reflects basin paleogeography and the sedimentary processes associated with the geologic setting; these factors, in turn, relate to reservoir heterogeneity. For example, the basement ridge play occurs in an updip paleogeographic setting associated with basement paleotopography around the margin of the depositional basin. Within this play, the Conecuh and Pensacola-Decatur ridge complexes subplay is characterized by a variety of reservoir lithofacies and pore systems that, in part, result from the sedimentological response to small-scale sea-level fluctuations superimposed on the overall upper Smackover regressive trend. Heterogeneity is low within reservoir strata in the Choctaw ridge complex subplay. However, these grainstone reservoirs are generally thin and are intercalated with a variety of nonreservoir strata that result from the depositional conditions in the updip paleogeographic setting. Thus, rocks in the basement ridge play exhibit the effects of small-scale perturbations on depositional environments in updip areas around the basin periphery. Conversely, reservoirs of the Pickens, Gilbertown, and West Bend fault systems subplay and the Mississippi interior salt basin play, which include strata that were deposited in a more seaward position, are characterized by relatively homogenous, relatively

thick, widespread lithofacies and pore systems that reflect deposition in a stable marine shelf setting which was not dramatically affected by minor sea-level changes.

Smackover reservoir heterogeneity is a product of primary depositional patterns modified by diagenesis, mainly dolomitization and leaching of metastable particles. Upper Smackover strata accumulated as progradational, highstand deposits within a unconformity-bounded depositional sequence (fig. 5). The upper sequence boundary is above the Buckner Anhydrite Member of the Haynesville Formation. In southwest Alabama, the lower Buckner is dominated by sabkha and salina deposits on the basin margins and on the flanks of paleohighs, and by impermeable anhydritic subaqueous saltern deposits in the basin centers. During Buckner time, refluxed hypersaline fluids from the Buckner dolomitized much of the uppermost Smackover. After deposition of the Buckner and the lower Haynesville, the climate became less arid and much of the region was subaerially exposed along the type 2 sequence boundary. At this time, meteoric waters entered the Smackover through exposed permeable strata on the basin margins and from isolated emergent paleohighs such as the Wiggins arch and the Conecuh ridge complex. Meteoric water mixed with marine water and/or with Buckner-derived brines in the subsurface, dissolving metastable particles and forming dolomite in the upper Smackover. Some later stage dolomite not associated with the sequence boundary also appears to be important in the Smackover.

Smackover oil plays and subplays in southwest Alabama can be classified into three groups based on relative heterogeneity ranking (fig. 6). Low heterogeneity typifies reservoirs in the Choctaw ridge complex subplay, the Pickens, Gilbertown, and West Bend fault systems subplay and the Mississippi interior salt basin play and results from the restriction of reservoirs to thin, homogeneous intervals and the presence of areally extensive grainstone lithofacies with associated homogeneous pore systems. Reservoirs in the Conecuh and Pensacola-Decatur ridge complexes and Pollard and Foshee fault systems subplays exhibit moderate to high heterogeneity which can be attributed to the variety of reservoir lithofacies and pore systems present. Heterogeneity in the Mobile graben fault system is variable, ranging from low to high. High reservoir heterogeneity in the Wiggins arch complex play results from the variety of lithofacies present and the highly variable nature of the intercrystalline reservoir pore systems.

This research was partially funded by the United States Department of Energy under Contract No. DE-FG22-89BC14425.

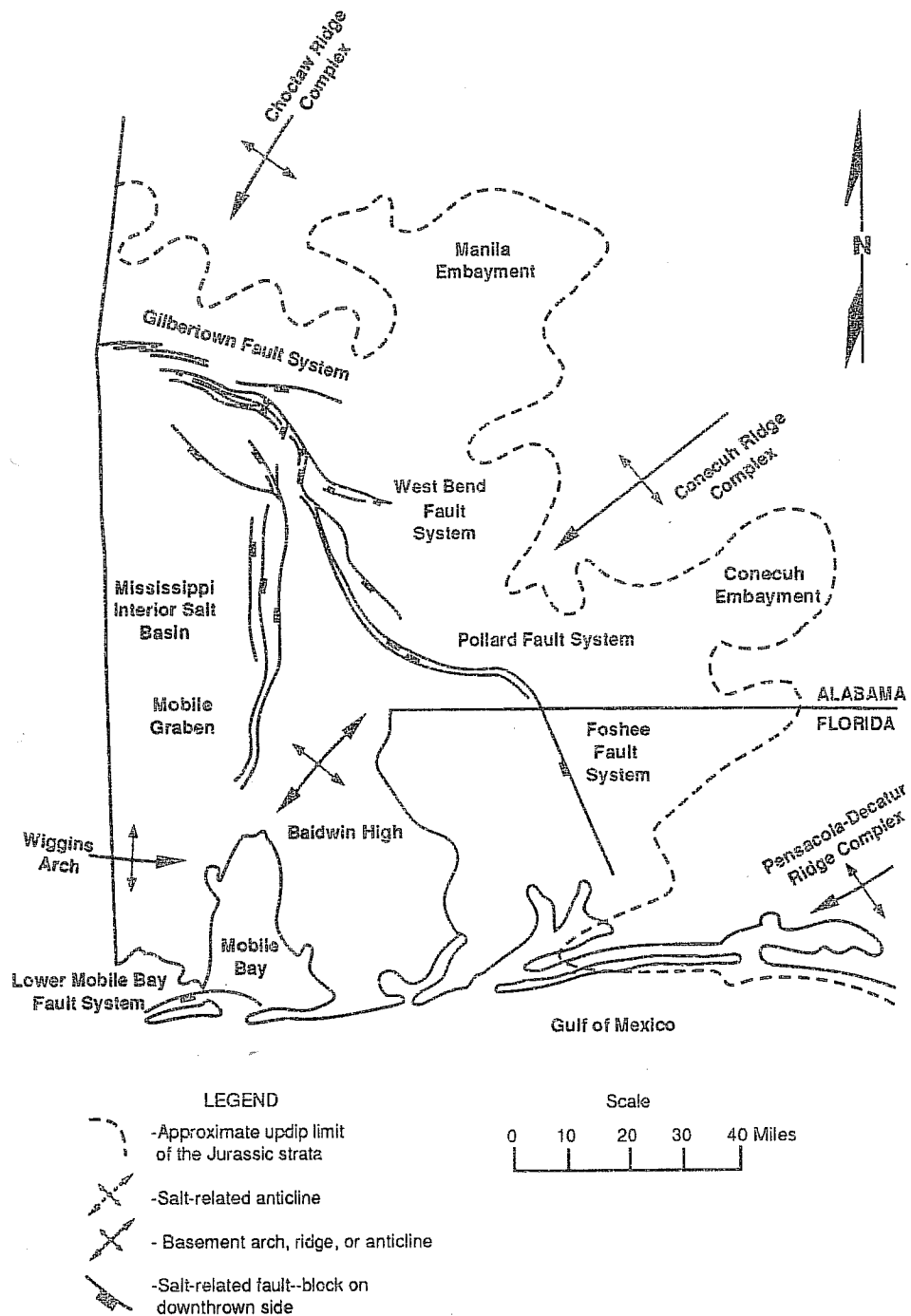


Figure 1. Map of southwest Alabama showing major structural features.

SERIES	STAGE	ROCK UNIT
Lower Cretaceous	Berriasian	Cotton Valley Group
----- ? -----	Tithonian	
Upper Jurassic	Kimmeridgian	Haynesville Formation
		Buckner Anhydrite Member
	Oxfordian	Smackover Formation
		Norphlet Formation
		Pine Hill Anhydrite Member
----- ? -----	----- ? -----	
Middle Jurassic	Callovian	Louann Salt
		Werner Formation
Lower Jurassic/ Upper Triassic		Eagle Mills Formation
		Undifferentiated Paleozoic and Proterozoic "basement" rocks

Figure 2. Jurassic stratigraphy of southwest Alabama.

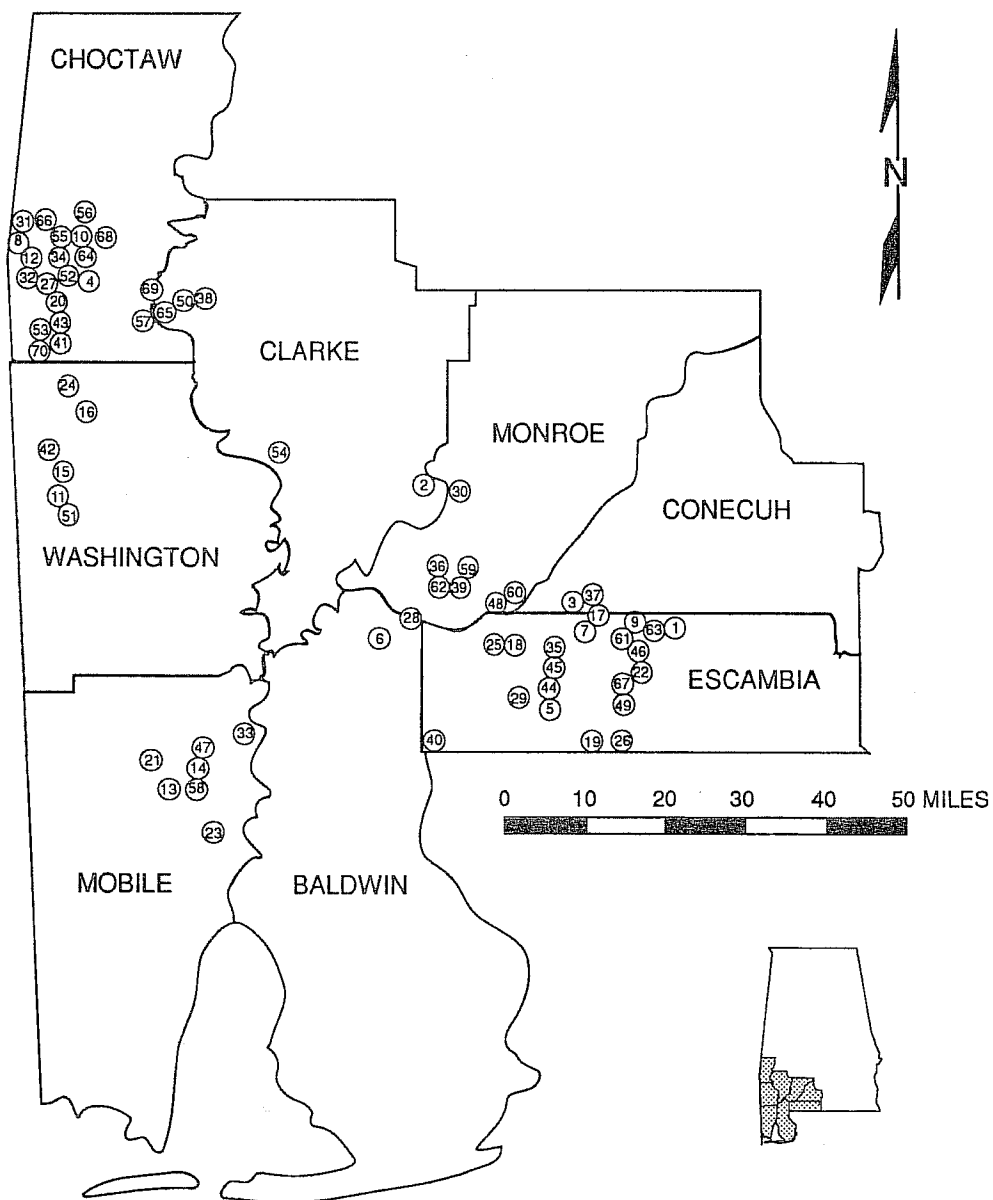


Figure 3. Location of Smackover fields in southwest Alabama.

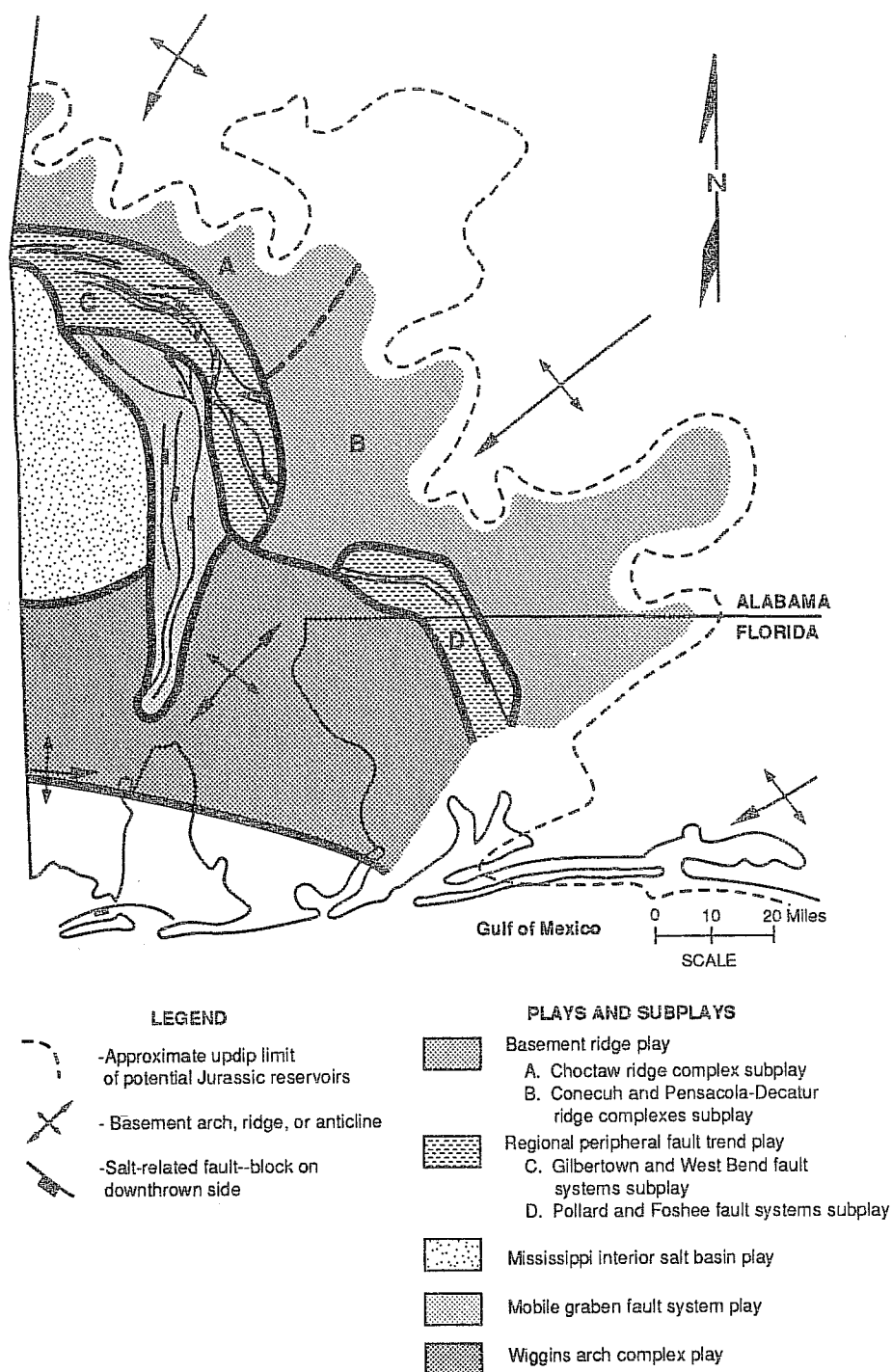


Figure 4. Smackover oil plays in southwest Alabama.

Cycles	Relative changes in coastal onlap Landward Seaward	Lithostratigraphy	Deposits	Stages
LZAGC-4.2		upper Haynesville clastics & anhydrites	Highstand	Kimmeridgian
		upper Haynesville carbonates & shales	Condensed	
		upper Haynesville sandstones	Transgressive	
LZAGC-4.1		middle Haynesville clastics, evaporites & carbonates; Buckner anhydrites; Smackover mudstones to grainstones	Highstand	Oxfordian
		Smackover carbonate mudstones	Condensed	
		Smackover carbonate mudstones, wackestones & packstones	Transgressive	
		Norphlet marine sandstones	Shelf Margin	
		Norphlet continental clastics	Highstand	
LZAGC-3.1		Pine Hill anhydrites & shales	Condensed	Callovian
		Louann salt; Werner evaporites & clastics	Transgressive	

Figure 5. Jurassic sequence stratigraphy in southwest Alabama.

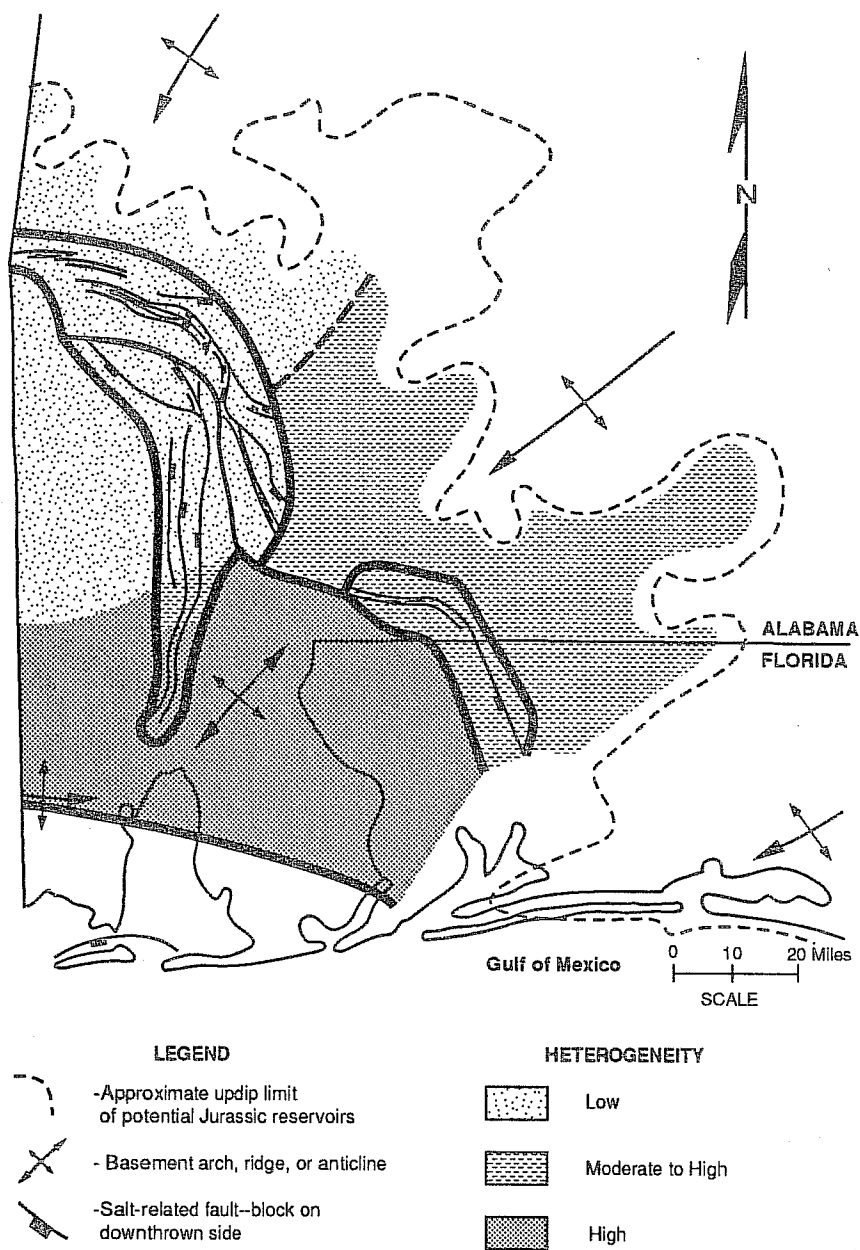


Figure 6. Relative levels of heterogeneity of Smackover oil plays and subplays in southwest Alabama.

Table 1. List of Smackover fields in southwest Alabama.

Field No.	Field Name	County	Hydrocarbon Type
1	Appleton	Escambia	Oil
2	Barlow Bend	Clarke and Monroe	Oil
3	Barnett	Conecuh and Escambia	Oil
4	Barrytown	Choctaw	Oil
5	Big Escambia Creek	Escambia	Condensate
6	Blacksher	Baldwin	Oil
7	Broken Leg Creek	Escambia	Oil
8	Bucatumna Creek	Choctaw	Oil
9	Burnt Corn Creek	Escambia	Oil
10	Chappell Hill	Choctaw	Oil
11	Chatom	Washington	Condensate
12	Choctaw Ridge	Choctaw	Oil
13	Churchula	Mobile	Oil/Condensate
14	Cold Creek	Mobile	Oil
15	Copeland Gas	Washington	Condensate
16	Crosbys Creek	Washington	Condensate
17	East Barnett	Conecuh and Escambia	Oil
18	East Huxford	Escambia	Oil
19	Fanny Church	Escambia	Oil
20	Gin Creek	Choctaw	Oil
21	Gulf Crest	Mobile	Oil
22	Hanberry Church	Escambia	Oil
23	Hatter's Pond	Mobile	Condensate
24	Healing Springs	Washington	Condensate
25	Huxford	Escambia	Oil
26	Little Escambia Creek	Escambia	Oil
27	Little Mill Creek	Choctaw	Oil
28	Little River	Baldwin and Monroe	Oil
29	Little Rock	Escambia	Condensate
30	Lovetts Creek	Monroe	Oil
31	Melvin	Choctaw	Oil
32	Mill Creek	Choctaw	Oil
33	Movico	Baldwin and Mobile	Oil
34	North Choctaw Ridge	Choctaw	Oil
35	North Smiths Church	Escambia	Oil

Table 1. List of Smackover fields in southwest Alabama
(continued).

Field No.	Field Name	County	Hydrocarbon Type
36	North Wallers Creek	Monroe	Oil
37	Northeast Barnett	Conecuh	Oil
38	Pace Creek	Clarke	Oil
39	Palmers Crossroads	Monroe	Oil
40	Perdido	Baldwin and Escambia	Oil
41	Puss Cuss Creek	Choctaw	Oil
42	Red Creek	Washington	Condensate
43	Silas	Choctaw	Oil
44	Sizemore Creek Gas	Escambia	Condensate
45	Smiths Church	Escambia	Condensate
46	South Burnt Corn Creek	Escambia	Oil
47	South Cold Creek	Mobile	Oil
48	South Vocation	Monroe	Oil
49	South Wild Fork Creek	Escambia	Condensate
50	South Womack Hill	Choctaw and Clarke	Oil
51	Southeast Chatom	Washington	Condensate
52	Southwest Barrytown	Choctaw	Oil
53	Souwilpa	Choctaw	Condensate
54	Stave Creek	Clarke	Oil
55	Sugar Ridge	Choctaw	Oil
56	Toxey	Choctaw	Oil
57	Turkey Creek	Choctaw and Clarke	Oil
58	Turnerville	Mobile	Oil
59	Uriah	Monroe	Oil
60	Vocation	Monroe	Oil
61	Wallace	Escambia	Oil
62	Wallers Creek	Monroe	Oil
63	West Appleton	Escambia	Oil
64	West Barrytown	Choctaw	Oil
65	West Bend	Choctaw and Clarke	Oil
66	West Okatuppa Creek	Choctaw	Oil
67	Wild Fork Creek	Escambia	Oil
68	Wimberly	Choctaw	Oil
69	Womack Hill	Choctaw and Clarke	Oil
70	Zion Chapel	Choctaw	Oil

Table 2. Summary of reservoir characteristics and levels of heterogeneity for Smackover oil plays and subplays in southwest Alabama.

Play/Subplay	Reservoir	Pore System	Heterogeneity
Basement Ridge Play			
Choctaw Ridge Complex Subplay	Grainstone Dolograinstone	Moldic Intraparticle	Low
Conecuh and Pensacola-Decatur Ridge Complexes Subplay	Dolograinstone Dolopackstone Doloboundstone Dolostone Sandstone	Intercrystalline Moldic Intraparticle	Moderate to High
Regional Peripheral Fault Trend Play			
Pickens, Gilbertown, and West Bend Fault Systems Subplay	Grainstone Dolograinstone	Moldic Intraparticle	Low
Pollard and Foshee Fault Systems Subplay	Grainstone Packstone Wackestone Boundstone Dolograinstone Dolopackstone Dolowackestone Doloboundstone	Intercrystalline Moldic Intraparticle	Moderate to High
Mississippi Interior Salt Basin Play	Grainstone Packstone Dolograinstone Dolopackstone	Moldic Intraparticle	Low
Mobile Graben Fault System Play	Dolograinstone Dolopackstone Dolowackestone Dolostone	Intercrystalline Moldic Intraparticle Interparticle	Low to High
Wiggins Arch Complex Play	Dolograinstone Dolopackstone Dolostone	Intercrystalline	High

**Minipermeameter Study of Fluvial Deposits of the
Frio Formation (Oligocene), South Texas:
Implications for Gas Reservoir Compartments¹**

Dennis R. Kerr², Andrew R. Scott
Jeffrey D. Grigsby, and Raymond A. Levey
Bureau of Economic Geology
University Station, Box X
Austin, Texas 78713-7508

I. INTRODUCTION

Fluvial deposits of the Oligocene Frio Formation in South Texas contain significant natural gas reserves (1). Production history and completion pressure reports offer evidence for the existence of gas reservoir compartments within mature reservoirs and fields. A challenging question to the Secondary Natural Gas Recovery Joint Venture Program (cosponsored by the Gas Research Institute, the U.S. Department of Energy, and the State of Texas) is whether incompletely drained compartments exist in gas reservoirs in which sandstone-on-sandstone contacts are common. To address this issue, a minipermeameter study was undertaken on cores collected from Stratton field (Fig. 1).

Fluvial deposits at Stratton field are included in the Gueydan depositional system of the Texas Gulf Coast Basin (2). Four facies comprise the fluvial Frio (3): channel-fill, splay, levee, and floodplain. The channel fill facies is divided into three subfacies (Figs. 2, 3, and 4): (1) lower channel fill consisting of 0.5- to

¹Funded by the Gas Research Institute contract no. 5088-212-1718, the U.S. Department of Energy contract no. DE-FG21-88MC25031 and the State of Texas through the Bureau of Economic Geology*. Publication authorized by the Director, Bureau of Economic Geology, The University of Texas at Austin.

*The cooperation of Union Pacific Resources Company is gratefully acknowledged.

² Current address: Department of Geosciences, University of Tulsa, Tulsa, Oklahoma.

1.5-ft-thick sets of trough cross-stratified medium sandstone having intraclast lags, (2) middle channel fill consisting of low-angle parallel and ripple-stratified very fine to fine sandstone having chute channel-fill (Fig. 4) and lateral accretion surfaces, and (3) upper channel fill consisting of structureless to poorly developed parallel and ripple-stratified, muddy, very fine sandstone to sandy mudstone. Commonly associated with the upper channel fill are pedogenic carbonate and clay cements, and infiltrated fines lining intergranular pores, compacted fractures, and root molds. Architectural stacking patterns of discrete genetic intervals (i.e., deposits of a discrete channel system with attendant splays) range from *laterally stacked*, in which sandstone bodies contact one another or are separated by only a few feet of floodplain mudstones, to *vertically stacked*, in which sandstone bodies are separated by several feet of floodplain mudstones. Channel-on-channel contacts are prevalent in the laterally stacked architectural style. The question of whether enough permeability contrast exists among the *sandstones of the channel-fill subfacies* to produce a barrier or baffle to gas flow is key to this study.

Two distinct reservoirs (types I and II) are differentiated on the basis of framework mineralogy, diagenetic history, and reservoir quality in fluvial Frio sandstones (4; Fig. 5). Type I sandstones are poorly to moderately sorted feldspathic litharenites to litharenites; lithic fragments are predominantly volcanic and carbonate rock fragments. Major authigenic minerals are calcite, chlorite, and kaolinite; minor amounts of quartz and feldspar overgrowths and pyrite are present. Type I reservoirs have a strong positive correlation between porosity and permeability, with permeability reaching the 1,000's of millidarcies (Fig. 5). This relationship indicates a well-connected intergranular pore system. By contrast, type II sandstones are poorly to moderately sorted lithic arkoses to feldspathic litharenites; lithic fragments are predominantly volcanic, with carbonate rock fragments constituting less than 1 % of the rock volume. Volcanic glass detritus occurs exclusively in type II sandstones. Depositional matrix averages 20 %. Major authigenic minerals are calcite, analcime, and illite-smectite; minor minerals include pyrite and very finely crystalline quartz, feldspar, and chlorite. Type II reservoirs have a weak positive correlation between porosity and permeability, with permeability being limited to less than 100 millidarcies (Fig. 5). This relationship indicates that the pore networks are poorly connected even in rocks that have high porosity.

II. MINIPERMEAMETER STUDY

More than 1,000 permeability measurements were made on three core segments (Figs. 2, 3, and 4) using a minipermeameter (mechanical field permeameter). To evaluate the permeability distribution within major channel-fill subfacies of types I and II reservoirs, two parallel transects of closely spaced (0.1-ft) intervals were made on slabbed, air-dried cores. The depth and effective radius of investigation of the minipermeameter are 0.35 and 0.18 in, respectively. Abnormally high permeability values, resulting from the desiccation of clays in clayey intervals or hairline surface fractures on the core face, were eliminated from the data base.

A very good correlation exists between the average permeability determined from minipermeameter measurements and the permeability relative to air determined by conventional methods (Fig. 6), suggesting that the minipermeameter can be used reliably to evaluate permeability trends. However, at low values of permeability the minipermeameter is apparently less reliable (Fig. 6). This, plus the detection limit of the minipermeameter

(approximately 0.1 md), contributes to the distortion of the distribution of minipermeameter data (Fig. 6).

Semivariograms were generated to assess the spatial variation of permeability in types I and II reservoirs. The permeability data required a square-root transformation to achieve an approximation of a normal distribution required for the generation of semivariograms (Fig. 7). Square-root transformation of permeability data for statistical analysis of eolian sandstones has also been reported by Goggin *et al.* (5).

The upper channel-fill subfacies of both types I and II reservoirs show no spatial correlation of permeability, indicating that higher permeability zones are localized and have limited vertical extent (Fig. 8). Porosity and permeability are limited because of a clay matrix and calcite (micrite) cement. Semivariograms of the middle and lower channel-fill subfacies from both types of reservoirs indicate a spatial correlation of permeability (Fig. 8). Damped oscillations about the sill, called a hole effect, reflect the distribution of permeability. These quasi-periodic components are related to the thickness of cross-strata sets and stratification; at distances on the order of tens of feet, the larger oscillations are related to channel thicknesses (e.g., Figs. 2, 3, and 4). Both types of reservoirs have a nugget effect that is approximately 13 % of total variance, suggesting permeability heterogeneity at the finest scales. The middle and lower channel fill subfacies of type I reservoirs have a range larger (more than 1 ft) than that of type II reservoirs, which have ranges of less than 1 ft (Fig. 8), indicating that permeability can be correlated over relatively greater distances in type I reservoirs. The abundant detrital matrix material; pore-filling authigenic clays, calcite, and analcime; and grain-moldic porosity reduce the vertical continuity of permeability in type II reservoirs.

III. IMPLICATIONS

Thin-section petrography and semivariograms of upper channel-fill subfacies in both types I and II reservoirs indicate that the vertical distribution of permeability is limited because of abundant detrital clays and calcite cement. Therefore, the upper-channel-fill subfacies are likely baffles to gas flow, and understanding the distribution of this subfacies is important for evaluating reservoir compartmentalization within mature reservoirs and fields.

Semivariograms of middle and lower-channel-fill subfacies for types I and II reservoirs indicate vertical continuity of permeability. However, permeability continuity is more restricted in type II reservoirs because of extensive diagenesis.

REFERENCES

1. Kisters, E.C., Bebout, D.G., Seni, S.J., Garrett, C.M., Jr., Brown, L.F., Jr., Hamlin, H.S., Dutton, S.P., Ruppel, S.C., Finley, R.J., and Tyler, Noel, 1989, Atlas of major Texas gas reservoirs: The University of Texas at Austin, Bureau of Economic Geology, 161 p.
2. Galloway, W. E., Hobday, D. K., and Magara, K., 1982, Frio Formation of the Texas Gulf Coast Basin--depositional systems, structural framework, and hydrocarbon origin, migration, distribution, and exploration potential: The University of Texas at Austin, Bureau of Economic Geology Report of Investigations No. 122, 78 p.
3. Kerr, D. R., and Jirik, L. A., 1990, Fluvial architecture and reservoir compartmentalization in the Oligocene middle Frio Formation, South Texas: Gulf Coast Association of Geological Societies v. 40, p. 373-380.
4. Grigsby, J. D., and Kerr, D. R., 1991, Diagenetic variability in middle Frio Formation gas reservoirs (Oligocene), Seeligson and Stratton fields, South Texas: Gulf Coast Association of Geological Societies Transactions, v. 41 (in press).
5. Goggin, D. J., Chandler, M. A., Kocurek, G., and Lake, L. W., 1989, Permeability transects in eolian sands and their use in generating random permeability fields: Society of Petroleum Engineers paper 19586, p.149-164.

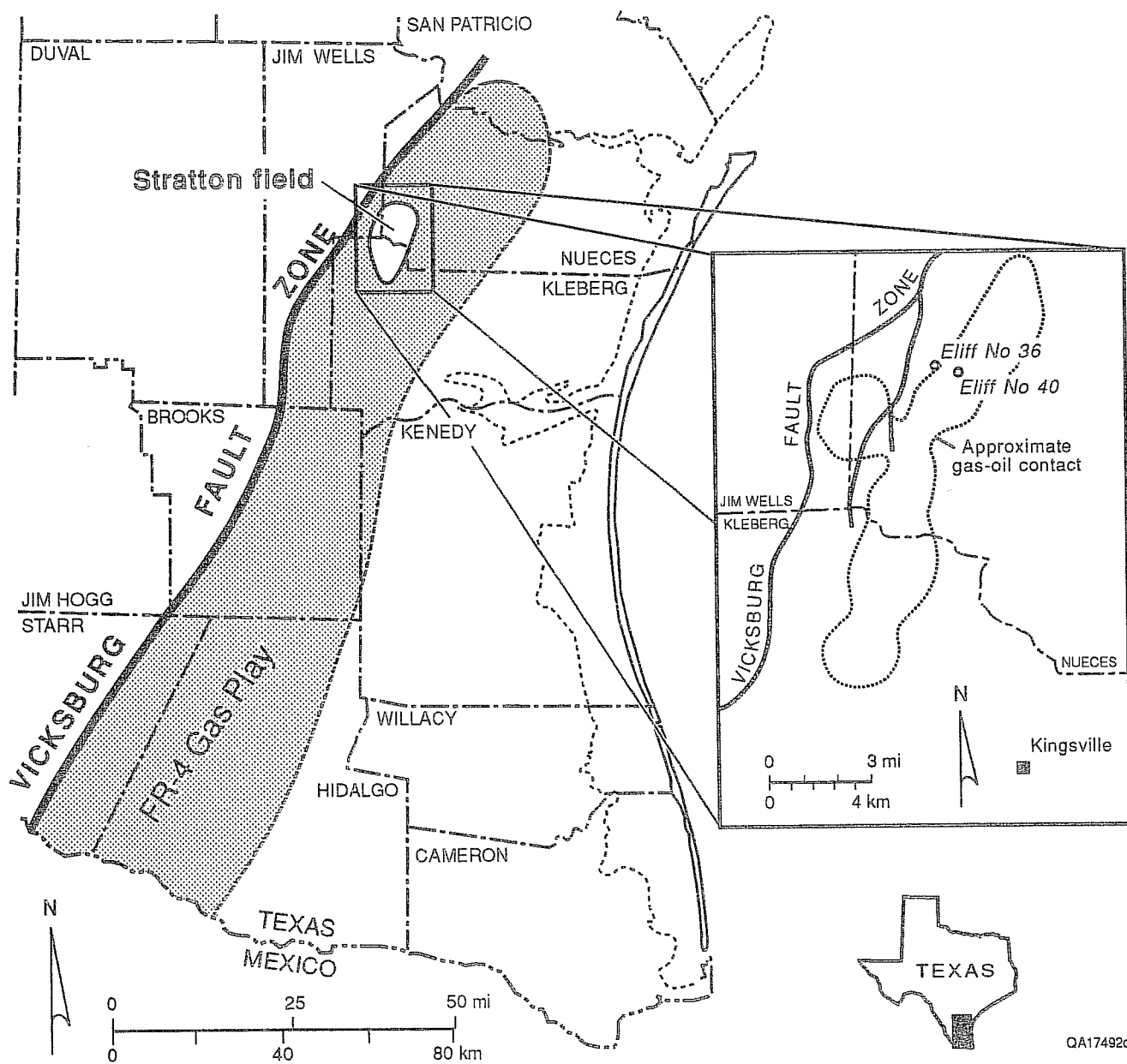


Fig. 1. Index maps showing the location of Stratton field within the FR-4 gas play (1) and the location of Eliff Nos. 36 and 40 wells within Stratton field.

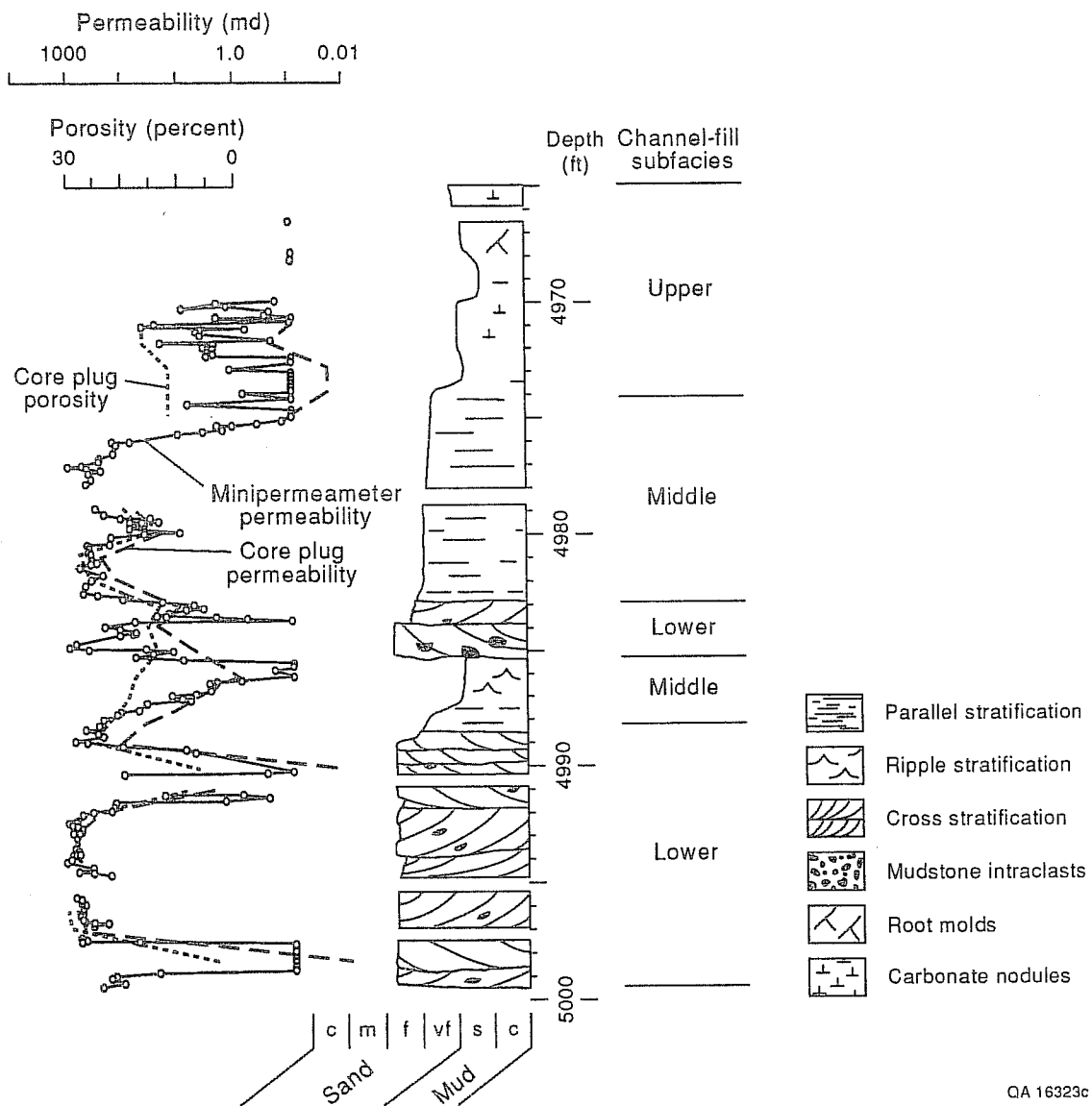


Fig. 2. Core graphic of Elliff No. 40 core 1 (C18 reservoir) showing minipermeameter, core plug permeability, and porosity profiles for a type I reservoir. Minipermeameter values are averaged from two closely spaced vertical transects.

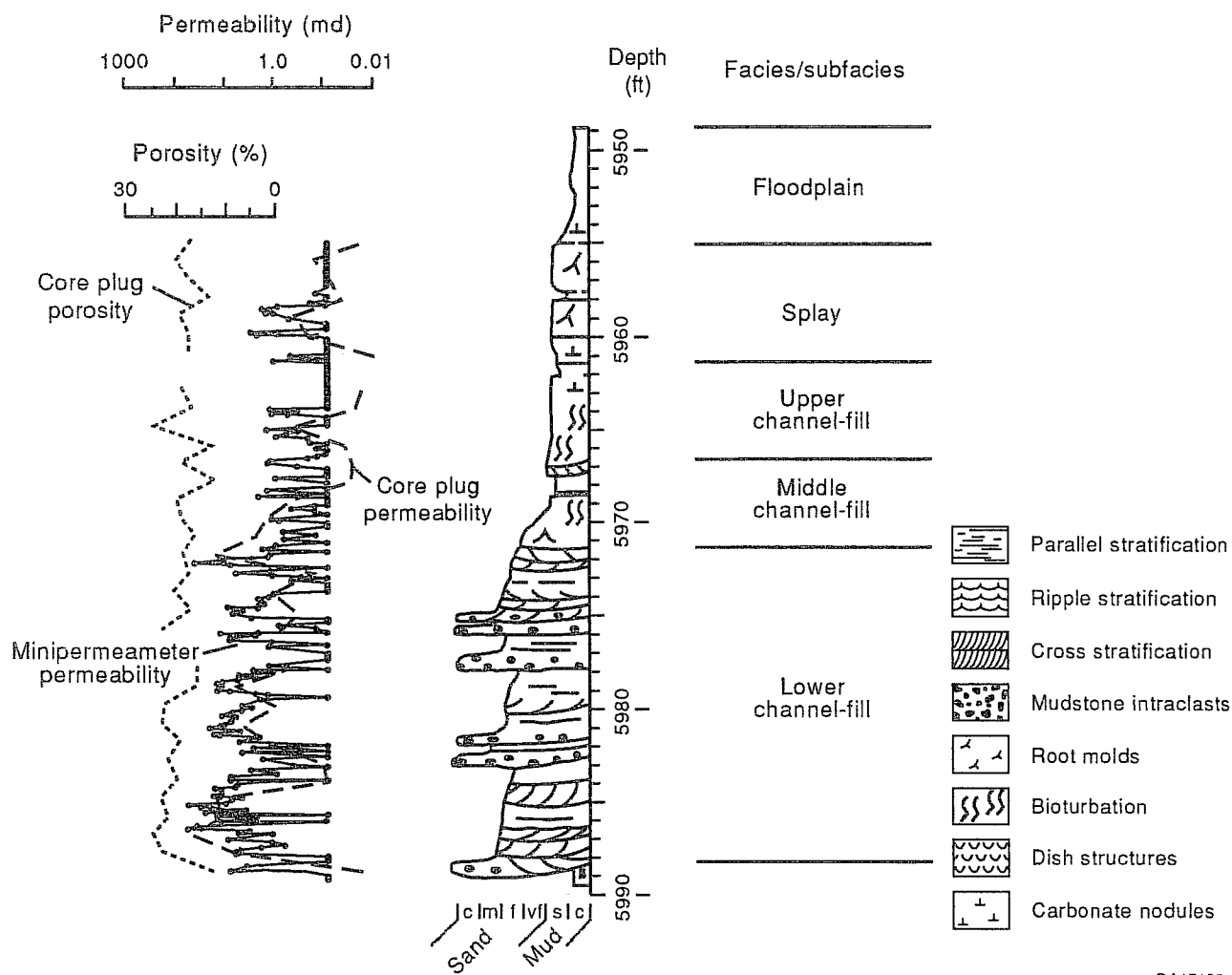
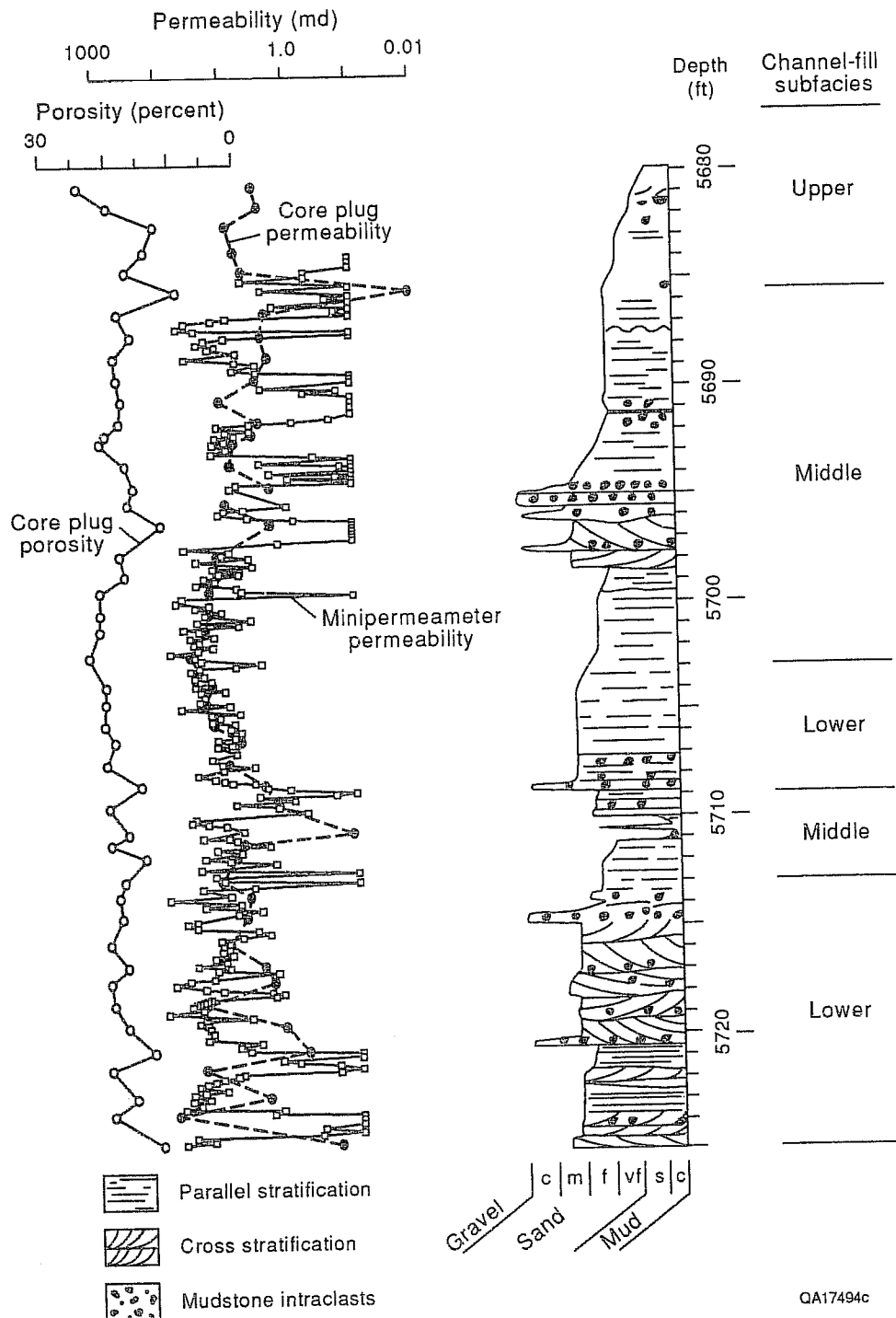


Fig. 3. Core graphic of Elliff No. 40 core 3 (E13 reservoir) showing minipermeameter, core plug permeability, and porosity profiles for a type II reservoir. Minipermeameter values are averaged from two closely spaced vertical transects. Permeability is significantly lower in type II reservoirs than in type I reservoirs (Fig. 2).



QA17494c

Fig. 4. Core graphic of Elliff No. 36 core 2 and 3 (D35 reservoir) showing minipermeameter, core plug permeability, and porosity profiles for a type II reservoir. Minipermeameter values are averaged from two closely spaced vertical transects. Chute channel-fill deposits (5691.0 to 5698.5) are interpreted from detailed cross-section correlation and facies mapping.

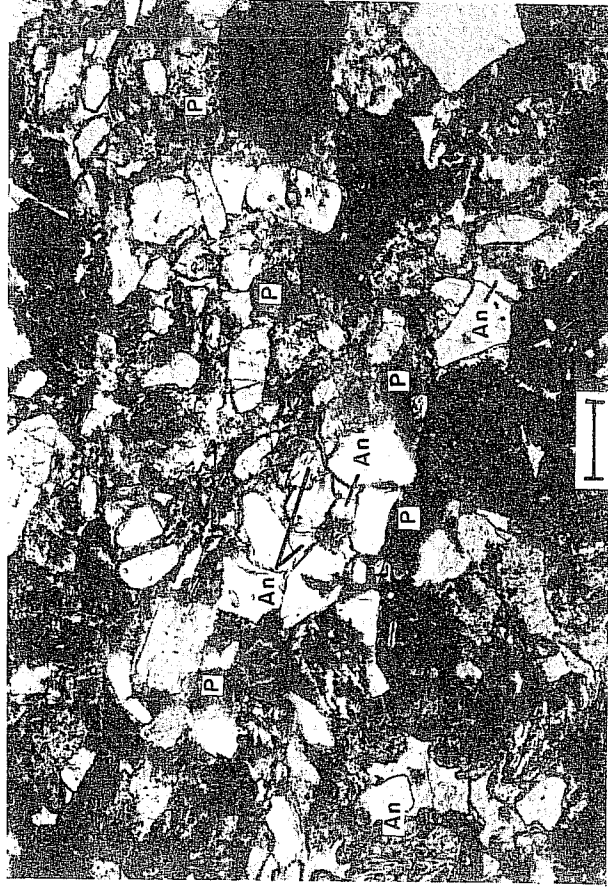
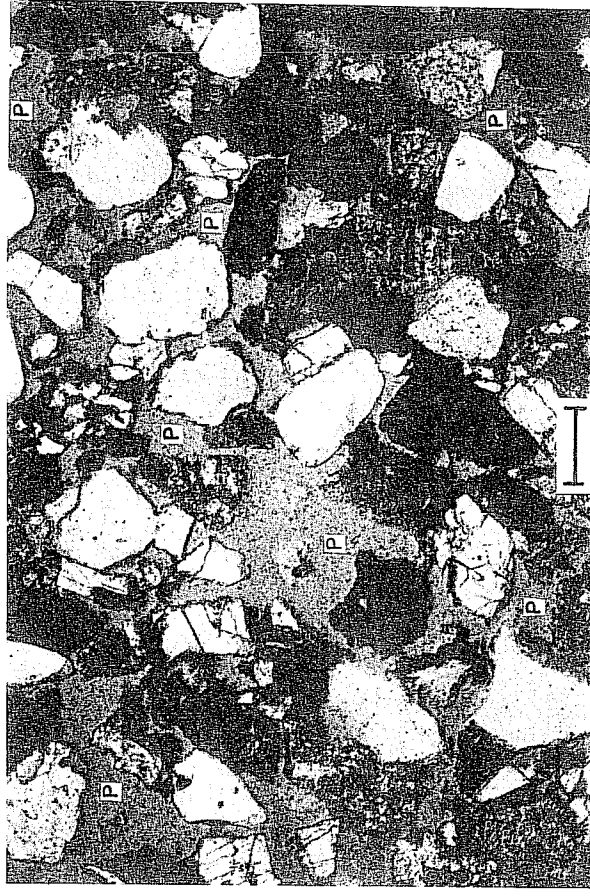
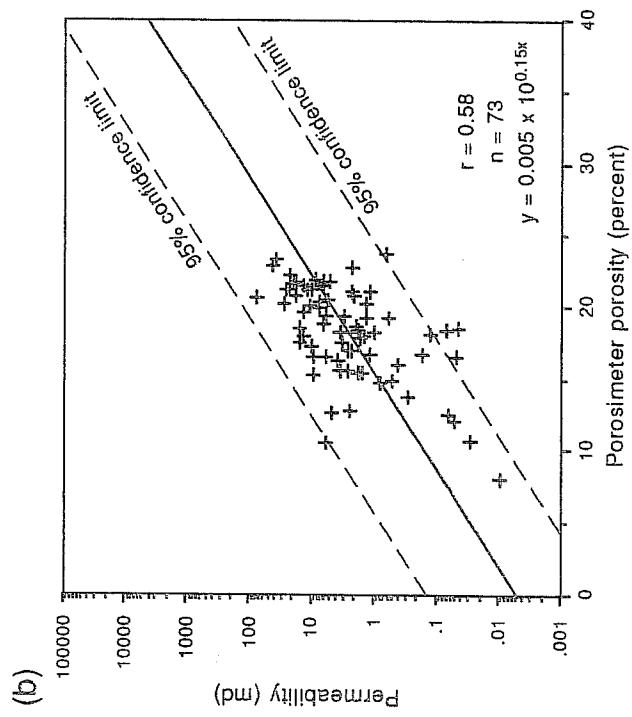
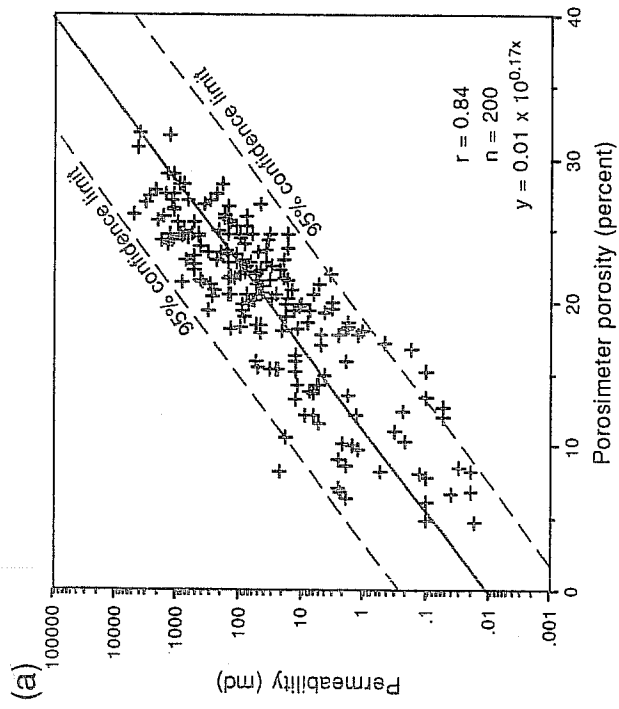


Fig. 5. Porosity-permeability cross plots for (a) type I and (b) type II reservoirs. The strong correlation between porosity and core-plug permeability in type I reservoirs indicates well-developed intergranular porosity and good permeability distribution. The weaker correlation in type II reservoirs demonstrates the effect of poorly developed intergranular porosity and lower permeability. Photomicrographs illustrate the differences in porosity development between types I and II reservoirs. Note poorly connected pores in type II reservoirs. An=analcime; P=pore. Length of bar is 250 microns.

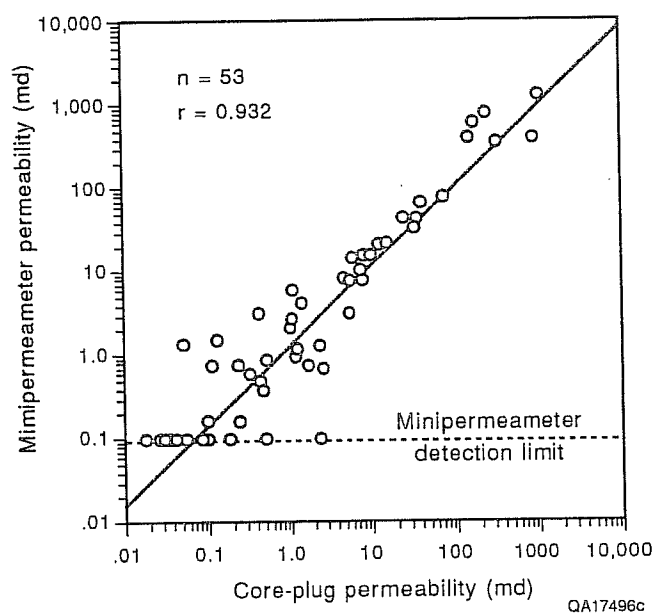


Fig. 6. Permeability-permeability cross plot showing the relation between minipermeameter and conventional core plug permeability measurements. Minipermeameter measurements were taken from the ends of the core plugs after the plug permeability measurements were made. The high correlation coefficient supports the reliability of minipermeameter measurements.

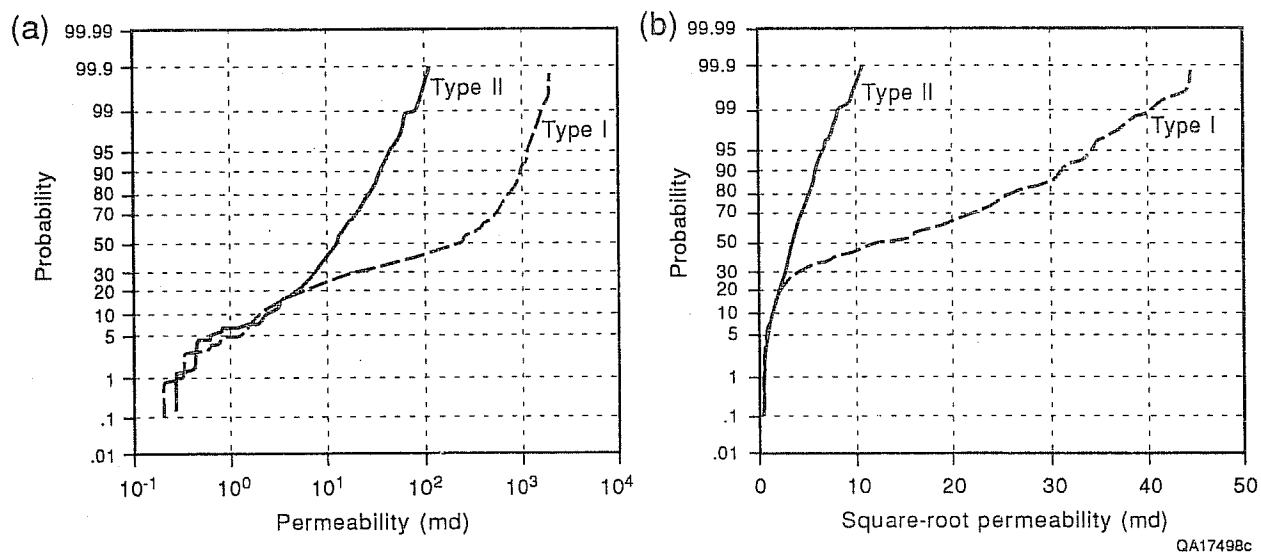


Fig. 7. Cumulative relative frequency plots of minipermeameter data from types I and II reservoirs: (a) log transformation and (b) square-root transformation. Note how the square-root transformation provides a better approximation of a normal distribution (except at low permeability values) than the log transformation.

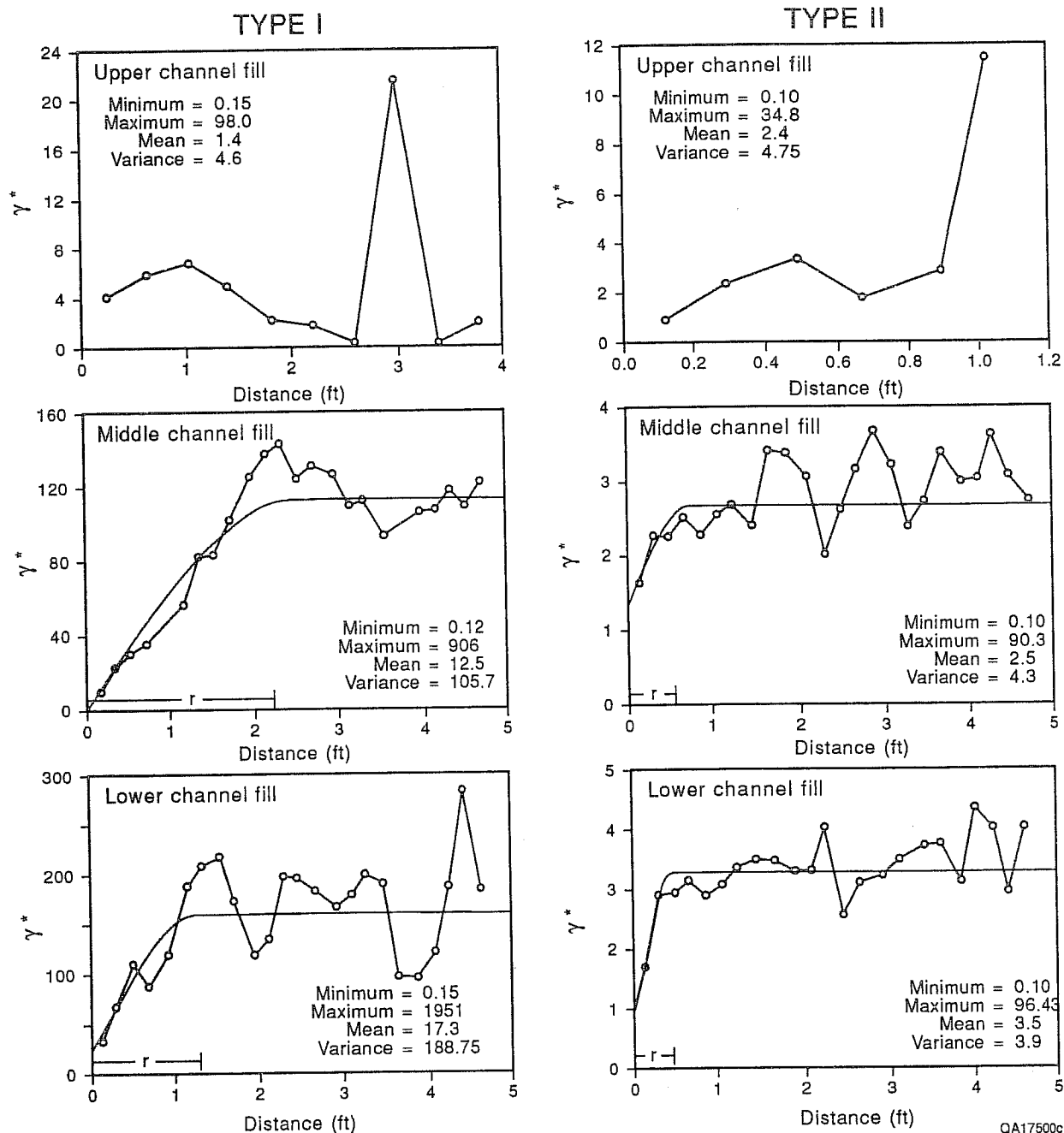


Fig. 8. Semivariograms for upper, middle, and lower channel-fill subfacies for types I and II reservoirs (Figs. 2, 3, and 4). Semivariograms for the upper channel-fill subfacies of both types of reservoirs indicate no spatial correlation of permeability, suggesting that higher permeability zones within this subfacies are localized. Structural analysis of the semivariograms was done using spherical modeling (γ^* =gamma function; r =range). The mean and variance are given in square-root units.

HIGH RESOLUTION SEISMIC IMAGING OF FRACTURED ROCK

Ernest Majer
Larry Myer
John Peterson

Earth Sciences Division, Lawrence Berkeley Laboratory
University of California, Berkeley, California 94720

I. INTRODUCTION

From 1987 through 1989 the U. S. Department of Energy (DOE) participated in an agreement with the Swiss National Cooperative for the Storage of Radioactive Waste (Nagra) to perform joint research on various topics related to geologic storage of nuclear waste. As part of this Nagra-DOE Cooperative (NDC-I) project Lawrence Berkeley Laboratory (LBL) participated in several projects at an underground research facility in fractured granite in Switzerland (Grimsel) which were directed towards improving the understanding of the role of fractures in the isolation of nuclear waste. Described here are the results of a series of experiments at Grimsel called the Fracture Research Investigation (FRI). The FRI project was designed to address the effects of fractures on the propagation of seismic waves and the relationship of these effects to the hydrologic behavior. The fundamental design of the project was to find a simple, well defined, accessible fracture zone surrounded by relatively unfractured rock and use this zone as a point of comparison for seismic, hydrologic and mechanical behavior. The FRI site was designated in the Grimsel Rock Laboratory for this purpose and field work was carried out during each year of the three year NDC-I project (1987-1989). The FRI project has involved separate and simultaneous, detailed geologic studies, field measurements of seismic wave propagation, geomechanical measurements of fracture properties, and the hydrologic response of the fractured rock.

Laboratory measurements of core have also been carried out to address the fundamental nature of seismic wave propagation in fractured rock. Because all these studies were focussed on the same fracture zone, the study provided insight into new theories of seismic wave propagation through fractures, how changes in the fracture properties affect seismic wave propagation, interpretation of seismic tomography to identify hydrologic features, and integration of seismic data into a hydrologic testing plan.

II. SEISMIC IMAGING EXPERIMENTS

The FRI experiment offered an excellent opportunity to perform calibrated experiments in a rock mass where the fracture locations and characteristics are relatively well known. An advantage of the FRI site was that there is access to the fracture zone from all four sides which allowed a comparison of techniques between two-, three-, and four-sided tomography. The greatest attraction, however, was the opportunity to evaluate theories of wave propagation in fractured media and to evaluate these theories at several different scales. For example, Pyrak *et al.*, (1990a) have performed laboratory experiments which have confirmed the effect of fracture stiffness at small scales. The scaling of this phenomenon to larger distances is yet unknown. Therefore, one of the main objectives of the FRI experiments was to observe the effect of individual fractures as well as a fracture zone on the propagation of seismic waves. A second objective was to relate the seismic response to the hydrologic behavior of the fractures, i.e., do all fractures effect the seismic wave, or do just fluid filled, or partially saturated fractures effect the seismic waves in a measurable amount. The final objective of the study was to assess the amount of seismic data necessary to provide useful information, and how one would process data for the maximum information in a routine fashion. These are important questions when one progresses to the point of applying these techniques to actual field sites.

A. FRI Zone Experimental Procedure

Shown in Figure 1 is a map showing the FRI zone in the plane of boreholes BOFR 87.001 and BOFR 87.002. As shown in this figure, there is a common shear feature crossing the FRI zone. The boreholes were drilled to intersect this fracture zone as shown in Figure 1. Three

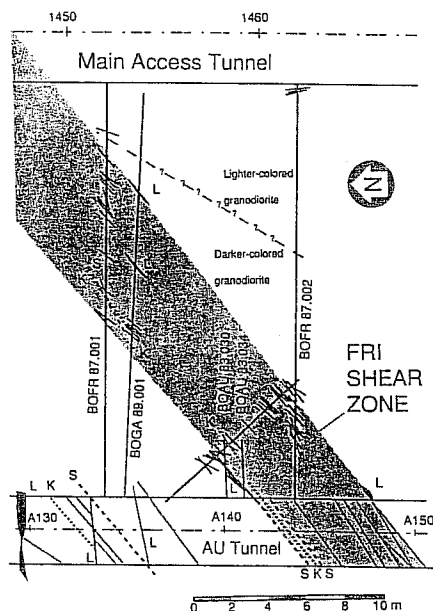


Figure 1. A plan view of the layout of the experimental area used in this study. The area is 10 meters by 21 meters.

long boreholes were drilled through the FRI zone for seismic investigations. Boreholes BOFR 87.001 and BOFR 87.002 are 86 mm diameter, 21.5 m long holes that were drilled from the AU tunnel to the access tunnel to provide a means of performing crosshole seismic work, core of the fracture zone, measuring fracture response in-situ, and for carrying out hydrologic experiments. Borehole BOFR 87.003 is a 127 mm diameter, 9 m long hole drilled through the fracture zone for obtaining large core for laboratory analysis and also for hydrologic testing. In addition to these holes, 76, 74 mm diameter, 50 cm long holes were drilled into the AU and access tunnel walls between boreholes BOFR 87.001 and BOFR 87.002 at 0.25 meter spacing to allow the placement of the seismic sources and receivers.

For the collection of the data piezoelectric seismic sources were placed in the holes (boreholes BOFR 87.001, BOFR 87.002, and the shallow holes in the sides of the tunnel) and activated. The data from a clamped three component accelerometer package was recorded at 0.5 meter spacing in boreholes BOFR 87.001 and BOFR 87.002. The receiver package was also placed in the shallow (.25 m spacing) holes to give complete four sided coverage. In the 1987 studies the source and three component receiver package were clamped to the bore hole wall to provide good seismic coupling. For the acquisition of 1987 cross well

data, the source was in a dry hole and the receiver was in a fluid filled hole. In the 1988 studies, both boreholes were filled with fluid. Thus, the fluid in the borehole provided improved coupling between the source and the rock. We found that fluid coupling was more efficient than mechanical coupling and also allowed for faster data acquisition. The data were recorded on an in-field PC-based acquisition system. Four channels of data were acquired, the x, y, and z receivers and the "trigger" signal. The sample rate was 50,000 samples/sec on each channel with 20 milliseconds of data being recorded for each channel in the 1987 experiments and 250,000 samples/second in the 1988 data. Typical travel times were less than 5 milliseconds for the P-wave and 10 milliseconds for the shear wave. Seismograms were acquired from nearly 60,000 ray paths (X, Y, and Z components) in the FRI zone, at distances from 1/2 meter to nearly 23 m. The peak energy transmitted in the rock was at frequencies from 5,000 to 10,000 Hz, yielding a wavelength of approximately 1 to 0.5 meter in the 5.0 km/sec velocity rock.

B. Data Processing Sequence

The travel times were picked manually using an interactive picking routine developed at LBL. The times were picked on the radial component (component 3), which is in the direction of strongest P-wave motion. This was confirmed by rotating the data into the P-, SV- and SH-directions. Due to field equipment modifications the data quality was improved from 1987 to 1988. After the travel times have been picked, they were initially checked by plotting a time-distance curve, a velocity-distance curve, and a velocity vs. incidence angle curve. Any large variation from the general trend would indicate picking errors or acquisition problems. The most obvious deviating sweeps were removed entirely from the data used to perform the inversion. The removal of these data had little effect on the major features in resultant image. No additional travel time corrections were necessary in either the 1987 or 1988 data, and few of the signals were too noisy or did not have sufficient amplitude to pick times accurately.

The travel times were inverted using a simple algebraic reconstruction technique (ART) (Peterson, 1986). A 44 x 88 array of pixels was chosen for the tomographic inversion. This produces a pixel size of 0.25 m which is the size of the smallest anomaly we can expect to see given the wavelength of 0.7 m and station spacing of 0.5 m. Our previous experience has shown that for this geometry a pixel size of half the sta-

tion spacing gives the optimal combination of resolution and inversion stability.

An image was produced using the entire 1987 data set, all four sides.

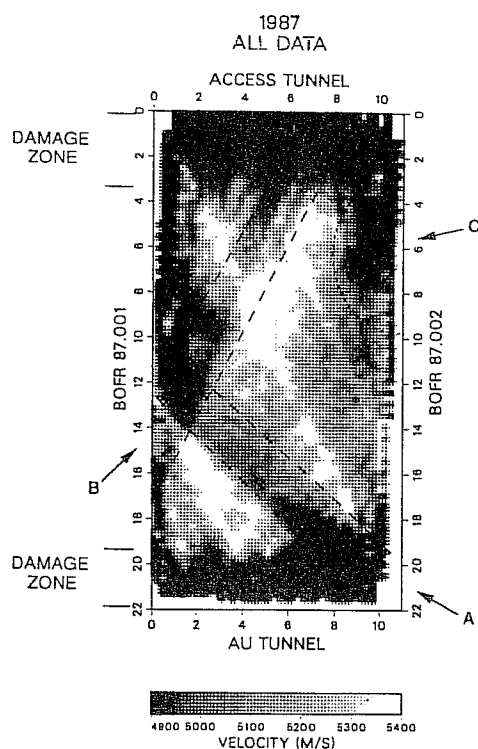


Figure 2. The final result of inverting all the good data from the 1987 tests.

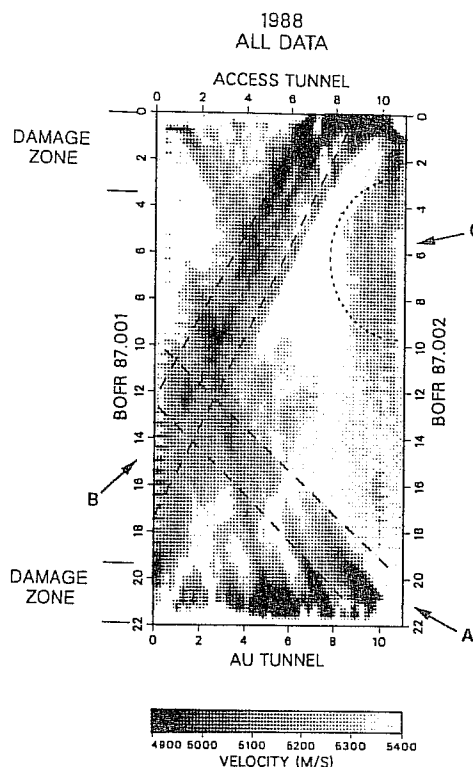


Figure 3. The final result of inverting all of the good data from the 1988 tests. No anisotropic corrections, all poor data ray paths deleted.

This image can be compared to the 1988 results (Figure 3) using the same velocity intervals and same number of rays (4.9 km/s to 5.4 km/s). The main features identified in the 1987 results (Figure 2) are the low velocity zones adjacent to the tunnels, assumed to be damaged zones, and a low velocity zone (Feature A) extending from the middle of borehole BOFR 87.001 to the AU tunnel/borehole BOFR 87.002 intersection, and two other low velocity zones (B and C in Figure 2).

The 1988 image has many differences from the 1987 results. The main differences are:

1. There is little evidence of the extensive 1987 damaged zones near the tunnels in the 1988 results. Also, the average velocity values in the entire 1988 field (5.2 km/s) are higher than the average velocities in the 1987 field (4.9 km/s).
2. The prominent feature (Feature A, Figure 2) is observed in 1987 results as a single strong low velocity zone about 2 m wide. The corresponding zone in the 1988 results, Figure 3, consists of two or three very thin (< 0.5 m thick) zones which become discontinuous at about 4 or 5 m from the laboratory tunnel and are located in a different orientation and place. Also, Feature C is not as pronounced in the 1988 results as in the 1987 results.
3. There appears to be an additional structure, Feature B, in the 1988 image which was masked by the low velocity zone on the center-north edges of the 1987 result. This feature in the 1988 results extends from near the access tunnel/BOFR 87.002 intersection, to the middle of BOFR 87.001, and is, in fact, the dominant feature of the 1988 results. Evidence of this feature exists in the 1987 data, but is obscured by a low velocity feature on the east side of the tomogram.

The discrepancies between the two images seem severe and will be discussed in detail later. These differences between 1987 and 1988 results were very significant. The 1988 hydrologic testing program was based on the results of the 1987 tomogram. Features A and C were the target of these tests and Feature B had not yet been identified as a major feature. Therefore we were very interested in the appearance of Feature B and its hydrologic significance.

C. Anisotropy Corrections

There is a strong foliation in the Grimsel granodiorite which suggests that the rock may be highly anisotropic with respect to wave propagation. An obvious step was to correct for this anisotropy in order to improve the image.

In general, the P wave anisotropy may be approximately represented as

$$V_p^2 = A + B\sin(2\phi) + C\cos(2\phi) + D\sin(4\phi) + E\cos(4\phi) \quad (1)$$

where ϕ is the angle of direction of propagation. A function of this form is fitted to the data. The coefficients A, B, C, D and E represent the strength of the anisotropy. These values may be determined in the laboratory or in the field. The laboratory values are difficult to determine and may not adequately represent the in-situ anisotropy. In the field, the same travel times gathered for the tomographic survey may be used to determine the coefficients or a separate test may be set up in a more homogeneous (though not differing in anisotropy) area.

The anisotropy coefficients calculated from the 1987 and 1988 cross well data show rock matrix anisotropy in the direction of the foliation. Table 1 shows these values are slightly different.

Table 1. Anisotropy coefficients

coef	A	B	C	D	E
1987	26.211	0.544	-1.122	-0.331	-0.185
1988	27.942	1.375	-0.633	-0.309	-0.196

Although it is not likely that the background anisotropy changed from 1987 to 1988, the anisotropy was removed from each data set using their respective correction coefficients. In each case the contribution of the anisotropy was calculated and removed from the observed travel times. This was done by calculating the difference between the travel times calculated with coefficients A-E and the travel time calculated with only coefficient A, and then subtracting this value from the measured travel time.

The travel times corrected for anisotropy were inverted in the same fashion as the uncorrected data. The effect of the anisotropy corrections on the 1987 results (Figure 4) change the magnitude of the anomaly corresponding to the shear zone. The corrections also cause the amplitude of the anomaly to vary along the strike of the main fracture zone. Also, smaller zones within the large low velocity feature adjacent to borehole BOFR 87.001 are more resolved and coincide with similar features in the 1988 result.

The result of applying the correction to the 1988 data is shown in Figure 5. The uncorrected image has been smoothed with the low velocity zones more distinct. The inversion also appears to remove some artifacts

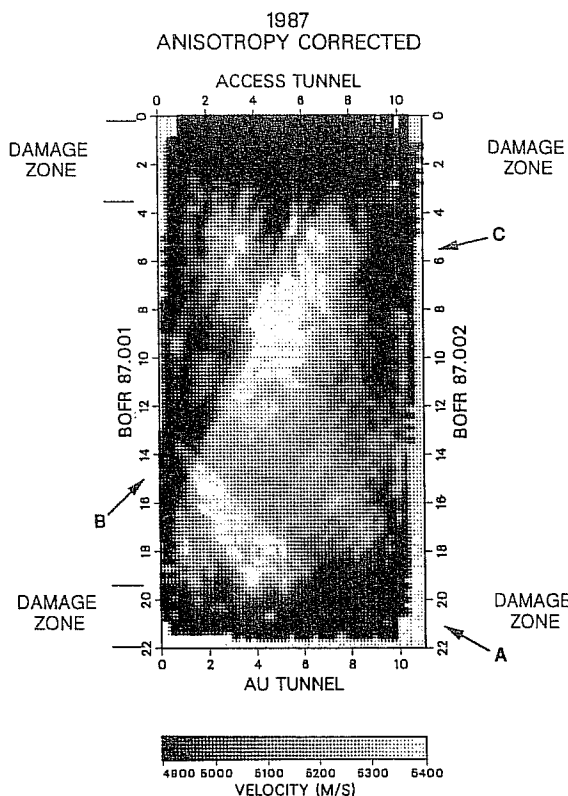


Figure 4. The final 1987 inversion after correcting for anisotropy.

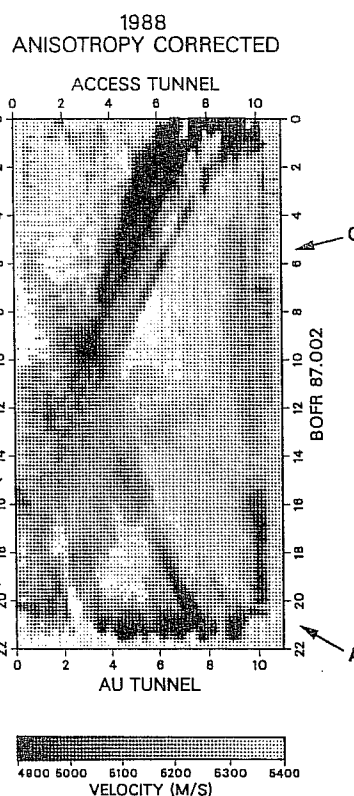


Figure 5. The final 1988 inversion after correcting for anisotropy. The "unusual" rayshave been deleted.

that are produced in the original inversion. The smearing seen to the upper left of Figure 3 is reduced, as is the effect of a strong, thin low velocity feature extending from the middle of the laboratory tunnel to the center of BOFR 87.001. The "secondary" features which parallel the main low velocity zone (Feature A) in Figure 3 are also greatly reduced leaving a single zone whose intersection with the laboratory tunnel coincides with the large fracture observed on the wall of the AU tunnel.

D. Discussion of Results

Although not immediately obvious, after anisotropy corrections, the 1987 and the 1988 results show essentially the same features. We will first discuss how the two results compare, then analyze the best image in terms of what is known of the geology in the FRI site.

An obvious difference between the two results is the disappearance of the low velocity features near the tunnels in 1988 results (Figures 4 and 5). As previously stated, the data quality was much better in 1988 than 1987 for several reasons. The source was more powerful and its repeatability improved. Also, when the source and/or receiver were in BOFR 87.001 and BOFR 87.002 the coupling was improved over 1988 because both holes were water filled. We also stacked from 2 to 9 traces for each source receiver pair. These improvements increased the signal to noise ratio providing much more accurate travel time picks on higher frequency first arrivals. In effect, the reduced data quality in 1987 prevented the "proper" first arrival travel times to be picked in 1987. In some cases the value picked was a pulse or two later than the time picked in 1988. This is especially true where the attenuation is greater, e.g., the damaged zones adjacent to the tunnel and in the main shear zone. The entire 1987 travel time data for sources or receivers along the tunnels are probably picked consistently late, producing a velocity reconstruction which shows consistently lower velocities near the tunnels and resulting in a lower average velocity. This means that the 1987 tomogram was essentially a mixed velocity-attenuation tomogram.

Another difference in the results is that the shear zone (Feature A, Figures 4 and 5) becomes discontinuous and less dominant in 1988. This result is of great interest because this is the zone that we were initially trying to image. Also, Feature C is less obvious in the 1988 results, again a target of the hydrologic tests. In 1987, we had assumed that we had imaged Feature A satisfactorily as a several meter wide low velocity zone. However, the 1988 inversion does not show such an extensive feature, but a thinner zone which extends to about 4 m from the laboratory tunnel. The zone dies out for a meter, then reoccurs as a more massive feature with variable velocity. To show the actual difference in the results, the 1988 image is subtracted from the 1987 image pixel by pixel (Figure 6). (An inversion using the differences in travel times could not be performed because slightly different stations were used for a few of the sweeps). As can be seen from Figure 6, there is little difference between the two images except at the tunnels, suggesting that the 1987 low velocity zone in the region of the shear zone and Feature C exists in the 1988 result, but has a slightly different form and magnitude.

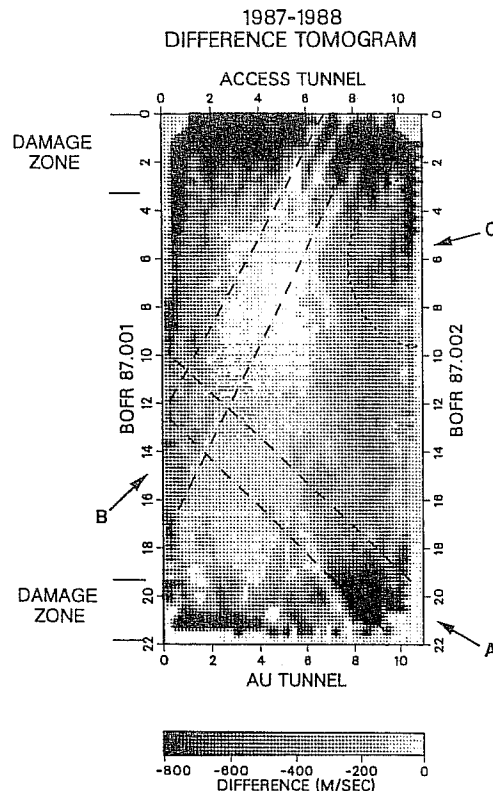


Figure 6. Difference between the 1988 and 1987 tomograms after anisotropy corrections.

Both 1987 and 1988 images show a lower velocity near the intersection of the AU tunnel and the shear zone where the excavation of the tunnel may have “loosened” the fractures. The large low velocity features toward borehole BOFR 87.001 on strike with the shear zone are also comparably imaged in the 1987 and 1988 results.

The most unexpected result from the 1988 inversion is the dominance of the low velocity feature (Feature B), which extends from the intersection of the access tunnel and BOFR 87.002 intersection to the large low velocity feature near BOFR 87.001. As mentioned earlier extensive efforts through careful examination of the data were made to determine whether this is an actual zone of low velocity material or an artifact of the inversion process or some kind of error. The 1987 result does show a hint of this feature protruding from the large low velocity zone adjacent to the access tunnel. However, in the 1987 results it is not a dominant continuous feature and is obscured by the extensive damaged zone.

Checking the plots of the difference between the 1987 and 1988 data, Figure 6, we see again that the difference is not significant. This indicates that the anomaly actually exists in the 1987 results, but it is overshadowed by the effect of the damaged zones. There is always the possibility that errors occurred in both years for several of the sweeps whose source was in this region, but this is unlikely. However, if these sweeps were removed from the data, the region of interest would not be fully sampled and the anomaly would not be adequately resolved.

E. Geologic Interpretation of the Results

The geologic map of the structures at FRI is shown next to the "final" 1988 tomographic image to assist in the interpretation (Figure 7). To be useful the interpretation of the tomographic images must include the geologic structure that is associated with each of the main features that are imaged and an explanation for the differences between the results of the 1987 and 1988 experiments. These include:

1. The large low velocity anomalies observed along the tunnels in the 1987 image which do not exist in the 1988 result.

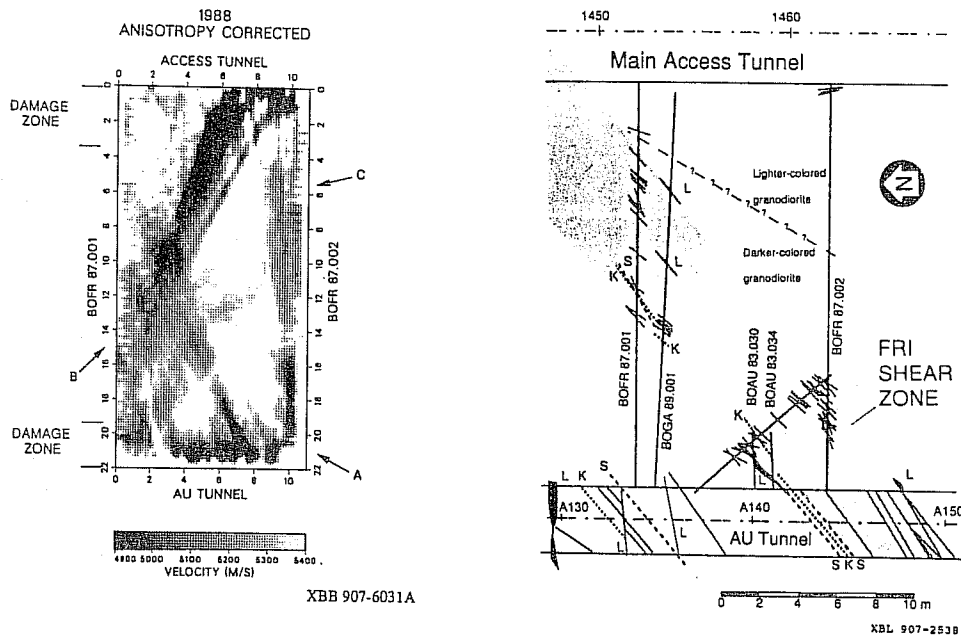


Figure 7. (a) The velocity tomogram for 1988 compared to (b) the geologic map of the FRI site.

2. The shear zone (Feature A) is observed in 1987 as a single large low velocity zone about two meters wide. The corresponding zone in the 1988 results consists of a very thin (< 0.5 m thick) zone which become discontinuous.
3. Feature B, which extends from near the access tunnel BOFR 87.002 intersection, to the middle of BOFR 87.001, and is, in fact, the dominant feature of the 1988 results.
4. Two strong low velocity features at the intersection of Feature B and the shear zone.

We have already mentioned that the low velocity zones associated with the tunnels in the 1987 results may be due to the initial P-wave pulse being highly attenuated. This was primarily due to a weaker source being used in the 1987 experiment. However, this does not explain why the 1988 velocity data did not resolve the damage zones, i.e., if there are damage zones with high fracture content, why did we not detect them in the 1988 velocity data. It is true that one explanation may be that the 1987 result only detected the damage zone by picking later arrivals because the initial pulse was attenuated, not slowed, and thus an artificially low velocity result was obtained. The attenuation data from 1988, however, did detect the damage zones near the tunnels. This suggests that at the frequencies we used, 5 to 10 KHz, the effect of these thin fractures on the velocity was much less than that on attenuation. This is in fact what the "stiffness" theory predicts. As frequency increases, for a constant stiffness, the velocity or delay becomes less relative to the attenuation effect. Apparently we were at frequencies where for the stiffnesses involved, attenuation is important and delay is less important.

In the final 1988 tomogram, the shear zone appears to produce a relatively weak velocity anomaly. The zone appears as expected from the 1987 results, but its form is altered in 1988. Although there is a visual difference, the actual differences are not great and may be due to the better resolution obtained in 1988. The 1988 results indicate that it is likely that the zone is not a simple single planar feature and thus the permeability along the zone may also be variable rather than being a single well connected feature. Figure 7 indicates that the shear zone produces a large velocity anomaly near the AU tunnel wall, until the point where this anomaly intersects a lamprophyre at about 4 m from the AU tunnel wall along the strike of the shear zone. The intersections of lamprophyres and shear zones are areas of more intense fracturing, probably causing larger velocity anomalies. This lamprophyre is probably discontinuous, being stretched along the shear zone during deformation. After this velocity anomaly dies out, another small low velocity anomaly is encountered at about

2 m further along strike of the shear zone. This anomaly may be another piece of lamprophyre or a region of high fracturing.

The most dominant feature in Figure 7 is Feature B, which extends from a highly fractured area in the access tunnel to the shear zone. It is unlikely that the anomaly is totally an artifact of the inversion or due to data errors since it occurs in the results from both years. The anomaly may not actually extend to the shear zone, but may be smeared somewhat in this direction. The visible fractured area at the access tunnel where the anomaly begins consists of subhorizontal fractures and a tension fissure.

From geologic considerations, it is most likely that this feature is associated with a lamprophyre or an especially large tension fissure. The strike is different from the lamprophyres in the immediate area, but as noted in the geology section, lamprophyres are not consistent in their behavior, especially when associated with shear zones. Since the geologic information about this feature is sparse, the only way to validate its presence is to drill into it. A subsequent borehole (BOGA 89.001) was drilled parallel to BOFR 87.001, but unfortunately it was several meters away from the anomaly and could not validate the prediction.

Where Feature B intersects the shear zone, Feature A, two large anomalies are also observed. These anomalies may be areas of intense fracturing, most likely due to lamprophyres intersecting the shear zone. A small lamprophyre was logged in borehole BOGA 89.001 which coincides exactly with one of these anomalies. The other anomaly coincides with a kakirite zone which also indicates a region of increased fracturing. These anomalies also suggest that there may be hydrologic communication across the shear zone in this region.

Except for Feature B, all the anomalous velocity zones are coincident with geologic structures. Feature C is still not verified, but the core suggests a different rock type, lighter colored granite, rather than fracturing may be the cause of this feature. Although the core from this region were not tested, the testing of the other core from the FRI zone suggested that the lighter colored granite has lower velocity than the more altered darker colored granite. The two low velocity anomalies near borehole BOFR 87.001 were interpreted as zones of intense fracturing likely due to the presence of lamprophyres. Borehole BOGA 89.001 was drilled, and validated this interpretation. Though the geologic information determined the possibility of such fractured regions, these anomalies could not be located by geologic data alone. It is always possible that feature B could be an artifact caused by some data error. However, there is no basis on which to reject its existence since it is observed in both the 1987 and 1988 results. Direct examination leaves little doubt that there is some anomalous zone

that exists near the tunnel wall, probably a tension fissure.

III. IN-SITU GEOMECHANICAL MEASUREMENTS

In addition to the tomographic measurements, another test referred to as the inflation test was performed. The objectives of the inflation test were to determine the mechanical stiffness of the kakarite fracture and one to evaluate the effects of hydraulically pressurizing the fracture on its seismic response. To perform this test instrumentation was configured as shown in Figure 8. Bofex instrumentation was used to measure fracture displacements during pressurization in boreholes BO87.001 and BO87.003 across the main fracture zone. The linkage between the anchors is decoupled from the packers to prevent contamination of displacement measurements by deformation of the packer system. Displacement resolution was 0.6μ .

The locations of the seismic transmitter and receiver are indicated by T and R, respectively in Figure 8. During the first 45 hours of the testing the transmitter and receiver were held stationary at one location (R_1 and T_1 in Figure 8). The transmitter and receiver were then moved to locations R_2 and T_2 for the remainder of the testing.

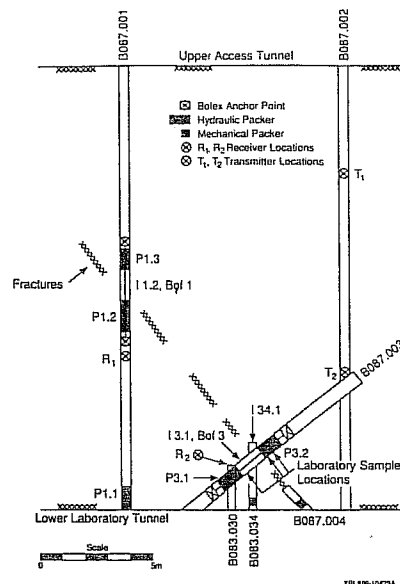


Figure 8. Plan view showing instrumentation locations for inflation test.

Measurements were made over the course of six days. For the first 45 hours the fracture was pressurized in interval I1.2 in BO87.001 while the water pressure was monitored in interval I3.1. Displacements across the fracture were monitored continuously during this time and seismic measurements were made periodically at locations R_1 and T_1 . At 48 hours, in order to pressurize a larger portion of the area of the fracture, the pressure was made equal in both I1.2 and I3.1. Periodic seismic measurements were made with the receiver and transmitter in positions R_2 and T_2 respectively. After both intervals were depressurized displacements were monitored and seismic measurements were periodically made until the testing was concluded after 115 hours.

A. Analysis of Deformation Measurements

The displacement of the kakarite fracture in response to fluid pressurization was measured in order to determine the stiffness of the fracture. Fracture stiffness is given by the ratio of incremental stress to incremental displacement, when in concept, the displacement can be equated to the change in volume of voids in the plane of the fracture. Since the hydrologic properties of a fracture are closely related to the void geometry, fracture stiffness is an important parameter in the evaluation of the fracture fluid flow properties (Witherspoon *et al.*, 1980). Studies e.g. Majer *et al.*, 1988, have also shown that fracture stiffness affects both the velocity and attenuation of propagating seismic waves. Schoenberg, 1980 and Pyrak-Nolte *et al.*, 1990b developed explicit relationships between the stiffness of a single fracture and the group time delay and amplitude of a wave transmitted across it.

Displacements measured in BO87.001 increased steadily with time after interval I1.2 was initially pressurized to 19 bars, and more rapidly when the interval was pressurized to 36 bars. During this time negligible displacement was measured in BO87.003. The time dependent nature of the displacements meant that the fluid pressure in the fracture was increasing over an ever increasing area of the fracture.

Since fluid pressures were not uniform, it was necessary to assume a model for the fracture void geometry in order to calculate stiffness. As a first approximation the fracture was represented by a row of co-planar cracks of equal length, $2c$, and uniform spacing, $2b$, subjected to a pressure distribution as shown in Figure 9. In this model the ligaments of material between cracks represent the areas of contact in the fracture and the cracks represent the void space. The pressure distribution was approximated by a linear distribution with a maximum value of 19 bars at a

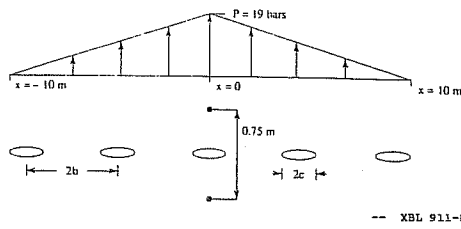


Figure 9. Model of fracture as co-planar parallel cracks. Pressure varying linearly with distance was applied internally to cracks.

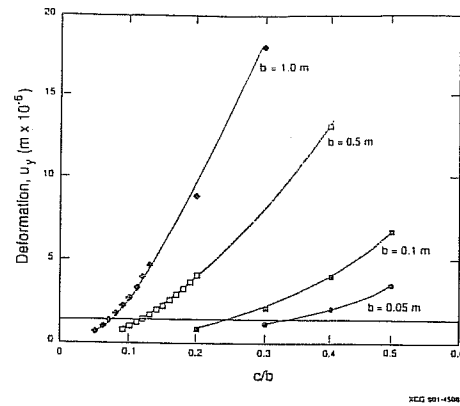


Figure 10. Displacements between two points located 0.75 m either side of the midpoint of the center crack of a row of pressurized co-planar cracks. Horizontal line corresponds to in-situ measurement (after Hesler *et al.*, 1990).

location $x = 0$ and a value of 1.9 bars at $x = \pm 10$ m. Calculations were carried out for different values of crack lengths and spacing to match the observed maximum fracture displacement measured in BOFR 87.001 under 19 bars of pressure (Hesler *et al.*, 1990). Results are shown in Figure 10. Displacements were calculated at a location of 0.75 m on either side of the row of cracks to coincide with the location of the Bofex anchors relative to the fracture. Figure 10 shows that for any given crack size large spacings are required to match the observed displacement of 1.4×10^{-6} m. These results suggested a contact area in the fracture on the order of 60%.

Having determined a range of crack sizes and spacings for the idealized model, the stiffness of the fracture could be estimated analytically. Using solutions from fracture mechanics, for a row of co-planar cracks the average displacement, $\bar{\delta}$, is given by:

$$\bar{\delta} = \frac{-8\sigma b(1-\nu^2) [\ln \cos(\pi c/2b)]}{\pi E} \quad (2)$$

where σ is the far field stress and ν and E are Poisson's Ratio and Young's modulus, respectively. Since, by definition, stiffness, κ , is related to $\bar{\delta}$ by:

$$1/\kappa = \bar{\delta}/\sigma,$$

the stiffness of a row of co-planar cracks is given by:

$$1/\kappa = \frac{-8b(1-\nu^2)[\ln \cos(\pi c/2b)]}{\pi E} \quad (3)$$

Using equation 3 and values of c and b from Figure 10, values of κ were calculated which ranged from 2×10^{11} Pa/m to 3×10^{11} Pa/m. These values are about one half to one order of magnitude less than those obtained in laboratory tests on a natural fracture from the FRI study area, but direct comparison is not possible since the laboratory specimen was not from the kakirite fracture and did not contain gouge material.

The effect of a single fracture with a stiffness of 3×10^{11} Pa/m on seismic wave propagation can be evaluated using the seismic displacement discontinuity model described by Pyrak-Nolte *et al.*, 1990b. Figure 11 is a plot of the magnitude of the transmission coefficient, $|T|$ and normalized group time delay, t_g/t_{g0} , for a wave normally incident upon a fracture. Values of $[\omega/\kappa/Z]$ were calculated for $\kappa = 3 \times 10^{11}$ Pa/m, $z = 1.4 \times 10^7$ kg/m²s, and ω corresponding to the center frequency of the P-waves in the tomographic survey. For the 1987 survey this frequency was about 6 kHz while for the 1988 survey it was about 10 kHz. In Figure 11 the corresponding values of $|T|$ and t_g/t_{g0} are plotted as circles for the 1987 survey and squares for the 1988 survey.

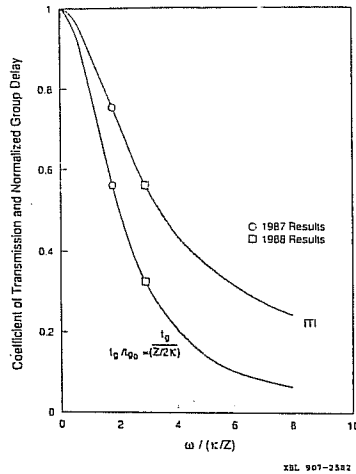


Figure 11. Magnitude of the transmission coefficient and normalized group delay for a seismic wave normally incident upon a displacement discontinuity as a function of normalized frequency.

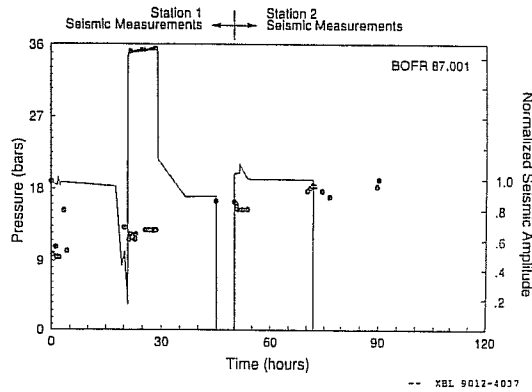


Figure 12. Normalized seismic amplitudes obtained at two stations superimposed on pressure history of interval I1.2.

For a 6 kHz wave normally incident on a fracture with stiffness of 3×10^{11} Pa/m the value of $|T|$ is seen to be about 0.75, while for a 10 kHz wave it is about 0.56. A value of $|T| = 0.75$ means that, a wave propagated across the fracture would have an amplitude about 25% lower than one propagating over the same path length of intact rock. Because of the higher frequency used in the 1988 survey, the amplitude reduction (i.e. $|T| = .56$) is predicted to be greater. From Figure 11 it is seen that the value of t_g/t_{go} for the 1987 survey was about 0.55 while for the 1988 survey it was about 0.31. This means that the delay in measured travel time caused by the fracture is predicted to be less for the 1988 survey run with the higher frequency source. This may explain in part why the fracture was less distinct in the 1988 tomogram.

Finally Figure 12 presents the results of the seismic measurements made periodically during the test. Amplitudes were normalized to the maximum P-wave amplitude measurement obtained while the source and receiver were held stationary. For position 1 (T_1 and R_1 in Figure 8) the maximum amplitude was just prior to pressurization of the interval I1.2. Almost immediately following pressurization the amplitudes dropped by over 40%. Thereafter, amplitudes generally increased over the course of the experiment, without any obvious correlation to the pressure history observed in intervals I1.2 and I3.1. At position 2 the smallest amplitudes were again at the time of pressurization. Amplitudes then increased with the maximum occurring after depressurization of the test intervals. If all other factors are constant and assuming elastic behavior, increasing the fluid pressure in a fracture results in a decrease in contact area and hence a reduction in stiffness and a concomitant decrease in the amplitude of the transmitted wave. This could explain the decrease in amplitude at stations 1 and 2 after pressurization. The fracture displacement which would produce this change in stiffness was not observed. This may be because the seismic wave received at either station sampled only a small portion of the fracture plane, so the observed changes do not reflect the average deformation of the entire area pressurized. The increase in amplitudes following pressurization can be explained if the fracture and/or the rock adjacent to the fracture were not fully saturated prior to pressurization. If a fracture is envisioned as a collection of co-planar thin cracks, the stiffness of the fracture will increase as more of the cracks are filled with water. This increase in stiffness, according to the displacement discontinuity model will lead to an increase in transmitted P-wave amplitudes. Such an increase in amplitudes upon saturation has been observed by Pyrak-Nolte I. et al., 1990b in laboratory tests on granite specimens containing a single natural fracture. Saturation of intact specimens of the schistose rock from the FRI area also resulted in increased amplitudes of

the transmitted P-waves (Majer *et al.*, 1990).

IV. CONCLUSIONS

Overall, the tomographic inversions seem to successfully image the major structures in the test region. At the frequencies used, the tomograms do not successfully image the minor structures such as individual fractures. The main conclusions from these tests are:

1. The velocity anomalies observed associated with fracturing were not due to single fractures but groups of fractures.
2. The seismically important features associated with fracturing were fracture intersections and fracture-lamprophyre intersections. These are also the structures that should be hydrologically important.
3. An interpretation of the results can not be done adequately without knowledge of the geology.
4. Structures were resolved that could not be anticipated from the borehole and tunnel data.
5. Although shear wave data were sparse, it is obvious that given the proper source, S-wave data would greatly aid in the interpretation of the geologic features.
6. A method for obtaining in-situ fracture displacements for estimating fracture stiffness was successfully demonstrated.
7. The seismic visibility of the features from the amplitude and velocity tomograms seem to support the displacement discontinuity theory which relates these seismic properties to fracture stiffness.

ACKNOWLEDGEMENTS

This work was supported through U.S. Department of Energy Contract No. DE-AC03-76SF00098 by the DOE Office of Civilian Radioactive Waste Management, Office of Geologic Repositories. We also want to thank the personnel at NAGRA and the Grimsel Rock Laboratory for their help and support, in particular Piet Zuidema and Gerdt Sattel, as well as Eric Wyss of SOLEXPerts AG.

REFERENCES

- Hesler, G.J., Zheng, Z. and Myer, L.R. (1990). "In-situ fracture stiffness determination," in *Rock Mechanics Contributions and Challenges*, Proceedings of 31st U.S. U.S. Rock Mechanics Symposium, A.A. Balkema 405-412.
- Majer, E.L., McEvilly, T.V., Eastwood, F.S. and Myer, L.R. (1988). "Fracture detections using P- and S-wave vertical seismic profiling at the Geysers," *Geophysics* 53 No.1, 76-84.
- Majer, E.L., Myer, L.R., Peterson, J., Karasaki, K., Long, J.C., Martel, S., Blumling, P., and Vomvoris, S. (1990). *Joint Seismic, Hydrogeological, and Geomechanical Investigations of a Fracture Zone in the Grimsel Rock Laboratory, Switzerland, NDC-14, LBL-27913*, Lawrence Berkeley Laboratory, Berkeley, California, 173 pgs.
- Pyrak-Nolte, L.J., Myer, L.R., and Cook, N.G.W. (1990a). "Anisotropy in seismic velocities and amplitudes from multiple parallel fractures," *Journal of Geophysical Research* 95 No. B7, 11345-11358.
- Pyrak-Nolte, L.J., Myer, L.R., and Cook, N.G.W. (1990b). "Transmission of seismic waves across single fractures," *Journal of Geophysical Research* 95 No. B6, 8617-8638.
- Schoenberg, M. (1980). "Elastic wave behavior across linear slip interfaces" *Journal of the Acoustical Society of America* 68 No. 5, 1516-1521.
- Witherspoon, P.A., Wang, J.S.Y., Iwai, K. and Gale, J.E. (1980). "Validity of cubic law for fluid flow in a deformable rock fracture," *Water Resources* 16, 1016.

**Natural Gas Reserve Replacement through Infield
Reserve Growth: An Example from Stratton Field,
Onshore Texas Gulf Coast Basin¹**

Raymond A. Levey²
Mark A. Sippel³
Richard P. Langford²
Robert J. Finley²

² Bureau of Economic Geology, The University of Texas at Austin.

³ Research Engineering Consultants, Englewood, Colorado.

The major objective of a joint venture sponsored by the Gas Research Institute (GRI), the U.S. Department of Energy (DOE), and the State of Texas is to assess the distribution of incremental natural gas resources in conventional reservoirs within mature fields. Analysis of publicly available production data for a 50-year-old gas field indicates reserves may be effectively replaced with additional infield wells and recompletions within a mature gas field containing reservoirs that have conventional porosity (>15%) and permeability (>10 md). Historical evaluation of decline curves and cumulative production from 1979 through 1989 to quantify reserve growth within a field that has undergone a successful infield drilling program indicates that replacement of gas reserves approaching 50 Bcf is both technically and economically viable. The spacing of wellbore penetrations in the study area was less than 25 acres per wellbore across all reservoirs to an average completion depth of approximately 6,400 ft at the end of 1989.

¹ Funded by the Gas Research Institute contract no. 5088-212-1718, the U.S. Department of Energy contract no. DE-FG21-88MC25031, and the State of Texas through the Bureau of Economic Geology. The cooperation of Union Pacific Resources Company is gratefully acknowledged. Publication authorized by the Director, Bureau of Economic Geology, The University of Texas at Austin.

Control of depositional system on the reservoir geometry is a major factor related to the magnitude of incremental gas resource that may be accessed through additional infield completions. Analysis of produced and projected gas resources at less than 7,000 ft deep from a lease block within Stratton field of the Frio fluvial-deltaic play along the Vicksburg fault zone illustrates the impact of new infield drilling and recompletions within established wellbores in the onshore Texas Gulf Coast Basin. Gas reserve additions between 1979 and 1990 exceeded 13% of the developed extrapolated ultimate recovery at the end of 1989.

Stratton field, discovered in 1937 (fig. 1), is 1 of 29 multireservoir fields containing major gas resources in the Frio fluvial-deltaic play associated with the Vicksburg fault zone (Kosters *et al.*, 1984). Stratton field is an excellent candidate for detailed analysis because (1) it has a long development and production history exceeding 50 years, (2) an aggressive infield drilling and recompletion program during the late 1980's provides a strong basis for using a historical approach to resource assessment, and (3) the resulting development of the gas cap has provided a densely drilled area that is not commonly available in other Frio fluvial-deltaic fields.

Gas production data from the annual reports of the Railroad Commission of Texas indicate that more than 300 gas reservoirs have been defined in Stratton field from the initial field discovery in 1937 through continued development and production in 1989. Detailed well log stratigraphic correlations across Stratton field indicate this number of reservoirs is relatively high because of difficulties in correlation and variations in reporting practices for reservoir designations. Figure 2 shows a plot of depth versus discovery year from 1940 to 1989. Fieldwide cumulative production analysis is based on records of annual production for Stratton field from 1950 through 1989 (fig. 3). The primary development of middle Frio fluvial reservoirs took place from 1950 to 1968, and during this period reservoir pressure was partly supported by gas cycling to produce associated oil. Annual production peaked at >90 Bcf in 1973 from production of the prolific E41 and F11 reservoirs of the Stratton field gas cap. From 1974 to 1986 production declined substantially. The reversal in production decline from 1986 through 1989 is a function of recent infield drilling and recompletions of previous wells in the field.

This analysis will examine the number of completions and reserve estimates at two times in the history of Stratton field. In addition, the reserves will be addressed in two depth categories: those reserves shallower than 7,000 ft and those deeper than 7,000 ft. The timeframe utilized in this analysis compares completion history and gas reserves based on all completions in January 1979 to the same completions and additional completions from infield drilling after 1978 to January 1990.

An evaluation of secondary gas (incremental) reserve growth is indicated by assessment of the historical changes in gas reserves for a contiguous part of Stratton field (~7,400 acres) referred to as the study area (fig. 4). Figure 5 is a histogram of the number of completions made before January 1979 and between January 1979 and January 1990. In January 1979 a total of 53 active completions existed in the study area. The average completion spacing within the study area was approximately 132 acres in January 1979. Of these original 53 completions a total of 22 were still active in January 1990. A total of 149 new completions were made between 1979 and 1990. In January 1990 the cumulative completion density for both active and inactive completions was approximately 90 acres for the Frio reservoirs. Of the 149 new completions 82 were still active in January 1990.

Reserve additions are derived from three sources: (1) new reservoirs that are deeper pool than the current production, (2) reservoirs already contacted in wellbores but not effectively drained by the current completion spacing, and (3) reservoirs that were previously bypassed or new reservoirs encountered by infield drilling as untapped reservoir compartments. A histogram of gas volume for the two timeframes illustrates the degree of reserve growth attributed to incremental drilling and completions (fig. 6). In January 1979 a recovery of 52 Bcf from 53 completions in 43 wells was projected. From 1979 to 1990 a total of 38 Bcf was produced, leaving 10 Bcf as the reserves remaining from the 52 Bcf projected in 1979. By comparison, 149 completions were made in 84 wells between January 1979 and January 1990 that added 48 Bcf of developed reserves to the projections made for completions active on January 1979. From these new completions a total of 30 Bcf was actually produced between 1979 and 1990, and an additional 18 Bcf was projected as remaining to be produced after January 1990 to an operational ending rate of 30 Mcfd per completion. The additional completions from January 1979 to January 1990 provided >90 % reserve replacement beyond the projected remaining developed reserves for all completions active in 1979.

Comparison of reserve estimates using a depth cutoff of 7,000 ft demonstrates the overprint of depositional system on incremental gas reserves. Because of the simple low-relief structure and consistent elevation across the study area, the 7,000-ft depth value approximates the transition from the middle Frio (<7,000 ft) to the lower Frio and Vicksburg Formations (>7,000 ft). Figure 7 is a histogram of reserve growth for the completions less than 7,000 ft deep as of January 1979. A total of 39 Bcf is projected as the remaining recovery for the gas reserves compared with a total of 70 Bcf as actually produced and estimated to be remaining as of January 1990. Actual production and projected reserves in January 1990 indicate that of the projected 39 Bcf a total of 27 Bcf was produced, and 10 Bcf is projected as remaining for the completions made before January 1979.

Figure 8 is a histogram of gas reserve estimates for the completions deeper than 7,000 ft. For the 11 completions made before January 1979 a total of 13 Bcf is indicated. Analysis of the completions between January 1979 and January 1990 deeper than 7,000 ft indicates an additional incremental 15 Bcf was estimated for 59 post-1978 completions within 35 wells. Of that 15 Bcf a total of 9 Bcf was actually produced, and an additional 6 Bcf is projected as the ultimate estimated recovery remaining for these completions.

The contrast in gas production between reserves shallower than 7,000 ft and those deeper than 7,000 ft is thought to reflect the major change in depositional setting associated with the reservoirs of the fluvial middle Frio Formation (<7,000 ft) in contrast to the deltaic-dominated depositional setting in the lower Frio and Vicksburg reservoirs (>7,000 ft). In summary, an aggressive infield drilling and recompletion program has demonstrated an incremental gas resource within a mature field. Depositional system, which strongly affects the magnitude of incremental gas resources, is also a key control on secondary (incremental) gas reserve growth.

REFERENCES

- Kosters, E.C., Bebout, D.G., Seni, S.J., Garrett, C.M., Jr., Brown, L.F., Jr., Hamlin, H.S., Dutton, S.P., Ruppel, S.C., Finley, R.J., and Tyler, Noel, 1989, Atlas of major Texas gas reservoirs: The University of Texas at Austin, Bureau of Economic Geology, 161 p.

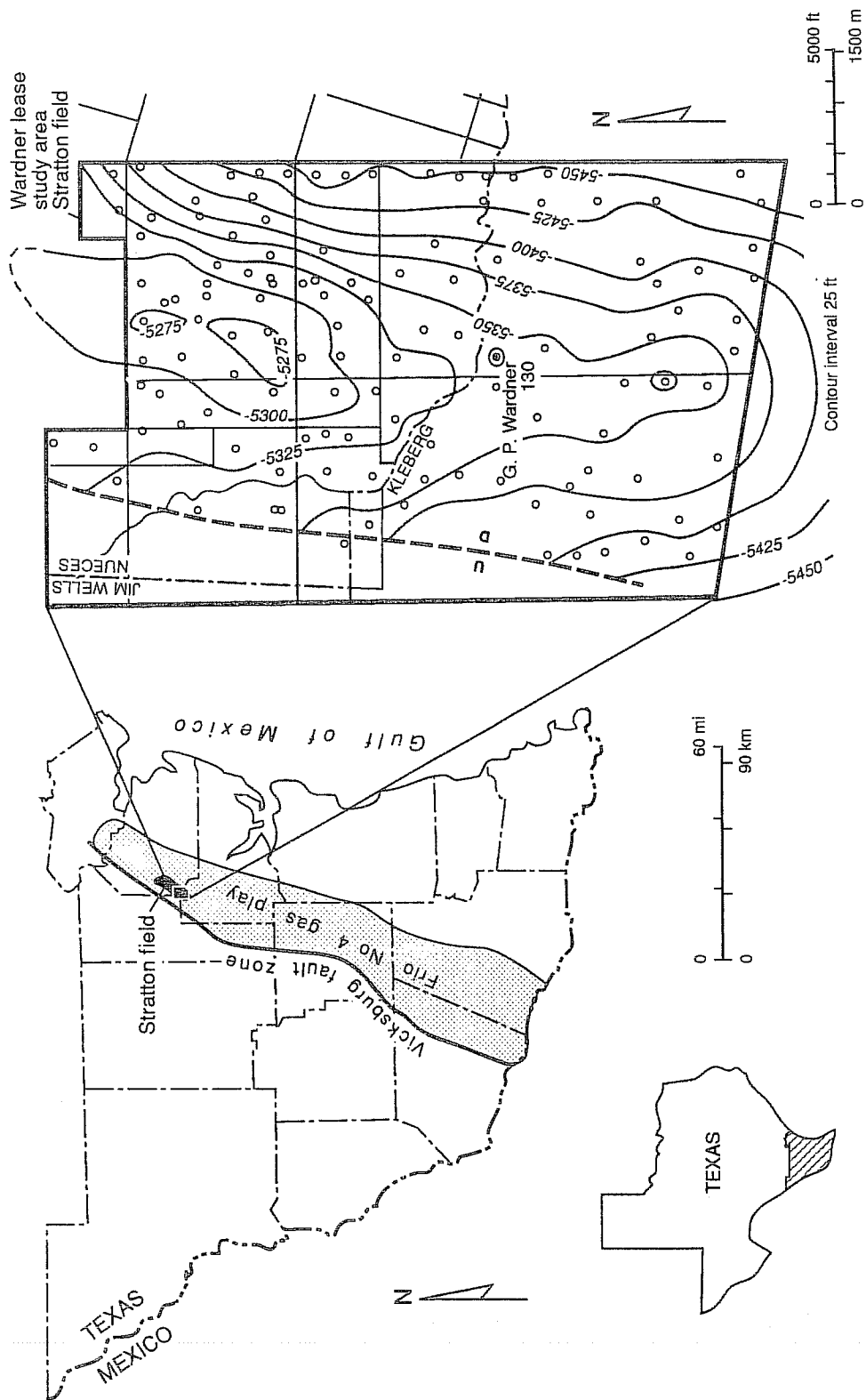


Fig. 1. Location map of Stratton field within the Frio fluvial-deltaic (FR-4) gas play and map of the Wardner lease study area.

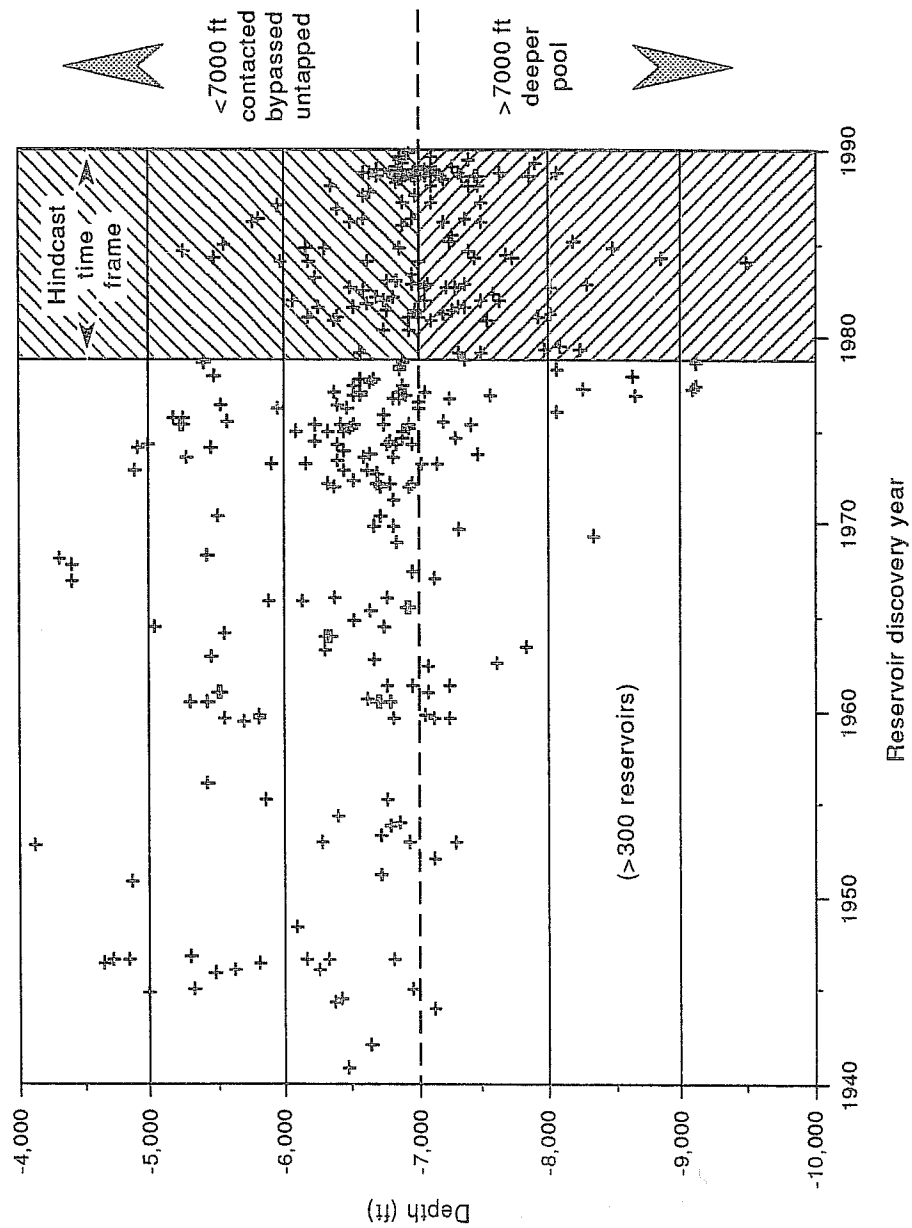


Fig. 2. Plot of discovery year of reservoir versus depth of the reservoir in Stratton field.

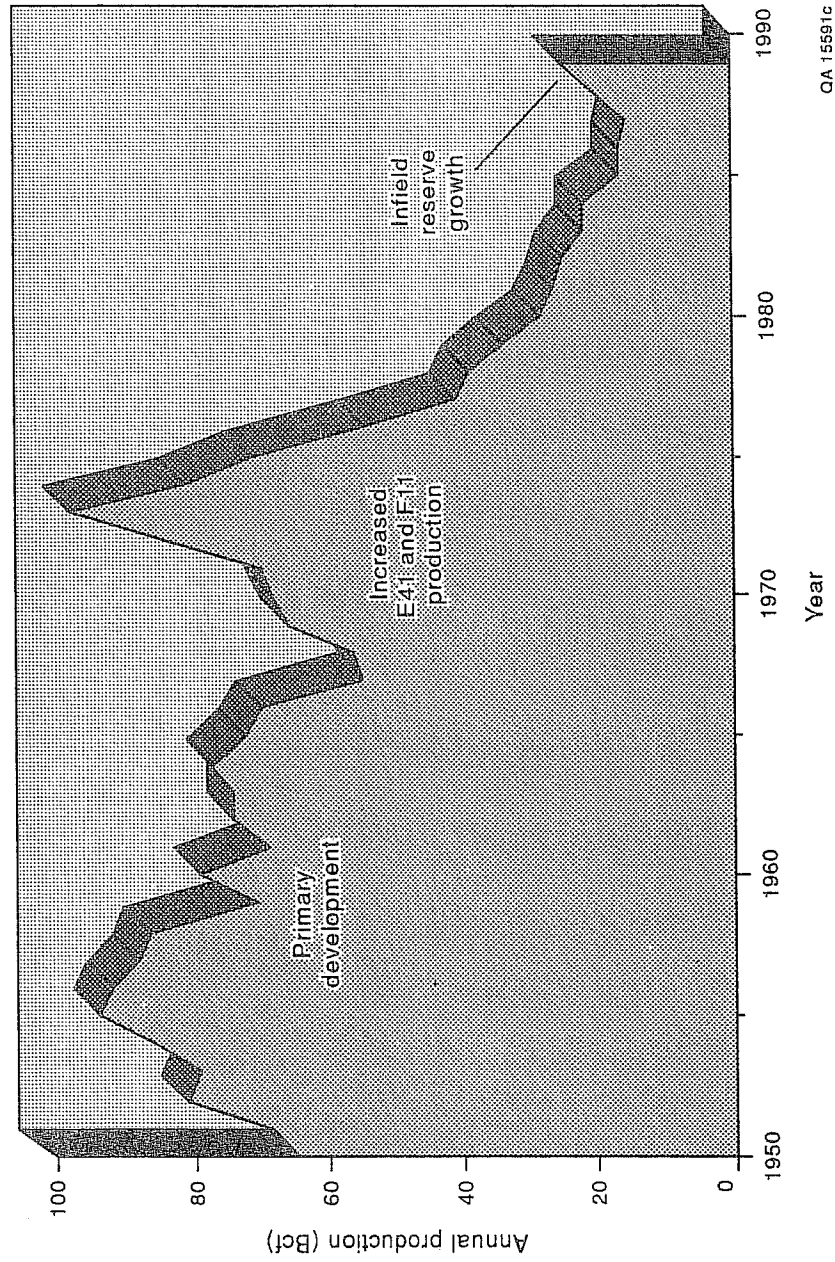


Fig. 3. Annual gas production of Stratton field from 1950 to 1990.

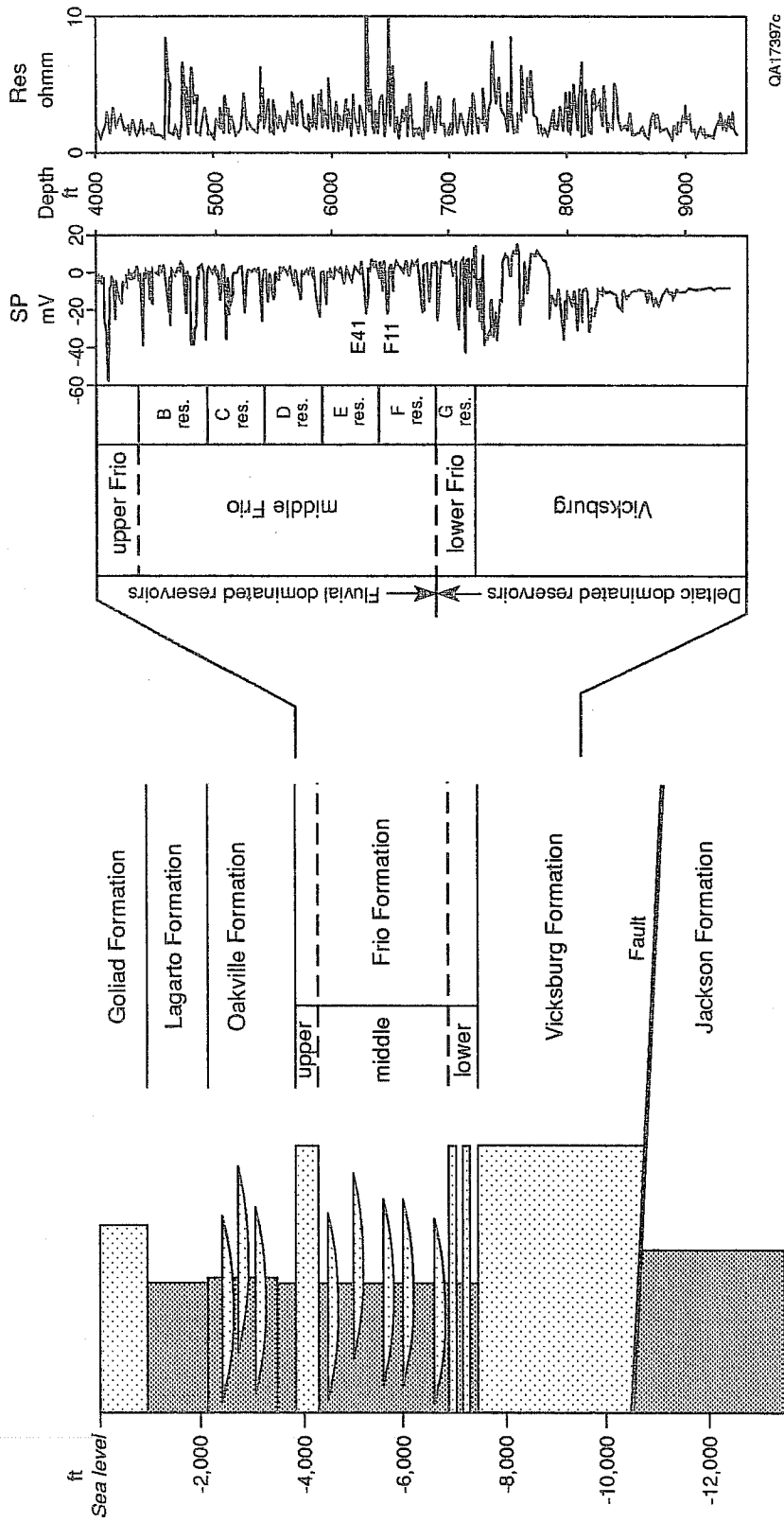


Fig. 4. Type well log from Wardner lease showing Frio and Vicksburg reservoir nomenclature.

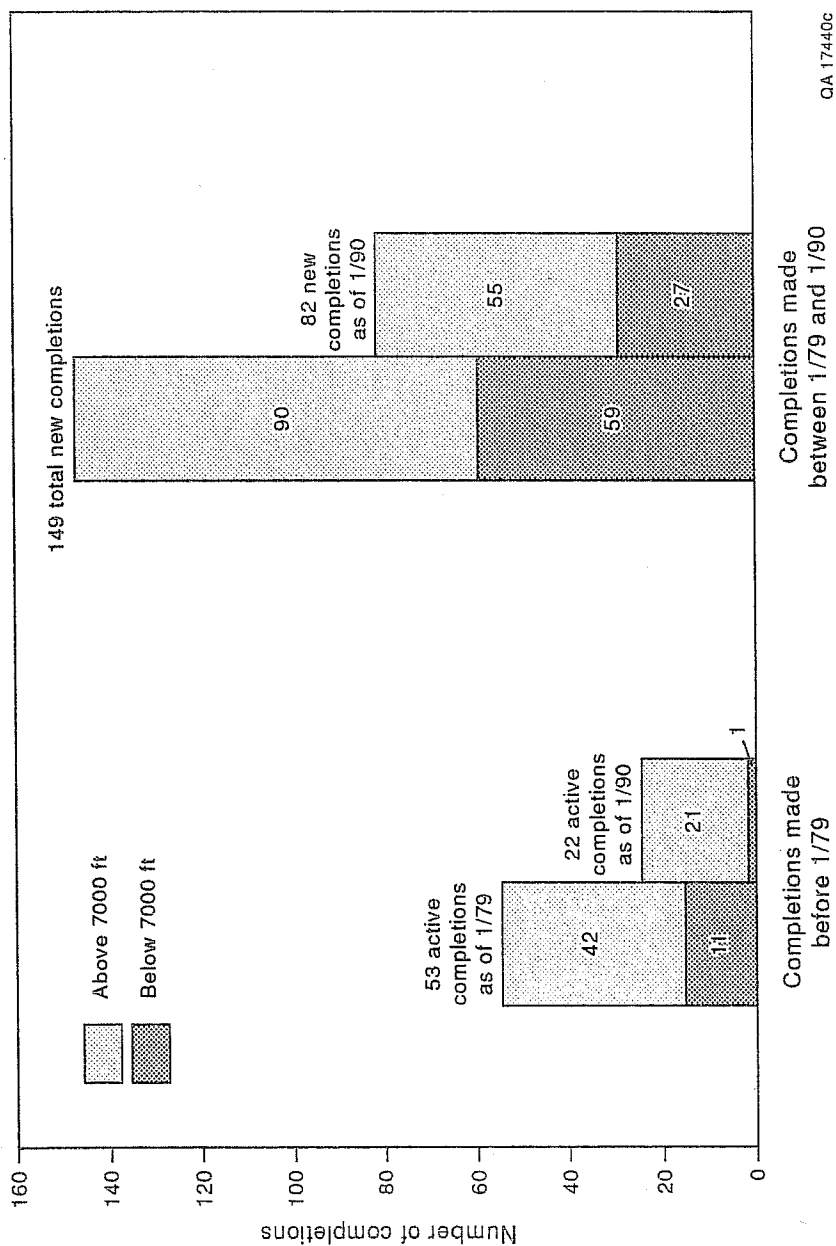
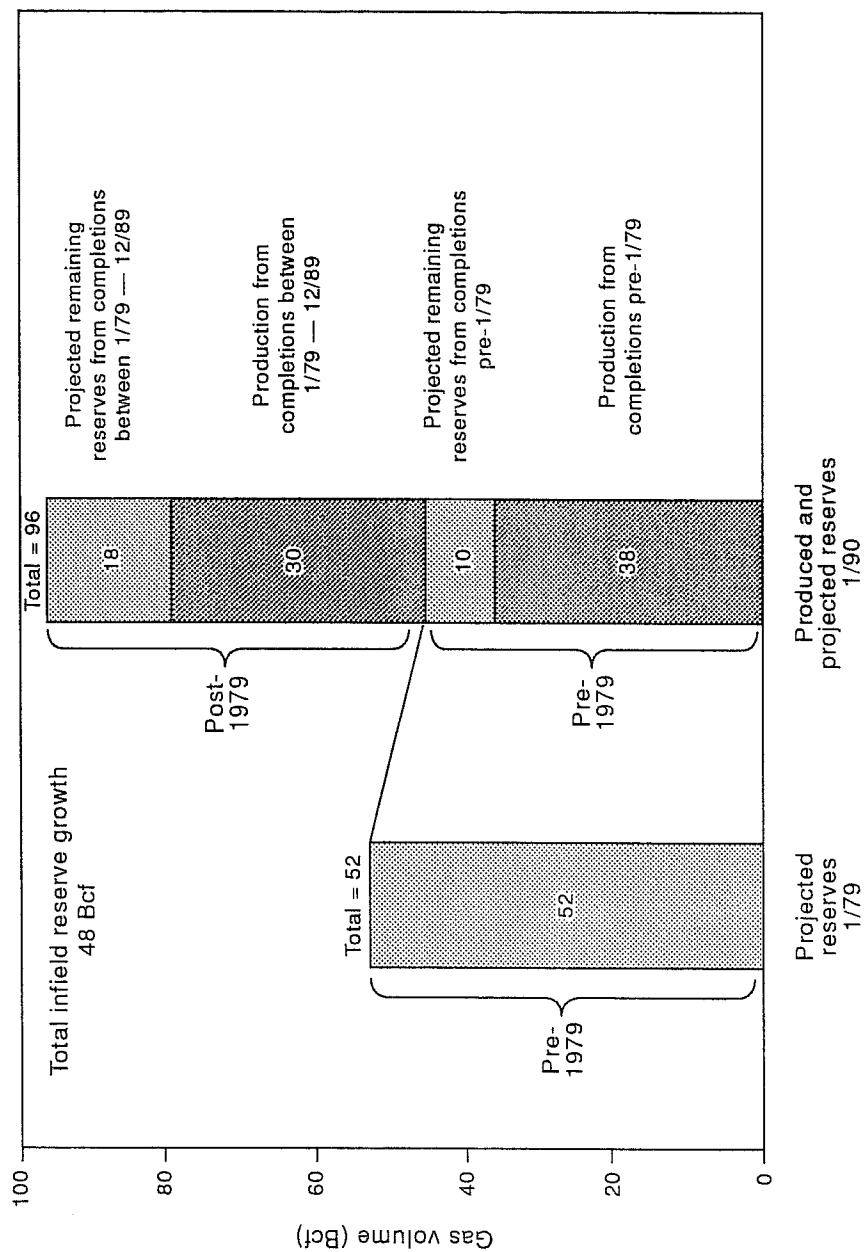
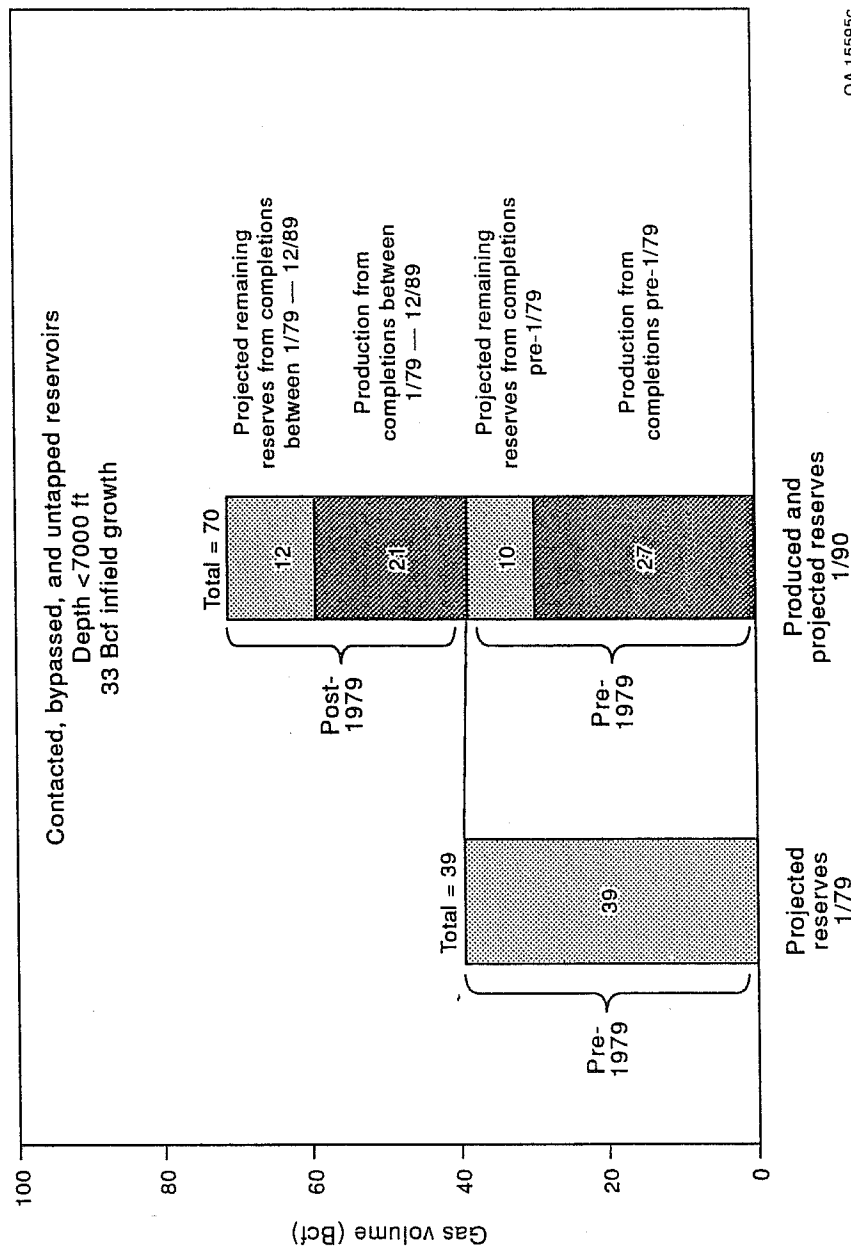


Fig. 5. Histogram of number of completions in the study area.



QA 15594c

Fig. 6. Histogram of total gas volume for all completions.



QA 15595c

Fig. 7. Histogram for gas volume for completions < 7,000 ft.

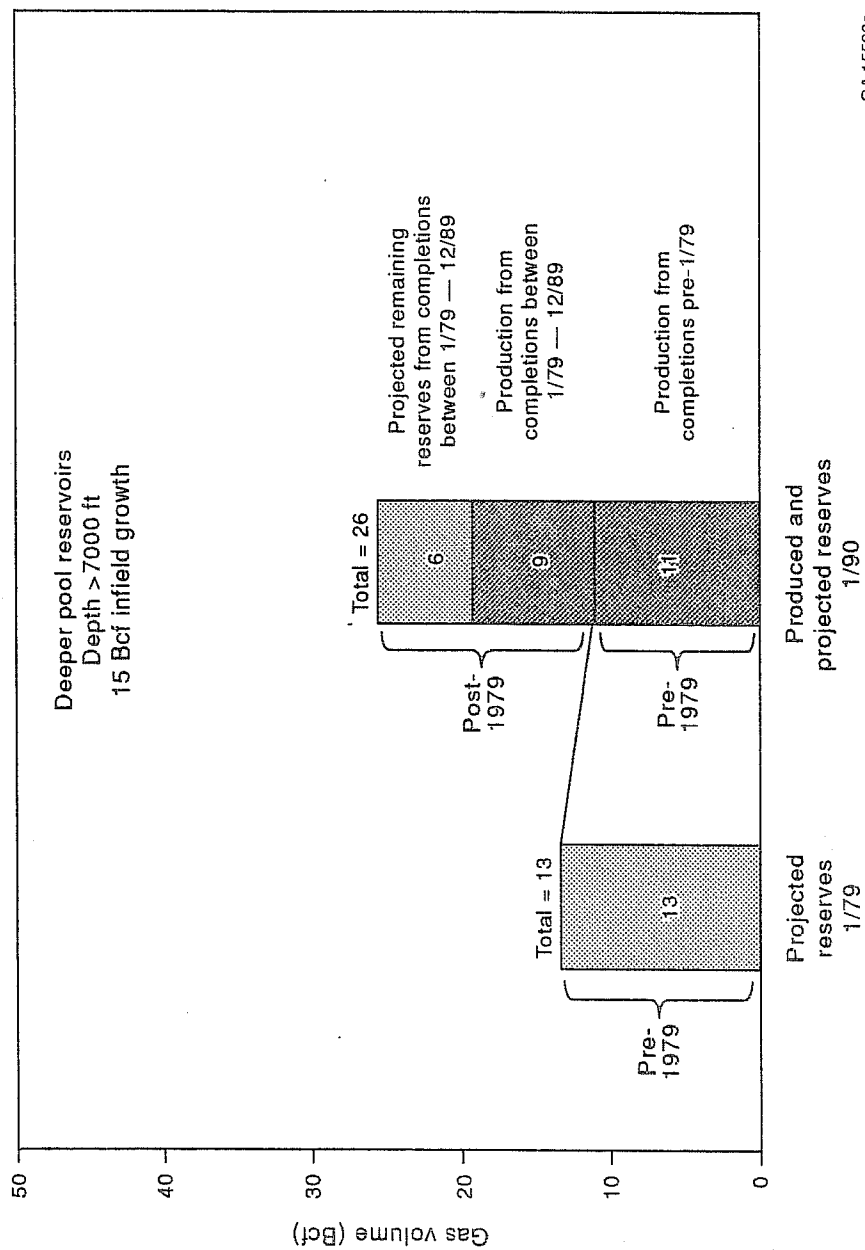


Fig. 8. Histogram for gas volume for completions >7,000 ft.

AN EXPERT SYSTEM FOR THE NETWORK MODELLING OF PORE STRUCTURE AND TRANSPORT PROPERTIES OF POROUS MEDIA

Ioannis Chatzis
Marios A. Ioannidis

Department of Chemical Engineering
University of Waterloo
Waterloo, Ontario, N2L 3G1

Apostolos Kantzas

Nova Husky Research Corp.
Calgary, Alberta

I. INTRODUCTION

The determination of transport and capillary equilibrium properties of sedimentary rocks, such as absolute and relative permeabilities, formation resistivity factor and capillary pressure curves, is of fundamental importance for the successful estimation of hydrocarbon reserves and for the design and application of production schemes. Despite the fact that much effort has been expended to theoretically simulate the aforementioned properties (1), the development of comprehensive predictive tools using microscopic pore structure parameters is still at its early stages. Consequently, the estimation of transport and equilibrium properties of reservoir rocks relies heavily on experimentation and on the use of empirical equations.

The purpose of this paper is to report on the development of an expert computer model, WATNEMO (WATERloo NETwork MOdel), which can be used to predict the transport and equilibrium properties of sandstones from readily available pore structure parameters. The performance of WATNEMO is illustrated by means of comparisons between the predicted and measured properties for a variety of sandstones. The most important features of the model are its rigorous formulation based on bond-correlated site percolation theory (2) and its ability to incorporate all the available pore structure information in a consistent manner (porosity, breakthrough capillary pressure/ absolute permeability, and photomicrographic information on pore structure).

II. SYSTEM DESCRIPTION

The pore structure of a reservoir rock is modelled as a cubic network consisting of pore throats and pore bodies of rectangular cross-section following respective pore size distributions. It is generally acknowledged that, the differences between the pore size distributions of various samples is the major cause of different macroscopic behavior(3). The problem of estimating the pore throat and pore body size distributions of different media is handled in WATNEMO by employing a set of deterministic and heuristic criteria. For each porous medium, the WATNEMO constructs a geometrically defined porous medium model according to the following rules:

- The number based pore throat size distribution is selected such that the pore throat size corresponding to the percolation threshold of the site percolation-bond correlated-cubic network leads to the same breakthrough capillary pressure as that measured in the real porous medium(2-5).
- The pore body size distribution is selected in such a manner, so that the average pore body size and the range of pore body sizes observed in pore casts of the real medium are also present in the simulated medium.
- The porosities of the real and simulated medium are identical.

The prediction of drainage capillary pressure curves for Hg-air or oil-water immiscible displacements is accomplished by using the generalized results of pore accessibility studies (2-4). Details of methodology used can be found elsewhere(2-4).

The prediction of absolute permeability and formation factor is performed by solving the linear electrical-resistor network problem for a fully saturated medium (5). Similarly, the drainage relative permeability curves are obtained by solving the analogous problem for a partially saturated medium, where the fluid distributions are dictated by the pore space accessibility results for oil-water displacement (6). In these computations, the individual conductances of pore throats and pore bodies are calculated using solutions of the appropriate momentum/ electric current transport equations. A simplified flow diagram, indicating the basic components of WATNEMO, is given in Fig. 1.

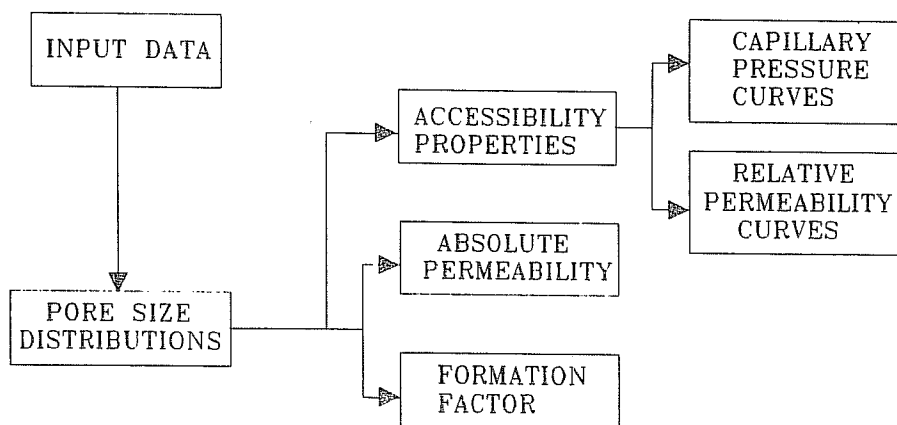


Fig. 1. Basic functions performed by the WATERloo NETwork MOdel.

III. RESULTS AND DISCUSSION

The potential value of WATNEMO in Computer Aided Core Analysis is best illustrated by comparing the model predictions to experimental results for various sandstones. The only input data required to predict transport and equilibrium properties of different samples using WATNEMO are: 1) the sample porosity, 2) the breakthrough capillary pressure, 3) the volume average pore body size and 4) the range of pore body sizes seen in photomicrographs of pore casts. The breakthrough capillary pressure and porosity can be obtained from conventional mercury porosimetry experiments.

The predicted drainage capillary pressure curves for Hg-air and oil-water displacements in a Berea sandstone are compared to the experimental ones in Fig. 2. The agreement for both cases is very good. The successful prediction of mercury porosimetry curves of sandstones using realistic pore structure information has important implications with regards to the characterization of porous media using mercury porosimetry experiments. In Fig. 3, the partitioning of pore volume of a simulated Boise sandstone into pore throats and pore bodies is compared to the "pore size distribution" that is obtained from the classical method of analysis(3). The inadequacy of the bundle-of-tubes model to describe the pore structure of sandstones is obvious. However, it is more important to note that WATNEMO may be useful in deconvolving the capillary pressure curves into information about the pore throat and pore body size distributions.

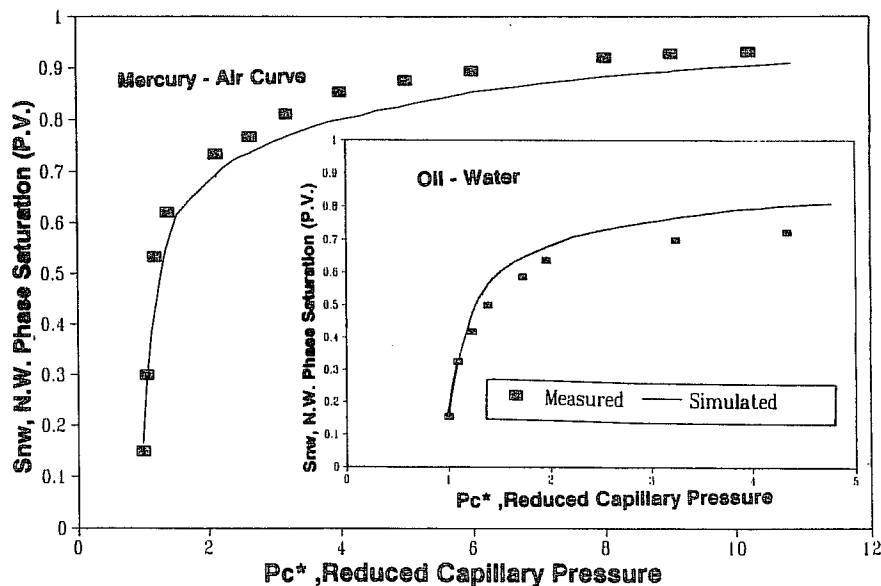


Fig. 2. Predicted vs. measured drainage capillary pressure curves of a Berea sandstone: (a) Mercury porosimetry; (b) Oil-water displacement.

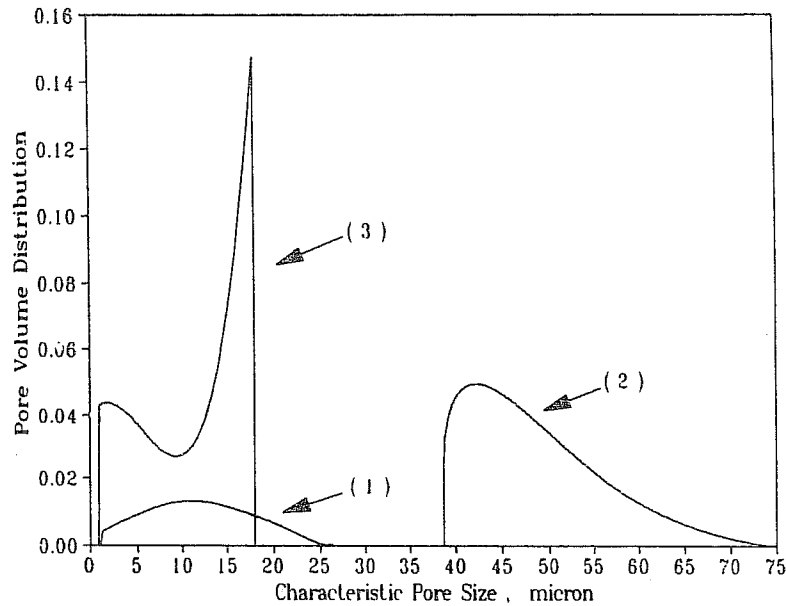


Fig. 3. Decomposition of model pore volume of Boise sandstone into its constituents: (1) Pore throat volume (20%); (2) Pore body volume (80%). Curve (3) is the result of differentiating the simulated intrusion mercury porosimetry curve.

The measured and the predicted drainage relative permeability curves of the same Berea sandstone sample are compared in Fig. 4. The successful prediction of both drainage relative permeability curves and drainage capillary pressure curves for oil-water displacement is strongly indicative of the appropriateness of the use of bond-correlated site percolation theory in combination with realistic estimates of the pore size distributions.

The measured and the predicted absolute permeabilities of 13 very different sandstones are compared in Fig. 5. The agreement is better than what could be expected from using empirical correlations(7). The prediction of the formation resistivity factor is accurate to within 20% of the measured values for sandstones with permeability higher than 200 mD. For lower permeability samples WATNEMO consistently overestimates the formation factor, probably because the conductance of clayey material is not taken into account in the model.

IV. CONCLUSIONS

An expert system (WATNEMO) was developed that is capable of approximating the pore structure of different sandstones from a minimum of information (porosity, breakthrough capillary pressure and photomicrographic data). Using this information, WATNEMO can successfully predict the absolute permeability, formation factor, drainage capillary pressure curves and drainage relative permeability curves of many different sandstones in a consistent manner. The results obtained provide strong indication that, upon further development, WATNEMO may become a useful tool for Computer Aided Core Analysis.

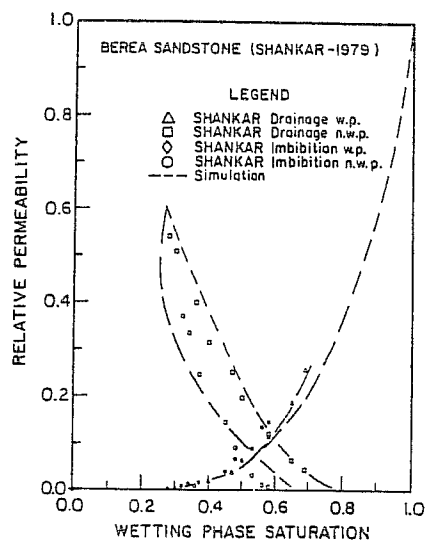


Fig. 4. Predicted vs. measured drainage relative permeability curves of Berea.

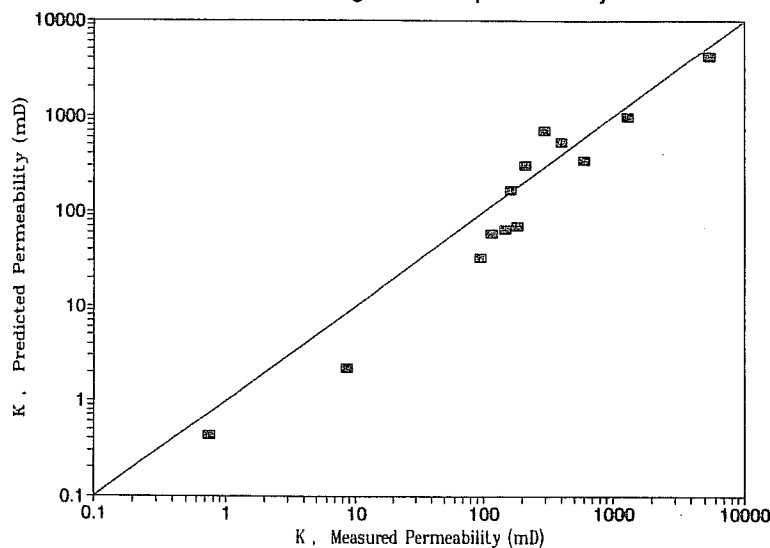


Fig. 5. Predicted vs. measured absolute permeabilities of 13 different sandstones.

REFERENCES

1. Adler, P.M., and Brenner, H. (1988). *Ann. Rev. Fluid Mech.* 20, 35.
2. Chatzis, I., and Dullien, F.A.L. (1985). *Int. Chem. Eng.* 25, 47.
3. Dullien, F.A.L., Porous Media: Fluid Transport and Pore Structure, 2nd Ed., Academic Press Inc. (1991)
4. Diaz, C.E., Chatzis, I., and Dullien, F.A.L. (1987). *Transp. Porous Media* 2, 215.
5. Ioannidis, M.A., and Chatzis, I. (1991). Submitted to *Chem. Eng. Sci.*
6. Kantzas, A., and Chatzis, I. (1988). *Chem. Eng. Commun.* 69, 169.
7. Kamath, J. (1988). *SPE paper No.18181*, 63th Ann. Fall Tech. Con., Oct.2-5, Houston.

FORMATION EVALUATION FOR IDENTIFYING SECONDARY
GAS RESOURCES: EXAMPLES FROM THE MIDDLE FRIO,
ONSHORE TEXAS GULF COAST BASIN¹

Jose' M. Vidal
William E. Howard

ResTech Houston, Inc.
Houston, Texas

Raymond A. Levey

Bureau of Economic Geology
The University of Texas at Austin

Effective formation evaluation is critical for evaluating producing and bypassed gas reservoirs in existing gas fields. As a part of the Infield Natural Gas Reserve Growth Project sponsored by the Gas Research Institute, The U.S. Department of Energy and the State of Texas, an integrated analysis of open hole and cased hole well logs, wireline pressure tests, combined with production tests results and core data analysis were used to evaluate Frio fluvial-deltaic sandstone gas reservoirs. Results for the study indicate that gas producing intervals can be identified using the methods described below.

Well logs were evaluated from older wells with limited logging suites and in more recent wells with complete logging

¹ Funded by the Gas Research Institute contract No. 5088-212-1718, the U.S. Department of Energy contract no. DE-FG-21-88MC25031 and the State of Texas through the Bureau of Economic Geology. The cooperation of Union Pacific Resources Company and Mobil Exploration and Producing U.S. Inc., and Oryx Energy Company is gratefully acknowledged.

suites. A shaly sand model (dual water method) was used in the formation evaluation. Computed results including shale volume, porosity, water saturation and empirical permeability were obtained from wells logged by different service companies. Figure 1 is an example of open hole evaluation for a typical middle Frio penetration. The perforated zone has a cumulative production of 48,144 mcf.

Because log responses differ among service companies, individual logs were corrected for environmental and borehole effects and standardized to the average field response. Figure 2 shows the standardization of a density log. Corrections for borehole washout were applied to the affected logs (density and neutron) using a model based on responses of other porosity dependent measurements. Figure 3 shows before and after results of the environmental and borehole washout corrections.

The values of formation water resistivity vary from .32 to .17 ohm-m at 75 F°. These values were determined from log data and from measurements of resistivity and salinity on 14 collected formation water samples. The measured formation water salinities were also corrected for the dilution problem associated with gas production.

The results of available core data analysis were used to calibrate log derived values. Figure 4 shows the agreement between the log derived porosity and shale volume vs. the core analysis results as well as displaying the irreducible water saturation derived by capillary pressure measurements. From core data a relationship was also obtained to predict permeability. Core permeability measurements revealed both high (>200 md) and low (<15 md) permeability sandstone reservoirs (see Figure 5). These two trends of permeability were incorporated into the computed log interpretation model.

Because many Frio reservoirs are gas depletion drive, identification of depleted zones is critical. Wireline pressure tests in open hole wells and short term production tests in cased hole wells are common techniques used to determine reservoir pressure. Some wireline formation pressures can be misleading due to tool defects, miscalibrations or incomplete pressure test sets. The validation of wireline pressures and close control of the operation at the wellsite is indispensable before selecting zones of interest.

One problem encountered obtaining valid formation pressure data is when insufficient setting time is allowed in order to measure stabilized shut-in wireline pressures. For example in Figure 6A, a 60 second wireline set leads a low pressure of 139 psi. By contrast, in Figure 6B, the tool was reset 1/2 foot higher in the wellbore and allowed to set for 251 seconds, yielding a more representative though not quite stabilized pressure of 3556 psi. A valid test is shown in Figure 7; here the tool was set for an adequate amount of time so that the shut in pressure has stabilized and can be used with confidence.. Another problem is depletion of the reservoir from the time that the open hole pressure was taken to the time that the zone was perforated and production tested.

For cased hole wells with incomplete logging suites a logging program was designed to complement the data already available. The cased hole interpretation model was applied to a 39 year old well that penetrated to the base of the middle Frio formation in Stratton Field. The original open hole logs consisted only of an electrical survey and a few sidewall core samples. A cased hole logging program was designed to fully evaluate the well. Pulsed neutron, gamma ray, dipole sonic, temperature, noise and cement bond logs were acquired using currently available technologies.

Porosities were derived from the combination of the compressional sonic porosity and the pulsed neutron porosity. These logs respond in a similar manner in oil zones as well as in zones with high water saturations. Gas presence is easily detected by observing the characteristic crossover of porosities (sonic > neutron porosity). Gas crossover is also observed in the normalized far and near pulsed neutron count rates. Combining that information with the sigma derived cased hole water saturation, and comparing it to the original open hole water saturation, it was possible to identify potential gas productive zones. Figure 8 shows the results in two gas zones, E41L was perforated and produced 316 mcf/d gas with 412 psi.

In conclusion: An interpretation model that identifies gas bearing intervals has been developed for open hole and cased hole wells in Frio sandstone gas reservoirs. This method can be applied to other sandstones with similar depositional environments. The method integrates logs with core analysis results and utilizes wireline pressures and production test results.

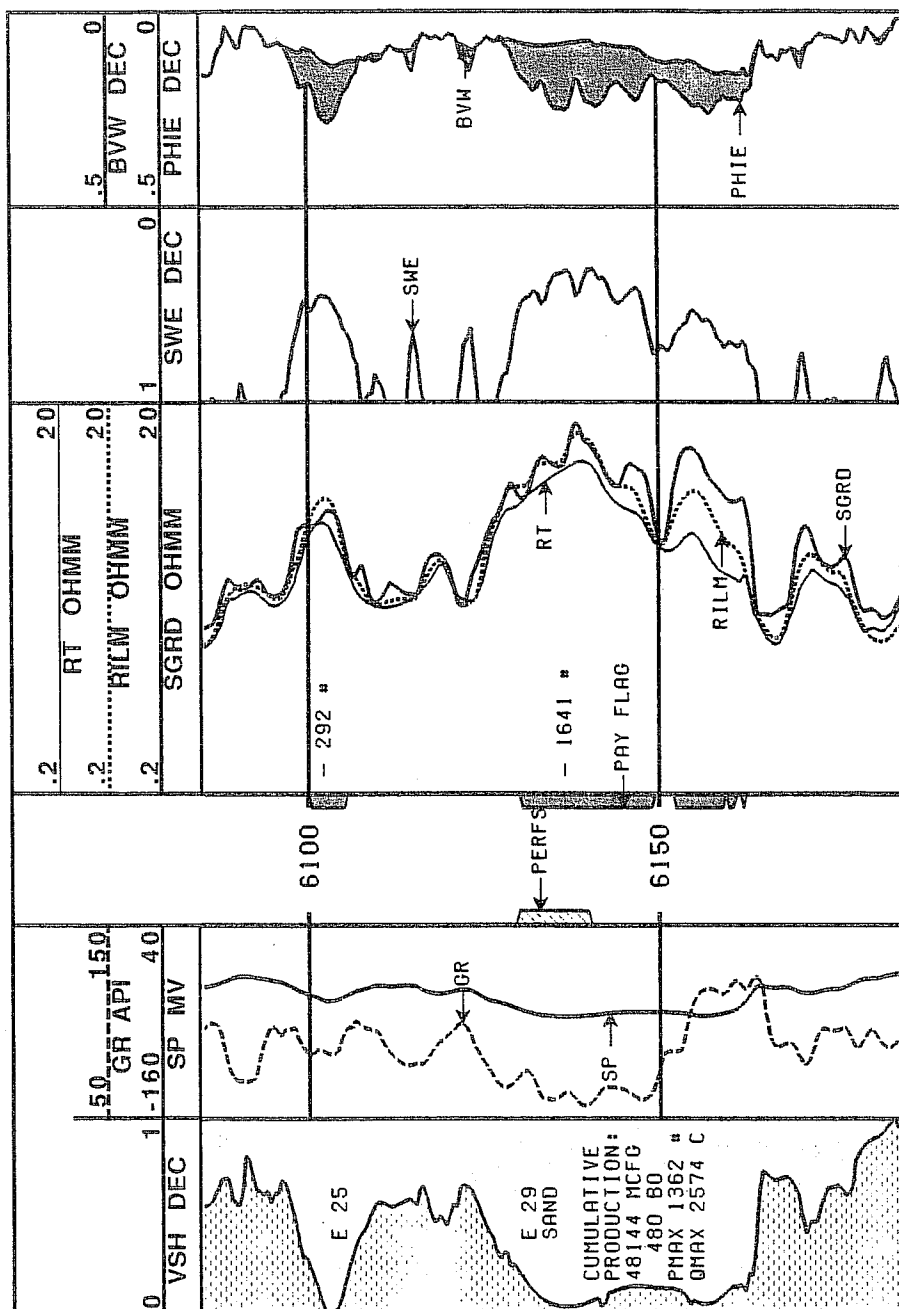


Figure 1. Open hole evaluation.

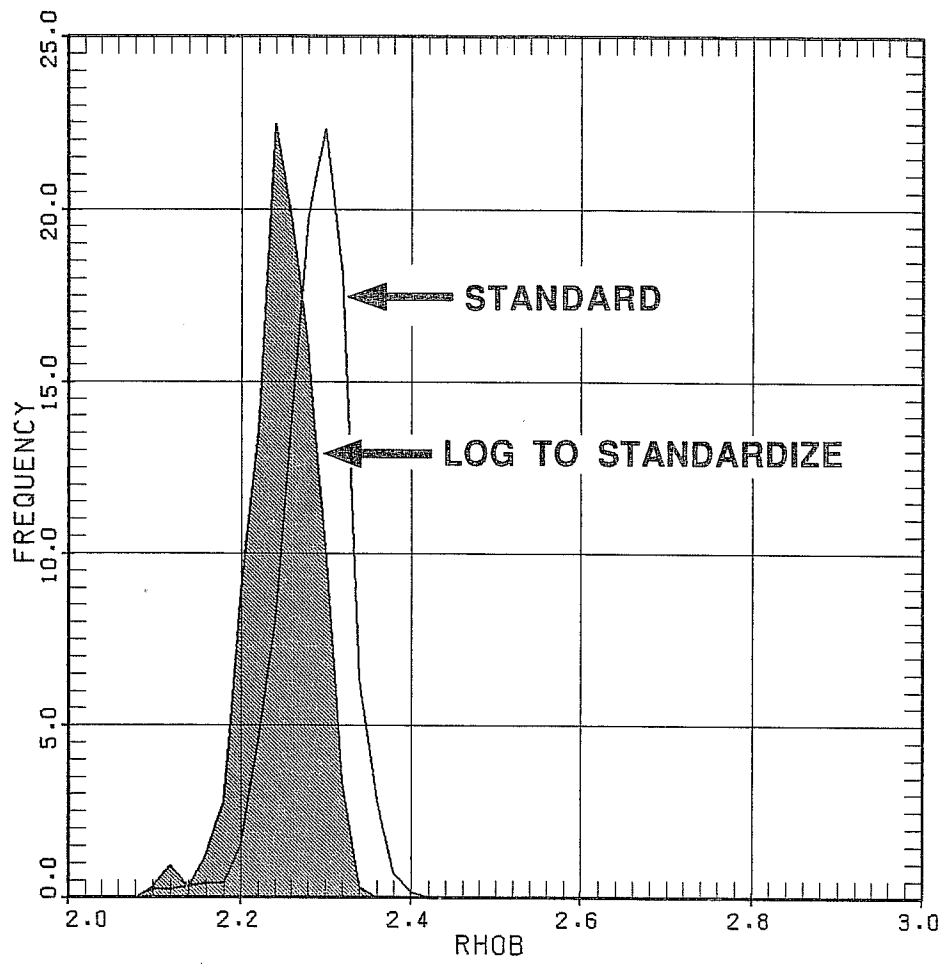


Figure 2. Standardization of density log to fieldwide standard.

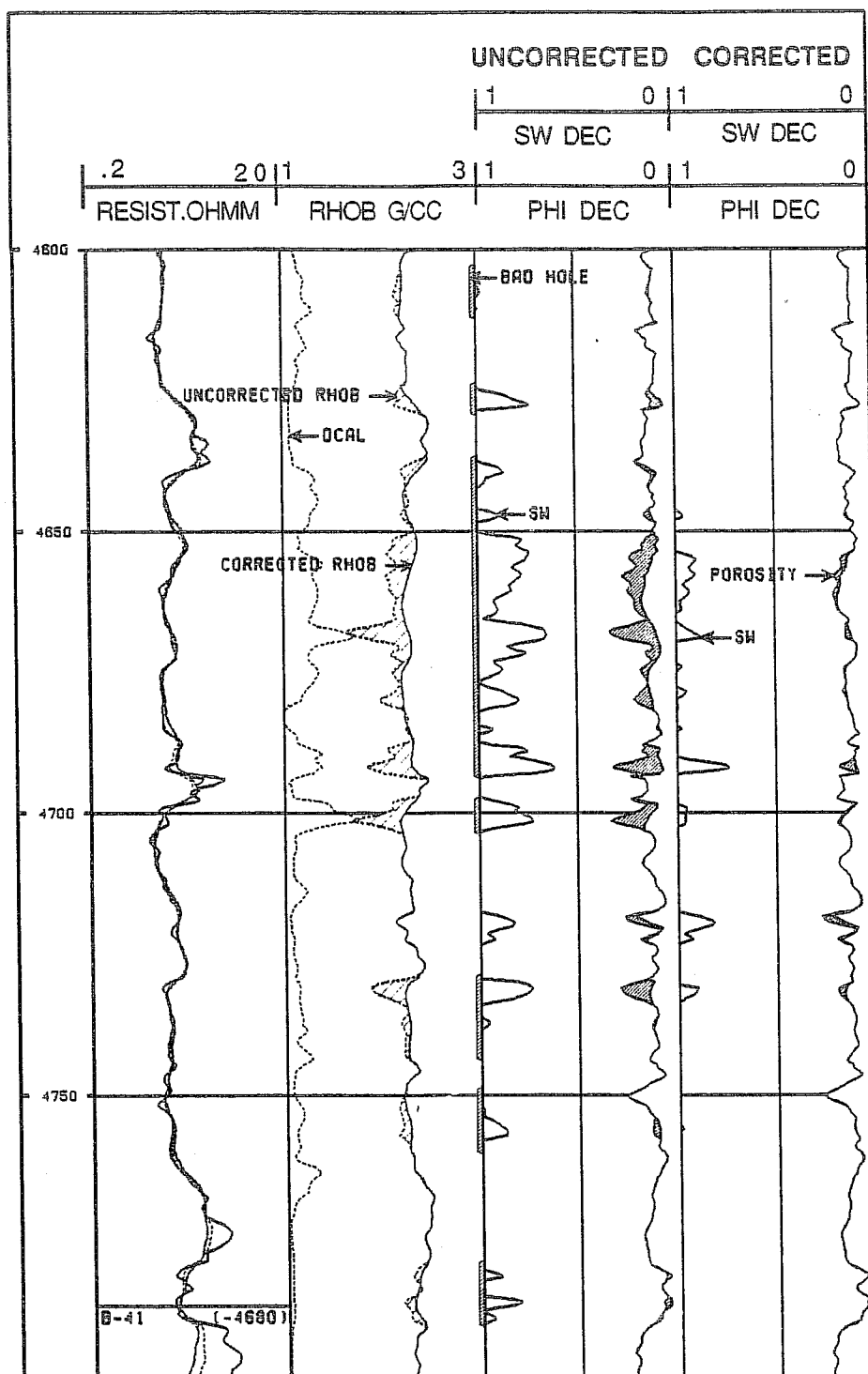


Figure 3. Log corrections in washouts.

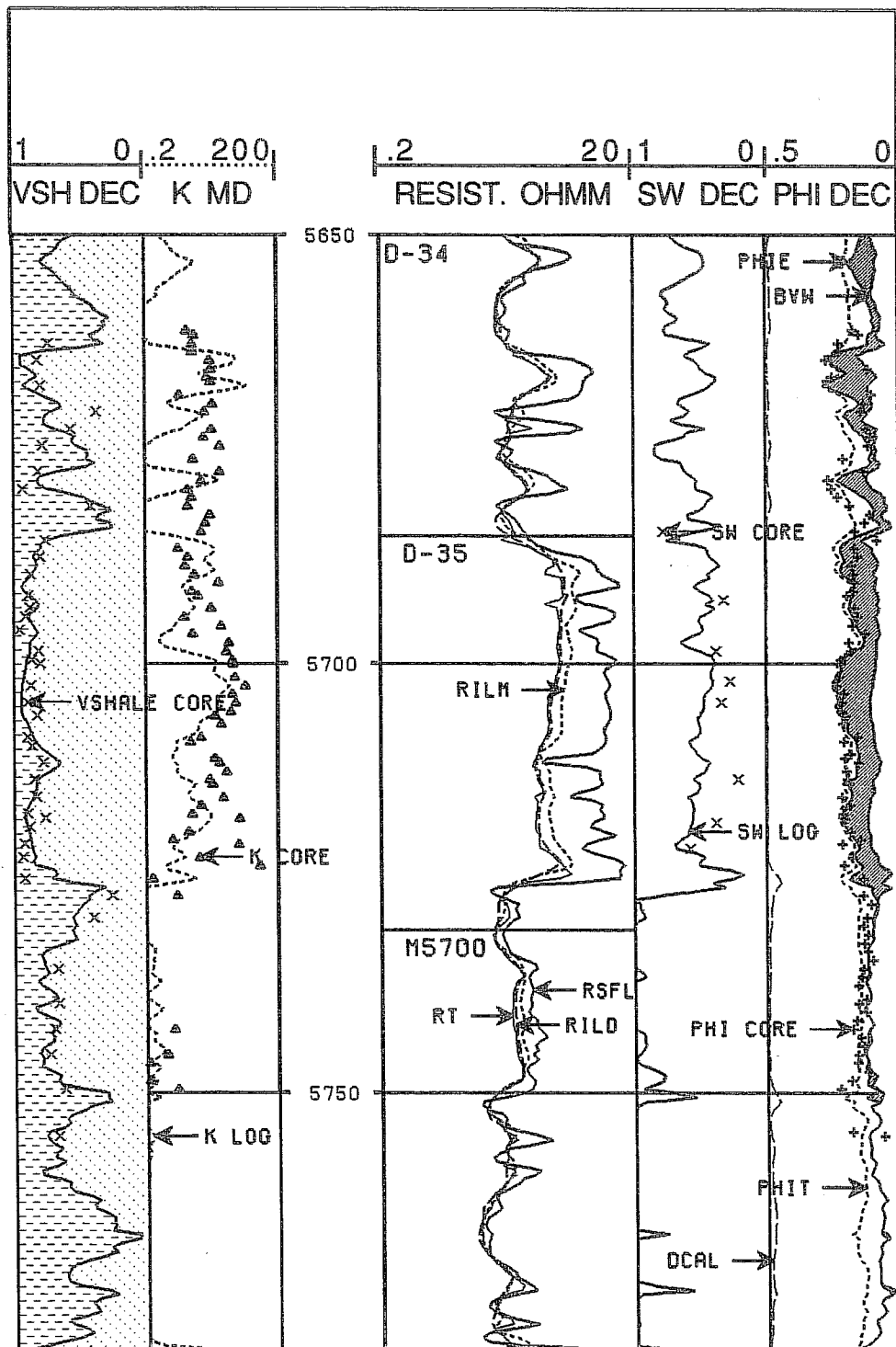
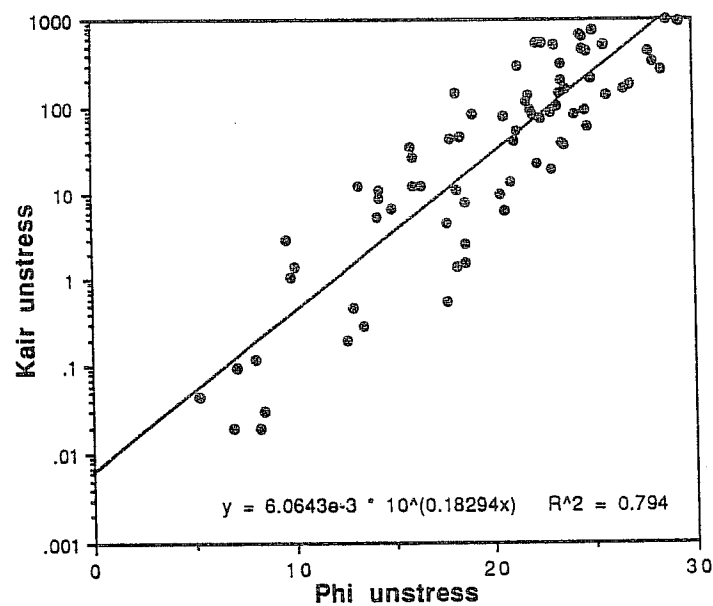


Figure 4. Comparison of results with core analysis.

Porosity and Permeability of Middle Frio Reservoirs Stratton Field, Kleberg and Nueces Counties

Higher Permeability Reservoirs



Lower Permeability Reservoirs

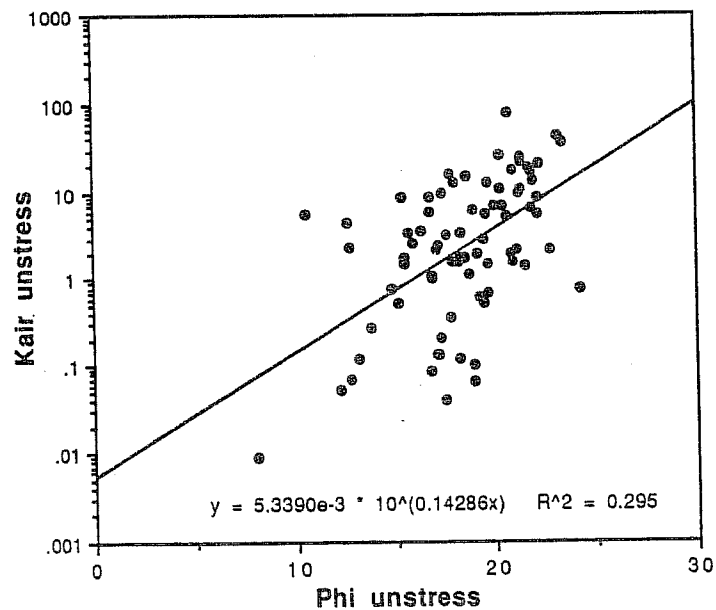


Figure 5.

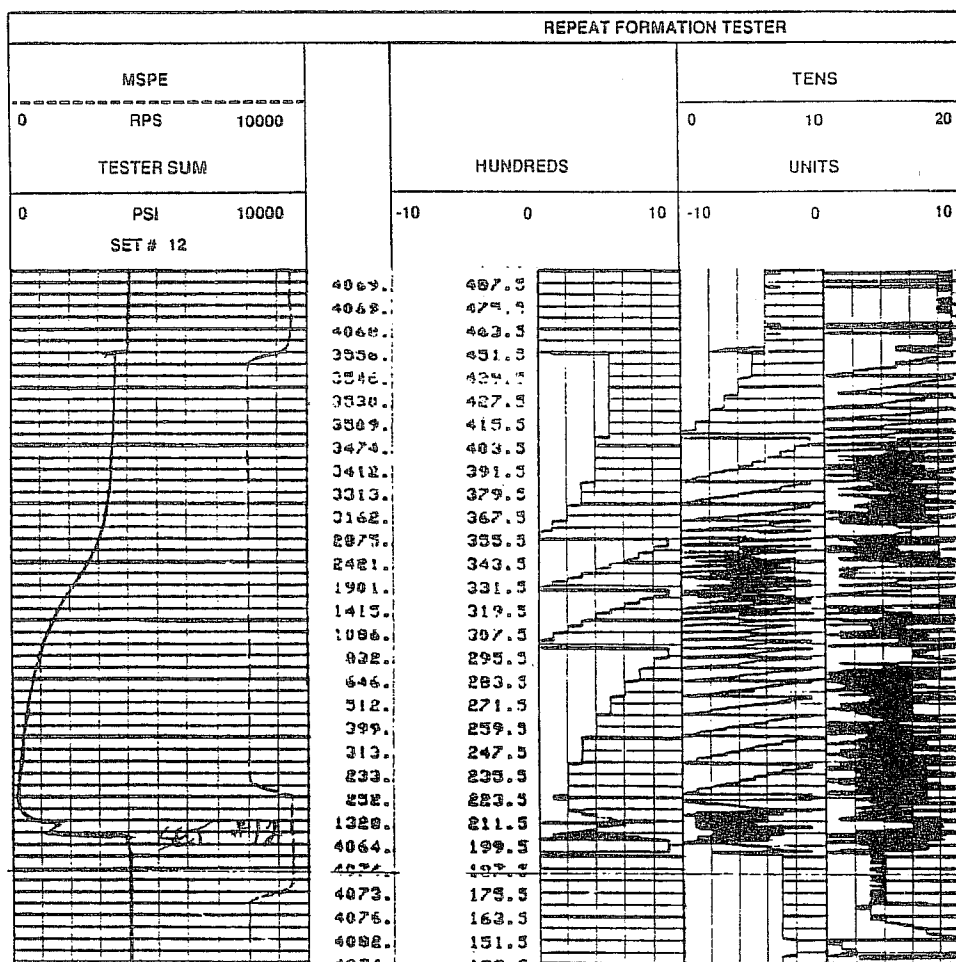


Fig. 6b

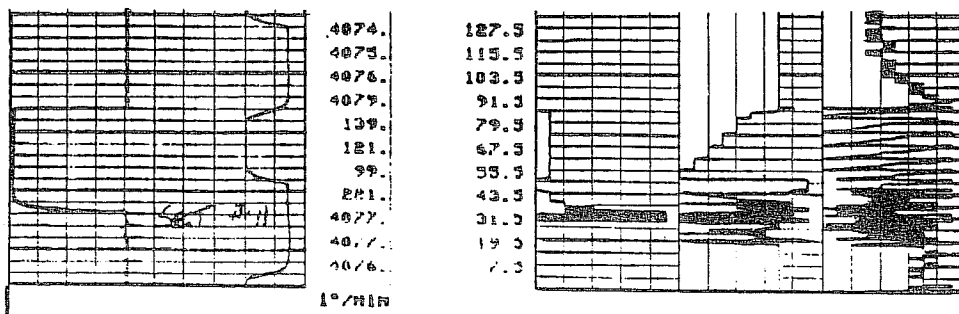



Fig. 6a

Incomplete sets.

		THOUSANDS		TENS			
		0	10	20	0	10	20
		HUNDREDS		UNITS			
		-10	0	10	-10	0	10
TESTER SUM							
PRESS		10000					
	04901	00154					
	04901	00154					
	04902	00154					
	04902	00154					
	04903	00154					
	04605	00152					
	04604	00142					
	04604	00131					
	04604	00121					
	04604	00110					
	04595	00100					
	04590	00079					
	04560	00060					
	04330	00050					
	00040	00047					
	01000	00037					
	04931	00026					
	04553	00016					
	TEST TIME						
	DEPTH		07341.0				
TESTER SUM							
PRESS		10000					

		THOUSANDS		TENS			
		0	10	20	0	10	20
		HUNDREDS		UNITS			
		-10	0	10	-10	0	10
PAD RETRACT							
PRETEST							
PRETEST							
PAD SET							

Figure 7. Valid wireline formation set.

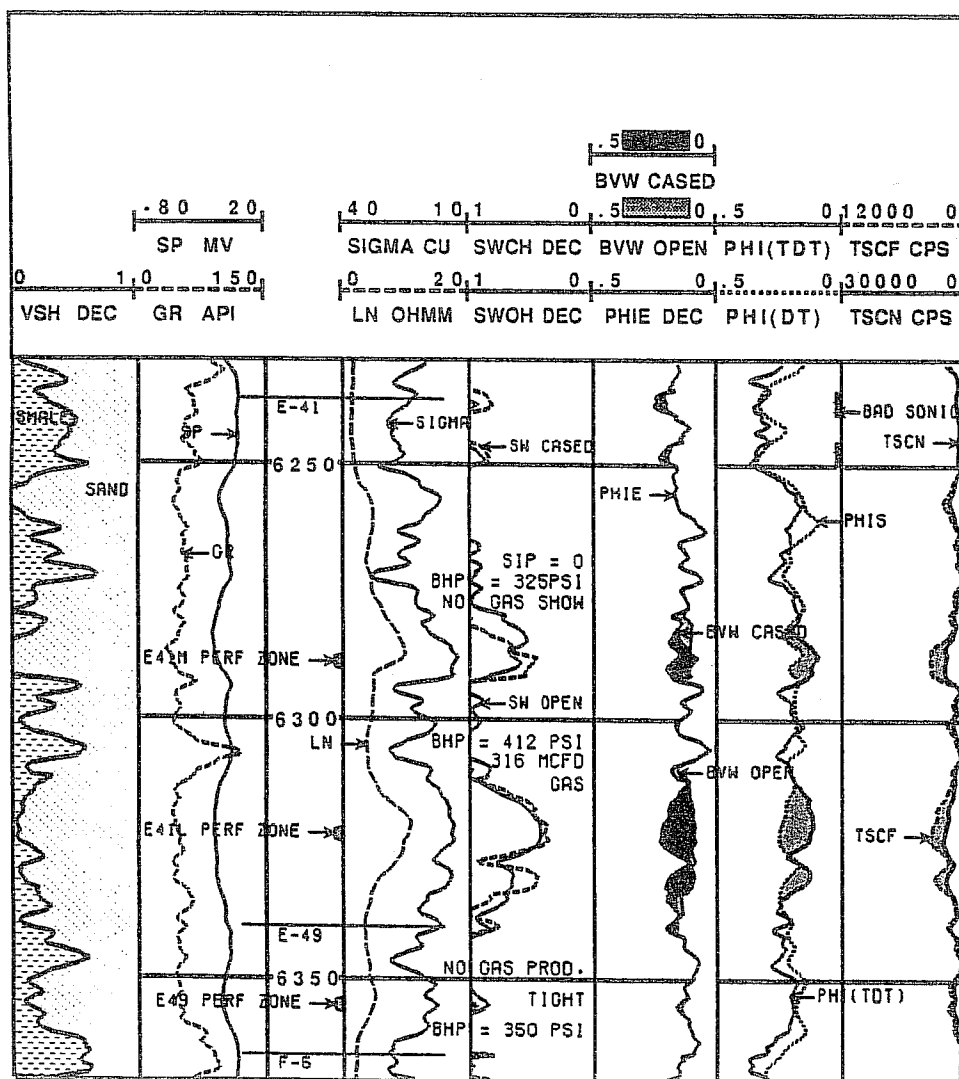


Figure 8. Cased hole evaluation.

RESERVOIR CHARACTERIZATION AND GEOSTATISTICAL MODELING--THE INTEGRATION OF GEOLOGY INTO RESERVOIR FLOW SIMULATION: EAST PAINTER RESERVOIR FIELD, WYOMING

By D. S. Singdahlsen
Chevron USA, Inc.
Denver, Colorado 80201

ABSTRACT

The East Painter structure is a doubly plunging, asymmetric anticline formed on the hanging wall of a back thrust imbricate near the leading edge of the Absaroka Thrust. The Jurassic Nugget Sandstone is the productive horizon in the East Painter structure. The approximately 900-foot thick Nugget is a stratigraphically complex and heterogeneous unit deposited primarily by eolian processes in a complex erg setting.

The high degree of heterogeneity within the Nugget results from variations in grain size, sorting, mineralogy, and degree and distribution of lamination. The Nugget is comprised of dune, transitional toeset, and interdune facies, each exhibiting different porosity and permeability distributions. Facies architecture results in both vertical and lateral stratification of the reservoir. Dune set orientations within the Nugget control directional permeability trends in the reservoir. Facies discontinuities, fractures, and faults offset the permeability trends in parts of the field.

Adequate representation of reservoir heterogeneity is the key to successful modeling of past and future production performance. In addition, detailed geologic models, based on depositional environment, must be integrated into the simulation to assure realistic results. Geostatistics provide a method for modeling the spatial reservoir property distribution based on the geologic model developed for the Nugget and the reservoir variability observed at East Painter. Results of detailed core and log analysis of dune set orientation, geometry, and directional permeability trends are imposed on directional variogram models resulting in both vertical and lateral correlation structures for the reservoir. Thus, vertical and lateral reservoir variability is integrated to characterize the spatial distribution of reservoir properties. Conditional realizations, based on the calculated variogram models, are used to combine the large scale reservoir heterogeneity with fractally generated, stochastic, small scale, variability.

INTEGRATED FIELD, ANALOG, AND SHELF-SCALE GEOLOGIC MODELING OF OOLITIC GRAINSTONE RESERVOIRS IN THE UPPER PENNSYLVANIAN KANSAS CITY GROUP IN KANSAS (USA)

John A. French, W. Lynn Watney, J.C. Wong, and W.J. Guy, Jr.
Kansas Geological Survey and the Department of Geology,
the University of Kansas, Lawrence, Ks 66047

I. INTRODUCTION

Significant quantities of unswept mobile oil are present in existing Pennsylvanian fields in the Mid-Continent region of the United States. To improve our ability to characterize such hydrocarbon reservoirs, surface and shallow subsurface analogs of these reservoirs are being investigated.

At and near the outcrop belt in southeastern Kansas, the lower Missourian Bethany Falls and Mound Valley limestones both contain oolitic grainstones similar to the lithofacies that produce from these units farther west. Depositional sequence analysis of these units suggests that 1) at least two cycles of relative sea-level change controlled the vertical distribution of porosity zones within this succession, and 2) the character and distribution of reservoir-scale grainstone buildups within these two depositional sequences were also influenced by pre-existing depositional topography.

II. OCCURRENCE OF RESERVOIR-TYPE UNITS

A. Description and Depositional Sequence Analysis of the Study Interval

The Bethany Falls and Mound Valley limestones of the Kansas City Group contain reservoir-type oolitic grainstones. These units are interpreted to be the highstand systems tracts of distinct depositional sequences, herein termed the Swope and Mound Valley sequences

(Figure 1). In the study area, the Swope sequence ranges in thickness from 31 ft to 44 ft (9.5 m to 13.4 m). The upper portion of this sequence is the upper Bethany Falls, which is variably developed and consists of generally porous, cross-bedded, ooid-biocl原因 grainstone and well-washed packstone. The upper surface is overlain in at least two cores by a mudstone unit that is interpreted to be a paleosol. The Bethany Falls Limestone is interpreted to be a regressive deposit that represents shallowing marine water and eventual subaerial exposure.

The Mound Valley sequence overlies the uppermost Swope carbonate unit. Where most completely developed, the Mound Valley sequence contains a zone of high-porosity oolitic and bioclastic grainstone and well-washed packstone that is analogous to reservoir lithofacies. Most of the Mound Valley should probably be considered as a highstand systems tract deposit that developed in a relatively shallow-water, high-energy setting.

B. Controls on Reservoir Distribution

Both the Swope and Mound Valley sequences contain porous oolitic zones in their upper parts (Figure 1) that are similar to lithofacies that comprise many of the hydrocarbon reservoirs that occur in the equivalent K zone in central and western Kansas.

The lowermost carbonate-dominated Missourian sequences (the Hertha, Swope, and Dennis) overlie the Pleasanton Shale (Figure 1). Oolitic grainstones within these two depositional sequences tend to be thickest and best developed along an eastward dipping paleoslope created by depositional thinning of the underlying Pleasanton Shale, presumably in response to prevailing higher-energy conditions. Areas of thick, lobate Bethany Falls Limestone range from about 1 to 3 mi (1.6 to 4.8 km) in width (north-south) and some are at least 10 mi (16 km) long (east-west). These oolitic lenses that trend normal to an underlying depositional slope resemble the tidally influenced oolitic sand bars that occur on the modern Bahamian platform.

A series of cores and associated wireline logs was acquired at well spacings near and under 40-acres. Strata in the same bar deposit crop out less than 1 mile from the core locations. The best development of porous oolitic carbonate in the Swope sequence occurs in the central portion of individual bars, where these lithofacies are up to 14 ft (4.3 m) thick, and the thickness of grainstone reaches almost 20 ft (6 m) (Figure 2). Porous oolite in the Mound Valley sequence is up to about 6 ft (1.8 m) thick and

13 T25S R21E

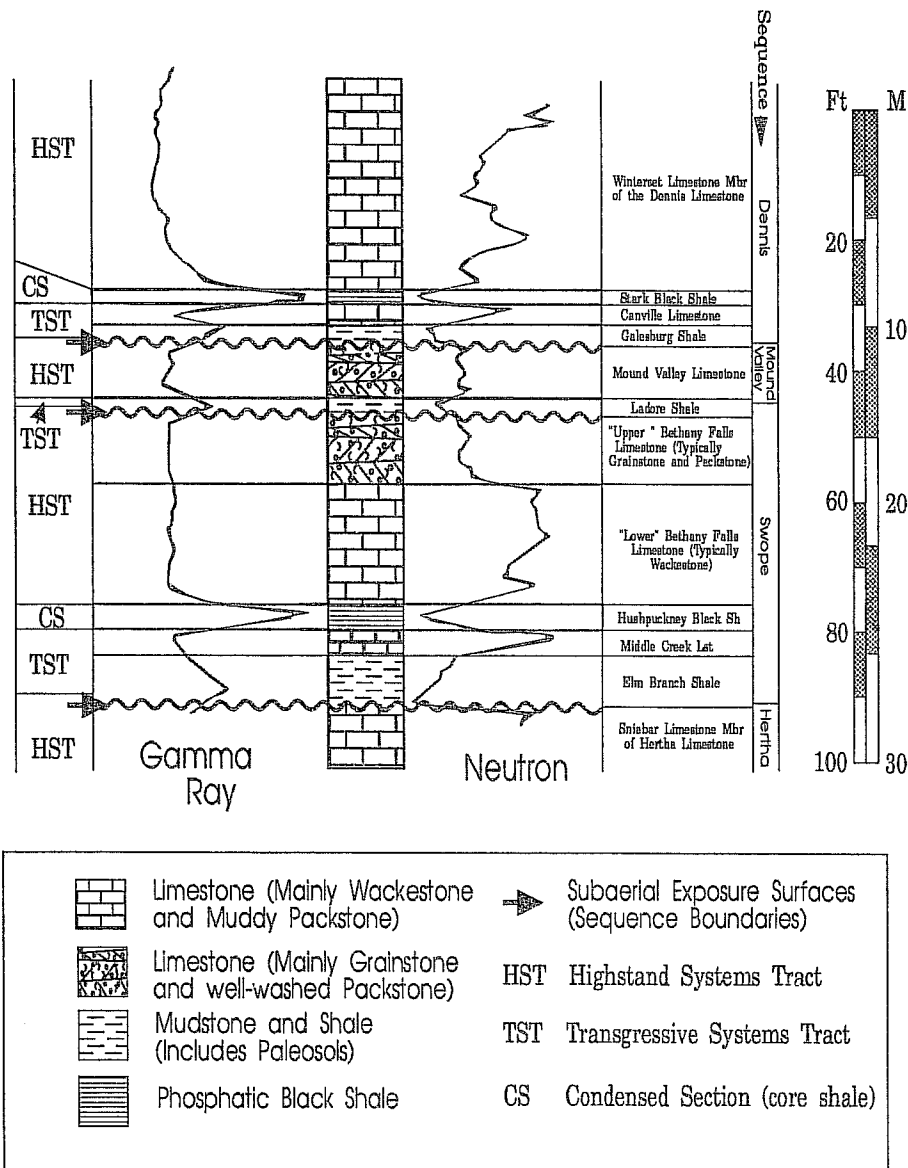


Figure 1. Representative gamma ray-neutron log and stratigraphic column of study interval in west-central Bourbon Co., Kansas. The grainstones and packstones of the Bethany Falls and Mound Valley limestones are the focus of this paper. Inferred depositional sequences and systems tracts are also shown.

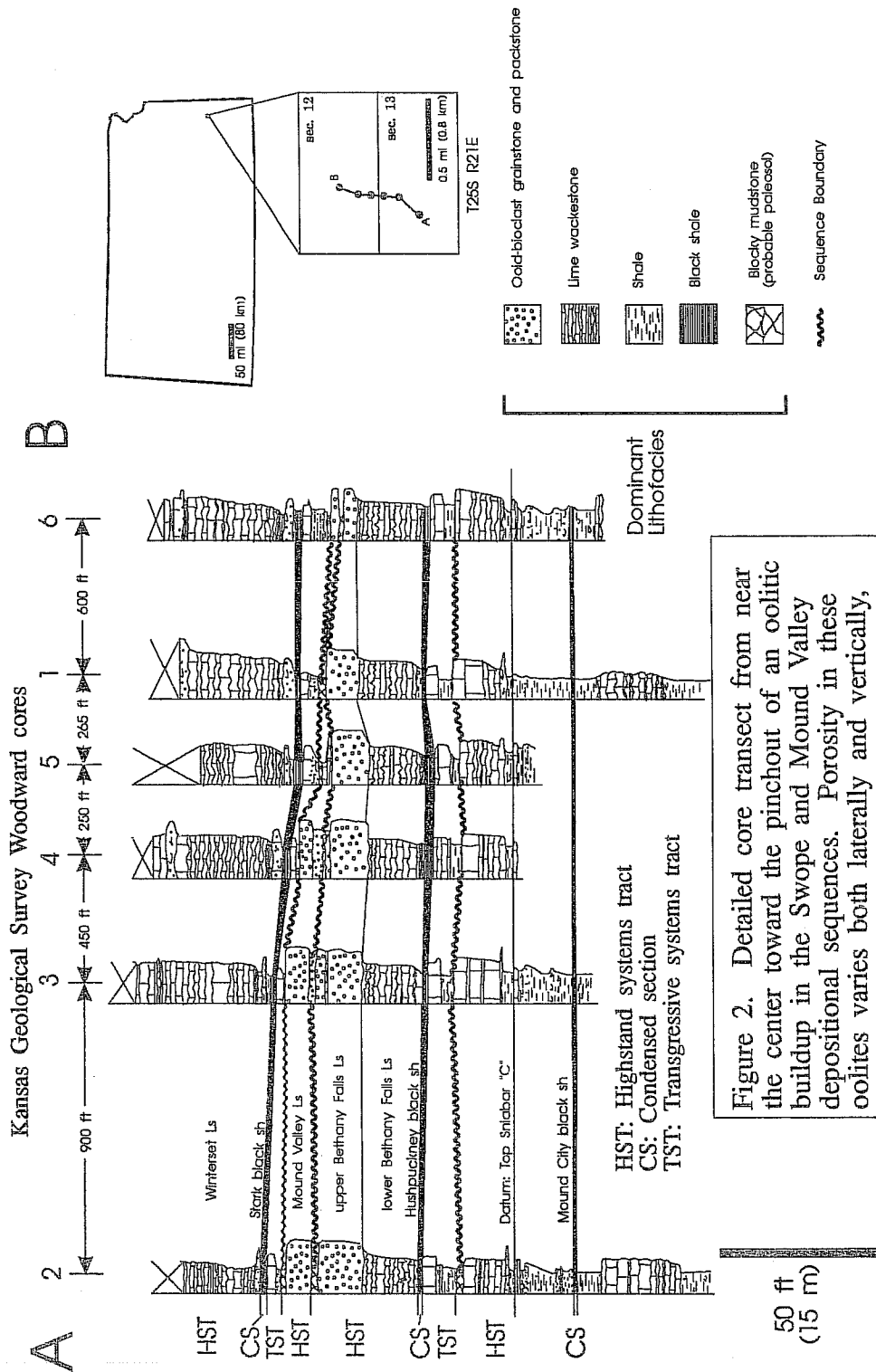


Figure 2. Detailed core transect from near the center toward the pinchout of an oolitic buildup in the Swope and Mound Valley depositional sequences. Porosity in these oolites varies both laterally and vertically,

is thickest where it overlies one of the best-developed bars in the Swope sequence. Interbar areas are essentially devoid of porous lithologies.

The Mound Valley oolite contrasts with the Bethany Falls oolite in both original grain size, grain composition and diagenesis. The differences in texture and the resultant porosity and permeability distribution within these oolites are significant, but generally result in only subtle differences in the response of wireline logs. Commingled production from juxtaposed oolites could permit fluid to selectively flow thorough the more permeable lower zone. Furthermore, the thin, discontinuous tight limestone or shale interval developed between the oolites could hydraulically isolate the zones, at least locally. This recognition in an oil field could provide additional potential for recovering bypassed oil via completion and/or treatment methods tailored to a given reservoir.

III. CONCLUSIONS

Carbonate grainstones similar to those that form important Missourian oil and gas reservoir facies are present in equivalent units at and near the outcrop belt in southeastern Kansas. Reservoir-type lithofacies are present in the highstand systems tracts of two distinct carbonate-dominated depositional sequences. At least two porous, oolitic zones, separated vertically and laterally by non-porous lithologies, are present. Their deposition was controlled by fluctuations of relative sea-level that were probably glacial-eustatic. In addition, the geometries of porous zones within each depositional sequence appear to have been influenced by pre-existing topography. These relationships provide evidence for predicting reservoir attributes in equivalent depositional sequences and shelf position in the deeper subsurface.

IV. ACKNOWLEDGEMENTS

Thanks is given to Paul Enos and Robert Goldstein for providing both logistical and conceptual ideas. This paper was prepared with the support of the U. S. Department of Energy (DOE Grant No. DE-FG22-90BC14434). However, any opinions, findings, conclusions, or recommendations expressed herein are those of the author and do not necessarily reflect the views of the DOE. This work is part of the ongoing Ph.D. research being done by John French at the University of Kansas.

CHARACTERIZATION OF RESERVOIR
HETEROGENEITIES FROM OUTCROP AND
WELLS (UPPER TRIASSIC FLUVIATILE
SANDSTONE, CENTRAL SPAIN).

Yves Mathieu
and
HERESIM Group

Institut Français du Pétrole
BP 311
92506 - Rueil Malmaison - France

François Verdier

Gaz de France DETN
93211 - La Plaine Saint Denis - France

I. INTRODUCTION

This paper deals with the initial phase of a project concerning reservoir heterogeneities, named PHEDRE (an IFP/GDF project). It includes an outcrop study and a well survey. All the results obtained on this field example constitute one of the available data banks used by HERESIM group (HEterogeneities REservoir SIMulations) for geostatistical studies.

II. OUTCROP STUDY

A 9 km-long cliff, located in central Spain (Ciudad Real province) has been analyzed. The 35m-thick series belong to the Upper Triassic continental red beds, deposited along the easter border of the Paleozoic Iberian

Meseta. Several geologic and geometric criteria determined the choice of this site:

- analogies with the subsurface case study (age, environment, sand body geometry),
- reliable key beds,
- continuous outcrops along a very long, sinuous, lowly tectonized and easily accessible cliff,
- presence of an open plateau just behind this cuesta, where wells could be drilled.

This part of the study was subdivided into three phases: data acquisition, interpretation and processing.

A. Data acquisition

A detailed lithological interpretation was made of the whole cliff, based on an atlas of 160 high-definition photographs. It was associated with a systematic topographic survey.

A practical facies code based on sandstone clay content (Facies 1 to 3), shale deposit subenvironment (Facies 4 to 6), carbonate presence (Facies 7) was used for the lithological interpretation. About 1000 measurements were performed during the topographic survey.

B. Data interpretation

The geologic series is subdivided into five lithostratigraphic units. On one hand, four fluviatile units, are composed of various channelized reservoir sand bodies and their associated floodplain deposits. On the other hand, a median lacustrine unit is made of purple shales and carbonates, including the main key bed. The sedimentology is typical of Triassic red beds, and the sand body geometry results from the evolution of fluviatile patterns correlated with base level variations (meandering, braiding).

C. Data processing

The cliff lithological draft was rectified by using various topographic methods. The obtained document was discretized along 942 digitized 10m-spaced vertical lines, considered as virtual wells. Hence, these were directly usable for geostatistical studies.

III. WELL SURVEY

A. Well data

Eleven wells (eight cored and three bored), 60 m-deep, were spudded on the plateau according to geologic and geostatistical criteria (less than 300 m spacing). The well grid gave a subsurface equivalent of the cliff section and allowed to extrapolate the observations. A complete data set is available for each well (composite logs, cores, petrophysical measurements, and core photographs)

B. Well data interpretation

It was necessary to establish a link between cliff lithofacies and electrofacies. For example, on logs it is important to discriminate between floodplain and plug shales because the size of the heterogeneities induced by these various argillaceous deposits, is quite different. To obtain this link, the following procedure was adopted:

- creation of a lithologic column for each cored well,
 - attribution of a cliff lithofacies code number to each lithologic interval,
 - calibration of the logging responses with these intervals,
 - creation of a lithofacies column for the three bored wells.

C. Comparison between outcrop and subsurface cross-sections

Without the cliff section interpreted, it was difficult to obtain a reliable and detailed representation of sand body architecture. In consequence, all the subsurface cross sections related to the cliff were strongly influenced by the cliff observations. In this context, it appears that many precautions are necessary to have a satisfactory drawing of sand bodies on an hectometric scale.

IV. CONCLUSION

The result was the acquisition of a large set of data, from an outcrop equivalent to a 5 km-long oilfield in fluviatile series. This is the compulsory first step to make geostatistical calculations for low and medium heterogeneities.

GLOBAL SEDIMENTARY DATABASES AS ENGINEERING RESOURCES

By Jim Myers
Department of Electrical Engineering
University of Houston
Houston, Texas 77004

ABSTRACT

Quantitative geologic knowledge is now expanding at its maximum rate. Analysis of engineering data on earth formations cannot be undertaken efficiently without access to this volume of knowledge in depth.

This access will become practical when engineers and geoscientists begin submitting their data, opinions, and questions to large scale databases. The breadth of questions to be posed and answers to be sought defies most other approaches.

The engineer exploiting natural resources is a natural colleague of the geoscientists, with their traditions and cultures of examination, description, and imagination. The engineer's quantitative results and evaluations are legitimate geologic data. The geologists' hierarchical systems of classification, for example, hold great promise as scientific schema for creating databases. These systems hold great potential to organize engineering data for later retrieval. The development and maturity of engineering and scientific concepts will be accelerated by use of these structures.

Thus engineers and geoscientists can complement each other to allow analysis far beyond local trends and rules of thumb. The availability of several extensive international electronic mail networks and structured query languages are likely structures for cost-effective data entry, retrieval, and query.

These structures are available, yet largely unimplemented, for the fast and effective transfer of data among reservoirs of similar sedimentary and/or diagenetic histories. It is also likely that transfer methods will be developed for marginally similar reservoirs.